# An Electron Paramagnetic Resonance (EPR) Study of Battery and Functional Materials

Jacob Spencer

A Thesis submitted for the degree of Doctor of Philosophy

School of Chemistry
Cardiff University

March 2021

# Acknowledgements

First and foremost, I would like to gratefully acknowledge Prof. Damien Murphy for the opportunity to undertake this PhD, his continuous support, and encouragement throughout this journey.

My thanks must also be expressed to Dr. Luciana Gomes Chagas, and to my previous supervisors, Dr. Noelia Cabello Moreno and Dr. Peter Ellis, for allowing me to visit JMTC, their insights during progress meetings and continuous support throughout the projects.

To Dr. Andrea Folli and Dr. Emma Richards, a special thanks for your advice and guidance, in addition to your assistance performing W-band and Pulsed EPR measurements. To the rest of my colleagues in the EPR group, past and present; Thanks for your company, and for making lab work so enjoyable.

I also want to acknowledge Dr. James Stevens, Dr. Nick Carthey and Dr. Hong Ren in addition to the rest of the JM staff I have worked with, for the opportunity to work on a range of interesting projects and materials. In particular, for their helpful discussions and advice during site visits to JMTC, progress meetings, and for the provision of samples.

My thanks also go to the following: Dr. Christopher Perry for performing the geometry optimisation calculations, and Dr. James Stevens for performing the UV measurements in Chapter 3; Danielle Merrikin, Prof. Simon Pope, for performing the photoluminescence measurements in Chapter 4; Dr. David Morgan for performing the XPS measurements in Chapter 4; The JM battery materials group for the additional characterisation data in Chapter 6; CHEMY and PHYSX workshop staff for making the prototype cells in Chapter 7; and Dr. Richard Wingad for access to the glovebox.

To my family and my partner, thanks for your continuous love and support throughout the last four years.

Finally, I would like to acknowledge Johnson Matthey and the EPSRC for funding the studentship, without which the work outlined in this Thesis would not have been possible.

# Abstract

The optimisation of solid-state functional materials towards the desired redox activity, optical or magnetic properties is fundamental in the understanding and development of important industrial materials. These properties are generally afforded by the inclusion of metal ions, point defects, or other local centres that can participate in single-electron transfer processes. Electron Paramagnetic Resonance (EPR) spectroscopy is clearly a powerful, but often under-utilised tool in their characterisation and development.

Chelating exchange resins (CERs) are a widely used technology for metal extraction in aqueous acidic media. A systematic CW EPR study was performed on a range of model complexes to identify uptake and speciation of $Cu^{2+}$ within two commercial chelating exchange resins, Dowex M4195 and CuWRAM.

Rare earth activated phosphors have long been of interest owing to their efficient luminescent properties and tuneability, for a variety of optical applications. A series of commercial and prepared $CaS:Eu^{2+}$ phosphors were investigated to understand process control and defect chemistry with respect to their luminescent properties.

Disordered glassy materials have attracted considerable interest for application as solid-state Li-ion battery components. The local defect structure was investigated for a series of $LiBO_2$-$V_2O_5$ mixed conductive glasses of varying $V_2O_5$ content, providing a detailed insight into distinct network-forming and modifying sites.

The characterisation of Li-ion battery materials is a critical aspect in the continued development of energy storage systems. A systematic *ex situ* EPR investigation of common electrode materials was performed to understand the relation of local electronic structure, and electrochemical activity. The development of a home-built *in situ* electrochemical cell was also presented, with respect to the challenges of *in situ* electrochemical measurements.

The outcomes of this work have illustrated that through careful investigation, EPR can provide a mechanistic understanding of important commercially relevant function materials often not available *via* other techniques.

# Preface

An outline of the Thesis structure is briefly summarised, highlighting authored publications relating to the content of the Thesis chapters.

**Chapter 1** Presents an extensive review in the recent applications of EPR spectroscopy in the characterisation and understanding of industrially important materials. Part of this review was adapted from a published review article: J. Spencer, A. Folli, E. Richards and D. M. Murphy, *Electron Paramagnetic Resonance*, 2018, pp.130-170.

**Chapter 2** Presents a brief overview of EPR theory in relation to solid state semiconductor materials, metals and defect chemistry; in addition to a brief overview of electrochemical measurements.

**Chapter 3** Reports the investigation of N-donor chelating exchange resins (CERs) for the selective uptake of $Cu^{2+}$ from aqueous media. This chapter has been published as an article: J. Spencer *et al.*, *Inorg. Chem.*, 2018, **57**, 10857-10866.

**Chapter 4** Reports a multi-frequency investigation of local electronic structurein $CaS:Eu^{2+}$ red-emitting phosphors for luminescent applications. This chapter has been published as an article: J. N. Spencer *et al.*, *Advanced Optical Materials.* 2001241.

**Chapter 5** Reports an investigation of mixed conductive $V_2O_5-LiBO_2$ glasses as a function of composition, of interest as solid state electrode/ electrolyte materials. This work has been submitted for publication (20/03/21).

**Chapter 6** Presents a systematic *ex situ* EPR investigation of common Li-ion battery electrode materials and the relation of their local electronic structure to their electrochemical activity. This work is intended to be submitted in part as a future publication.

**Chapter 7** Reports the development and proof-of-concept of a home-built *in situ* electrochemical EPR cell based on recent designs.

**Chapter 8** Outlines the general conclusions of the Thesis, with respect to the aims of the project outlined in Chapter 1.

# Contents

# Chapter 1

# Review of EPR applications to solid state functional materials of environmental and industrial significance

## 1.1 Introduction

In recent decades, the design and manufacture of modern solid state functional materials has become an important field across many industries; from heterogeneous catalysis and energy storage, to recycling and manufacture. This range of important materials are constantly developing and typically optimised towards a particular function, which are highly sensitive and dependent on their local structure. One of the most important modification tools in solid state chemistry, is the inclusion of dopants into the system, which facilitates control or modification of the underlying bulk properties including magnetism, superconductivity and colour/ optical band gaps. Many of these properties are facilitated by species containing unpaired electrons, or electron transfer properties, which in turn provide a means by which to sensitively characterise the system in question.

In many cases, there is a significant overlap in the types of materials (such as metal oxides) used for different catalytic and functional applications. At the heart of a given photo-physical, photochemical, catalytic step or electrochemical process *etc.* are generally one or more of the following fundamental or elementary steps: i) single electron transfer processes; ii) metals with one or many unpaired electrons; iii) defects and/ or trapping states; iv) small molecule radicals. Individually or collectively, these processes can be intrinsic to the functional properties and performance of the material. Electron Paramagnetic Resonance (EPR) spectroscopy is a characterisation technique used to determine the ground state electronic structure of such systems bearing unpaired electrons, and offers a sensitivity and resolution benefit that is not often afforded *via* other techniques. The electron $g$ factor, a quantity which relates its magnetic moment to its spin, is one of the most precisely known quantities in science due to its measurement *via* magnetic resonance techniques (Chapter 2).[1] Despite the inherent sensitivity of EPR spectroscopy, it can sometimes suffer from low resolution due to the effect of line broadenings or line splitting effects, due in part to the interaction of electron-electron and electron-nuclear spins within the spin system. A number of advanced measurement and hyperfine (electron-nuclear interaction) techniques are then necessary in order to extract further information about the system in question.

EPR is therefore a powerful technique for the characterisation and understanding of industrially relevant materials that could be implemented far more extensively, since its use is generally restricted to academic settings. The following sections of this Chapter will present an extensive, but non-exhaustive review of EPR applications in the study of functional solid state materials including heterogeneous catalysis, microporous materials, luminescent materials, functional glasses and enamels, and materials for energy storage, many of which are relevant to the materials explored in this Thesis.

This chapter also outlines the motivation underpinning research activities associated with this work, and summarises recent examples in the application of EPR spectroscopy in the understanding of key functional elements of catalytic and functional solid state systems. The review begins with heterogeneous catalytic systems and functional materials; to which EPR spectroscopy and related resonance techniques have been applied extensively. The applications of EPR will then progress to other key industrial materials and systems (Energy storage, Glasses *etc.*), where its impact has been relatively limited, or its application relatively new, will then be discussed where further exploration should be performed.

### 1.1.1 Catalytic Systems

Electron Paramagnetic Resonance (EPR) spectroscopy, which includes continuous wave (CW) and pulsed methods, is frequently used in the study of catalytically active systems. The role of EPR in these studies varies considerably from, on the one hand, a comprehensive description of the electronic states of the paramagnetic active site in the catalytic cycle to, on the other hand, a simple analytical confirmation that a radical centre is present. In some cases, EPR can also indirectly provide valuable insights into diamagnetic catalytic systems, by employing suitable paramagnetic spin probes that can access the structural aspects of an oxide surface to revealing dynamic aspects of the system, or (less common now) by employing transition metals as probe ions. In all cases the paramagnetic species, which are directly or indirectly studied by EPR, may include surface defects on metal oxide surfaces, transition metal complexes in solution or supported on surfaces, anchored radical anions or cations, or ROS at the solid-liquid interface, which all provide valuable information concerning the catalytic reaction.

Traditionally, EPR has been widely used in the broad field of catalysis from homogeneous to heterogeneous to enzymatic catalysis. There are numerous and outstanding review articles devoted to this topic. In the current Chapter, recent literature covering the past 4-5 years will be presented, illustrating the applications of EPR for studies of heterogeneous catalytic systems. Most attention is devoted to CW EPR, as this traditional method is still the most widely used and readily accessible method of choice in the catalysis field. Recent developments in *in situ* EPR techniques provide further insight into the electronic structure of important reactive sites upon changes in structure, oxidation state or relative spin density that may be correlated more closely to the catalytic reaction conditions and mechanism. Due to the relatively extreme temperatures and pressures required for many commercial heterogeneous catalysts, for activation or reactivation of the catalytic sites, achieving true *operando* conditions is challenging; is this is often accompanied by a loss in sensitivity due to relative populations of trapping states and spin relaxation times at considerably elevated temperature.

### Heterogeneous catalytic systems

An extensive literature existing on EPR studies of heterogeneous catalytic systems. The quality of many such studies is however less than inspiring, wherein EPR is used, sometimes crudely, as an ancillary technique to prove a radical species is present. However, there are excellent examples in the literature exemplifying the real power of EPR when studying complex catalytic systems. Excellent examples are provided in the works from Chiesa and Giamello. For example, Morra *et al.*,[2, 3] summarise some of their own results on Ti-based heterogeneous catalytic materials, particularly isomorphously substituted Ti in open framework materials, including tetrahedrally coordinated Ti ions in silicalite TS-1, TiAlPO-5 and ETS-10,[3] but also on systems relevant to Ziegler Natta catalysts and $TiO_2$ based photocatalysts.[2] These review articles illustrate nicely how a thorough and comprehensive understanding, at the molecular level, of the structure-property relationships between catalytically active sites and the surrounding matrix, as well as the interaction with selective adsorbates, can be obtained through pulsed hyperfine EPR methods, such as HYSCORE. Sobanska *et al.*,[4] present a detailed description of the diagnostic features of the superoxide radical anion ($O_2^{\bullet -}$) on catalytic surfaces and how the $g$ and $A$ tensors can be used to interpret the molecular framework of the radical. This radical is commonly involved in heterogeneous oxidation reactions, and unfortunately is also commonly mis-assigned in the analysis of EPR spectra in the literature.

However, in this review, Sobanska *et al.*,[4] provide an excellent account on the electronic nature of the $g$-tensor, for both electrostatic and covalent adducts, and on the analysis of the $^{17}$O hyperfine $A$-tensor. Any practitioner of EPR employing the technique to study heterogeneous oxidation reactions, where $O_2^{\bullet-}$ anions will most certainly be involved, should refer to this work,[4] and the references therein. Finally, in their review, Manck and Sarkar[5] have summarised, through some selected examples, the use of EPR to unravel reaction mechanism of relevance to catalytic bond action reactions.

### Supported metal complexes

The functionalization of surfaces with transition metal complexes, or simply anchoring homogeneous catalysts onto heterogeneous supports, has remained a very popular means of generating novel heterogeneous catalysts. In many cases, organic ligands capable of strongly binding redox active metal ions are employed, such as Schiff base ligands[6] or phthalocyanines.[7] Anbarasu *et al.*,[6] used EPR as an analytical tool to demonstrate the formation of the Cu(II)-Schiff base complex on a silica surface. The EPR spectrum obtained was poorly resolved, so only limited diagnostic information could be extracted about the catalyst. Huang *et al.*,[7] also studied the generation of reactive oxygen species by EPR using an anchored Co(II)-phthalocyanine complex on activated carbon fibres, where the focus of their study was primarily the chemistry of the ROS.

Bilis *et al.*,[8] provided an in-depth catalytic study of non-heme Fe based catalysts covalently grafted onto a silica support for catalytic oxidation of cyclohexene. These heterogeneous anchored catalysts proved to be very resilient and displayed improved oxidative stability compared to the homogeneous analogues. In addition to the high spin ($S$ = 5/2) Fe(III) centres, characterised by a broad peak at $g$ = 9.2 and with higher field peaks at $g_1$ = 4.63, $g_2$ = 4.21, $g_3$ = 3.80, EPR also revealed the presence of a low spin ($S$ = 1/2) Fe intermediate, in the presence of $H_2O_2$, and tentatively assigned to a Fe(III)-OOH hydroperoxide centre. This centre was characterised by the principal $g$-values of $g_1$ = 2.02, $g_2$ = 1.96, $g_3$ = 1.86 and the high spin to low spin transition only occurred in the presence of hydrogen peroxide. The involvement of free radicals was demonstrated by complimentary spin trapping studies using DMPO and TEMPO. This excellent paper illustrates nicely the wealth and depth or information that EPR can provide in catalysis studies. Barman *et al.*,[9] recently prepared a series of vanadium-based catalysts for the oxidative dehydrogenation of propane. The catalysts were prepared on silica using surface organometallic chemistry to deliver a $\mu^2$–oxo-bridged, bimetallic $[V_2O_4(acac)_2]$ complex precursor which, following activation, leads to a well-defined and isolated monovanadate $VO_x$ species. The well resolved EPR signals of the catalyst revealed the spin Hamiltonian parameters of $g_{\parallel} = 1.94$, $g_{\perp} = 1.98$, $A_{\parallel} = 17.4 \cdot 10^{-3}$ cm$^{-1}$, $A_{\perp} = 6.8 \cdot 10^{-3}$ cm$^{-1}$, and revealing that the first coordination sphere is completed by singly bound oxygen atoms.

### Microporous catalytic systems

Microporous materials present an incredibly important research topic for modern day catalytic processes, molecular separations, and technologies for energy and health.[10] The range of porous-type materials, and variations thereof, are continually growing as more applications and tailored designs become apparent. One of the current limitations is the ability to improve upon the industrially established materials,[10] but their inexpensive preparations, coupled with superior surface areas, modification, tuneability and porosities make them a highly attractive tool for improving upon current protocols. Once again, EPR techniques play an important role in the characterisation of these microporous materials in catalytic applications.

### Zeolites and Zeotype materials

Zeolites, and more generally the related 'zeotype' materials, are a class of crystalline microporous aluminosilicates, primarily consisting of $AlO_4^-$ and $SiO_4^-$ tetrahedra. A massive variation and arrangement of subunits provide a degree of tuneability, with regards to the physical and chemical properties of the materials, only paralleled by other related microporous materials. They have had a huge impact on modern science and technology, in particular, playing a key role in modern sorption[11] and catalytic processes.[12] The global annual demand has been reported to be several thousand metric tons.[13] Zeolites can be catalytically active via the inclusion of redox-active dopant ions within or anchored to their framework, adopting multiple low symmetry sites that are often highly sensitive to experimental and synthetic conditions.

EPR spectroscopy, coupled with the related hyperfine techniques, have been successfully used in the characterisation of zeolites for over 40 years. Many recent investigations of the local environment of redox-active metal centres,[14–19] radical intermediate species and spin probes,[20–22] have been readily evaluated with significant implications for understanding catalytic pathways and with complementary spectroscopic techniques. Recent technological advances have seen an increased use of *in situ* spectroscopic investigations, for the quantitative real-time[23] and even spatial[24] (EPR-imaging) analysis of catalytic processes, although the experimental conditions required for true *operando* studies remain difficult to achieve.

A recent paper by Godiksen *et al.*,[25] presented a CW EPR investigation of Cu(II) sites in Cu-CHA zeolites for the selective catalytic reduction of nitrogen oxide using ammonia ($NH_3$-SCR). Conventional frequency CW EPR (X-band) provided ready accessibility to the magnetic parameters of the Cu(II) ions inherent to their electronic structure, and by extension, local coordination environment. Cu(II) has been well characterised in the literature and therefore allows for a straightforward comparison between the experimental parameters, and hence coordination geometries, owing to the early work of Peisach and Blumberg.[26] In the fully hydrated state, Godiksen *et al.*,[25] showed that the Cu-CHA sample presented two distinct Cu(II) environments. The first constituted a broad isotropic signal with the absence of a hyperfine splitting, attributed to a hydrated Cu(II) centre in which free movement or rotation is relatively unhindered. The second species was identified as an axially symmetric signal, from interaction with the Cu nucleus ($^{63,65}$Cu, $I = 3/2$), assumed to be a restricted Cu(II) environment in which the framework oxygen is involved within the coordination sphere. Upon dehydration, under a flow of $O_2$/He at 400°C, Godiksen *et al.*,[25] reported that the EPR spectrum changed significantly, showing a complex anisotropic signal because of speciation within the zeolite framework. Simulation of the signal revealed three distinct isolated Cu(II) species, with the spin Hamiltonian parameters, labelled 'A1' ($g_{\parallel} = 2.325$, $A_{\parallel} = 487$ MHz), 'A2' ($g_{\parallel} = 2.358$, $A_{\parallel} = 464$ MHz) and 'B' ($g_{\parallel} = 2.388$, $A_{\parallel} = 530$ MHz) respectively, all with axial symmetry and observed orders of magnitude of $g_{\parallel} > g_{\perp}$ and $A_{\parallel} > A_{\perp}$, indicative of Cu(II) in a distorted octahedral or square planar geometry, with a $d_{x^2-y^2}$ ground state. Both 'A1' and 'A2' were attributed to Cu(II) residing within a 6-membered ring site with two aluminium T-sites (Figure 1.1). This was supported by the spin Hamiltonian parameters corresponding to a tetragonal 4O coordination mode, and comparison with alternative zeolites not containing the same ring sizes.

### Metal-organic Frameworks (MOFs)

Another growing and significant class of microporous materials in catalysis are MOFs. Although zeolites, are more suited to extreme temperature conditions due to their inorganic nature, the inclusion of organic components in MOFs presents an

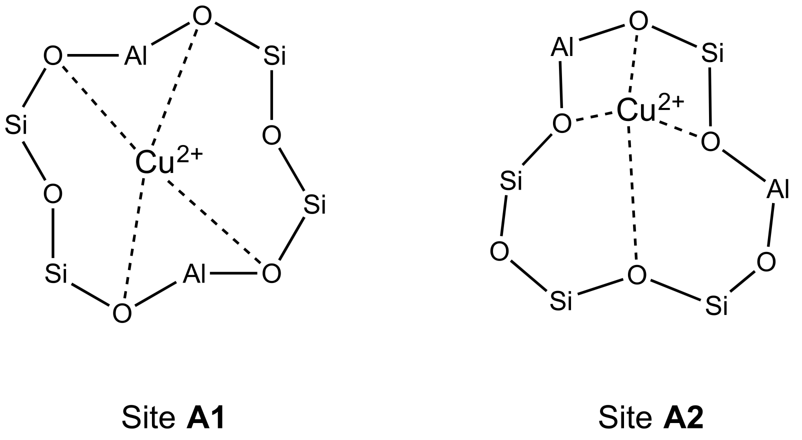

**Figure 1.1:** Structures attributed to the A1/A2 sites in Cu-CHA zeolites (after ref. [25])

almost unlimited arrangement of sub-units, topologies, porosities and functions.[27] In fact, the precise control of the MOF assembly allows almost tailored designs to its application, with typically large surface areas, and densities of catalyst sites.[28] In contrast to zeolites, MOFs typically contain redox-active metal centres embedded within the framework, which can be an issue for EPR spectroscopy, due to dominating electron spin-exchange interactions that encompass signal features relating to more sensitive, and informative interactions. However, this is not significant in every case, and routes to magnetic dilution, such as co-metal syntheses, and post-synthesis modification are readily available. Although research into MOFs has only become significant within the last 20 years, a number of recent studies demonstrating the power of EPR spectroscopy to characterise the redox centres,[29–34] and adsorption properties via spin probe studies,[20, 35, 36] have been reported.

### Porous carbon materials

Porous carbon materials, in particular activated carbons, are another industrially important class of frameworks used as heterogeneous catalyst supports, as water desalination systems, for photochemical and sensing applications.[37] The molecular design of the systems, with respect to the various morphologies of carbon materials along with framework modification by incorporation of heteroatoms, leads to efficient tailoring of the system in terms of porosity, electrochemical response, surface polarity and wettability.[37] The application of EPR spectroscopy is less well known in this class of materials, however a number of interesting uses have been reported recently to probe the nature of incorporated metal sites,[38] defect chemistry[39] and radical generation,[40–44] in steady-state and *in situ* applications. Due to its inherent sensitivity of the technique, EPR is a useful tool in identifying structural features and radical intermediates, not usually detectable by other means.

A study by Wang *et al.*[45] investigated nano zero-valent iron, encapsulated in porous carbon spheres ($Fe^0/Fe_3C@CS$) for the activation of peroxymonosulfate (PMS) for phenol degradation. A remarkable catalytic activity, and stability, was reported by the authors, due to subsequent encapsulation and magnetic separation. This class of catalyst acts via an advanced oxidation process, employing oxidising substances such as sulfate ($SO_4{}^{\bullet -}$ and hydroxyl $OH^{\bullet}$) radicals, or non-radicals such as singlet $O_2$ to degrade pollutants. Although structural components within forms of carbon are not paramagnetic, important features of the degradation mechanism, involving the radicals, listed vide infra, were investigated using EPR spectroscopy and radical trapping methods, which is a subject of much debate among recent literature on porous carbon materials for oxidative degradation.[38, 40, 42, 46, 47]

### 1.1.2 Functional glasses and enamels

The terms glass and glass-ceramic identify a huge class of disordered (or partially-ordered) materials with complex local structures and properties, that may be classified further in terms of their precursors. They include oxide glasses, consisting of silicate, borate, phosphate, germanium oxide *etc.*, and non-oxide glasses, containing chalcogenide, halide, or metallic type phases. A glass material in its simplest form is made of a binary mixture of phases, but is not limited to a given number of precursors or phases. Due to the wide variety of precursors, and tuneable properties that depend on the chosen composition, glasses have an equally large range of applications covering optical, photonic, thermal, electronic, mechanical and chemical applications.[48]

The applications of glasses overlap considerably with other areas highlighted in this Chapter, such as catalysts,*vide infra*, and energy storage materials, *vide supra*, as similar species are responsible for their functional properties (3d, 4f metals, semiconductor phases *etc.*) are readily incorporated into them. Their properties are often unique to their crystalline counterparts, often due to the complex interplay between phases in its composition and disorder within the glass network. Constituents can broadly be classified by their behaviour within the glass, including network formers, and network modifiers. Their behaviour is often composition dependent.

The characterisation of glass materials is also markedly different to ordered systems: for example, conventional structural characterisation methods, such as XRD, are often uninformative and other routes towards understanding the structure of the material are therefore necessary. Due to the nature of functionalisation of glasses, for example by the incorporation of paramagnetic metals, the presence of defects, or even intrinsic electron transfer events, EPR spectroscopy is highly informative in the evaluation of speciation, local structure correlations and disorder, that directly affect their function. EPR has hence commonly been employed in the characterisation of functional glass materials, although extent of its application is often limited to the confirmation of paramagnetic species within the material, where a far more informative approach may be accessible.

Franco and co-workers investigated the optical and electronic structure of ternary phosphate-based ($50\,P_2O_5-30\,Na_2O-20\,ZnO$) glasses doped with varying MnO contents,[49] where EPR was one of the primary characterisation methods used. At low contents, a superposition of weakly resolved signals was reported near $g_e$ with resolved hyperfine structure, $a_{iso}$ = 269 MHz, and weakly resolved fine structure (from ZFS), with $D$ = 703 MHz, characteristic of high-spin $Mn^{2+}$ ($S$ = 5/2; $I$ = 5/2). The refined spin Hamiltonian parameters were consistent with other similar glasses and indicated an axially distorted octahedral environment. The distribution in $D$ was also indicative of disorder within the material due to the inhomogeneity of local $Mn^{2+}$ sites in the glass although this was not discussed in detail by the authors.

Srinivas *et al.* investigated the characterisation of $VO^{2+}$ and $Cu^{2+}$ doped into $BaO-TeO_2-B_2O_3$ glasses, as these materials are of interest for laser technologies, optics, photonics and radiation detectors.[50] The incorporation of $VO^{2+}$ into the glass network was characterised by a single structure in the EPR spectrum with spin Hamiltonian parameters $g_{\parallel}$ =1.929, $g_{\perp}$ =1.997 and $A_{\parallel}$ = 183 10 $^{-4}$cm$^{-1}$; $A_{\perp}$ = 52 10 $^{-4}$cm$^{-1}$ which varied slightly between samples. The observed ordering $g_{\parallel} < g_{\perp}$ and $A_{\parallel} > A_{\perp}$ was attributed to $V^{4+}$ in a tetragonally compressed octahedral environment with $C_{4v}$ symmetry and a $d_{xy}$ ground state. Measurements of $Cu^{2+}$ doped glasses also indicated a tetragonally compressed octahedral coordination, and the covelancy of in-plane $\sigma$-, $\pi$- and out of plane $\pi$-bonding was rationalised from the EPR parameters. The $VO^{2+}$ coordination was found to be highly covelant, whereas a dominant ionic character was determined for the $Cu^{2+}$ glasses.[50]

Rare-earth ion-based glasses, $Yb^{3+}$ doped $(100-x)B_2O_3-xPbF_2$ and $50\,B_2O_3-(50-x)PbO-xPbF_2$ glasses, of interest for telecommunications, solar cells and other photonic devices were studied by Zhang and co-workers using solid-state NMR and pulsed X-band EPR spectroscopy.[51] $Yb^{3+}$ is a $S$=1/2 ion with a $^2F_{7/2}$ ground state term which was observed as a very broad, asymmetric resonance in FSE-EPR measurements with no resolved hyperfine pattern due to the interaction with the nuclear spin of $^{171}Yb$ and $^{173}Yb$ (natural abundances of 14.3 and 16.1%, respectively).[51] The authors attributed the line shape to $g$-anisotropy and site heterogeneity and noted no spin echo was detected at zero field which is indicative of rare-earth clustering.[52] 3-pulse ESEEM and HYSCORE measurements, advanced pulsed hyperfine techniques capable of resolving small unresolved hyperfine couplings, were then performed to extract further information about the local electronic and nuclear structure. A set of resonances were observed at Larmor frequencies corresponding to $^{10}B$,$^{11}B$,$^{207}Pb$ and $^{19}F$ nuclei in the weak coupling limit ($A < \nu_L$) due to interaction with the electron spin in the 4f orbitals of $Yb^{3+}$. HYSCORE measurements provided access to estimation of the relatively small hyperfine couplings to each nucleus which were observed to be rhombic for $^{10}B$,$^{11}B$ and axial for $^{19}F$,$^{207}Pb$, the latter attributed to a purely dipolar contribution present as second-nearest or more distant neighbours.

A final example is the characterisation of $Li_2O-V_2O_5-P_2O_5$ glass systems by Garbarczyk *et al.* for application as solid state cathode/ electrolytes in next-generation Li-ion batteries[53] due to its content-dependent, mixed ionic and electronic conductivity. Electronic conduction is afforded by high $V_2O_5$ contents due to polaronic hopping between aliovalent $V^{4+}$ and $V^{5+}$ centres. At low $V_2O_5$ contents, a resolved hyperfine structure was observed with reported values $g_{\|} = 1.935$; $g_{\perp} = 1.98$; $A_{\|} = 17.00 \cdot_{10}{}^{-3}\,\mathrm{cm}^{-1}$; $A_{\perp} = 6.18 \cdot_{10}{}^{-3}\,\mathrm{cm}^{-1}$ characteristic of paramagnetic $V^{4+}$ ions ($S = 1/2$). As the content was increased, a collapse of the hyperfine structure was observed which was attributed to polaronic hopping. The exchange narrowing process was not mentioned, but this is presumably the cause of the loss of structure at high contents. No further efforts were made by the authors to characterise this site further.

### 1.1.3 Energy storage materials

With the current environmental crisis and our societal dependency on fossil fuel consumptions as an energy source, the development of renewable energy sources such as wind, solar, hydro and wave power are of paramount importance. However, these sources of energy are frequently non-continuous, or even sporadic, and therefore energy storage systems are a necessity to fully harness the generated power.

[54] Energy storage systems are also critical for several other applications, particularly in the consumer and transport sectors, where the advent of electric cars and increasingly demanding electronics systems, such as phones and computers, are of particular importance. With the fast pace of technologies requiring greater energy consumption, coupled with the drive for renewable energy sources, efficient methods of energy storage are paramount for development and growth.

Several forms of energy storage have been developed and can be broadly categorised as follows: i) mechanical energy storage; ii) chemical energy storage (fuel cells, biofuels); iii) electrochemical energy storage and iv) thermal energy storage. Each broad class of storage system is used for a variety of applications, under different environmental conditions based on their storage capacity, energy loss and efficiency. Perhaps the most important, and familiar, enabling energy storage technologies are capacitors and Li-ion batteries.

Several highly sensitive characterisation techniques are popular in rationalising the local structure and function of energy storage systems. [55] Of most interest and value is the development of *operando* or *in situ* characterisation techniques that can correlate electrochemical activity to the local structure. Generally, the participation of metals and defect chemistry in electron transfer processes is inherent in electrochemical energy storage materials and their performance. This may be as part of an intended mechanism, process, or by degradative action, each of which are important to understand in the development of more efficient materials.

This section of the Chapter will provide examples of recent investigations in each area, primarily focusing on the use of *ex situ* and *in situ* EPR spectroscopic

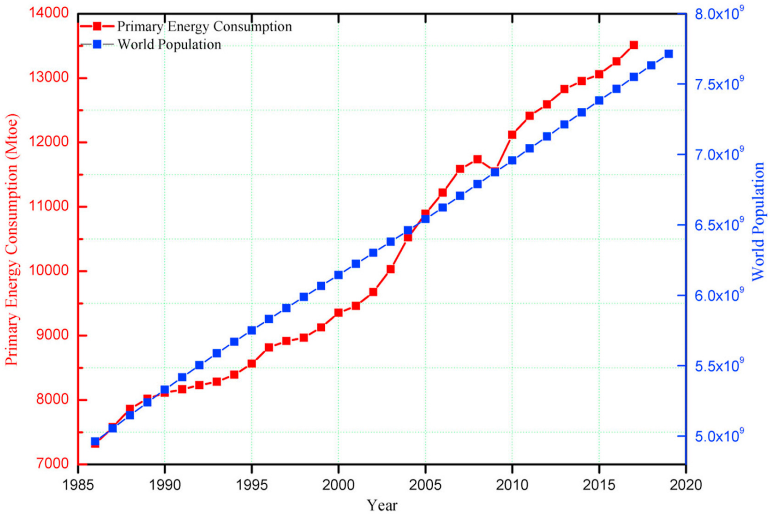

**Figure 1.2:** Correlation of primary energy consumption and world population, reproduced[54] with permission from Elsevier, Copyright 2021.

techniques, for which the latter is still undergoing early development in the design of suitable electrochemical devices to study the systems of interest.

### Li-ion battery technologies

Li-ion batteries have an unmatchable combination of high energy and power density, making it the technology of choice for portable electronics, power tools and electric/hybrid vehicles.[56] Their high energy efficiency also facilitates their use in various electric grid and infrastructure applications for the harnessing of wind, solar, geo-thermal and other renewable energy sources.[57] The first commercial Li-ion battery system was developed through the work of Whittingham, Goodenough and Yoshino with the $LiCoO_2$ (LCO) battery, using a graphite anode.[58] The commercialisation of Li-ion batteries revolutionised several technological markets in the 1990's and was fittingly recognised in 2019 by the Nobel prize for chemistry. Several technologies have since been commercialised and find widespread use in a variety of domestic and military applications. Goodenough and Kanamori are also well known for their contributions to magnetism, and their study of super-exchange interactions in transition metal compounds which led to the Goodenough-Kanamori rule in ligand field theory,[58] for which EPR (and magnetometry) is one of the primary techniques to investigate these interactions.

There are several recent, high quality reviews discussing the importance and development of Li-ion technologies,[54, 57–66] and beyond Li technologies as the maximum theorised power density/ gravimetric capacity is fast approached for this particular system. [58, 59] The modern-day rechargeable battery is a device that stores energy *via* the reversible shuttling of a mobile ion (*e.g.* $Li^+$, $Na^+$) between two electrodes through an electronically insulating and ionic conducting electrolyte.[67] The type of electrode is determined by the mechanism of storage, including: i) the relatively fast, reversible storage of ions within channels of a host lattice (intercalation); ii) the storage of ions *via* the plating (alloying) and iii) incorporation through phase transformation of the host (conversion). A typical modern Li-ion battery is typically an intercalation-type cell with a graphite anode, a separator to prevent short-circuit, and a transition metal oxide cathode. The energy stored by the system, *i.e.* the free energy, $\Delta G$, is directly proportional to the cell potential, and the number of electrons, or $Li^+$, ($\Delta G = -nFE$) that can be reversibly inserted and extracted from the electrode materials. This is therefore a primary consideration in the design of Li-ion electrodes and systems.

The most ideal anode for Li-ion batteries would be pure Li metal; which has an unrivalled theoretical specific energy (≈ 3500 Wh $kg^{-1}$).[68] However, several practical limitations prevent its use in this application. Other anode materials have been reported to replace graphite, such as other porous carbons or $Li_4Ti_5O_{12}$ (LTO). This material has received the most significant attention within the battery area, since it provides the best performance within currently practical systems. The electrolyte, which is typically a toxic mixture of a Li salt and flammable organic solvent, is also an important consideration in terms of cell performance, stability and safety. The operating potential window for a Li-ion cell is limited by the oxidation and reduction potentials, *i.e.*, the stability of the electrolyte. Several efforts have focused on the development of safer electrolytes, including solid-state replacements.[59]

One of the ongoing challenges for Li-ion electrode materials is their comparatively poor electronic and ionic conductivity. The incorporation of active carbon is then often used to increase the electronic conductivity. However the incorporation of dopants, and intrinsic defects such as oxygen vacancies, are a straightforward route to improve conduction performance and activity of Li-ion electrode materials as has been covered for other semiconductor materials *vide infra.* Bulk oxygen vacancy defects are of particular interest to many groups,[65] due to their sensitivity to synthetic conditions and morphologies.[62] The performance and stability of Li-ion systems may therefore be related directly to the local structure and reactivity; redox-active metal ions, intrinsic (and extrinsic) point defects, short-lived inorganic radicals are all important participants in a rich and complex range of chem-

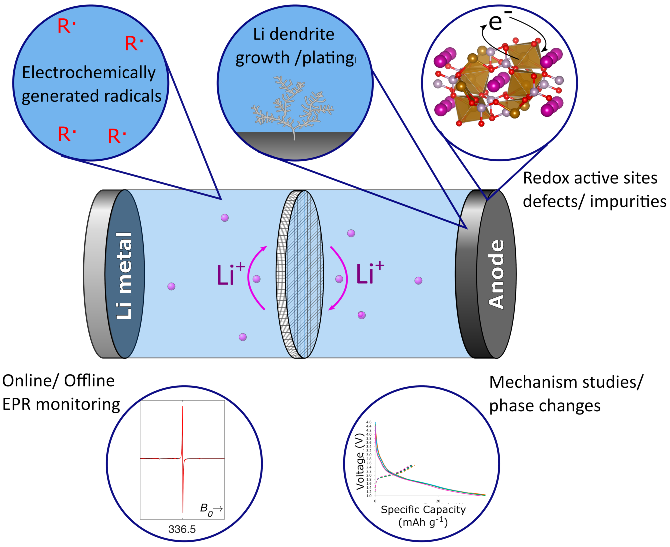

**Figure 1.3:** Schematic of Li-ion battery half cell *v.s.* Li/$Li^+$ and processes detectable using EPR spectroscopy.

ical and electrochemical interactions (including single electron transfer processes) which can be readily monitored using EPR spectroscopy.[66] Some of the main important elements that can be investigated *via* EPR are included in the schematic (Figure 1.3) above. Several examples of the application of EPR spectroscopy in the understanding of this rich and complex chemistry are now presented.

One of the main techniques for improving the electrochemical performance (*viz.* cycling stability, reversible specific capacity, ionic and electronic conductivity) of a cathode material is the *isovalent* substitution and *aliovalent* doping of transition metal ions into the material.[69] Jakes *et al.* investigated the coordination of $Mn^{4+}$ ($S = 3/2$; $I = 5/2$) centres in layered $LiCo_{0.98}Mn_{0.02}O_2$ cathode materials using a joint XRD and multi-frequency EPR characterisation approach.[69] High-field or high-frequency EPR ($\nu_{MW} > 95$ GHz) EPR is highly informative in the description of the $g$ tensor anisotropy (for low spin systems), and the resolution of large fine structure transitions from zero-field splitting, exchange or dipolar interactions (for high spin systems). The authors highlight that the role of manganese dopants in $LiCo_{0.98}Mn_{0.02}O_2$ is still unclear (as is the case for many doped systems). It was proposed to be electrochemically inactive, and provides a passive stabilisation of the layered $LiCoO_2$ structure during Li intercalation in addition to the potential clustering of Mn centres, where their activity is unclear.

Initially, Jakes *et al.*[69] reported cyclic voltammetry (CV) measurements which indicated only a single resolved redox couple for $Co^{3+}/Co^{4+}$ associated with a single phase-transition throughout the whole discharge cycle, different from pure $LiCoO_2$ (multiple phase transitions).[69] Multi-frequency EPR analysis at $\nu_{MW}$ = 9.85, 108.0-406.4 GHz was then reported which indicated the presence of substitutional $Mn^{4+}$ in tetragonally distorted octahedral Co sites ($\mathrm{Mn}^{\bullet}_{\mathrm{Co}}$), with resolved fine structure, in addition to a broad featureless resonance attributed to the Mn clusters. At X-band, the $Mn^{4+}$ centre fine structure was only partially resolved due to a comparable energy differences ($3B_2^0 \approx \nu_{MW}$) between the Kramers doublets ($m_s = \pm 1/2, \pm 3/2$) and the incident microwave frequency (intermediate field limit), which was subsequently resolved with high-frequency measurements. Taking into account considerations from the XRD crystal structure, refined spin Hamiltonian parameters were reported for the substitutional site as $g_{xx} = 1.9890$, $g_{yy}$ =1.9888, $g_{zz}$ =1.9820 and ZFS parameters $3B_2^0$ = -1150 MHz, $|B_2^2|$ = 400 MHz (with $D = 3B_2^0, 3E = B_2^2$) which corresponded to a lower site symmetry than the $Co^{3+}$ site and elongation in the oxygen octahedron,[69] which could impose additional strain in the material upon Li intercalation. In addition, the conduction electron density was expected to be increased due to charge compensation from the donor sites (*i.e.* $\mathrm{Mn}_{\mathrm{Co}}^{\bullet}$).

A series of $Li_2MnO_3$ (LMO), $Li_{1.2}Ni_{0.2}Mn_{0.6}O_2$ (LNMO) and $Li_{1.2}Ni_{0.13}Mn_{0.54}Co_{0.13}O_2$ (LNMCO) layered oxide cathodes were also studied by Tang *et al.* using *operando* EPR spectroscopy in a pouch cell type arrangement using Ti meshes as the current collectors.[70] These spectra were particularly complex since each metal has a different paramagnetic redox state, and since they are part of the lattice, have complex exchange and dipolar interactions between the inequivalent ions. No structure was observed for the EPR signal pertaining to the metal sites, and therefore could not be distinguished from one another, presumably due to weak spin-orbit coupling (that shifts $g$ away from $g_e$), exchange narrowing (loss of hyperfine and dipolar structure), and averaging of the Zeeman energies (strong exchange limit). Monitoring of the relative integral upon charge/discharge was however possible and contributions from the redox processes of the various metals were correlated with the EPR response. The authors also attributed oxygen anionic redox processes (${O_2}^{n-}$) to part of the relative integral response, although this was also not resolved from the broad featureless signal.

The formation of mossy lithium and dendrites is an inherent degradative problem for safety and performance in Li-ion cells mainly due to the irreversible electrolyte consumption, and potential short-circuiting of the cell. This potential for formation limited the commercial use of Li metal as an anode with liquid electrolytes, which has a very high specific capacity (3860 $\mathrm{mAh\,g^{-1}}$), and would enable vastly improved energy densities, but for the short cycle life due to formation of these structures. The use of a Li-metal anode is central to a number of next-generation battery technologies which will be discussed briefly in the next section *vide supra*. This was the reason that graphite anodes became widespread commercially, despite their lower energy density. However, the reduction potential of graphite is very close to that of $Li/Li^+$ and therefore Li plating/dendrite growth is also possible, being a primary mode of degradation for Li-ion cells.

Wandt *et al.*[71] investigated the formation of mossy Li structures in an $LiFePO_4$ (LFP) half-cell using *operando* EPR spectroscopy and a home-built coaxial electrochemical cell, which was based on an earlier design by Zhuang *et al.*.[72] EPR is a more sensitive technique for their detection compared to other methods (*e.g.* $^7$Li NMR) due to the limiting penetration of microwave fields into conductors within the markedly smaller skin depth, which is proportional to the frequency. This facilitates a surface-sensitive detection method ideal for microstructures of Li.

In this experimental assembly, the working electrode was a printed film of LFP directly onto a Celgard separator, and rolled Li foil counter electrode (which was of interest for the deposition of micro-structured Li during the charging step) with a concentric arrangement of the cell components confined within a 6mm quartz cell. Comparisons with standard cells for electrochemical measurements determined a similar practical specific capacity for relatively low current densities to facilitate comparison to electrochemical behaviour.[71] The plating and stripping behaviour of Li at the anode was investigated upon charge/discharge cycles for a standard electrolyte, and with an FEC additive that suppresses the formation of microstructured Li. The *in situ* EPR spectra of the two cells showed a series of phase shifted, asymmetric Lorentzian lineshapes close to $g_e$, characteristic of diffusing conduction band electrons within the skin depth of metallic Li ($\approx 1.1 \mu m$ for Li).[71] The phase shift of the signal (absorption *v.s.* dispersion) was correlated to the Li particle size, which was also investigated with *ex situ* SEM. Monitoring of the signal with the FEC additive showed a more reversible behaviour upon plating/stripping processed when compared to the cell without, and presented an effective and selective means of characterising the Li deposition processes.

In the final example, another interesting *operando* EPR imaging (EPRI) and spectroscopy study was reported by Sathiya *et al.* for the monitoring of a high capacity (>270 $\mathrm{mAh\,g^{-1}}$) Li-rich layered oxide, labelled $\mathrm{Li_2Ru_{0.75}Sn_{0.25}O_3}$.[73] This *in situ* electrochemical cell design had a more regular cell arrangement comparable to the coin cells; *i.e.* electrode discs, separated by a wetted Celgard separator (LP30 electrolyte) and connected to Cu and Al current collectors respectively, and all contained within a PCTFE housing. In addition to the Li metal EPR signal, cationic ($Ru^{4+} \rightarrow Ru^{5+} + e^-$) and anionic ($O^{2-} \rightarrow O_2^{n-}$ where $3 \geq$ n $\geq$ 1) redox processes were also monitored upon charge/discharge *via* the detection of $\mathrm{O_2}^{3-}$, $\mathrm{O_2}^{-}$, ($S$=1/2), along with a broad signal at $g$ = 2.0002 attributed to $\mathrm{Ru^{5+}}$ ($4\,\mathrm{d}^3$, $S$=3/2). Finally, EPRI (comparable in principle to MRI, still in its infancy) was performed on the *in situ* cell to provide spatial resolution of the EPR detection, which determined a homogeneous distribution of $\mathrm{Ru^{5+}}$ at the electrode surface. However, a heterogeneous distribution was reported for the $\mathrm{O_2}^{n-}$ species, related to the sluggish kinetics of the anionic redox processes. A relatively constant intensity was observed for Li metal plating at the anode upon cycling. In summary, the detection of these species facilitated the direct, real-time monitoring of redox processes in addition to degradative processes during cell cycling.

In addition to the extensive research on the positive and negative electrode materials of Li-ion batteries, there is also extensive research devoted to next-generation Li-ion battery systems.[58] Battery scientists and engineers have been making batteries with 5-10% more effeciency every year, and the theoretical limit for its efficiency has almost been achieved.[59] As mentioned *vide infra*, the Li-metal anode facilitates specific capacities and energy densities that are $\approx$ 10x greater than traditional graphite anodes and is therefore of interest to include in commercial cells, which has not yet been possible due to the tendency for Li plating and dendrite growth upon charging of the cell. To facilitate their use, solid-state electrolytes such as glasses, ceramics, plastics and polymers have been under intense investigation, as these offer greater safety compared to their liquid electrolyte counterparts, some of which have been covered *vide infra*. The current challenges with these systems arise mainly from the poor conductivity and inhomogeneous contact at the electrode/ solid electrolyte interface, which in turn limits their power density. Currently glass and ceramic electrolytes offer better conductivity than plastic or polymer.[59]

Another route being explored by Duduta *et al.*,[74] is a type of flow battery, in which a semi-solid electrolyte is used with liquid electrolyte pumped through the cell to facilitate ion transport. To date, no *in situ* EPR investigations have been reported on full solid-state systems and the literature surrounding their characterisation is relatively sparce. The investigations discussed *vide infra* for Li metal plating/ dendrite formation are highly relevant,[71, 73] in addition to *ex situ* studies reported in the section on functional glass materials. Furthermore, the types of materials used for solid state electrolytes and their characterisation using EPR spectroscopy will not be discussed further.

The lithium metal anode (hence, the solid-state electrolyte system) is also important for next-generation battery technologies such as Li-S and $Li-O_2$ cells, which are not classified as Li-ion systems as they undergo *conversion* rather than *intercalation* upon charge/discharge. The cells for Li-S and $Li-O_2$ typically consist of a Li metal electrode, a porous carbon electrode with S or $O_2$ additive, and either an aqueous, non-aqueous or solid-state electrolyte, all of which are being actively investigated. Conversion-type electrodes undergo phase transformations through the alloying of Li, which offer vastly greater specific capacity, specific energy (per unit mass) and energy density (per unit volume) to their intercalation-type counterparts. However, they do suffer from huge volume changes and instability that limit their practical use.[57] Practical specific capacities are still nowhere near the predicted specific energies, mainly due to the mass and volume of other components such as the electrolyte, carbon and binder,[75] in addition to their short cycle life due to deactivating irreversible redox processes with the electrolyte and electrode materials. The application of EPR to these cutting-edge technologies is relatively limited to date, however there are still some excellent examples where

EPR has been used for mechanistic and structural determination. Amunchukwu *et al.* reported interesting *ex situ* EPR spin-trapping work for an Li-$O_2$ system, looking at a CNT electrode after discharging and soaking in a solution of DMPO or BMPO in DMSO.[76]

The technique indirectly detected the presence of $O_2^{\bullet -}$ based adducts in the system, suggesting one-electron transfer processes participated in the anionic redox mechanism. Wandt *et al.* also reported an interesting *operando* study of Li-$O_2$ systems using the spin trap 2,2,6,6-tetramethyl-4-piperidone (4-Oxo-TEMP), that reacts with singlet oxygen ($^1O_2$, a highly short-lived and transient excited state of $^3O_2$) to form 4-Oxo-TEMPO.[77] $^1O_2$ is a strong oxidising agent and is known to cause corrosion/ degradation in Li-$O_2$ cells.[75] A multi-step charge/discharge behaviour was observed for the galvanostatic charge/discharge profile, which they were able to correlate with the relative intensity of the 4-Oxo-TEMPO signal, thereby demonstrating the transient formation and reactivity of $^1O_2$.[77]

Finally, another avenue of research for next-generation battery technologies is the replacement of Li-ion transport with other alkali ions such as $Na^+, Mg^{2+}, K^+$ *etc.* Li is the lowest mass element of these examples, and therefore possesses favourable transport kinetics and specific energies, in addition to the lowest reduction potential.[57] However, it is also classed as a critical element (from a supply perspective) and Li recycling is still an important issue concerning battery recycling.[78] Other alkali ion battery technologies have been proposed to replace Li with more renewable feedstocks, although these typically suffer from sluggish kinetics and low specific capacities compared to their Li-ion cousins. Several studies including the use of EPR spectroscopy have investigated these systems,[79–83] and the information provided is similar to the examples presented in this section *vide infra.*

### 1.1.4 Conclusions

The review of the application of EPR to solid-state functional materials presented in this Chapter has highlighted a number of similarities between seemingly different systems based on their structure and function:

1. Functional materials are often composed of similar precursors or materials (such as metal oxides, carbon materials) that ultimately produce the desired redox activity, optical and magnetic properties;

2. The function of the materials is often enhanced of fine-tuned by the inclusion of metal ions, point defects, or other local centres that can participate in

single electron transfer processes from non-paramagnetic states;

3. The functional properties of a material are therefore highly sensitive to the local electronic and structural environments, including the symmetry and interaction between active sites.

EPR spectroscopy is clearly a powerful, but often under-utilised tool in the characterisation and development of these functional materials. This Chapter has therefore provided a summary of the many studies applied to the field of heterogeneous catalysis, where the application of EPR spectroscopy and related techniques is substantial and well-known. Moving to the latter sections, covering other advanced functional materials, the applications of EPR spectroscopy are clearly less widely exploited, and certainly less extensively applied to materials beyond confirmation of the presence of a paramagnetic state. EPR therefore facilitates a much more powerful understanding of these materials than commonly used, particularly in industry, where the screening and research of materials could benefit from the magnetic resonance characterisation approach. The cutting-edge application of *in situ* spectroscopic methods is an additionally informative application that allows further correlation of the local electronic structure and magnetic properties to the functional properties (*ca.* optical, or electronic transitions).

Of the many sections reviewed in this Chapter, battery and energy storage materials have received notable attention as the application of the EPR technique is comparatively unexplored when compared to the more established research areas discussed *vide infra.* The important development of *in situ* spectroscopic techniques were briefly explored, and will be applied to this important field of research.

Herein, the key aims of the working presented in this Thesis will be the robust and systematic investigation by EPR of important solid state functional materials. Particular attention will be paid to their industrial applications, both in terms of their development, manufacture and applications. Furthermore, the full potential of EPR spectroscopy is afforded by the inclusion of complementary spectroscopic or analytical techniques, to further correlate their structure and function. These methods will be presented in Chapter 2, before the key application areas are delivered in later Chapters.

# References

[1] B. Odom, D. Hanneke, B. D'Urso, and G. Gabrielse. New Measurement of the Electron Magnetic Moment Using a One-Electron Quantum Cyclotron. *Physical Review Letters*, 97(3):030801, July 2006.

[2] Elena Morra, Elio Giamello, and Mario Chiesa. EPR approaches to heterogeneous catalysis. The chemistry of titanium in heterogeneous catalysts and photocatalysts. *Journal of Magnetic Resonance*, 280:89–102, July 2017.

[3] Elena Morra, Sara Maurelli, Mario Chiesa, and Elio Giamello. Rational Design of Engineered Multifunctional Heterogeneous Catalysts. The Role of Advanced EPR Techniques. *Topics in Catalysis*, 58(12):783–795, September 2015.

[4] Kamila Sobańska, Aneta Krasowska, Tomasz Mazur, Katarzyna Podolska-Serafin, Piotr Pietrzyk, and Zbigniew Sojka. Diagnostic Features of EPR Spectra of Superoxide Intermediates on Catalytic Surfaces and Molecular Interpretation of Their $g$ and $A$ Tensors. *Topics in Catalysis*, 58(12):796–810, September 2015.

[5] Sinja Manck and Biprajit Sarkar. Use of EPR Spectroscopy to Unravel Reaction Mechanisms in (Catalytic) Bond Activation Reactions: Some Selected Examples. *Topics in Catalysis*, 58(12):751–758, September 2015.

[6] G. Anbarasu, M. Malathy, P. Karthikeyan, and R. Rajavel. Silica functionalized Cu(II) acetylacetonate Schiff base complex: An efficient catalyst for the oxidative condensation reaction of benzyl alcohol with amines. *Journal of Solid State Chemistry*, 253:305–312, 2017.

[7] Zhenfu Huang, Haiwei Bao, Yuyuan Yao, Wangyang Lu, and Wenxing Chen. Novel green activation processes and mechanism of peroxymonosulfate based on supported cobalt phthalocyanine catalyst. *Applied Catalysis B: Environmental*, 154-155:36–43, July 2014.

[8] G. Bilis, P. Stathi, A. Mavrogiorgou, Y. Deligiannakis, and M. Louloudi. Improved robustness of heterogeneous Fe-non-heme oxidation catalysts: A catalytic and EPR study. *Applied Catalysis A: General*, 470:376–389, January 2014.

[9] Samir Barman, Niladri Maity, Kushal Bhatte, Samy Ould-Chikh, Oliver Dachwald, Carmen Haeßner, Youssef Saih, Edy Abou-Hamad, Isabelle Llorens, Jean-Louis Hazemann, Klaus Köhler, Valerio D' Elia, and Jean-Marie Basset. Single-site $VO_x$ moieties generated on Silica by Surface Organometallic Chemistry: A Way To Enhance the Catalytic Activity in the Oxidative Dehydrogenation of Propane. *ACS Catalysis*, 6(9):5908–5921, September 2016.

[10] Anna G. Slater and Andrew I. Cooper. Function-led design of new porous materials. *Science*, 348(6238):aaa8075, May 2015.

[11] Shaobin Wang and Yuelian Peng. Natural zeolites as effective adsorbents in water and wastewater treatment. *Chemical Engineering Journal*, 156(1): 11–24, January 2010.

[12] Bert M. Weckhuysen and Jihong Yu. Recent advances in zeolite chemistry and catalysis. *Chemical Society Reviews*, 44(20):7022–7024, October 2015.

[13] Bilge Yilmaz and Ulrich Müller. Catalytic Applications of Zeolites in Chemical Industry. *Topics in Catalysis*, 52(6-7):888–895, June 2009.

[14] S. K. Hoffmann, J. Goslar, S. Lijewski, K. Tadyszak, A. Zalewska, A. Jankowska, P. Florczak, and S. Kowalak. EPR and UV–vis study on solutions of Cu(II) dmit complexes and the complexes entrapped in zeolite A and ZIF-Cu(IM)2. *Microporous and Mesoporous Materials*, 186:57–64, March 2014.

[15] Tianyu Du, Hongxia Qu, Qiong Liu, Qin Zhong, and Weihua Ma. Synthesis, activity and hydrophobicity of Fe-ZSM-5@silicalite-1 for $NH_3$-SCR. *Chemical Engineering Journal*, 262:1199–1207, February 2015.

[16] R. Baran, L. Valentin, and S. Dzwigaj. Incorporation of Mn into the vacant T-atom sites of a BEA zeolite as isolated, mononuclear Mn: FTIR, XPS, EPR and DR UV-Vis studies. *Physical Chemistry Chemical Physics*, 18(17): 12050–12057, 2016.

[17] Rafal Baran, Frederic Averseng, Yannick Millot, Thomas Onfroy, Sandra Casale, and Stanislaw Dzwigaj. Incorporation of Mo into the Vacant T-Atom Sites of the Framework of BEA Zeolite as Mononuclear Mo Evidenced by XRD and FTIR, NMR, EPR, and DR UV–Vis Spectroscopies. *The Journal of Physical Chemistry C*, 118(8):4143–4150, February 2014.

[18] Piotr Pietrzyk and Kinga Góra-Marek. Paramagnetic dioxovanadium( iv ) molecules inside the channels of zeolite BEA – EPR screening of $VO_2$ reactivity toward small gas-phase molecules. *Physical Chemistry Chemical Physics*, 18(14):9490–9496, 2016.

[19] Nataliia Popovych, Pavlo Kyriienko, Sergiy Soloviev, Rafal Baran, Yannick Millot, and Stanislaw Dzwigaj. Identification of the silver state in the framework of Ag-containing zeolite by XRD, FTIR, photoluminescence, 109 Ag NMR, EPR, DR UV-vis, TEM and XPS investigations. *Physical Chemistry Chemical Physics*, 18(42):29458–29465, 2016.

[20] A. M. Sheveleva, A. V. Anikeenko, A. S. Poryvaev, D. L. Kuzmina, I. K. Shundrina, D. I. Kolokolov, A. G. Stepanov, and M. V. Fedin. Probing Gas Adsorption in Metal–Organic Framework ZIF-8 by EPR of Embedded Nitroxides. *The Journal of Physical Chemistry C*, 121(36):19880–19886, September 2017.

[21] Michele Mattioli, Matteo Giordani, Meral Dogan, Michela Cangiotti, Giuseppe Avella, Rodorico Giorgi, A. Umran Dogan, and Maria Francesca Ottaviani. Morpho-chemical characterization and surface properties of carcinogenic zeolite fibers. *Journal of Hazardous Materials*, 306:140–148, April 2016.

[22] Marat R. Gafurov, Ildar N. Mukhambetov, Boris V. Yavkin, Georgy V. Mamin, Alexander A. Lamberov, and Sergei B. Orlinskii. Quantitative Analysis of Lewis Acid Centers of $\gamma$-Alumina by Using EPR of the Adsorbed Anthraquinone as a Probe Molecule: Comparison with the Pyridine, Carbon Monoxide IR, and TPD of Ammonia. *The Journal of Physical Chemistry C*, 119(49):27410–27415, December 2015.

[23] Marta Moreno-González, Beatriz Hueso, Mercedes Boronat, Teresa Blasco, and Avelino Corma. Ammonia-Containing Species Formed in Cu-Chabazite As Per In Situ EPR, Solid-State NMR, and DFT Calculations. *The Journal of Physical Chemistry Letters*, 6(6):1011–1017, March 2015.

[24] Martin Spitzbarth, Andreas Scherer, Andreas Schachtschneider, Peter Imming, Sebastian Polarz, and Malte Drescher. Time-, spectral- and spatially resolved EPR spectroscopy enables simultaneous monitoring of diffusion of different guest molecules in nano-pores. *Journal of Magnetic Resonance*, 283: 45–51, October 2017.

[25] Anita Godiksen, Frederick N. Stappen, Peter N. R. Vennestrøm, Filippo Giordanino, Søren Birk Rasmussen, Lars F. Lundegaard, and Susanne Mossin. Coordination Environment of Copper Sites in Cu-CHA Zeolite Investigated by Electron Paramagnetic Resonance. *The Journal of Physical Chemistry C*, 118(40):23126–23138, October 2014.

[26] J. Peisach and W.E. Blumberg. Structural implications derived from the analysis of electron paramagnetic resonance spectra of natural and artificial copper proteins. *Archives of Biochemistry and Biophysics*, 165(2):691–708, December 1974.

[27] JeongYong Lee, Omar K. Farha, John Roberts, Karl A. Scheidt, SonBinh T. Nguyen, and Joseph T. Hupp. Metal–organic framework materials as catalysts. *Chemical Society Reviews*, 38(5):1450–1459, 2009.

[28] Hiroyasu Furukawa, Kyle E. Cordova, Michael O'Keeffe, and Omar M. Yaghi. The Chemistry and Applications of Metal-Organic Frameworks. *Science*, 341 (6149):1230444, August 2013.

[29] Sara Maurelli, Gloria Berlier, Mario Chiesa, Federico Musso, and Furio Corà. Structure of the Catalytic Active Sites in Vanadium-Doped Aluminophosphate Microporous Materials. New Evidence from Spin Density Studies. *The Journal of Physical Chemistry C*, 118(34):19879–19888, August 2014.

[30] Mantas Šimėnas, Aneta Ciupa, Mirosław Mączka, Andreas Pöppl, and Jūras Banys. EPR Study of Structural Phase Transition in Manganese-Doped $[(CH_3)_2NH_2][Zn(HCOO)_3]$ Metal–Organic Framework. 119(43):24522–24528, October 2015.

[31] W. Ren, J. Gao, C. Lei, Y. Xie, Y. Cai, Q. Ni, and J. Yao. Recyclable metal-organic framework/cellulose aerogels for activating peroxymonosulfate to degrade organic pollutants. *Chemical Engineering Journal*, 349:766–774, 2018.

[32] P.R. McGonigal, P. Deria, I. Hod, P.Z. Moghadam, A.-J. Avestro, N.E. Horwitz, I.C. Gibbs-Hall, A.K. Blackburn, D. Chen, Y.Y. Botros, M.R. Wasielewski, R.Q. Snurr, J.T. Hupp, O.K. Farha, and J.F. Stoddart. Electrochemically addressable trisradical rotaxanes organized within a metal-organic framework. *Proceedings of the National Academy of Sciences of the United States of America*, 112(36):11161–11168, 2015.

[33] Audrey T. Gallagher, Margaret L. Kelty, Jesse G. Park, John S. Anderson, Jarad A. Mason, James P. S. Walsh, Shenell L. Collins, and T. David Harris. Dioxygen binding at a four-coordinate cobaltous porphyrin site in a metal–organic framework: Structural, EPR, and $O_2$ adsorption analysis. *Inorganic Chemistry Frontiers*, 3(4):536–540, 2016.

[34] I. Nevjestić, H. Depauw, K. Leus, G. Rampelberg, C.A. Murray, C. Detavernier, Der Voort Van, F. Callens, and H. Vrielinck. In Situ Electron Paramagnetic Resonance and X-ray Diffraction Monitoring of Temperature-Induced Breathing and Related Structural Transformations in Activated V-Doped MIL-53(Al). *Journal of Physical Chemistry C*, 120(31):17400–17407, 2016.

[35] Matthias Mendt, Felix Gutt, Negar Kavoosi, Volodymyr Bon, Irena Senkovska, Stefan Kaskel, and Andreas Pöppl. EPR Insights into Switchable and Rigid Derivatives of the Metal–Organic Framework DUT-8(Ni) by NO Adsorption. *The Journal of Physical Chemistry C*, 120(26):14246–14259, July 2016.

[36] Benjamin Barth, Matthias Mendt, Andreas Pöppl, and Martin Hartmann. Adsorption of nitric oxide in metal-organic frameworks: Low temperature IR and EPR spectroscopic evaluation of the role of open metal sites. *Microporous and Mesoporous Materials*, 216:97–110, November 2015.

[37] Lars Borchardt, Qi-Long Zhu, Mirian E. Casco, Reinhard Berger, Xiaodong Zhuang, Stefan Kaskel, Xinliang Feng, and Qiang Xu. Toward a molecular design of porous carbon materials. *Materials Today*, 20(10):592–610, December 2017.

[38] Wenjie Tian, Huayang Zhang, Zhao Qian, Tianhong Ouyang, Hongqi Sun, Jingyu Qin, Moses O. Tadé, and Shaobin Wang. Bread-making synthesis of

hierarchically Co@C nanoarchitecture in heteroatom doped porous carbons for oxidative degradation of emerging contaminants. *Applied Catalysis B: Environmental*, 225:76–83, June 2018.

[39] Dariya Savchenko, Andrii Vasin, Shunsuke Muto, Ekaterina Kalabukhova, and Alexei Nazarov. EPR Study of Porous Si:C and $SiO_2$:C Layers. *physica status solidi (b)*, 255(6):1700559, 2018.

[40] Wenjie Tian, Huayang Zhang, Xiaoguang Duan, Hongqi Sun, Moses O. Tade, Ha Ming Ang, and Shaobin Wang. Nitrogen- and Sulfur-Codoped Hierarchically Porous Carbon for Adsorptive and Oxidative Removal of Pharmaceutical Contaminants. *ACS Applied Materials & Interfaces*, 8(11):7184–7193, March 2016.

[41] Wan-Kuen Jo, S. Karthikeyan, Mark A. Isaacs, Adam F. Lee, Karen Wilson, Seung-Ho Shin, Jun-ho Lee, Mo-Keun Kim, Byung-Sik Park, and G. Sekaran. NiO/nanoporous carbon heterogeneous Fenton catalyst for aqueous microcystine-LR decomposition. *Journal of the Taiwan Institute of Chemical Engineers*, 74:289–295, May 2017.

[42] Xiaoguang Duan, Kane O'Donnell, Hongqi Sun, Yuxian Wang, and Shaobin Wang. Sulfur and Nitrogen Co-Doped Graphene for Metal-Free Catalytic Oxidation Reactions. *Small*, 11(25):3036–3044, 2015.

[43] Xufang Qian, Meng Ren, Mengyuan Fang, Miao Kan, Dongting Yue, Zhenfeng Bian, Hexing Li, Jinping Jia, and Yixin Zhao. Hydrophilic mesoporous carbon as iron(III)/(II) electron shuttle for visible light enhanced Fenton-like degradation of organic pollutants. *Applied Catalysis B: Environmental*, 231: 108–114, September 2018.

[44] Zhigao Zhu, Jiaxiang Ma, Chenghan Ji, Yan Liu, Wei Wang, and Fuyi Cui. Nitrogen doped hierarchically structured porous carbon fibers with an ultrahigh specific surface area for removal of organic dyes. *RSC Advances*, 8(34): 19116–19124, 2018.

[45] Yuxian Wang, Hongqi Sun, Xiaoguang Duan, Ha Ming Ang, Moses O. Tadé, and Shaobin Wang. A new magnetic nano zero-valent iron encapsulated in carbon spheres for oxidative degradation of phenol. *Applied Catalysis B: Environmental*, 172-173:73–81, August 2015.

[46] J. Hou, S. Yang, H. Wan, H. Fu, X. Qu, Z. Xu, and S. Zheng. Highly effective catalytic peroxymonosulfate activation on N-doped mesoporous carbon for o-phenylphenol degradation. *Chemosphere*, 197:485–493, 2018.

[47] Jian Kang, Xiaoguang Duan, Chen Wang, Hongqi Sun, Xiaoyao Tan, Moses O. Tade, and Shaobin Wang. Nitrogen-doped bamboo-like carbon nanotubes with Ni encapsulation for persulfate activation to remove emerging contaminants with excellent catalytic stability. *Chemical Engineering Journal*, 332:398–408, January 2018.

[48] Basudeb Karmakar. *Functional Glasses and Glass-Ceramics*. Elsevier, 2017.

[49] Douglas F. Franco, Danilo Manzani, Eduar E. Carvajal, Gabriela Augusta Prando, José Pedro Donoso, Claudio J. Magon, Selma G. Antonio, Yara Galvão Gobato, and Marcelo Nalin. Optical and EPR studies of zinc phosphate glasses containing $Mn^{2+}$ ions. *Journal of Materials Science*, 55 (23):9948–9961, August 2020.

[50] B. Srinivas, Abdul Hameed, G. Ramadevudu, M. Narasimha Chary, and Md. Shareefuddin. Evaluation of EPR parameters for compressed and elongated local structures of $VO^{2+}$ and $Cu^{2+}$ spin probes in $BaO\text{-}TeO_2\text{-}B_2O_3$ glasses. *Journal of Physics and Chemistry of Solids*, 129:22–30, June 2019.

[51] Ruili Zhang, Marcos de Oliveira, Zaiyang Wang, Roger Gomes Fernandes, Andrea S. S. de Camargo, Jinjun Ren, Long Zhang, and Hellmut Eckert. Structural Studies of Fluoroborate Laser Glasses by Solid State NMR and EPR Spectroscopies. *The Journal of Physical Chemistry C*, 121(1):741–752, January 2017.

[52] S. Sen, R. Rakhmatullin, R. Gubaydullin, and A. Silakov. A pulsed EPR study of clustering of $Yb^{3+}$ ions incorporated in $GeO_2$ glass. *Journal of Non-Crystalline Solids*, 333(1):22–27, January 2004.

[53] J. E Garbarczyk, M Wasiucionek, P Jóźwiak, L Tykarski, and J. L Nowiński. Studies of $Li_2OV_2O_5P_2O_5$ glasses by DSC, EPR and impedance spectroscopy. *Solid State Ionics*, 154-155:367–373, December 2002.

[54] A. G. Olabi, C. Onumaegbu, Tabbi Wilberforce, Mohamad Ramadan, Mohammad Ali Abdelkareem, and Abdul Hai Al – Alami. Critical Review of Energy Storage Systems. *Energy*, page 118987, October 2020.

[55] Jun Lu, Tianpin Wu, and Khalil Amine. State-of-the-art characterization techniques for advanced lithium-ion batteries — Nature Energy. https://www.nature.com/articles/nenergy201711.

[56] J.-M. Tarascon and M. Armand. Issues and challenges facing rechargeable lithium batteries. *Nature*, 414(6861):359–367, November 2001.

[57] Naoki Nitta, Feixiang Wu, Jung Tae Lee, and Gleb Yushin. Li-ion battery materials: Present and future. *Materials Today*, 18(5):252–264, June 2015.

[58] Alain Mauger, Christian M. Julien, Michel Armand, and Karim Zaghib. Tribute to John B. Goodenough: From Magnetism to Rechargeable Batteries. *Advanced Energy Materials*, n/a(n/a):2000773, 2020.

[59] Eric C. Evarts. Lithium batteries: To the limits of lithium. *Nature*, 526(7575): S93–S95, October 2015.

[60] Meng Hu, Xiaoli Pang, and Zhen Zhou. Recent progress in high-voltage lithium ion batteries. *Journal of Power Sources*, 237:229–242, September 2013.

[61] Hapuarachchi Sashini N. S., Sun Ziqi, and Yan Cheng. Advances in In Situ Techniques for Characterization of Failure Mechanisms of Li-Ion Battery Anodes. *Advanced Sustainable Systems*, 0(0):1700182, February 2018.

[62] Shao-Lun Cui, Xu Zhang, Xue-Wen Wu, Sheng Liu, Zhen Zhou, Guo-Ran Li, and Xue-Ping Gao. Understanding the Structure–Performance Relationship of Lithium-Rich Cathode Materials from an Oxygen-Vacancy Perspective. *ACS Applied Materials & Interfaces*, October 2020.

[63] Joachim Maier. Review—Battery Materials: Why Defect Chemistry? *Journal of The Electrochemical Society*, 162(14):A2380, October 2015.

[64] Nasrullah Khan, Saad Dilshad, Rashid Khalid, Ali Raza Kalair, and Naeem Abas. Review of Energy Storage and Transportation of Energy. *Energy Storage*, March 2019.

[65] Yiqiong Zhang, Li Tao, Chao Xie, Dongdong Wang, Yuqin Zou, Ru Chen, Yanyong Wang, Chuankun Jia, and Shuangyin Wang. Defect Engineering on Electrode Materials for Rechargeable Batteries. *Advanced Materials*, 32(7): 1905923, 2020.

[66] Howie Nguyen and Raphaële J. Clément. Rechargeable Batteries from the Perspective of the Electron Spin. *ACS Energy Letters*, pages 3848–3859, November 2020.

[67] Anton Van der Ven, Zhi Deng, Swastika Banerjee, and Shyue Ping Ong. Rechargeable Alkali-Ion Battery Materials: Theory and Computation. *Chemical Reviews*, 120(14):6977–7019, July 2020.

[68] Bin Liu, Wu Xu, Jianming Zheng, Pengfei Yan, Eric D. Walter, Nancy Isern, Mark E. Bowden, Mark H. Engelhard, Sun Tai Kim, Jeffrey Read, Brian D. Adams, Xiaolin Li, Jaephil Cho, Chongmin Wang, and Ji-Guang Zhang. Temperature Dependence of the Oxygen Reduction Mechanism in non-aqueous $LiO_2$ batteries. *ACS Energy Letters*, 2(11):2525–2530, November 2017.

[69] Peter Jakes, Leonard Kröll, Andrew Ozarowski, Johan van Tol, Daria Mikhailova, Helmut Ehrenberg, and Rüdiger-A. Eichel. Coordination of the $Mn^{4+}$-Center in Layered $Li[Co_{0.98}Mn_{0.02}]O_2$ Cathode Materials for Lithium-Ion Batteries. *Zeitschrift für Physikalische Chemie*, 231(4):905–922, April 2017.

[70] Mingxue Tang, Annalisa Dalzini, Xiang Li, Xuyong Feng, Po-Hsiu Chien, Likai Song, and Yan-Yan Hu. Operando EPR for Simultaneous Monitoring of Anionic and Cationic Redox Processes in Li-Rich Metal Oxide Cathodes. *The Journal of Physical Chemistry Letters*, 8(17):4009–4016, September 2017.

[71] Johannes Wandt, Cyril Marino, Hubert A. Gasteiger, Peter Jakes, Rüdiger-A. Eichel, and Josef Granwehr. Operando electron paramagnetic resonance spectroscopy – formation of mossy lithium on lithium anodes during charge–discharge cycling. *Energy & Environmental Science*, 8(4):1358–1367, April 2015.

[72] Lin Zhuang and Juntao Lu. Flexible cell designs for simultaneous electrochemical electron spin resonance measurements with a coaxial microwave cavity. *Review of Scientific Instruments*, 71(11):4242–4248, November 2000.

[73] M. Sathiya, J.-B. Leriche, E. Salager, D. Gourier, J.-M. Tarascon, and H. Vezin. Electron paramagnetic resonance imaging for real-time monitoring of Li-ion batteries. *Nature Communications*, 6:ncomms7276, February 2015.

[74] Mihai Duduta, Bryan Ho, Vanessa C. Wood, Pimpa Limthongkul, Victor E. Brunini, W. Craig Carter, and Yet-Ming Chiang. Semi-Solid Lithium Rechargeable Flow Battery. *Advanced Energy Materials*, 1(4):511–516, July 2011.

[75] Peter G. Bruce, Stefan A. Freunberger, Laurence J. Hardwick, and Jean-Marie Tarascon. Li-$O_2$ and Li-S batteries with high energy storage. *Nature Materials*, 11(1):19–29, January 2012.

[76] Chibueze V. Amanchukwu, Hao-Hsun Chang, Magali Gauthier, Shuting Feng, Thomas P. Batcho, and Paula T. Hammond. One-Electron Mechanism in a Gel-Polymer Electrolyte li-$O_2$ battery. *Chemistry of Materials*, 28(19):7167–7177, 2016.

[77] Johannes Wandt, Peter Jakes, Josef Granwehr, Hubert A. Gasteiger, and Rüdiger-A. Eichel. Singlet Oxygen Formation during the Charging Process of an Aprotic Lithium–Oxygen Battery. *Angewandte Chemie*, 128(24):7006–7009, 2016.

[78] Joseph Heelan, Eric Gratz, Zhangfeng Zheng, Qiang Wang, Mengyuan Chen, Diran Apelian, and Yan Wang. Current and Prospective Li-Ion Battery Recycling and Recovery Processes. *JOM*, 68(10):2632–2638, October 2016.

[79] José R. González, Ricardo Alcántara, José L. Tirado, Alistair J. Fielding, and Robert A. W. Dryfe. Electrochemical Interaction of Few-Layer Molybdenum Disulfide Composites vs Sodium: New Insights on the Reaction Mechanism. *Chemistry of Materials*, 29(14):5886–5895, July 2017.

[80] Stanislav S. Fedotov, Nikita D. Luchinin, Dmitry A. Aksyonov, Anatoly V. Morozov, Sergey V. Ryazantsev, Mattia Gaboardi, Jasper R. Plaisier, Keith J. Stevenson, Artem M. Abakumov, and Evgeny V. Antipov. Titanium-based potassium-ion battery positive electrode with extraordinarily high redox potential. *Nature Communications*, 11(1):1–11, March 2020.

[81] D. M. Marinova, V. V. Kostov, R. P. Nikolova, R. R. Kukeva, E. N. Zhecheva, and R. K. Stoyanova. Redox properties of alluaudite sodium cobalt manganese sulfates as high-voltage electrodes for rechargeable batteries. *Chemical Communications*, 54(43):5466–5469, 2018.

[82] Dharmendra Pal, Shahanshah Haider Abdi, and Manisha Shukla. Structural and EPR studies of Lithium inserted layered Potassium tetra titanate $K_2Ti_4O_9$ as material for K ions battery. *Journal of Materials Science: Materials in Electronics*, 26(9):6647–6652, September 2015.

[83] Yongzheng Fang, Yingying Zhang, Chenxu Miao, Kai Zhu, Yong Chen, Fei Du, Jinling Yin, Ke Ye, Kui Cheng, Jun Yan, Guiling Wang, and Dianxue Cao. MXene-Derived Defect-Rich $TiO_2$@rGO as High-Rate Anodes for Full Na Ion Batteries and Capacitors. *Nano-Micro Letters*, 12(1):128, June 2020.

# Chapter 2

# Brief Overview of EPR spectroscopy and complementary techniques in the characterisation of solid-state functional materials

The following section initially presents an overview of the theoretical aspects of Continuous Wave (CW) Electron Paramagnetic Resonance (EPR) spectroscopy, and its application to solid-state systems. The information provided herein is a summary of a number of texts and reviews in the respective areas.[1–11]

## 2.1 Theory of CW EPR spectroscopy

The basis of the EPR experiment relies on the property of spin for the unpaired electron. For the simplest case of a free electron, $S = 1/2$ which is quantised into $2S + 1$ electronic states, $m_s$ +1/2 and -1/2 (spin *up*, $|\alpha\rangle$, and *down*, $|\beta\rangle$), which are equally populated and degenerate in the absence of any external stimuli. In the classical treatment, the magnetic dipole moment for the electron, $\mu_S$, as a result of its spin, is described by the following equation:

$$\mu_S = -g_e \mu_B \cdot \mathbf{S} \tag{2.1}$$

where $\mathbf{S}$ is the spin angular moment quantum number; $\mu_B$ is the Bohr magneton ($\mu_B = 9.274 \cdot 10^{-24} J T^{-1}$) and $g_e$ is the free electron gyromagnetic (*g*-) factor ($\approx 2.00232$)) that corrects for the quantum result from the classical model.

In the presence of an applied magnetic field, $B_0$, the electronic states become non-degenerate, due to their preferential orientation with respect to the magnetic field vector. The magnetic moment, $\mu_S$ is redefined by projection onto the magnetic field vector $\mathbf{B}$ to give $\mu_z$, and can then be related to the $m_s$ electron states:

$$\mu_z = -g_e \mu_B m_s \tag{2.2}$$

The relative energy, $E$, of the two electronic $m_s$ states (the *Zeeman* levels) is then given by:

$$E = g_e \mu_B m_s \cdot \mathbf{B} \tag{2.3}$$

Irradiation by microwave photons (of energy $h\nu_{MW}$) will result in absorption when the energy difference between states matches that of the photon (equation 2.1), which results in a transition between the electronic states, and a characteristic resonance (Figure 2.1) following the EPR selection rule $\Delta m_s = \pm 1$. In CW EPR, the microwave frequency $\nu_{MW}$ is held constant and the magnetic field range $B$ is varied, since the resonance offset can be extremely large when compared to NMR (where the frequency is swept and the field held constant). The detection method for CW EPR (modulation of the applied magnetic field $B_0$) results in a first derivative signal (Figure 2.1).

$$\Delta E = h\nu_{MW} = g_e \mu_B \cdot \mathbf{B} \tag{2.4}$$

It follows that the free electron description is inappropriate for real systems, which are localised to an orbital, contain several unpaired electrons and possibly magnetic nuclei. Each is a source of additional local magnetic fields, which perturb the effective field at the electron site.

$$\mathbf{B}_{eff} = (g/g_e) \cdot \mathbf{B} \tag{2.5}$$

which is manifested in $g$, the effective gyromagnetic factor, for the real system. The effective $g$-factor is therefore characteristic of the local environment of the

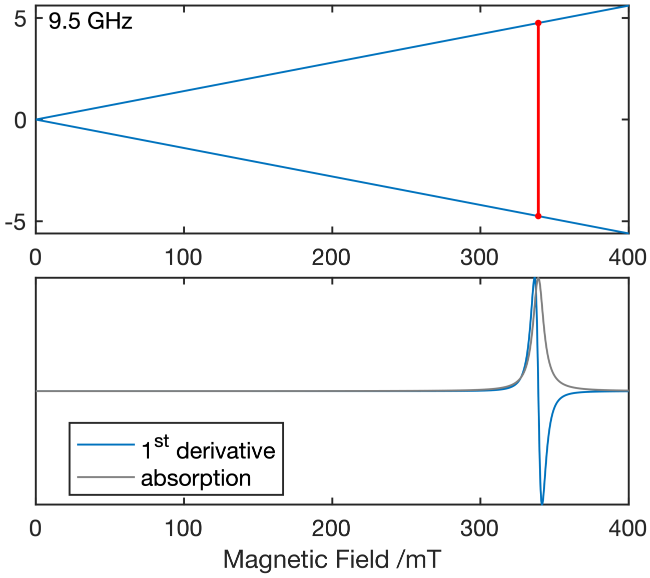

**Figure 2.1:** Zeeman diagram for a simple $S$=1/2 system in the presence of an applied magnetic field, $B_0$. *Top*: Zeeman energy diagram showing removal of degeneracy of the $|\alpha\rangle$, and $|\beta\rangle$ electronic states. The red line corresponds to the magnetic field resonance at which $\Delta E = h\nu_{MW}$ and a transition occurs between the states. *Bottom*: Simulated EPR spectrum showing the first derivative (*blue*) and absorption (*grey*) signals for $g = 2$ corresponding to the resonance.

electron, and hence identifies the nature of the electron spin with respect to its orbital environment, and proximity to local magnetic spins.

### 2.1.1 The Spin Hamiltonian

Real systems will likely contain one or more distinct electronic states, in addition to multiple magnetic nuclei. Contributions to the total energy of the system is then a complex interplay of several interactions, not only with the external field, but also between electrons, and nuclei, and each must be treated in turn (if they are significant in energy) in order to obtain a meaningful description of the system. The total energy of the system, described by the Hamiltonian $\hat{H}_{total}$, may be defined as a summation of individual magnetic Hamiltonians, which describe the separate interaction terms, equation 2.6.

$$\hat{H}_{total} = \hat{H}_{EZ} + \hat{H}_{NZ} + \hat{H}_{HFI} + \hat{H}_{NQI} + \hat{H}_{ZFS} + \hat{H}_{EE} \tag{2.6}$$

Where $\hat{H}_{EZ}$ (met in the previous section) and $\hat{H}_{NZ}$ are Hamiltonians defining interactions of an electron or magnetic nucleus with the magnetic field, *viz.* the *Electron Zeeman* and *Nuclear Zeeman* interactions; $\hat{H}_{HFI}$ the electron-nuclear *Hyperfine* interaction; $\hat{H}_{ZFS}$ and $\hat{H}_{EE}$ describe the electron-electron interactions; the intra-electronic *Zero Field Splitting*, and the inter-electronic *Exchange, Dipolar* interactions (represented as a single Hamiltonian term). Each interaction is described by one or more characteristic spin Hamiltonian parameters that modulate the magnitude of the given interaction between dipoles or the external field. Clearly, the size of the total interaction matrix, and therefore the complexity of the system, then increases with the number of introduced terms, the number of inequivalent interactions, and the number of magnetically inequivalent sites. Each of these interactions will be treated separately, and briefly summarised in turn.

### 2.1.2 Electron Zeeman interaction

The basis of the EPR experiment, the *electron Zeeman* (EZ) interaction, was introduced in the first section. The corresponding spin Hamiltonian is described by the following equation:

$$\hat{H}_{EZ} = g\mu_B \hat{S} \cdot B \tag{2.7}$$

which describes the electronic eigenstates of the quantum system for given $S$. The interaction is characterised by the effective $g$ factor, which is shifted away from the free electron $g_e$ value by spin-orbit coupling. This was introduced as a simple scalar quantity, however it follows that the relative deviation, and orientation with respect to the external magnetic field vector is critical to the magnitude of the interaction, which is manifested in the anisotropy of $g$. We therefore replace the scalar quantity with a (3x3) tensor quantity to fully represent the orientational dependence. We may then rewrite equation 2.1 as follows:

$$h\nu_{MW} = g(\theta, \phi)\mu_B B \tag{2.8}$$

where $g(\theta, \phi)$ is the effective $g$ tensor, which (assuming the off-diagonal matrix elements are zero) may be further expressed as a function of the polar, $\theta$ (rotation from $z$), and azimuthal, $\phi$ (rotation in $x, y$ plane), angles:

$$g^2(\theta, \phi) = g_{xx}^2 sin^2\theta cos^2\phi + g_{yy}^2 sin^2\theta sin^2\phi + g_{zz}^2 cos^2\theta \tag{2.9}$$

which may be used to determine the value of $g$ at any given orientation with respect to **B**. A more complete description is afforded by the following spin Hamiltonian:

$$\hat{H} = \mu_B \mathbf{B}^T \cdot \mathbf{g} \cdot \hat{\mathbf{S}} \tag{2.10}$$

where $\hat{S}$ are the Pauli spin operators; $B_i$ are the principle values of **B**, defined in equation 2.11, and **g** is the $g$ matrix as a function of the relative orientation. The superscript 'T' indicates a vector transposition. In full form:

$$\hat{H}_{EZ} = \mu_B \begin{bmatrix} B_x & B_y & B_z \end{bmatrix} \cdot \begin{bmatrix} g_{xx} & 0 & 0 \\ 0 & g_{yy} & 0 \\ 0 & 0 & g_{zz} \end{bmatrix} \cdot \begin{bmatrix} \hat{S}_x \\ \hat{S}_y \\ \hat{S}_z \end{bmatrix} \tag{2.11}$$

where $B_x$, $B_y$ and $B_z$ are the diagonal values of the **B** matrix. The principle values $g_{xx}$, $g_{yy}$ and $g_{zz}$ directly correlate to the symmetry and orientation of the paramagnetic centre in question. It is not always possible to assign the directions from CW EPR, without the aid of single crystal measurements (where the crystal face or plane is aligned with $B_0$ and rotated), or quantum chemical calculations (to predict the magnitude and orientation of the principle coordinate axes of the $g$ tensor). In the liquid state, molecules are able to undergo molecular tumbling. If the frequency far exceeds that of the frequency difference for the anisotropic interactions, complete averaging occurs and the system may be described by a single value ($g_{iso}$).

### Effect of spin-orbit coupling on $g$

The deviation of $g$ away from the free electron value (*i.e.* the resonance offset), which is indicative of the chemical nature of the spin, arises due to the effect of spin-orbit coupling (SOC). The total spin quantum number is no longer appropriate to accurately describe the nature of the system. In addition to the intrinsic spin angular momentum, the orbital occupation introduces another effective magnetic field due to the intrinsic *orbital angular momentum*, $\mathbf{L}$:

$$\mu = \mu_B(\mathbf{L} + g_e\mathbf{S}) = \mu_B(g_J\mathbf{J}) \tag{2.12}$$

where $g_J$ is a constant known as the Landé factor. The Hamiltonian may then be expressed, to first-order as:

$$\hat{H} = \mu_B\mathbf{B}^T(\hat{\mathbf{L}} + g_e\hat{\mathbf{S}}) + \lambda\hat{\mathbf{L}}^T\hat{\mathbf{S}} = \mu_B\mathbf{B}^T(g_J\hat{\mathbf{J}}) + \lambda\hat{\mathbf{L}}^T\hat{\mathbf{S}} \tag{2.13}$$

which takes into account the spin, orbital and spin-orbit coupling contributions, respectively. This assumes that the states are well separated in energy when compared to the perturbation introduced by SOC, otherwise second-order corrections to the energies can be necessary.

In the ground state, the orbital angular momentum is typically quenched, however spin-orbit coupling reintroduces the orbital momentum by admixture of excited state contributions into the spin Hamiltonian. The experimentally derived values can be related to the spin-orbit coupling constant using the following equation:

$$g_{ij} = g_e \pm \frac{n\lambda}{E_0 - E_n} \tag{2.14}$$

Where $n$ is a numerical value dependent on the coupling of electronic states $E_0$ and $E_n$. $\lambda$ can take positive or negative values depending on the electron or hole-character of the electronic structure, which will determine the relative ordering of the $g_{ij}$ values. From this equation, it can be noted that the $g$ tensor is therefore sensitive to the ligand field splitting, the orbital occupancy, and subsequent total electronic spin. Analysis of the principle values can then be used to determine the coordination environment and relative energy level splitting in an applied ligand field, providing the value of $\lambda$ is known.

### The single crystal spectrum

In the previous section, the EZ interaction and anisotropic $g$ tensor were defined, which was shown to vary with respect to orientation with the external magnetic field, $B_0$. The variation of $g$, with respect to $B_0$, is therefore characteristic of the symmetry of the paramagnetic site, which is manifested in the $g$-anisotropy. In a single crystal measurement, where the orientation of the spin Hamiltonian parameters is related to the crystallographic sites, a single set of resonances pertaining to a single orientation of $g$ with respect to $B_0$ is observed. The $g$-tensor need not be diagonal, and may therefore contain off-diagonal elements due to the rotation of $g$ away from the crystallographic axes. In principle, the full $\mathbf{g}$ matrix may be determined by careful analysis. The symmetry of the $\mathbf{g}$ tensor can be defined in three classes based on the orientational equivalence (alternative definitions for $g$ values given in brackets):

(i) isotropic symmetry, $g_1 = g_2 = g_3$ ($g_{iso}$);

(ii) axial symmetry, $g_1 = g_2 \neq g_3$ ($g_{\|} \neq g_{\perp}$);

(iii) rhombic symmetry, $g_1 \neq g_2 \neq g_3$.

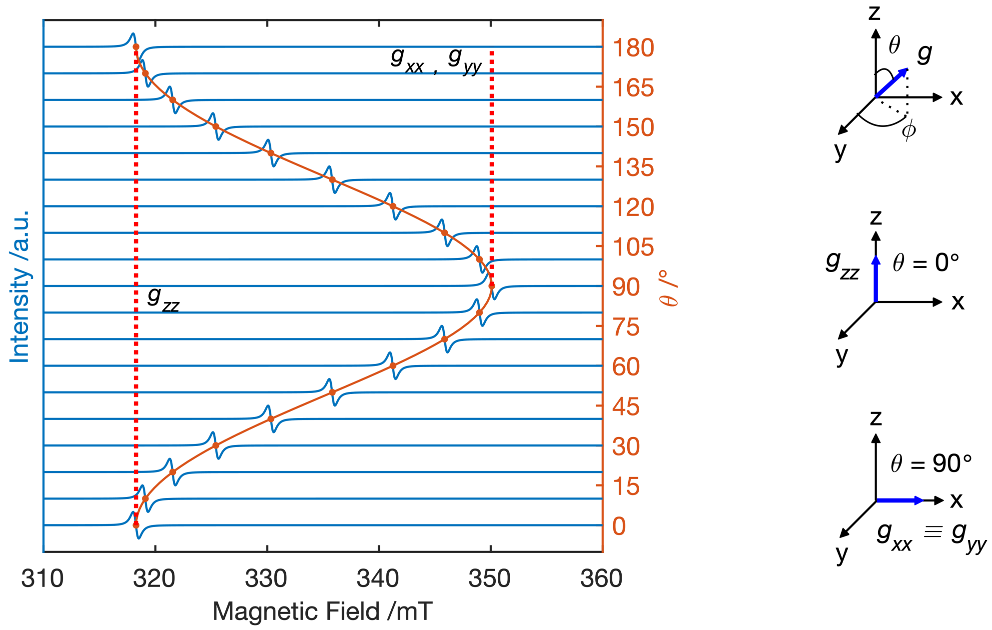

**Figure 2.2:** *Left:* Calculated EPR spectra (*blue*) and resonant field positions (*orange*) as a function of $\theta$, for the projection of $g \parallel B_z$ of an axially symmetric system with P1 symmetry and $g_{xx} = g_{yy} = 2.00$; $g_{zz} = 2.20$, $\nu_{MW} = 9.80$ GHz. The dotted red lines highlight the rotation turning points which are equivalent to the diagonal $g_{xx}$, $g_{yy}$ and $g_{zz}$ values. *Right*: (a) definition of angles $\theta$ and $\phi$ with respect to the magnetic field vector; (b) projection of $g$ onto $\mathbf{B}$ at $\theta = 0$, 180°, equivalent to $g_{zz}$; (c) projection of $g$ onto $\mathbf{B}$ at $\theta = 90°$, equivalent to $g_{xx}, g_{yy}$.

The number of turning points, providing the anisotropy is resolved upon variation of the angles $\theta$ and $\phi$ with respect to $B_0$, is indicative of the particular class of symmetry that a paramagnetic species possesses. The variation of the resonant field position with $\theta$ is shown in Figure 2.2, for a simple case of axial symmetry, assuming the orientation of the $g$ tensor is collinear with the magnetic field vector with no other interactions considered. Two extreme values for $B_{res}$ are observed at $\theta = 0$, 90, 180° which correspond to $g_{\|}$ and $g_{\perp}$.

A final point to note is that it may be practically difficult, or impossible, to prepare a suitable single crystal for orientation-dependent measurements. It is much more common to encounter polycrystalline samples, in which the spins are randomly oriented with respect to $B_0$. This situation is generally less informative, however more straightforward to characterise.

### The polycrystalline (powder) spectrum

If the sample is totally randomly oriented (*e.g.* powder, frozen solution), all orientations are equally probable and therefore the spectrum is observed as an envelope due to the summation of the resonances over all orientations, which produces a characteristic line shape. The turning points, *i.e.* the effective principle values due to the projection of $g$ along $B_z$ are possible to determine from the spectrum, how-

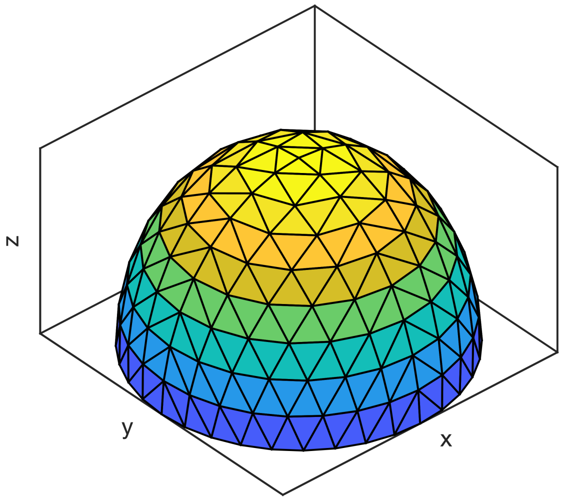

**Figure 2.3:** Triangular hemispherical grid for the summation of calculated single orientations to produce a powder spectrum. Spin Hamiltonian parameters possess a centre of inversion, hence only one half of the sphere is needed. Each point represents a given orientation of the principle coordinate axes of the spin Hamiltonian parameter, defined relative to $B_0$.

ever the orientation of the principle $g$ coordinate axes are not, since the variation with respect to the crystallographic orientation is not resolved.

The observed line shape can be understood by calculation of the summed average envelope over a suitable number of orientations. Powder line shapes are then generally broad in comparison to single crystal measurements. Modern simulation software (such as EasySpin, a MATLAB toolbox developed at ETH Zurich[12]) achieves this by utility of a spherical grid, Figure 2.3, which represents the molecular coordinate frame. The resonance position and intensities (due to transition probability) are calculated for each orientation (vertex) on the grid which then recreates the experimental powder line shape. The characteristic absorption and first-derivative line shapes for the three symmetry classes are shown in Figure 2.4.

The resonance probability,$P(B)$ for axial symmetry at a single field $B$ is given by the following equation:

$$P(B) = C\frac{1}{2}sin\theta(\frac{dB}{d\theta})^{-1} \tag{2.15}$$

Where C is a normalisation constant. P(B) is therefore proportional to $sin\theta$ and $B^{-1}$ assuming a totally randomly oriented sample, where all orientations are equally probable. For lower symmetry, $dB/d\phi$ must also be considered.

### Partially ordered systems

When the sample is not completely polycrystalline, either due to local ordering of the crystallites, or the absence of long range order (*i.e.* amorphous samples), the probability of a given orientation is no longer described by equation 2.15. The relative intensities of the respective turning points may therefore be different to the expectation for polycrystalline systems. For axially symmetric systems, where the local ordering is described between the xz, yz and xy planes, this may be accounted for using the following equation instead:

$$P(\theta) = exp(-U(\theta)) \tag{2.16}$$

$$U(\theta) = -\lambda(3cos^2(\theta) - 1)/2 \tag{2.17}$$

where $\lambda$ is a value that describes the ordering potential. Finally, if the symmetry is lower than axial, a more complex expression may need to be developed in order to account for the observed line intensities, which is not straightforward. For this reason, the partially ordered state is avoided if possible, *e.g.* by grinding of a polycrystalline sample to ensure a homogeneous orientational distribution.

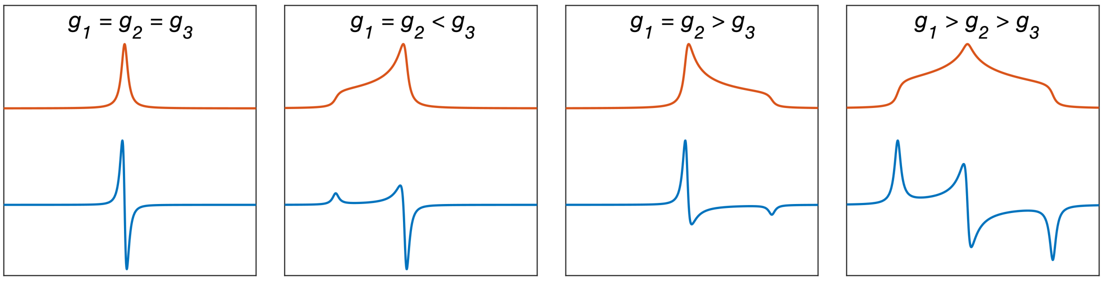

**Figure 2.4:** Simulated polycrystalline line shapes which relate to the symmetry of the $g$ tensor, annotated for each case. *Orange:* absorption spectrum; *Blue:* first derivative spectrum. *From left to right:* isotropic; axial with $g_3 > g_{1,2}$; axial with $g_3 < g_{1,2}$; rhombic symmetry.

### 2.1.3 Nuclear Zeeman (NZ) Interaction

Similar to the electron spin, a nucleus with $I \neq 0$ will also have an associated magnetic dipole moment, $\mu_I$:

$$\mu_I = g_n \mu_N \hat{I} \tag{2.18}$$

where $g_n$ is the nuclear $g$-factor, which can take positive or negative values; $\mu_N$ is the nuclear magneton; and $I$ is the nuclear spin quantum number. Analogous to the EZ interaction, the $m_I$ moments are non-degenerate in an applied magnetic field relative to its orientation, which leads to a splitting of the electronic states by $2I + 1$. This is the *nuclear Zeeman interaction* (which is orders of magnitude smaller than the EZ; $\mu_B/\mu_N > 1800$) which is described by the following Hamiltonian term:

$$\hat{H}_{NZ} = g_n \mu_N \hat{I} \cdot \vec{B} \tag{2.19}$$

However, the NZ term is relatively uninformative (since we are not directly probing the nuclear transitions) without the effect of the hyperfine interaction, described in the next section.

### 2.1.4 Hyperfine Interaction

The interaction of the electron ($\mu_S$) and nuclear ($\mu_I$) magnetic moments with the applied external field $B_0$ were defined *vide infra* for a simple $S$=1/2, $I$=1/2 system, *i.e.* the EZ and NZ interactions. If these were the only interactions to take place, the EPR spectrum would be relatively uninformative as the allowed transitions are degenerate in energy, producing only one resonant field in the spectrum, independent of the nuclear spin $I$. It follows that the electron and nuclear moments also interact to produce a characteristic splitting, independent of applied external field. This interaction is termed the *hyperfine interaction* (HFI), which perturbs the energies of the electron and nuclear eigenstates and thus removes the degeneracy of the allowed electronic transitions $\Delta m_s = \pm 1; \Delta m_I = 0$(Figure 2.5):

$$E = g\mu_B m_s \cdot B + g_n \mu_N m_I \cdot B - m_s \cdot A \cdot m_I \tag{2.20}$$

Where $A$ is the hyperfine coupling constant, which determines the magnitude of the interaction between the $m_s$ and $m_I$ states. $A$ may take positive or negative values, dependent on the relative sign of $g_n$, and reflects the relative orientation of the magnetic dipole moments. The interaction with an electron spin is not restricted to one nucleus; for highly delocalised aromatic molecules, for example, several small couplings are often detected which lead to an increasingly complex hyperfine structure that provides detailed structural information about the nature of the radical; and the localisation of the electron spin. In the case of multiple nuclei, the number of transitions that compose the hyperfine structure may be calculated by the product of each set of equivalent nuclei, $\prod(2nI+1)$. Similar to the situation for the $g$-tensor for solid systems, the hyperfine interaction is also dependent on the orientation with respect to the external field, **B**. The fast molecular motion in solution will average out these anisotropic contributions leading to

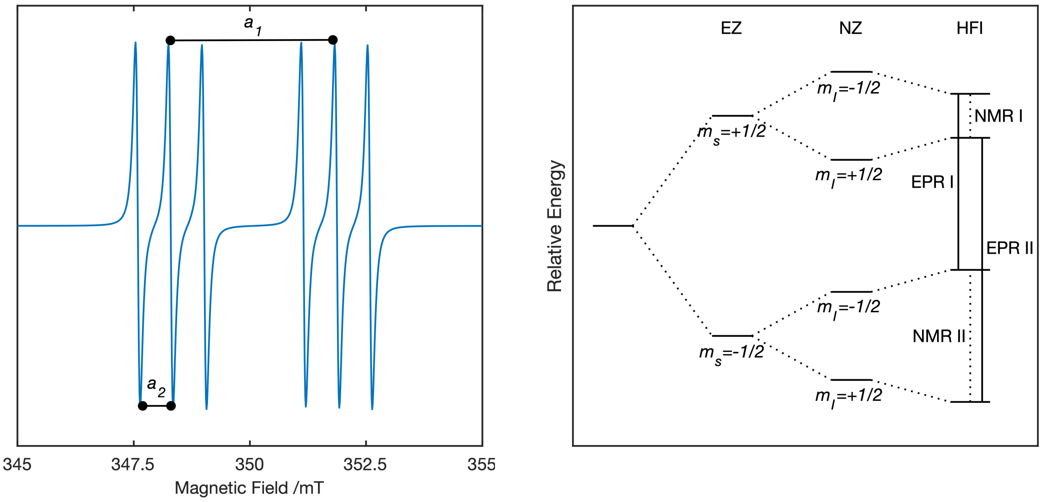

**Figure 2.5:** *Left:* Simulated EPR spectrum for $S = 1/2$ ($g = 2.00$) with two interacting nuclei; $I_1 = 1/2$, $a_1 = 100$ MHz; $I_2 = 1$, $a_2 = 20$ MHz. *Right:* Energy levels schematic for a simple $S = 1/2$; $I = 1/2$ system, labelled assuming positive $g_n$ and $a$. The solid vertical lines denote the allowed EPR transitions (EPR I, EPR II) and dashed vertical lines the allowed NMR transitions (NMR I, NMR II).

a simpler case. Therefore, for solid systems we must define the anisotropic spin Hamiltonian:

$$\hat{H}_{HFI} = \hat{\mathbf{S}}^T \cdot \mathbf{A} \cdot \hat{\mathbf{I}} \tag{2.21}$$

Where $A$ is the anisotropic hyperfine matrix. We may further decompose the matrix by subtracting $a_{iso}$ from the hyperfine matrix, which leads to the definition of the purely anisotropic dipolar matrix, $\mathbf{T}$:

$$\mathbf{A} = \begin{bmatrix} A_{xx} & A_{xy} & A_{xz} \\ A_{yx} & A_{yy} & A_{yz} \\ A_{zx} & A_{zy} & A_{zz} \end{bmatrix} = a_{iso} \cdot \hat{\mathbf{1}} + \mathbf{T} \tag{2.22}$$

Where $\hat{\mathbf{1}}$ is an identity matrix, and $\mathbf{T}$ is a traceless, axially symmetric tensor, which corresponds to the *through-space* interaction of electron spin density in the axially symmetric, *i.e.* p, d, f orbitals. The isotropic hyperfine interaction, $a_{iso}$, is a term arising from the *Fermi contact interaction*, *i.e.* the *through-bond* interaction of electron and nuclear moments due to unpaired spin density at the magnetic nucleus (*i.e.* the $s$-character of the hosting orbitals).The hyperfine field is constant and *isotropic* inside the nuclear volume, and furthermore the value can be related to $|\Psi(0)|^2$ in the following expression:

$$a_{iso} = (\frac{2\mu_0}{3}) g \mu_B g_N \mu_N |\Psi(0)|^2 \tag{2.23}$$

The anisotropic dipolar hyperfine tensor, $T$, is then dependent on the angle ($\theta$) between the applied field $\mathbf{B}$ and is characteristic of the radial and angular nature of the hosting orbital:

$$T_{ij} = \frac{\mu_0}{4\pi} \frac{g_e \mu_B g_N \mu_N}{r^3} \langle 3cos^2\theta - 1 \rangle \tag{2.24}$$

Where $r$ is the distance between the electron and nuclear moments Finally, the hyperfine matrix (hence the $T$ matrix) are usually diagonalised to obtain the principle (diagonal) values of the tensor. For the simple case of an axial tensor, we may re-write equation 2.1.4 in a simpler form:

$$\mathbf{A} = \begin{bmatrix} A_{xx} & 0 & 0 \\ 0 & A_{yy} & 0 \\ 0 & 0 & A_{zz} \end{bmatrix} = \begin{bmatrix} a_{iso} - T & 0 & 0 \\ 0 & a_{iso} - T & 0 \\ 0 & 0 & a_{iso} + 2T \end{bmatrix} \tag{2.25}$$

Which allows the user to obtain further information about the system by decomposition of the experimentally obtained values. The anisotropic $T$ tensor can also be of rhombic symmetry; however, the hosting orbitals (p,d,f) that contribute to $T$ are always axially symmetric, possessing at least $C_{2v}$ symmetry. The rhombic $T$ (or $A$) tensor is then a summation of axial tensors (which will have different relative orientations), corresponding to contributions from unpaired spin density in more than one orbital (*e.g.* $\mathrm{d_{xz}}$, $\mathrm{d_{yz}}$) and can then be related to the partial orbital occupancy in the electronic ground state.

### 2.1.5 Quadrupole Interaction

In addition to the hyperfine interaction, if a nucleus has $I$ >1/2 then an additional dipolar interaction arises, the *nuclear quadrupole interaction* (NQI), due to the non-spherical distribution of the electric field gradient at the nucleus. This is observed as a splitting of the nuclear eigenstates into $2I$ levels which contribute additional structure. The spin Hamiltonian term for the quadrupolar interaction is as follows:

$$\hat{H}_{NQ} = \hat{I}^T \cdot \mathbf{P} \cdot \hat{I} \tag{2.26}$$

Where $\mathbf{P}$ is the anisotropic quadrupolar matrix, which is a symmetric, traceless tensor. $\mathbf{P}$ may be further defined in terms of an *axial*, $P$, and *rhombic* parameter, $\eta$, for convenience:

$$\mathbf{P} = P \begin{bmatrix} \eta - 1 & 0 & 0 \\ & -\eta - 1 & 0 \\ & & 2 \end{bmatrix} \tag{2.27}$$

$P$ and $\eta$ are defined as:

$$P = \frac{e^2qQ/h}{4I(2I-1)} \tag{2.28}$$

$$P_{zz} = \frac{e^2qQ}{2h} \tag{2.29}$$

$$\eta = \frac{P_{xx} - P_{yy}}{P_{zz}} \tag{2.30}$$

where $e$ is the elementary charge, $q$ is the electric field gradient at the nucleus ($q = \partial^2 V/\partial z^2$; $V$ is the electrostatic potential) and $Q$ is the electric quadrupole moment. The interaction is usually described in terms of the axial quantity $e^2qQ/h$, and the rhombicity parameter $\eta$, which describes the deviation of the quadrupolar field gradient from axial symmetry (*i.e.* the anisotropy of the principle $x$ and $y$ components of the tensor). The quadrupolar interaction is generally small (<1 MHz) and therefore rarely observed using the conventional EPR technique, treated as only a minor perturbation of the eigenvalues. Advanced hyperfine techniques (ENDOR, ESEEM) can instead be used to characterise the interaction, which are able to resolve weak hyperfine couplings (<10 MHz).

### 2.1.6 Zero Field Splitting

Analogous to the nuclear quadrupole interaction, but more importantly for EPR, paramagnetic systems such as transition metals may also possess more than one unpaired electron ($S > 1/2$). The anisotropic, dipolar interaction between spins is termed *zero field splitting* (ZFS), which arises from spin-orbit and spin-spin coupling mechanisms. The term 'ZFS' highlights the field-independent nature of the interaction, since even at zero field a characteristic splitting (*fine* structure) of the $2S$ electronic states arises. ZFS interactions can be very large, greater than the microwave quantum at conventional frequencies, which can limit the information afforded without appropriate high field, high frequency (HF-EPR) measurements. The Hamiltonian term for the ZFS interaction is as follows:

$$\hat{H}_{ZFS} = \hat{S}\cdot\mathbf{D}\cdot\hat{S} \tag{2.31}$$

$$= (D_x\hat{S}_x^2 + D_y\hat{S}_y^2 + D_z\hat{S}_z^2) \tag{2.32}$$

Where $\mathbf{D}$ is the second-order anisotropic dipolar matrix that describes the magnitude of interactions between the unpaired electron spins, as a function of relative orientation. Analogous to the case for NQI, the ZFS tensor is symmetric and traceless, therefore we may define the ZFS term with an axial ($D$) and rhombic ($E$) term:

$$\hat{H}_{ZFS} = D\{\hat{S}_z^2 - \frac{1}{3}S(S+1)\hat{1}\} + E(S_x^2 + S_y^2) \tag{2.33}$$

Where $D$ and $E$ are related to the principle values of the traceless $D$ tensor as follows:

$$D = \frac{3}{2}D_{zz} \tag{2.34}$$

$$E = \frac{1}{2}(D_{xx} - D_{yy}) \tag{2.35}$$

The orientation of the principle values of the dipolar tensor are chosen according to the convention $|D_{zz}| > |D_{yy}| > |D_{xx}|$ which results in the limit $3|E| \leq |D|$, representing maximum rhombic symmetry.

Some simple examples are now presented for two different systems: Kramers (half-integer) and non-Kramers (integer) ions, whose behaviour is drastically different when considering ZFS. The simplest system that will undergo ZFS is $S = 1$ (Figure 2.6, *left*), which is commonly found for organic triplets, with 3 microstates $m_s$ = -1, 0, +1. For this discussion, it is assumed that $D \ll h\nu_{MW}$ and therefore all allowed transitions are accessible. In the absence of a magnetic field, and in the absence of the ZFS term, these states are the same in energy, and the corresponding allowed transitions ($\Delta m_s = \pm 1$) are degenerate, leading to a single line in the spectrum. There is also the possibility of a forbidden, double quantum transition ($\Delta m_s = \pm 2$), however this is totally forbidden in the absence of ZFS. Upon the application of an axial term ($D > 0, E = 0$) the $m_s$ levels are separated in energy by $D$.

If the rhombic term is also introduced $E > 0$, a separation of $2E$ is introduced in the $m_S = \pm 1$ doublet which totally removes the degeneracy of the electronic microstates; giving zero field energies $E_i = 0$, $D - E$; $D + E$. Finally, upon application of the magnetic field, the perturbed eigenstates at zero field are perturbed by the Zeeman interaction which further split the $m_s = \pm 1$ levels (by $g\mu_B B$ while the $m_s = 0$ levels are invariant with applied field.

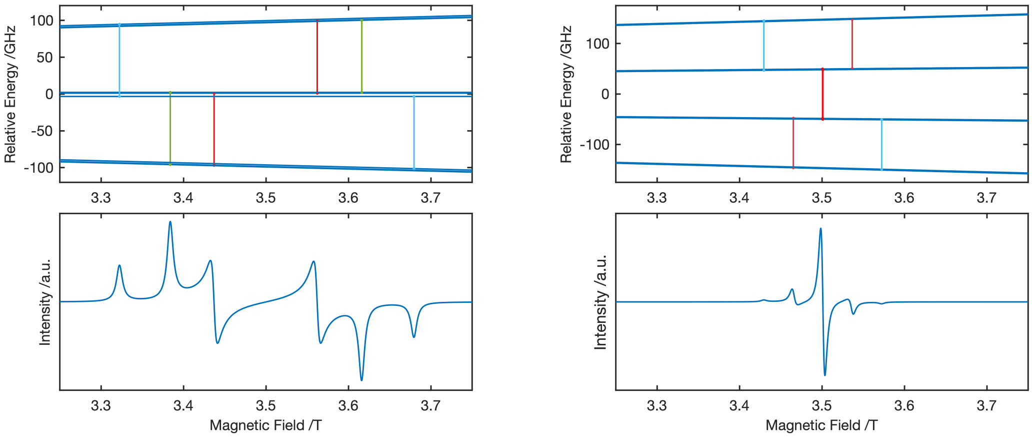

**(a)** $S = 1$; $g = 2.00$;
$D/h = 5000$ MHz; $E/D = 0.1$

**(b)** $S = 5/2$; $g = 2.00$;
$D/h = 1000$ MHz; $E/D = 0$

**Figure 2.6:** Examples of non-Kramers and Kramers high spin systems with resolved ZFS. *Upper:* Calculated (and superimposed) energy level diagrams obtained by matrix diagonalisation of the spin Hamiltonian and resonant transitions for $\nu_{MW} = 98$ GHz. The transition selection threshold was set to a relatively low value (0.1) to remove temperature polarisation and probability effects from the allowed transitions. The transitions are coloured according to their orientation with the external field, $B_0$. *blue*: $x \parallel B_0$; *green*: $y \parallel B_0$; *red*: $z \parallel B_0$ *Lower:* Simulated powder EPR spectra using the spin Hamiltonian parameters in (a) and (b).

The second example concerns a Kramers system, $S = 3/2$, (example shown in Figure 2.6) which is commonly met for metals such as $Cr^{3+}$. In contrast to the non-Kramers $S = 1$ system, the micro-states are always doubly degenerate at zero field, even in the presence of a rhombic ($E$) term. The fine structures observed for Kramers systems are usually very similar, and can even lead to misinterpretation since the additional lines from higher $m_s$ states are generally weaker (due to the thermal populations) when $D$ is large and may not be resolved, dependent on the quality of the spectrum. At zero field, with an axial ZFS ($D > 0$) the Kramers doublets are separated by $2D$, $4D$ respectively. Upon introduction of the rhombic term, $E$, the degeneracy of the doublets is preserved and the energy gap *between* the Kramers doublets is instead perturbed to give $2\sqrt{D^2 + 3E^2}$.

For the two examples, it was assumed that $D \ll h\nu_{MW}$, which is not necessarily the case for ZFS, particularly for metal ions. The relative energies of the microwave quantum, $\nu_{MW}$ compared to the $D$ term is therefore of critical importance. An example of the calculated energy level diagrams and transitions for an exemplary $S = 5/2$ system is presented in Figure 2.7 with $D/h = 40$ GHz. The three examples illustrate the accessible transitions upon increasing the microwave frequency; the *weak* ($D \gg h\nu_{MW}$),*intermediate* ($D \approx h\nu_{MW}$) and *strong* ($D \ll h\nu_{MW}$) field limits respectively.

**Weak field limit:** For Kramers systems, when the splitting between doublets

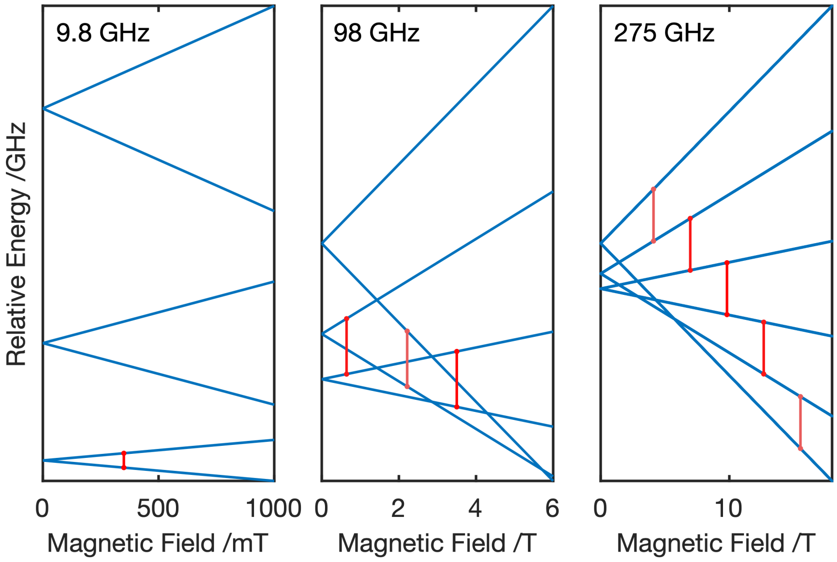

**Figure 2.7:** Calculated energy levels for an $S$=5/2 system with $g = 2.00$, $D/h = 40$ GHz, $E/D = 0$; with calculated transitions as a function of $\nu_{MW}$. *Left:* Weak field limit, $D \ll h\nu_{MW}$; *Centre:* Intermediate field limit, $D \approx h\nu_{MW}$; *Right:* Strong field limit, $D \gg h\nu_{MW}$.

is much greater than the microwave quantum, the only possible allowed transition is $|5/2, \pm 1/2\rangle \leftrightarrow |5/2, \mp 1/2\rangle$, within the lowest energy doublet (assuming $D$ is positive), and the forbidden transitions between the $|5/2, \pm 3/2\rangle \leftrightarrow |5/2, \mp 3/2\rangle$ and $|5/2, \pm 5/2\rangle \leftrightarrow |5/2, \mp 5/2\rangle$ levels, respectively. In this situation, the $g$-anisotropy is only a minor perturbation of the Zeeman states and is often omitted. Additionally, the observed EPR spectrum is not dependent on the magnitude of $D$, but rather the magnitude of $E$ (or ratio $E/D$) and the sign of $D$, assuming temperatures are low enough for population effects to be observed. Transitions are then observed at *effective* $g$-values, dependent on $E/D$. and the intrinsic $g$-values may be calculated by using a set of equations from Banci *et al.*[13] The relationship between the $E/D$ ratio and effective $g$ values is often illustrated by using "rhombograms", which can be used to determine $E/D$ given the apparent $g$ value, $g_{eff}$.

**Intermediate field limit:** When the microwave quantum is of similar magnitude to $D$, the most complicated situation arises. The observable transitions are then dependent on (i) the magnitude of $D$ and $E$; (ii) the $g$-anisotropy; and (iii) the temperature. The number of transitions, with respect to the orientation, is usually difficult to predict. It is often impossible to fully characterise the system within this regime.

**Strong field limit:** In the situation where $D \gg h\nu_{MW}$, all allowed transitions are possible and the full fine structure is observed in the EPR spectrum. This is the situation in which the examples *vide infra* were described. It should then be possible to fully characterise the ZFS terms, the $g$-anisotropy, and their relative orientation.

In summary, the different regimes in which ZFS can manifest itself were briefly discussed for Kramers systems. Related back to the non-Kramers example, the situation can be very different. Recall that the $|1, 0\rangle$ and $|1, \pm 1\rangle$ levels are separated by $D$. The number of accessible transitions are therefore far more sensitive to the magnitude of $D$, since after application of the applied magnetic field, the $|1, 0\rangle$ states remain invariant. Therefore, the allowed transitions occur between the $|1, 0\rangle \leftrightarrow |1, \pm 1\rangle$ levels, and if $D$ is large enough, no allowed transitions may occur at all. This is the reason for the common misconception that non-Kramers ions are "EPR-silent", however, $D$ is often large and therefore HF-EPR measurements may be necessary to characterise these systems. The utility of HF-EPR is therefore illustrated, for high-spin systems with large $D$, in order to access all transitions within the *fine* structure. The parameters are typically refined by simultaneous fitting at multiple frequencies in order to improve precision, particularly when the situation may be complicated by additional structures (*e.g.* $g$-anisotropy, hyperfine, exchange)

The origins of the ZFS interaction, in terms of the spin-spin coupling (SSC) and spin-orbit coupling (SOC) contributions, will now be discussed. In real systems, the ZFS is manifested by the crystal field, so that the nature of the *spin* and its *local environment* determine its magnitude and symmetry. Both interactions contribute to the total ZFS, however are of different magnitudes depending on the system in question. The SSC interaction is a direct dipole-dipole interaction between unpaired electrons, analogous to the anisotropic hyperfine interaction discussed earlier. The SSC interaction is defined by the following general Hamiltonian:

$$\hat{\mathcal{H}}_{SSC}(\overrightarrow{r}) = \frac{\mu_0}{4\pi} g_e^2 \mu_B^2 \cdot \{ \frac{\hat{S}_1 \cdot \hat{S}_2}{r^3} - \frac{3(\hat{S}_1 \cdot \overrightarrow{r})(\hat{S}_2 \cdot \overrightarrow{r})}{r^5} \} \tag{2.36}$$

where $\overrightarrow{r}$ is the inter-electron vector, and $r$ is the magnitude as a function of orientation ($r^2 = x^2 + y^2 + z^2$). From the expression it can be seen that the SSC has an inverse cube dependence of the distance, analogous to other dipolar interaction cases. The calculation of the SSC term is difficult using classical ligand field methods, and instead, can be calculated using a multi-electron spin-orbital Hamiltonian of the form:

$$\hat{\mathcal{H}}_{SSC} = -\rho \{ (\hat{\mathbf{L}} \cdot \hat{\mathbf{S}})^2 + \frac{1}{2}(\hat{\mathbf{L}} \cdot \hat{\mathbf{S}}) - \frac{1}{3} L(L+1) S(S+1) \hat{1} \} \tag{2.37}$$

where $\rho$ is the SSC constant, which can be calculated directly using quantum chemical methods. The SSC interaction is usually dominant for organic radicals where the SOC is small, and contrastingly, usually negligible for transition metals.

On the other hand, the SOC interaction gives rise to $g$-anisotropy, resulting from the spatial dependence of the orbital angular momentum projections ($m_I$) which adds an orbital contribution to the total angular momentum. It can be relatively easily rationalised using Russell-Saunders coupling schemes that the orbital occupancies will give rise to different orbital mixing of the possible electronic states for $S > 1/2$, which will therefore act to remove the degeneracy of the $m_s$ levels. The SOC interaction may be described by a multi-electron spin-orbital Hamiltonian of the following form:

$$\hat{H}_{LS} = \mu_B B \cdot (\hat{L} + g_e \hat{S}) + \lambda (\hat{L} \cdot \hat{S}) \tag{2.38}$$

Where $\lambda$ is the multi-electron SOC constant, which is zero for half-filled shells; positive for less than half-filled; and *vice versa.* However, the multi-electron method of determination only treats a single ${}^{2S+1}L_J$ term and does not include contributions from excited state terms (which admix to some degree with the ground state terms). This can lead to an underestimation of the ZFS parameters, especially when $\lambda$ is relatively small (and the excited states relatively close in energy). A single-electron spin-orbital Hamiltonian is instead often used:

$$\hat{\mathcal{H}}_{ls} = \sum_{i}^{m} \zeta_i \hat{l}_i \cdot \hat{s}_i) + \mu_B \mathbf{B} \cdot (\hat{l}_i + g_e \hat{s}_i) \tag{2.39}$$

Where the spin-orbit coupling term is a sum over all $m$ valence electrons in the $nd^m$ configuration, and $\zeta$ is the single electron SOC constant, which is related to the multi-electron constant (equation 2.38) by:

$$\lambda = \pm \frac{\zeta}{2S} \tag{2.40}$$

The expression in equation 2.39 does not include the effects of inter-electronic repulsion, or bonding, which act to quench the orbital angular momentum and hence the ZFS terms can be slightly over-estimated. Nevertheless, it is an informative method of estimating the ZFS contributions. Analogous to the $g$-anisotropy, the SOC term is usually dominant for transition metal ions with a large orbital contribution and is therefore the primary mechanism by which ZFS arises.

### 2.1.7 Exchange and Dipolar Interactions

Similar to the case of ZFS, which was defined as the total $S > 1/2$ spin on a single nucleus, electron-electron interactions can be very large in magnitude and act over large distances. Furthermore, the coupling of spins on individual sites can produce additional electron-electron interaction terms, such as the *exchange interaction*. These electron-electron interactions are often much weaker, and the coupled states are a function of symmetry, and orbital overlap. The *exchange* interaction is effectively a weak bonding, or electron correlation interaction; the pairing of unpaired spin density due to Hund's rules. This gives rise to *ferro-* (parallel) or *antiferromagnetic* (antiparallel) alignment of spins which ultimately determines the bulk magnetic properties of the system. The *direct* overlap of orbitals with unpaired spin density is intrinsically (and strongly) *antiferromagnetic*, and is termed *direct exchange*, which is rarely observed for this reason. More commonly, the exchange interaction is observed through indirect overlap *via* a non-magnetic bridging atom (*super-exchange*), or *via* molecular collisions in solution (*kinetic exchange*). The full electron-electron interaction matrix, $\mathbf{J}$, is defined by the following spin Hamiltonian:

$$\hat{H}_{EE} = \vec{s_i}\cdot\mathbf{J}\cdot\vec{s_j} \tag{2.41}$$

where **J** fully describes the magnitude, and orientation of the various interactions that may take place between two coupled spins, $\hat{s}_i$ and $\hat{s}_j$ in the non-coupled basis. The Hamiltonian may be further deconvolved to separate the independent contributions, which arise from different origins:

$$\hat{H} = \hat{s}_1\cdot J\cdot\hat{s}_2 = -2J\hat{s}_1\hat{s}_2 + \hat{s}_1\cdot D_{12}\cdot\hat{s}_2 + d_{12}\cdot\hat{s}_1\times\hat{s}_2 \tag{2.42}$$

where the terms describe the *isotropic exchange interaction*, the *anisotropic dipolar interaction*, and the *antisymmetric Dzyaloshinskii–Moriya exchange interaction*, respectively. Each interaction will be briefly discussed in turn.

### Isotropic exchange integral, $J$

$$\hat{H} = -2J\hat{s}_1\cdot\hat{s}_2 + \sum_i \mu_B B\cdot g_i\cdot\hat{s}_i \tag{2.43}$$

The *isotropic exchange* interaction was defined for the various possible mechanisms of interaction; of which the most commonly met, and perhaps the most important, is *super-exchange*. Furthermore, the coupling of two electron spins can be described in terms of their uncoupled ($s_1$ and $s_2$) and coupled ($S$) basis, since the former is generally not appropriate to describe the electronic state of the system.

In the simplest case, *i.e.* the coupling of 2 spin $s_1 = s_2 = 1/2$ and only isotropic ($J$) exchange coupling, there are 4 possible magnetic states arising from the vector combinations of $s_1$ and $s_2$: $|\alpha\alpha\rangle$; $|\alpha\beta\rangle$; $|\beta\alpha\rangle$ and $|\beta\beta\rangle$ which correspond to $\sum m_i$ = +1, 0, 0 and -1, arising from the preferential orientation of local spins to one another. Dependent on the relative energies of the coupled states, the isotropic exchange interaction will give rise to *ferromagnetic* or *antiferromagnetic* ordering in order to minimise inter-electronic repulsions, which is dependent on the sign of $J$. The reader should note that other definitions of the isotropic exchange term are commonly used; and therefore it is important to define the term. The difference in energies between the ground and excited state terms is then defined as $2J$.

The ground state is $S = 0$ if $J$ is negative; or $S = 1$ for positive values of $J$. The possibility of observing both ground and excited state coupled terms is dependent on the relative magnitude of the energy gap, to the Boltzmann term $k_BT$, and thus the thermal population of the energy states. Additionally, for more than two spins, the resulting matrix at zero field is of dimension $\prod_n(2s_i+1)$. The interaction of the uncoupled spins, $s_1$ and $s_2$ is now described on the assumption that $J$ is the dominant term in the spin Hamiltonian. When considering the nature of the uncoupled spins, each will have characteristic energy levels due to the effect of $g$, $A$, $D$, *etc.* as a consequence of their local environment. The Wigner-Eckart theorem may be applied to develop the contribution of each uncoupled spin, $s$, to the coupled basis, $S$, relative to the inequivalence of $g_1$ and $g_2$:

$$\mathbf{g_S} = c_1\mathbf{g_1} + c_2\mathbf{g_2} \tag{2.44}$$

$$c_1 = \frac{1+c}{2}; c_2 = \frac{1-c}{2}; c = \frac{s_1(s_1+1) - s_2(s_2+1)}{S(S+1)} \tag{2.45}$$

where $c_i$ are the projection coefficients that define the contribution of the respective uncoupled spins. Similar terms are defined for additional interactions, such as $A$ or $D$, which will be omitted for the sake of clarity. The possible spin Hamiltonian terms are typically orientation-dependent, which must be considered when defining their coupled state. This situation can be simplified by symmetry rules; *i.e.* assuming co-linear orientation. If the Zeeman energies of the states are identical, the spectrum will give rise to a single resonance, independent of $J$.

However, if the Zeeman energies are different, a resonance will appear at an average $g$ defined in equation 2.1.7. In the *strong exchange limit*, it is therefore often impossible to directly probe the nature of the uncoupled states (their $g$, $A$, $D$ values that are averaged by strong exchange). In addition, the exchange interaction will not associate with any additional splitting of the signal, *ca.* ZFS, that may be used to characterise the magnitude of the interaction. In this situation, the exchange interaction can be characterised *directly* by increasing the microwave frequency (and hence the microwave quantum) to resolve additional structure; however, the exchange interaction can usually be greater in magnitude than possibly obtained by HF-EPR.

An *indirect* method of probing the exchange magnitude is by harnessing its temperature-dependent nature; as the Boltzmann energy ($k_BT$) is reduced, and falls below the threshold of the exchange magnitude. The excited coupled states will no longer be accessible, or populated, and the magnitude of the exchange term may then be estimated *via* a change in its spin relaxation properties, double integral (spin concentration), or another *resolved* interaction.

The temperature-dependent behaviour is usually described by the Curie-Weiss law, which can be used to estimate the exchange integral:

$$\chi = \frac{C}{T + \Theta_{CW}} \tag{2.46}$$

$$3k_B\Theta_{CW} = 2JZS(S+1) \tag{2.47}$$

Where $\chi$ is the magnetic susceptibility (related to the double integral in EPR); $C$ is the Curie constant, which is material-specific; $\Theta_{CW}$ is the Curie temperature, which is positive for ferro- and negative for antiferromagnetic coupling; and $Z$ is the number of nearest neighbours.

The discussion of isotropic exchange has so far assumed that $J$ is the dominating interaction term in the spin Hamiltonian; however this is not necessarily the case. If $J$ is small, or rather of the order of the additional interaction terms, then the situation is more difficult to quantify. This situation is defined as the *weak exchange limit*, in contrast to the former *strong exchange limit*. Figure 2.8 illustrates the extreme cases, relative to the magnitude of $J$ *v.s.* $\Delta g$ (the inequivalence of the uncoupled $g$ values).

In the absence of exchange, $J = 0$, the EPR spectrum is identical to that of the uncoupled spins, $s_1$ and $s_2$. As the magnitude of $J$ increases, in the weak exchange limit, $J < \Delta g \mu_B$, the simple description of the uncoupled and coupled states does not fully describe the system; the spectrum results from mixing of the

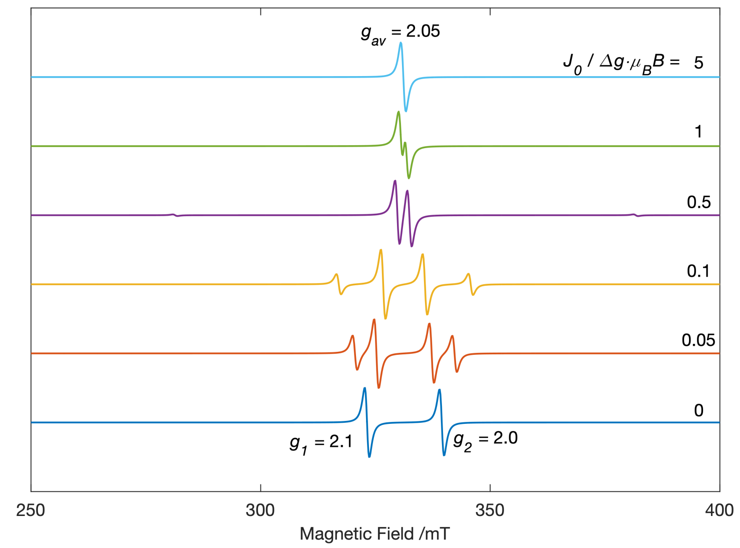

**Figure 2.8:** Simulations of an exchange-coupled pair with $s_1$=$s_2$=1/2; $g_1$=2.1; $g_2$=2.0; as a function of the magnitude of $J$. The relative magnitude of the exchange and Zeeman terms is defined on the right. Adapted from reference [2].

singlet and triplet states. The (uncoupled) transitions converge towards a value defined in equation 2.1.7, and additional outer transitions appear which diverge and become weaker in intensity.

The outer transitions correspond to the formally forbidden transitions ($\Delta m_s = \pm 2$), due to mixing induced by the Zeeman terms. Finally, as $J$ becomes the dominant term ($J > \Delta g \mu_B$), the strong exchange limit, the spectrum is described by a single transition, the coupled basis, as assumed for the previous discussions. This illustrates the importance of the magnitude of $J$ on the observed spectrum, for a simple case (in the absence of additional $A$, $D$ terms *etc.*).

### Anisotropic dipolar interaction, $D_{12}$

$$\hat{H}_{dip} = \hat{s}_1 \cdot D_{12} \cdot \hat{s}_2 \tag{2.48}$$

The $D_{12}$ term arises from the dipolar spin-spin interaction of unpaired electrons *through-space*, composed of a traceless 3x3 tensor, and is directly analogous to the ZFS interaction introduced in the previous section. The $D_{12}$ term is then, effectively, the ZFS interaction of the coupled states ($S = 1$ and 0 for $s_i = s_j = 1/2$). The origin of the term (through SSC, SOC and admixture of excited states) is synonymous with that already described, and will therefore not be discussed further. A few important considerations must be taken into account, however: (i) the interaction magnitude is typically much smaller due to the inverse distance dependance; (ii) the uncoupled spins (taken as $s_i = s_j = 1/2$ for simplicity) may also be $s > 1/2$, and therefore have individual ZFS terms before the coupled basis is considered; (iii) the $D_{12}$ may therefore have $S > 7/2$ in the coupled basis (greater than the spin state limit determined by orbital occupancy for ZFS); (iv) The relative orientation of the interaction coordinate frames is defined by the symmetry and orientation of the uncoupled spins, rather than spatial symmetry considerations (through occupancy of orbitals on the same nucleus).

The culmination of these effects is that the $D_{12}$ may have a drastically different nature, in definition as well as magnitude, when compared to the ZFS tensor described *vide infra*. The dipolar interactions are often used to measure long inter-electronic distances through the incredibly weak couplings, *via* advanced double-resonance pulsed EPR techniques (DEER). Finally, another possible contribution to the exchange term is the antisymmetric Dzyaloshinskii–Moriya (DM) interaction, which is covered briefly in Appendix 1.

### Exchange broadening and Narrowing

Another important consequence of electron-electron interactions is the broadening or narrowing of lines due to the *static* magnitude of the present interactions, spin concentration, and their *dynamic* relaxation properties. This effect is commonly observed in solution, due to indirect overlap of spin density due to collisions, as well as in solids.The phenomenon was first demonstrated mathematically by Van Vleck,[14] and later developed by Anderson and Weiss,[15] with the random frequency modulation model. They defined the rate of motion (*i.e.* the oscillation frequency of the spins), for the respective exchange, dipolar, hyperfine interactions *etc.* and provided a model for estimating the broadened (or narrowed) line shape. When the exchange frequency ($\approx J/\hbar$) is much less than the other terms, the line shape is Gaussian due to the effect of the dipolar (and hyperfine) broadening. Conversely, when the exchange frequency increases, and becomes much greater than the other terms, the interactions are effectively screened from the electron spin, which only perceives an average field due to the interactions with other electrons (dipolar interactions) and nuclei.

The effect of this is that the line shape narrows and becomes Lorentzian, characteristic of the spin relaxation time. In addition, resolved structures due to the dipolar and hyperfine terms collapse to leave the resonance due to $g$-anisotropy. This mechanism is indicative of the extremely strong exchange, and is commonly observed for electronically-conducting solids. Information is then lost from the system, regarding its local structure, which can sometimes be recovered *via* low temperature measurements (*vide supra*).

### Extended lattices

The final consideration for the discussion of exchange and dipolar interactions is the situation of extended lattices. In this case, it is difficult to define the individual uncoupled states, for which their number are effectively infinite. In this situation, it is customary to define the exchange and dipolar couplings in terms of their nearest-neighbour interactions (Figure 2.9).

The magnitude of $J$ between these neighbours ($J, J', J$") determines the dimensionality of the lattice, and is therefore an important implication in electron transfer mechanisms (which are exchange-mediated). In the case of multiple interactions between spins along different dimensional orientations, single-crystal EPR measurements (and multi-frequency EPR) are again the most informative routes for characterisation of these systems. Pulsed EPR techniques may also facilitate

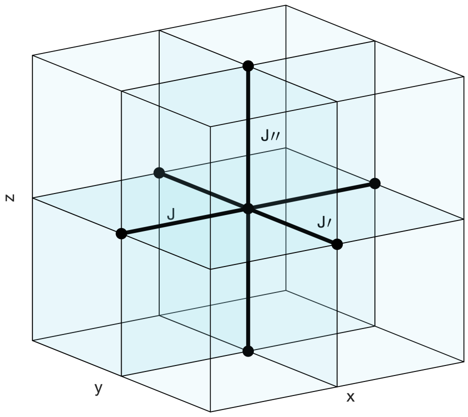

**Figure 2.9:** Schematic of extended lattice system and defined exchange couplings between nearest-neighbour sites. The vertices represent the interacting spins, $s_i$, at lattice sites, and the edges represent the distinct couplings between them ($J$, $J\prime$, $J\prime\prime$).

separation of the respective contributions, if the coupled systems have different $S$, $m_s$ values (through nutation measurements), hyperfine interactions, or distinct spin relaxation properties.

### 2.1.8 Magnitude of EPR interactions

The nature of the various interactions of principle importance in EPR characterisation were discussed in terms of the local structural information they provide, in the context of solid-state systems. In real solids, their chemistry and functional properties, whether catalytic, photocatalytic, luminescent, electrochemical *etc.*, can be generalised to several factors, such as (i) a distribution of several distinct (paramagnetic) sites, such as metals, point defects, many of which can be characterised using EPR; (ii) the nature of surface *v.s.* bulk chemistry, due to the lowering of symmetry and increased free energy at the surface.

From the viewpoint of EPR, this manifests as a rich, diverse and often complex array of interactions, characterised by spin Hamiltonian parameters. To facilitate a complete and meaningful interrogation of these sites, not only is the *nature* of these interactions important, but also their *relative magnitude*. This was considered for the ZFS and exchange interactions when compared to their Zeeman energies. It follows that the magnitude (and relative orientation) of *all* present interactions is of critical importance. Figure 2.10 illustrates the common relative magnitudes of the discussed interactions on a frequency scale, in addition to the Boltzmann energy afforded to the system.

Of particular importance is the considerable overlap between the respective interactions, and illustrates the complexity in structural determination of systems where several interactions and/ or distinct sites are present. It also illustrates the facility of advanced resonance techniques. Lower frequency interactions (such as hyperfine, dipolar) can often be unresolved within the relatively broad EPR line width, in which situation, pulsed EPR techniques (ENDOR, ESEEM, DEER) are typically employed in order to resolve them due to the fundamental control of the spin dynamics.

Conversely, for extremely large interactions, high frequency EPR measurements are often employed to access transitions large in magnitude, which is illustrated by the Zeeman range. Finally, the thermal quantum ($k_BT$) range illustrates the effect of lowering the temperature, which mediates the accessibility (and therefore population) of the higher electronic structure terms. In addition to the spin polarisation, this effect is often utilised in order to separate contributions from excited states; indirectly probe interaction magnitudes *via* monitoring of *e.g.* the spin relaxation properties; or to access fast-relaxing species that are not resolved at higher temperatures.

### 2.1.9 Relaxation Processes

So far the theoretical treatment has only considered a *static* model to describe a given system of electron and nuclear spins. Real systems are then a macroscopic

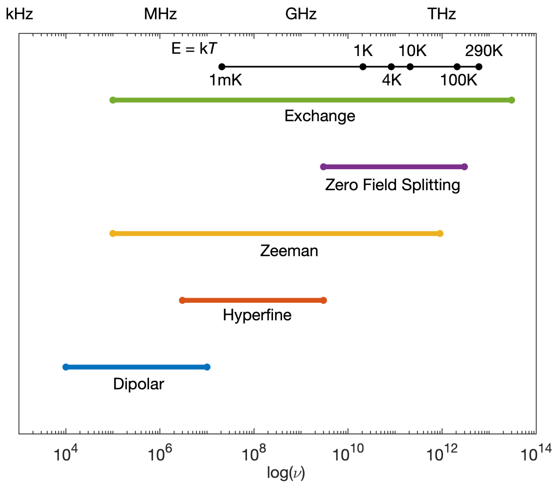

**Figure 2.10:** Approximate frequency ranges of interactions commonly encountered in EPR, in addition to available thermal energy as a function of temperature. Adapted from reference [5]

ensemble of electronic and nuclear states, and we can redefine the electron spin moment as the *bulk magnetisation vector*, provided by the Bloch model:

$$\mathbf{M} = \frac{1}{V}\sum \mu_{\mathbf{S}} \tag{2.49}$$

In a real system, the absorption of energy by an element of the spin ensemble (which removes the system from *thermal equilibrium*) is acted upon to restore the system to its lowest energy state. Therefore, the *time evolution* of the magnetisation vector is an important additional consideration to describe *real* systems. Furthermore, the *spin relaxation* is a fundamental consideration

At thermal equilibrium, the relative populations of the electron spin manifolds may be described:

$$\frac{N_\alpha}{N_\beta} = e^{-\frac{\Delta E}{k_B \cdot T_S}} \tag{2.50}$$

where $N_\alpha$ and $N_\beta$ are the populations of the electron spin manifolds (spin *up* and *down*); $\Delta E$ is the energy difference between the manifolds (defined in equation 2.1), $k_B$ is the Boltzmann constant, and $T_S$ (=$T$ at thermal equilibrium) is the spin temperature. The excess of spins in a given manifold is termed *spin polarisation*, which is perturbed by (i) absolute temperature, due to the energy separation $\Delta E$; (ii) absorption of the microwave quanta. The spin polarisation, which has shown to be *temperature*- and *field*- (or *frequency*-) dependent, is necessary for net absorption to occur between the electron spin manifolds, and is therefore a limiting factor for the experimental sensitivity.

Therefore, when the condition $N_\alpha = N_\beta$ is reached, the system is then *saturated*, which corresponds to the maximum entropy of the system, and no further transitions occur. The spin temperature, $T_S$, is a term for condensed matter that allows a negative absolute temperature, *i.e.* the possibility of *both* $\alpha$ and $\beta$ states being preferentially occupied (rather than the lowest energy state, $\beta$, only).

The time evolution of the spin magnetisation vector components (x,y,z) may then be defined, which correspond to the restoration of $\mathbf{M}$ along the $z$-axis (assuming $\mathbf{B}$ is co-linear with $z$):

$$\frac{dM_x}{dt} = \gamma_e B M_y - \frac{M_x}{T_2} \tag{2.51}$$

$$\frac{dM_y}{dt} = \gamma_e B M_x - \frac{M_y}{T_2} \tag{2.52}$$

$$\frac{dM_z}{dt} = \frac{M_z^0 - M_z}{T_1} \tag{2.53}$$

Which are characterised by two time constants, $T_1$, the *longitudinal* relaxation of **M** along the projection of the $z$-component; and $T_2$, the *transverse* relaxation of **M** along the projection of the $x$- and $y$-components. These time constants are characteristic of the energy transfer mechanisms that restore **M** to thermal equilibrium (along the $z$-axis). They are defined as follows:

- **spin-lattice relaxation time,** $T_1$: characterises energy transfer *to* or *from* the lattice *via* spin-phonon coupling modes, *viz.* the restoration of $M_z$ to $M_z^0$;
- **spin-spin relaxation time,** $T_2$: characterises energy transfer *within* the system, *via* coupling of the electron spin to surrounding electronic and nuclear moments.

Therefore, the $T_1$ and $T_2$ values are characteristic of the nature of the spin, its interaction with the surrounding field (from local magnetic dipole moments) and the local environment (the lattice). There are several mechanisms by which the spin-lattice relaxation may occur, for which their varying contributions become dominant upon changing temperature. Their origin will not be discussed in detail here. The $T_1$ and $T_2$ times are typically of distinct magnitudes (generally with $T_2 < T_1$). The time constants provide further information about the *dynamic* properties of the system, which can then be related back to the local electronic (and nuclear) structure. It is possible to measure these quantities *via* spin relaxation measurements, afforded by pulsed EPR methods.

### 2.1.10 Line broadenings

The line width and line shape is another important source of information in EPR spectroscopy, which define the dynamic properties, and distribution of sites in solid-state systems. For example, the exchange broadening/ narrowing mechanism was discussed *vide infra* which was characteristic of the spin relaxation pathways, and relative magnitudes of the Hamiltonian terms. This was further supported by the comparison of interaction magnitudes commonly observed in EPR. Furthermore, the line width can be used as an indirect means of quantifying temperature dependent interactions in the absence of additional structure in the EPR spectrum. The important considerations of line broadenings are briefly summarised.

### Homogeneous broadening

The concept of the electron spin-spin and spin-lattice relaxation times was introduced in the previous section. Homogeneous broadening of the EPR signal is a consequence of the isotropic nature of the effective field at the electron site, which leads to the identical spin relaxation properties with respect to the orientation. Homogeneous broadening therefore arises as a direct consequence of the spin relaxation, and is characterised by a Lorentzian line shape. In general, $T_2 \ll T_1$ and therefore the shorter spin-spin relaxation time has a dominant effect on the linewidth. These two properties may be related by the following expression:

$$T_2 = 2|\gamma_e \Gamma|^{-1} = 2|\sqrt{3}\gamma_e \Delta H_{pp}|^{-1} \tag{2.54}$$

where $\Gamma$ is the FWHM (for absorption signals), and $\Delta H_{pp}$ is the peak-to-peak linewidth. Therefore, if homogeneous broadening is apparent, the line width is a measure of the relaxation time, $T_2$. However, this condition is rarely met in real systems, especially in the solid state, due to inhomogeneous broadening effects.

### Inhomogeneous broadening

More commonly, inhomogeneous broadening effects are apparent for a solid-state system. Inhomogeneous broadening is not a consequence of the spin relaxation times (although this will contribute to the intrinsic line width of the signal). In contrast to the homogeneous case, inhomogeneous broadening is typical of anisotropic systems where the orientation dependence of the magnetic parameters needs to be considered.

A Gaussian line shape is characteristic of inhomogeneous broadening, which is the summation of several Lorentzian line shapes, shown as an example in Figure 2.11. Instead, the inhomogeneous contribution is generally afforded by two situations.

The first is a *distribution* in one (or more) of the spin Hamiltonian parameters (strain); $g$, $A$, $D$, *etc.* The parameter distribution is understood in terms of variations between the site conformations, symmetry and orientation. This manifests generally as a distribution of the dominant parameter, and is characteristic of lower symmetry systems. The distribution in parameters affords further indirect information about the local sites, in terms of disorder, and rigidity of the lattice, for example. It is typically necessary to accurately model the strain effects, in order to accurately quantify the spin system in question, especially when multiple

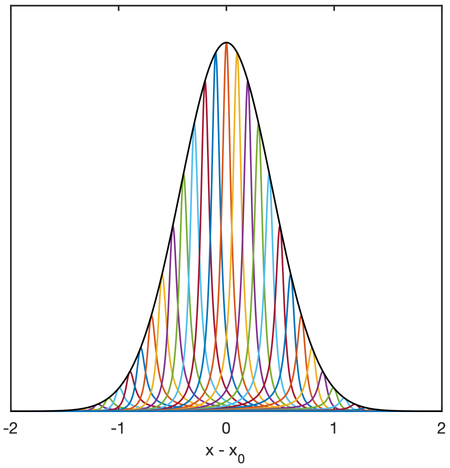

**Figure 2.11:** Illustration of the effect of the superposition of several Lorentzian line shapes arising from unresolved splitting of the electronic structure. The individual coloured lines represent the Lorentzian (absorption) signals. The black Gaussian line was calculated by summation of the underlying signals (half of the Lorentzian signals were removed for clarity).

overlapping resonances or structures are present. When the distribution is small, a linear dependence can be assumed to estimate the strain (*ca.* a tangent to a Gaussian function) which drastically simplifies the calculation. The strain effects can however be very large, where the distribution is on the order of the magnitude of its central value.

In this case, the distribution must be calculated explicitly, and a Gaussian distribution is usually assumed. Finally, the orientation of the principle spin Hamiltonian parameter axes (the coordinate frames) need not be aligned, which can further complicate the analysis of the parameter distributions as a function of orientational dependence. Nevertheless, this is an informative consideration when modelling solid-state systems.

The second common case of inhomogeneous broadening arises due to unresolved structure (from fine, hyperfine) where the magnitude of the interaction is comparable to, or smaller than, the intrinsic line width of the signal. This manifests as a net broadening of the central lineshape, and therefore an uncertainty in the determination of the spin Hamiltonian parameter responsible. Additional hyperfine techniques (ENDOR, ESEEM) or pulsed methods are usually then employed in order to resolve these interactions, which can resolve these comparatively small interactions. Again, this can present a challenge in accurate determination of the spin Hamiltonian parameters responsible for the structure of the EPR signal.

## 2.2 Electrochemical techniques

The application of electrochemical techniques facilitates monitoring of important thermodynamic and kinetic parameters in the understanding of the fundamental redox processes that are pertinent to an electrochemical storage system. The generation of radical species, defects, paramagnetic and participation in single electron transfer processes, are commonly encountered in such processes and their magnetic behaviour can drastically influence the electronic structure of the bulk and surface sites that play an important role in their chemistry and function. The direct correlation of local electronic structure and electron transfer processes (selective to paramagnetic sites by EPR) to the direct monitoring of the changes in redox state and electron density (through electrochemical measurements), a mechanistic resolution can be afforded for complex processes occurring at the solid/ solution interface.[16]

Several different processes facilitate charge storage, which may be broadly classified based on the response to an external bias:

- **Faradaic current**: current generated by heterogeneous electron transfer reactions between the electrode and electrolyte due to redox processes;
- **non-Faradaic current**: current due to processes not involving electron transfer, such as double layer charging (due to the reorganisation of electrolyte at the interface) or electrode polarisation (due to the capacitative response to the potential change).

In response to the polarisation of an electrode, the electrolyte components will respond to the change in potential gradient by reorganising against this, and a current will flow until the alignment has minimised the interaction with the gradient, at which it will drop to zero. Redox species will act to depolarise the electrode, and the reaction rate and storage capacity will facilitate a current flow over a longer period. The Faradaic current that can be provided is diffusion limited, and is the desired process in battery technologies.

The free energy change associated with a redox process can be related to the standard cell potential, $E^0_{cell}$, which is the maximum amount of electrical work afforded by the reaction of a system on its surroundings:

$$\Delta G = \Delta H - T\Delta S = -nFE^0_{cell} \tag{2.55}$$

which provides a direct relationship to the thermodynamic properties of the process. The cell potential is invariant with the number of electrons transferred in the overall reaction. The Nernst equation (which arises from the mass action law)[6] relates the cell potential to the concentration (or activity, $\alpha = \gamma[X]$ where $\gamma$ is the activity coefficient) and the standard reduction potential:

$$aA + ne^- \rightleftharpoons bB$$

$$E = E^0 - \frac{RT}{nF} lnQ \tag{2.56}$$

or

$$E = E^0 - \frac{RT}{nF} ln(\frac{\alpha_B^b}{\alpha_A^b}) \tag{2.57}$$

where $Q$ is the reaction quotient, which is equivalent to $K_{eq}$ when the cell potential is zero. In practice, the activities of the redox species at low concentrations approximates $\gamma = 1$ and therefore $\alpha_{M^+} \approx [M^+]$. The redox processes occurring in the cell electrodes facilitate the storage of charge in the system due to the reversible extraction of electrons to and from sites in the material. The theoretical specific capacity can be calculated based on the number of electrons (or equivalently $\text{Li}^+$) exchanged by the redox site:

$$Q_{theory} = \frac{1000 \cdot nF}{3600 \cdot M_r} / mAhg^{-1} \tag{2.58}$$

and the practical specific capacity may be calculated by the following equation using an appropriate measurement:

$$Q_{practical} = \frac{i \cdot t}{3600 \cdot M_r} / mAhg^{-1} \tag{2.59}$$

where $i$ is the current density ($A \cdot m^{-2}$), and $t$ is the cut-off time in seconds.

Another important quantity for batteries is the charge (C)-rate (the current required to reach a maximum capacity in one hour), $R_C$, which defines the rate at which the potential changes in response to the current, which should be considered relative to the rate at which it can respond due to limiting mass transport and diffusion steps in the redox process. $R_C$ can be calculated using equation 2.2:

$$R_C = \frac{I/M}{Q_{theory}} \tag{2.60}$$

where $I$ is the current, $M$ is the electrode mass, $Q_{theory}$ is the theoretical specific capacity defined in equation 2.58 (except with normalisation to electrode mass,

$M$, replacing $M_r$).

### Electrochemical reaction kinetics

The rate constant for a general single electron redox process may be calculated using the Eyring-Polanyi equation:

$$k = B{\cdot}e^{\frac{-\Delta G}{k_B T}} \tag{2.61}$$

which will have forward and backward rate constants associated with the free energy barrier $\Delta G$. $B$ is a pre-exponential factor which is defined as:

$$B_c = \frac{\kappa k_B T}{h} \tag{2.62}$$

where $\kappa$ is the transmission coefficient. The overall rate of reactions occurring in the electrochemical system can be influenced by one of several limiting processes, which influence the current afforded by the cell:[6]

- heterogeneous electron transfer kinetics
- chemical reactions
- reorganisation (solvent, ions)
- adsorption/ desorption at electrode surface
- mass transport (diffusion, migration, convection)

Kinetics are therefore an important consideration in the understanding of electrochemical measurements, and optimising the performance of energy storage systems.

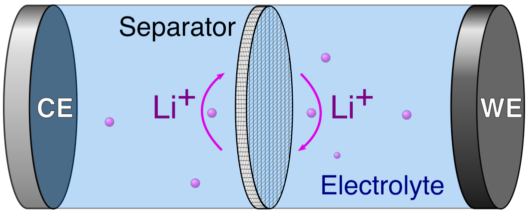

**Figure 2.12:** Schematic illustrating the basic system components of a Li-ion cell. CE = counter electrode, which is either Li foil (for half cell) or anode material (*e.g.* graphite); WE = working electrode, cathode (or also anode for half-cell) material.

### Components of the Li-ion battery

A schematic of a 2-electrode cell is presented in Figure 2.12. The counter and reference electrodes are shorted, therefore the potential is measured between the WE and CE, whereas the current flows through an external circuit. This arrangement is straightforward for measurement and standard electrochemical testing of battery materials, in addition to relatively easy mathematical modelling of the potential and rate response.

The open-circuit potential (OCP) of the cell can be simply described as the difference in chemical potentials between the cathode, $E_+$, and anode, $E_-$, equation 5.1:

$$U_{OCP} = E_+ - E_- \tag{2.63}$$

Where the anodic and cathodic potentials vary with the local electronic structure of the electrode materials. The output potential of the cell can then be related to the OCP depending on the internal resistance, $IR$, equation 5.2

$$U_{out} = U_{OCP} - IR \tag{2.64}$$

where $I$ is the current passed through the cell, and $R$ is the net internal resistance of the cell. A summary of the cell components, their role and considerations for their choice in Li-ion batteries are briefly presented.

- **current collectors**:
  Electronically conducting foil. electrode material printed as homogeneous film on surface. Maintains contact between the active material and therefore maximises conductivity. Considerations for potential window when selecting material.

- **separator**:
  Porous polypropylene (PP) or polyethylene (PE) membrane (or glass fibre filter for lab-scale cells) used as a matrix for electrolyte absorption, and preventing contact between the components to prevent short circuit. The separator is therefore an important component in minimising distance between the WE and CE (and hence resistance contribution of the circuit), and maintaining safe operation. It can however serve as a nucleation point for deposition of materials transferred through the electrolyte.

- **anode material**:
  Ideally Li foil, however safety hazard and poor cycle life currently due to

dendrite formation: the drive for solid state batteries. Commonly graphite; good capacity, however susceptible to exfoliation which can reduce the cycle life. Therefore requires electrolyte that can form a solid electrolyte interphase (SEI) to minimise damage during cycling.

- **electrolyte**:
  Li-containing salt in organic solvent. responsible for ion transport. Has a marked effect on the kinetics at play: depolarisation of the electrode surface. Limits upper potential window due to decomposition. Plays role in passivation (SEI formation).
- **cathode material**:
  The cathode is generally the theoretical capacity-limiting component of the electrochemical cell for two reasons: (i) The number of $Li^+$ ions that can be reversibly stored in the material is determined by the cathode material; (ii) the reduction potential of the redox processes determines the potential window in which the cell can operate (the practical window being limited by the electrolyte). Furthermore, the cell EMF can be maximised to maximise the specific energy density afford by the cell.

This arrangement is straightforward for measurement and standard electrochemical testing of battery materials, in addition to relatively easy mathematical modelling of the potential and rate response.

### Chronopotentiometry

Chronopotentiometry measurements (or Galvanostatic charge-discharge) are the principle perturbation technique for monitoring the electrochemical mechanism, kinetics and degradation of Li-ion cells due to its simple cell design and comparatively straight-forward mathematical reproduction.[17]

In the chronopotentiometry experiment, a constant current is applied to the cell and the resulting change in potential is measured as a function of time. Although the current applied to the cell is constant, the Faradaic (electrochemical process) current is time-dependent due to the effect of double layer capacitance ($i_c$), which is proportional to the rate of change of potential with time:[17]

$$i_{app} = i_f + i_c \tag{2.65}$$

where

$$i_c = C_{dl}\frac{dE}{dt} \tag{2.66}$$

and $C_{dl}$ is the differential capacitance of the double layer. The electrochemical and capacitative contributions to the potential change therefore give rise to a slope; with plateaus associated with oxidation or reduction events in the cell through heterogeneous electron transfer; and potential drops due to reorganisation of the double layer in response to the electrostatic gradient at the electrode surface/ electrolyte interface. The kinetics of the respective homogeneous and heterogeneous events, such as diffusion, also has a significant impact in the potential response, and several models have been proposed to understand their effect.[17]

One of the variable parameters by which kinetic contributions can be modified is the charge or $C$-rate $\mathrm{h}^{-1}$, which is calculated based on the electrode density in addition to the theoretical specific capacity calculated for the redox process occurring at the WE. Lower current rates allow time for rate-limiting processes to proceed and reorganise in response to the potential change, and subsequently maximises the practical specific capacity. Conversely, at higher current values, equilibrium kinetics will have a limiting effect on the charge storage processes, and the contribution to the specific capacity is largely due to the capacitative action of the cell.

In practice, a number of processes will be occurring in the cell during the perturbation experiment, and their relative contributions can be difficult to seperate. Nevertheless, chrono- methods are a valuable tool in monitoring changes in the bulk electronic structure upon application of a bias.

### Chronoamperometry

Chronoamperometry (potentiostatic) methods involve the application of a constant potential or potential step, and measurement of the current in response as a function of time. This simple technique facilitates the monitoring of known processes occurring at a threshold potential which is related to the free energy change associated with the chemical or electrochemical process. CA has been shown to also provide capacity-rate data and kinetic information (as in GCD) up to three times faster.[18]

Chronocoulometry is a somewhat analagous technique that provides essentially the same information. If the response of a system to the potential perturbation is $i(t)$, then the chronocoulometric response follows to be:

$$Q(t) = \int_0^t i(t)dt \tag{2.67}$$

And is therefore related to the area under the current response curve as a function of time. Upon application of an applied potential that is less or greater than the cell potential, a response in current will be observed due to the non-instantaneous processes occurring at a comparatively slower rate to electron transfer. In the absence of active redox species, the current response to a change in polarisation should be close to zero. However, reorganisation of the electrolyte in the double layer will result in a transient current.[6]

Using these methods, the Faradaic and non-Faradaic contributions can generally be discerned from the current response which can be useful in disentangling the complicated processes that occur within a practical cell.

In summary, this chapter has focused on the application of CW EPR techniques and its synergy with complementary characterisation techniques to access excited states, surface resolution, and local structural information for solid state functional materials. The EPR interactions encountered in such systems were outlined in detail, with particular attention to those electron-electron interactions arising from high spin ions. A brief overview was supplied for the additional techniques which were applied in this work.

# References

[1] Victor Chechik, Emma Carter, and Damien Murphy. *Electron paramagnetic resonance.* Oxford chemistry primers. Oxford Univ Press, Oxford, 2016. OCLC: ocn945390515.

[2] Eric J. L. McInnes and David Collison. EPR Interactions – Coupled Spins. In *eMagRes*, pages 1445–1458. American Cancer Society, 2016. _eprint: https://onlinelibrary.wiley.com/doi/pdf/10.1002/9780470034590.emrstm1502.

[3] Joshua Telser. EPR Interactions - Zero-Field Splittings. In Robin K. Harris and Roderick L. Wasylishen, editors, *eMagRes*, pages 207–234. John Wiley & Sons, Ltd, Chichester, UK, June 2017.

[4] Peter Gast and Edgar J.J. Groenen. EPR Interactions - g-Anisotropy. In Robin K. Harris and Roderick L. Wasylishen, editors, *eMagRes*, pages 1435–1444. John Wiley & Sons, Ltd, Chichester, UK, September 2016.

[5] A. Schweiger and Gunnar Jeschke. *Principles of pulse electron paramagnetic resonance.* Oxford University Press, Oxford, UK ; New York, 2001.

[6] Wesley R Browne. *Electrochemistry.* 2018. OCLC: 1096325766.

[7] M. P. Seah. The quantitative analysis of surfaces by XPS: A review. *Surf. Interface Anal.*, 2(6):222–239, December 1980.

[8] Paul S. Bagus, Eugene S. Ilton, and Connie J. Nelin. The interpretation of XPS spectra: Insights into materials properties. *Surface Science Reports*, 68 (2):273–304, June 2013.

[9] Timothy H. Gfroerer. Photoluminescence in Analysis of Surfaces and Interfaces. In Robert A. Meyers, editor, *Encyclopedia of Analytical Chemistry*, page a2510. John Wiley & Sons, Ltd, Chichester, UK, September 2006.

[10] Allen J. Bard, editor. *Encyclopedia of Electrochemistry: Online.* Wiley, 1 edition, December 2007.

[11] Thomas Marks, Simon Trussler, A. J. Smith, Deijun Xiong, and J. R. Dahn. A Guide to Li-Ion Coin-Cell Electrode Making for Academic Researchers. *Journal of The Electrochemical Society*, 158(1):A51, 2011.

[12] Stefan Stoll and Arthur Schweiger. EasySpin, a comprehensive software package for spectral simulation and analysis in EPR. *J. Magn. Reson.*, 178(1): 42–55, January 2006.

[13] L. Banci, A. Bencini, C. Benelli, R. Bohra, J.-M. Dance, D. Gatteschi, V. K. Jain, R. C. Mehrotra, A. Tressaud, R. G. Woolley, and C. Zanchini. *Structures versus Special Properties.* Structure and Bonding. Springer-Verlag, Berlin Heidelberg, 1982.

[14] J. H. Van Vleck. The Dipolar Broadening of Magnetic Resonance Lines in Crystals. *Phys. Rev.*, 74(9):1168–1183, November 1948. Publisher: American Physical Society.

[15] P. W. Anderson and P. R. Weiss. Exchange Narrowing in Paramagnetic Resonance. *Rev. Mod. Phys.*, 25(1):269–276, January 1953.

[16] Richard D. Webster, Robert A. W. Dryfe, Barry A. Coles, and Richard G. Compton. In Situ Electrochemical EPR Studies of Charge Transfer across the Liquid/Liquid Interface. *Anal. Chem.*, 70(4):792–800, February 1998.

[17] Digby D. Macdonald. Chronopotentiometry. In *Transient Techniques in Electrochemistry*, pages 119–184. Springer US, Boston, MA, 1977.

[18] Ruiyuan Tian, Paul J. King, Joao Coelho, Sang-Hoon Park, Dominik V. Horvath, Valeria Nicolosi, Colm ODwyer, and Jonathan N. Coleman. Using chronoamperometry to rapidly measure and quantitatively analyse rate-performance in battery electrodes. *arXiv:1911.12305 [physics]*, November 2019. arXiv: 1911.12305.

# Chapter 3

# EPR investigation of N-donor chelating exchange resins for selective $Cu^{2+}$ extraction from aqueous media

## 3.1 Introduction

Porous separation materials, such as resins, are a fundamental technology for the purification and concentration of transition metals for domestic and industrial applications, with each process requiring robust separation performance in a variety of medias, conditions or mixtures. The emission of copper and other so-called 'heavy metals' from industrial, military, agriculture and waste disposal sectors has implications that can be broadly classified into two areas: (i) the environmental impact of adventitious materials and (ii) the economic impact of spent metals recovery of utility and financial value, which contribute to renewable feedstocks. The development of technologies for important manufacturing processes are fundamental to the drive for greener, cheaper and more efficient products.

Worldwide, over 25 million tonnes of copper are used in various manufacturing practises, of which approximately one-third of global demand is met by recycling.[1] A number of conventional methods for metal recovery are currently employed industrially, including chemical precipitation,[2] cementation,[3] solvent extraction,[4] and ion exchange.[5–7]Whilst Ion Exchange Resins (IERs) are amongst the most expensive technologies, these adsorbents are also amongst the most efficient and selective methods. Sources of copper waste, such as metallurgy processes and electroplating, are typically highly acidic and frequently contain various toxic organic by-products and complexing agents. This presents a challenge in terms of conventional extraction methods, where additional steps may be required to neutralise or treat the effluent in order to retrieve the metal in appreciable quantities.[8]

Instead, it is possible that complexing agents may be introduced as active site functionalities onto resin framework supports. These specialised frameworks are known as 'Chelating Exchange Resins' (abbreviated as CERs), and they can be advantageously employed in metal pre-concentration or recycling processes on an industrial scale.[9–11] CERs are usually functionalised porous materials that coordinate to metals *via* a combination of ionic, electrostatic and primarily coordinative interactions, in contrast to the active exchange of labile functional groups (as in IERs). CERs act to remove metal ions through conventional Lewis acid-base interactions between the metal substrate and immobilised ligand. Lewis base sites, in IERs, often struggle to achieve the required rates and capacities in acidic media, due to competitive protonation which reduce the site nucleophilicity. CERs containing weakly basic sites have been reported to work in acidic media, even down to pH = 1, as a sufficient number of sites remain deprotonated. Typically, CERs facilitate increased adsorption rates, efficiencies and surface areas when compared to IERs. Metal uptake kinetics, capacities and other operational properties are highly dependent on the choice of polymer, or support, particle sizes and functional group attached to the polymer backbone. As such, CERs may facilitate increased adsorption rates, tuneability and surface areas in comparison to IERs.[7]

Surprisingly, very little is known about the Cu(II) binding environments on these exchange resins, particularly at variable Cu(II) concentrations and pH's, so we therefore used EPR spectroscopy to investigate the binding. In this study, we have investigated the exchange properties of two typical types of commercially available CER resins, namely Dowex® M4195 and CuWRAM® (see figure 3.1). Both of these CERs employ similar N-donor ligands for the metal uptake and both have been shown to be highly selective towards Cu(II) uptake, even in mixed metal effluent systems. However, understanding the nature of the Lewis acid-base interaction, and indeed the Cu(II) binding environments which afford this high selectivity, is not straightforward.

In brief, Dowex M4195 (figure 3.1, *left*) is a macroporous, cross-linked DVB-polystyrene composite, functionalised with partially protonated tridentate di(2-picolylamine) (BPA) chelating units.[5] The cross-linked polymer support affords good mechanical durability, while the weakly basic di(2-picolylamine) group allows good sorption efficiency, even at low pH values (pH=1). This is due to the presence of pyridyl nitrogen donor atoms, which due to the electron-withdrawing effect of the heterocyclic rings, remain deprotonated even at extremely low pH. CuWRAM on the other hand (figure 3.1, *right*) is a silica-polyamine composite bearing 2-picolylamine (PA), developed in order to address some of the limitations of other analogous functional materials. For example, the Dowex M4195 system suffers from poor elution characteristics, with relatively strong $NH_4OH$ solutions necessary to strip most of the metal ions from the support. Whereas, the selectivity of CuWRAM is observed to be sufficient such that separation of Cu(II) is feasible even in a 250 fold excess of Zn(II),[12] and yet the metal is more easily eluted. Other advantages include a decreased shrink-swell action, faster operational flow rate at higher capacities, longer useable lifetimes, higher operational temperatures and 'inert' operation across a wide range of acidic and basic media.[13]

Whilst much of the past investigations on these materials have focused on the support structure, absorption properties and uptake kinetics,[12, 14–16] very little is known about the local metal binding environments within CERs. For example, the nature of how the Cu(II) ions are actually coordinated by the supports is not clear. Many aspects of the structure, steric hindrance and competitive equilibria, arising from the grafting of the chelate units onto a polymer, remain inadequately described. Electron Paramagnetic Resonance (EPR) spectroscopy is the ideal technique to probe the local binding of copper ions by the N-donor chelating ligands for metal extraction[17] and obtain this important information. The purpose of this investigation is therefore to primarily provide a meaningful evaluation of local metal binding environments and Cu speciation within these two CERs, in order to address the currently unknown features associated with uptake behaviour and copper coordination environments.

The salient features of the experimental and theoretical investigations are briefly summarised. The characterisation of transition metal associated solid-state resins using spectroscopic techniques can be reasonably complex mainly due to three primary factors: (i) the superposition of several components arising from the speciation of complex ions within different sites on the porous network; (ii) the superposition of several components due to structures from (electron, nuclear) spin-spin interactions, particularly of similar relative magnitude; (iii) broadening of signals related to the orientational anisotropy, and a distribution of spectroscopic properties associated to the confinement of the solid hierarchical structure. One of the most significant origins of this is due to micro-environments in imperfect solids as a consequence of slight variations in bond lengths and angles.

As a result of these consideration, a systematic and convincing determination of the local electronic structure, and in turn the functional properties is chal-

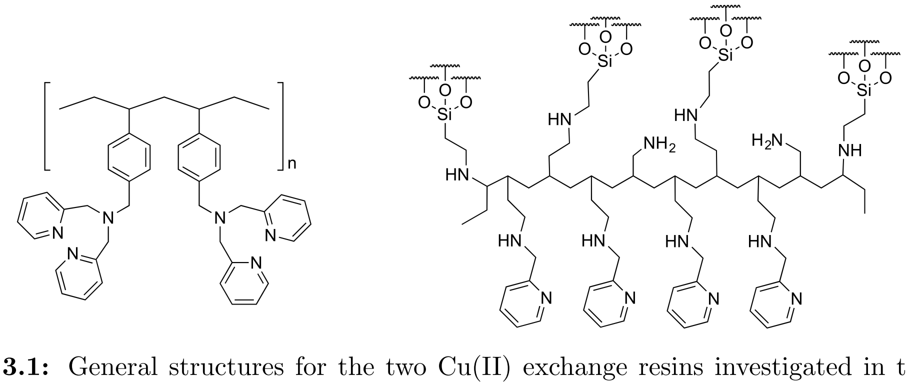

**Figure 3.1:** General structures for the two Cu(II) exchange resins investigated in this work. *Left*: Dowex M4195; *Right*: CuWRAM.

lenging. Initially, a series of well-defined [$\mathrm{Cu^{II}(PA)}_x$] and [$\mathrm{Cu^{II}(BPA)}_x$] complexes were prepared as reference compounds and characterised using EPR and UV-Vis spectroscopy. The comparison of well-defined models facilitated the deconvolution of the complex resin spectra, and the contributions from individual Cu(II) coordination modes were determined that contributed to the broad EPR spectra of the loaded resins. The experimental spin Hamiltonian parameters derived for the distinct coordination sites were compared with quantum chemical calculations for geometry optimised structures calculated *via* density functional theory.

To further support the detailed characterisation of the local electronic structure for Cu(II) - resin adducts, a series of dehydration/ rehydration experiments were performed to explore the role of coordinated water in the various binding structures. Furthermore, the method for removal of Cu(II) from the resin framework was elution with an appropriate acid/base solution, so to evaluate the effective binding strength of distinct coordination sites, a series of acid (for CuWRAM and Dowex) and basic (for Dowex) elution experiments were performed and compared to equilibrium batch uptake measurements. Since the absorption bands for the solid resins are reasonably broad, the complementary EPR analysis provides a detailed insight into the selective removal of binding sites and the properties of various arrangements of chelating N-donor ligands around the Cu(II) metal ions. The experimental and theoretical results provide an insight into the local structural environments of coordinated Cu(II) metals ions; interactions between associated metal sites and resin framework; and finally a relation to the kinetic properties on the selective uptake behaviour, and thermodynamic properties associated with the relative binding strength of coordinated metal ions.

## 3.2 Results and Discussion

### 3.2.1 X-band EPR of Cu(II) loaded resins

The low temperature X-band CW EPR spectra of the Cu(II) loaded CuWRAM and Dowex resins are shown in Figure 3.2. In each case, the samples were loaded with increasing amounts of copper (0.1, 1 and 10 mg g$^{-1}$ of the resin support using a $CuSO_4$ solution). For clarity and comparison purposes, the EPR spectra shown in Figure 3.2 are normalised to the same intensity in order to highlight the complexity and speciation of Cu(II) centres present. The spectra are noticeably broadened, with reduced resolution at higher copper loadings, as expected due to spin-spin broadening. Despite the presence of the chelating N-donor ligands (namely BPA and PA), the $^{14}$N super-hyperfine splittings are all but obscured from the powder EPR spectra, making the characterisation of the contributing Cu(II) complexes more difficult.

Nevertheless, in all cases, a clear speciation of Cu(II) environments is evident in the spectra. This indicates that the Cu(II) ions exist in different coordination environments when anchored onto the resin support, contrary to the assumed uptake mechanism reported in the literature.[12, 14] This agrees well with the partial protonation equilibria expected at low pH, owing to competition between $H_2SO_4$/$CuSO_4$ as a function of acid dissociation equilibria and operational pH. Subtle changes in the coordination environment as a function of pH have been suggested based on DFT studies,[18] and less favourable intermolecular ligand site coordinations, relative to the kinetic effect of chelation, are likely to become more important at the lower limits of the operational pH's. CuWRAM also possesses alternative potential donor sites in the support matrices, in the form of primary and secondary amines. However, these would be expected to be insignificant compared to the stronger bi/tri-dentate coordination from the abundant PA N-donor chelator groups. It should also be noted that partial protonation of the donor sites under the low pH conditions (as used in the extraction experiments) coupled with additional outer-sphere coordination, may cause considerable change to the spin Hamiltonian parameters and the perceived Cu(II) speciation.

Clearly, deconvolution of the EPR spectra (Figure 3.1) is necessary in order

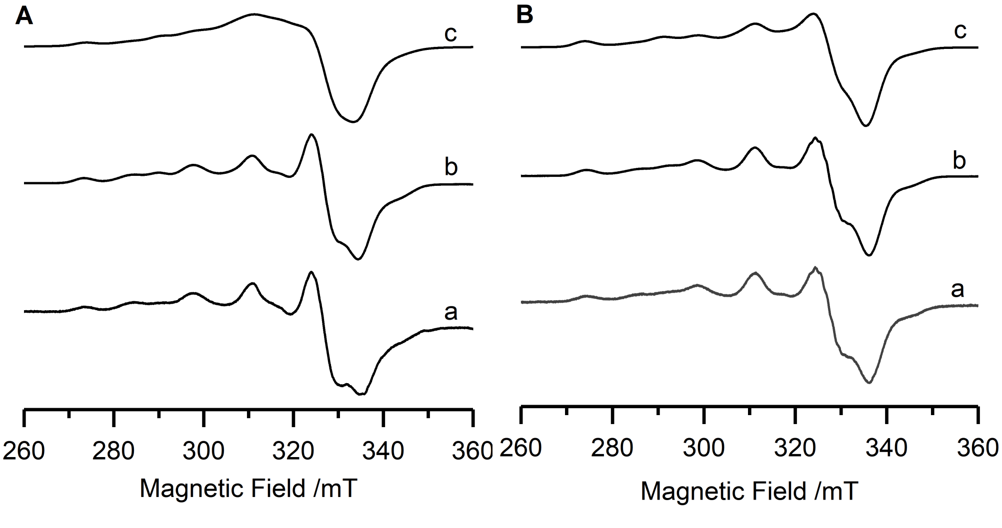

**Figure 3.2:** X-band CW EPR spectra (120 K) of A) CuWRAM and B) Dowex M4195 powders with copper loadings of: a) 0.1, b) 1 and c) 10 mg/g of the polystyrene or silica resin.

to confidently identify the individual Cu(II)-ligand environments present on the loaded resins. Therefore, in order to determine the distinct coordination centres present on these resins, a series of [$Cu^{II}(PA)_x$] and [$Cu^{II}(BPA)_x$] model complexes were prepared in aqueous solution by varying the ratio of Cu(II) ions to PA or BPA ligands. Analysis of the individual EPR spectra for the individual [$Cu^{II}(PA)_x$] and [$Cu^{II}(BPA)_x$] complexes formed, should then enable one to de-convolute the spectra of the loaded samples (Figure 3.2).

### 3.2.2 X-band EPR analysis of [$\mathbf{Cu^{II}(PA)_x}$] and [$\mathbf{Cu^{II}(BPA)_x}$] model complexes

The experimental X-band CW EPR spectra of aqueous solutions of $CuSO_4$ titrated with increasing concentrations of the tridentate di(2-picolylamine) chelator (BPA) are shown in Figure 3.3. Throughout the experiments, glycerol was added as the glassing agent to the aqueous solution in order to produce a good polycrystalline EPR spectrum. Only the Cu:BPA ratios of 1:0.1, 1:1 and 1:2 are shown in Figure 3.3a-c. A more complete series of spectra showing the Cu:BPA ratios of 1:0.1, 1:05, 1:1, 1:2, 1:5, 1:10, 1:50 are shown in Appendix 2, from which it is clear that no changes occur in the EPR spectra for Cu:BPA ratios higher than 1:2.

In all cases, well defined EPR spectra characterised by axial symmetry can be observed (Figure 3.3 a-c). At sub-stoichiometric ratios of Cu:BPA (1:0.1), the spectrum is largely dominated by a single Cu(II) Species, consistent with the presence of the expected and well reported pseudo-octahedral [$Cu^{II}(H_2O)_6$] complex (Figure 3.3a).[19] A field-dependent strain effect is evident in the parallel hyperfine pattern, manifested as a progressive broadening of the peaks from the low field $m_I$=-3/2 to high field $m_I$=+3/2 transitions. This effect is readily simulated using a correlated $g$- and $A$-strain, arising from the distribution of $g/A$ values associated with weakly perturbed micro-environments in the sample.[20] Hereafter this fully hydrated Cu(II) centre will be referred to as Species 1.

At higher Cu:BPA ratios (1:1), a change occurs in the EPR spectrum (Figure 3.3b) due to the emergence of a second Cu(II) signal. This new signal can be easily assigned to a heteroleptic Cu(II) complex bearing a single coordinating BPA unit (i.e., [$Cu^{II}(BPA)(H_2O)_m$)], resulting from the ligation of one tri-dentate BPA ligand to the Cu(II) centre and thereby reducing the $g_{\|}/A_{\|}$ values relative to [$Cu^{II}(H_2O)_6$]. Hereafter this second [$Cu^{II}(BPA)(H_2O)_m$] centre will be referred to as Species 2 (see Figure 3.5). At the stoichiometric Cu:BPA ratio of 1:1, an equilibrium exists since both Species 1 and 2 are present in the frozen solution,

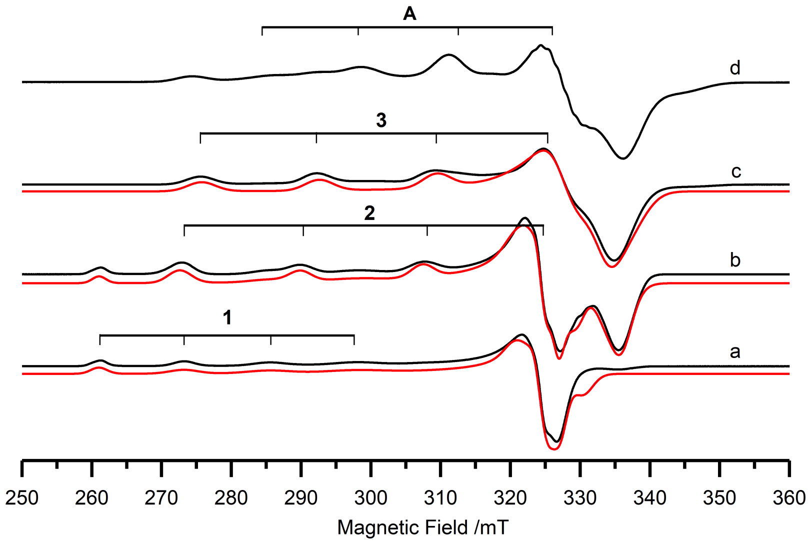

**Figure 3.3:** X-band CW EPR spectra (120 K) of Cu:BPA ratios of: a) 1:0.1, b) 1:1 and c) 1:2, recorded in a water:glycerol mixture (3:2). For comparison, the CW EPR spectra of the Cu-loaded Dowex samples bearing 1 mg/g copper loading (Dowex Figure 3.2, b) is shown in d). Experimental = black trace, simulated = red trace.

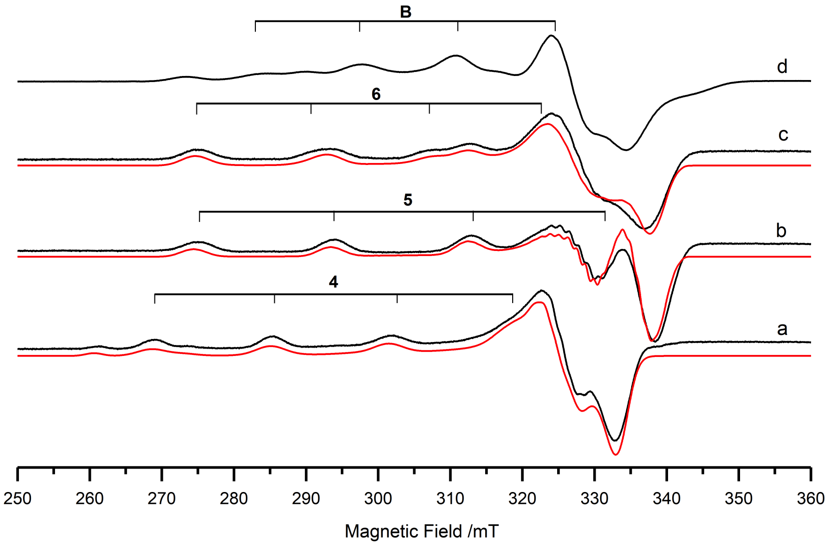

**Figure 3.4:** X-band CW EPR spectra (120 K) of Cu:PA ratios of: a) 1:1, b) 1:2 and c) 1:50, recorded in a water:glycerol mixture (3:2). For comparison, the CW EPR spectra of the Cu-loaded CuWRAM samples bearing 1 mg/g copper loading (CuWRAM Figure 3.2, b) is shown in d). Experimental = black trace, simulated = red trace

as evident in the EPR spectrum (Figure 3.3b). Finally, for any Cu:BPA ratios higher than 1:2, a third signal becomes apparent in the spectrum (Figure 3.3c). This EPR signal has $g$ and ${}^{Cu}A$ values which are distinctly different from those of Species 1 and 2 and therefore can be assigned to the homoleptic Cu(II) complex (Species 3) bearing two coordinating BPA ligands (i.e., $[Cu^{II}(BPA)_2]$). The observed behaviour of this Cu(II) speciation in solution also agrees with the UV-Vis. titration data *vide supra.* The experimental spin Hamiltonian parameters for each Species 1-3, as determined by simulations of the EPR spectra, and by comparison with DFT derived values for the Cu(II) complexes, are given in Table 4.2. The geometry optimisation calculations were performed by Johnson Matthey, which were used as a starting point for the calculation of spin Hamiltonian parameters using ORCA.The corresponding rotations to coordinate frames for the $g$ and $A$ tensors, derived from DFT and *via* simulation, can be found in Appendix 2.

To aid discussion of the reported $g_{\|}/A_{\|}$ values, a Peisach-Blumberg plot has been provided for reference to their correlation (Figure 3.6). The spin Hamiltonian parameters of $[Cu^{II}(H_2O)_6]$ (Species 1) listed in Table 4.2 are entirely consistent with those widely reported in the literature.[19] For Species 2, the observed $g$ and ${}^{Cu}A$ values are also consistent with a Cu(II) ion bearing a tri-dentate 3N-type ligand.[21] Substitution of the $H_2O$ ligands for strongly coordinating, electron-rich nitrogen atoms, is responsible for the expected decrease in the $g_{\|}/A_{\|}$ values, and these values are typical for square-based pyramidal Cu(II) geometry.[21] The

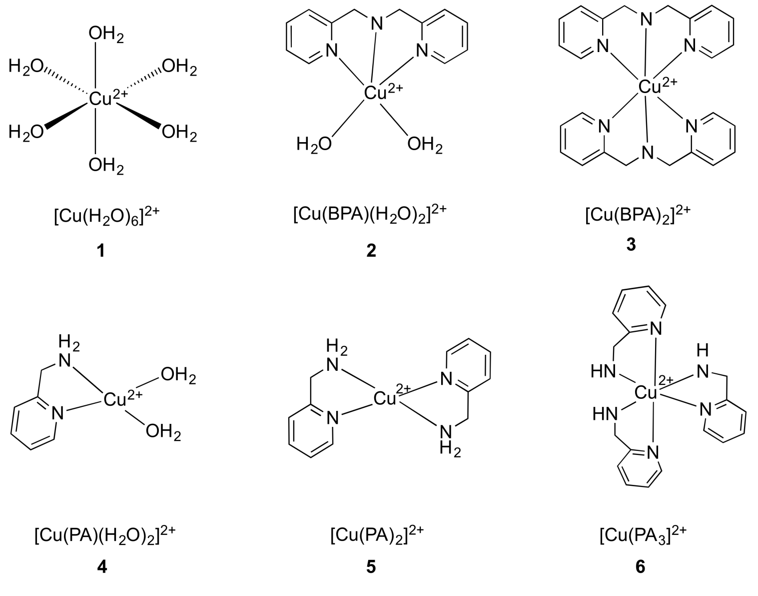

$[Cu(H_2O)_6]^{2+}$
**1**

$[Cu(BPA)(H_2O)_2]^{2+}$
**2**

$[Cu(BPA)_2]^{2+}$
**3**

$[Cu(PA)(H_2O)_2]^{2+}$
**4**

$[Cu(PA)_2]^{2+}$
**5**

$[Cu(PA_3]^{2+}$
**6**

**Figure 3.5:** Structures of the proposed $[Cu^{II}(PA)_x(H_2O)_y]$ and $[Cu^{II}(BPA)_x(H_2O)_y]$ model complexes.

| Species | | $g_x$ | $g_y$ | $g_z$ | $\|A_x\|$ | $\|A_y\|$ | $\|A_z\|$ | $\lambda_{max}$ |
|---|---|---|---|---|---|---|---|---|
| 1 | Exp | 2.094 | 2.072 | 2.418 | N.R. | N.R. | 413 | 710 |
| | DFT | 2.099 | 2.126 | 2.303 | 121 | 192 | -484 | |
| 2 | Exp | 2.062 | 2.065 | 2.262 | 46 | 70 | 556 | 610 |
| | DFT | 2.049 | 2.075 | 2.204 | -36 | 55 | -557 | |
| 3 | Exp | 2.046 | 2.072 | 2.243 | 30 | 42 | 535 | 710(890) |
| | DFT | 2.060 | 2.062 | 2.204 | 30 | 43 | -542 | |
| 4 | Exp | 2.061 | 2.071 | 2.303 | 23 | 45 | 530 | 690 |
| | DFT | 2.046 | 2.054 | 2.170 | -44 | -70 | -692 | |
| 5 | Exp | 2.050 | 2.058 | 2.229 | 34 | 62 | 593 | 590 |
| | DFT | 2.040 | 2.052 | 2.153 | -18 | -66 | -603 | |
| 6 | Exp | 2.038 | 2.038 | 2.213 | 55 | 55 | 436 | 590 |
| A | Exp | 2.038 | 2.038 | 2.213 | 55 | 55 | 436 | - |
| B | Exp | 2.050 | 2.050 | 2.220 | 45 | 45 | 410 | - |

**Table 3.1:** Experimental and calculated $g$ and ${}^{Cu}A$ spin Hamiltonian parameters for [Cu$^{II}$(BPA)$_x$] and [Cu$^{II}$(PA)$_x$] complexes. N.B. All $|A_i|$ values reported in MHz; $g_i$ ±0.003, $|A_{x,y}| \pm 10$ $|A_z| \pm 3$; $A_x$ and $A_y$ hyperfine components were not-resolved and therefore are estimated. $\lambda_{max}$ reported in nm; ±5nm. N.R. = not resolved.

| Species | | $g$ frame /rad | | | ${}^{Cu}A$ frame /rad | | |
|---|---|---|---|---|---|---|---|
| | | $\alpha$ | $\beta$ | $\gamma$ | $\alpha$ | $\beta$ | $\gamma$ |
| 1 | Exp | -1.60 | 1.54 | 2.96 | 1.63 | 1.58 | -1.55 |
| | DFT | -1.58 | 1.55 | 2.98 | 1.68 | 1.55 | -1.55 |
| 2 | Exp | -2.22 | 1.13 | 2.00 | 0.99 | 1.96 | 1.82 |
| | DFT | -1.79 | 1.18 | 2.04 | 0.48 | 1.97 | 1.79 |
| 3 | Exp | -2.04 | 1.84 | 2.13 | 1.15 | 1.36 | 1.86 |
| | DFT | -1.88 | 1.02 | 2.13 | 0.15 | 2.12 | 1.88 |
| 4 | Exp | -1.45 | 1.25 | 2.12 | -1.42 | 1.19 | 1.46 |
| | DFT | -1.47 | 2.19 | 2.12 | -0.78 | 0.97 | 1.46 |
| 5 | Exp | -0.57 | 2.70 | -2.09 | -0.57 | 2.70 | -2.09 |
| | DFT | -1.07 | 2.50 | 2.28 | 0.86 | 2.51 | -2.09 |

**Table 3.2:** Reference coordinate axes frames for $g$ and $A$ tensors, extracted from the EPR simulations and DFT calculations for the spectra of $CuSO_4$:PA and $CuSO_4$:BPA complexes.

rather large $A_{\parallel}$ values for Species 2 may indicate the inner-sphere coordination of a sulfate counter-ion, as previously suggested, which would have a small effect in $g_{\parallel}$, but a marked increase in $^{Cu}A_{\parallel}$.[19] The $g_{\parallel}/A_{\parallel}$ values of the co-ordinatively saturated $[\mathrm{Cu^{II}(BPA)_2}]$ complex (Species 3) are only slightly lower than those for Species 2 (Table 4.2). However, this Species has been reported to exist in both pseudo-octahedral and square-based pyramidal geometries, the latter associated with a non-coordinating pyridyl nitrogen (see Scheme A, Appendix 2, for proposed structure).[22] Nevertheless, the reported $^{Cu}A_{\parallel}$ values suggest the environment is closer to pseudo-octahedral geometry with a 4N-equatorial donor set.[21]

The above series of ligand titration experiments performed for the $[\mathrm{Cu^{II}(BPA)}_x]$ complexes were then repeated using the 2-picolylamine (PA) ligands. The resulting X-band CW EPR spectra for the resulting $[\mathrm{Cu^{II}(PA)}_x\mathrm{(H_2O)}_m]$ complexes formed by increasing the Cu:PA ratios are shown in Figure 3.4a-c. The more complete series of spectra showing the Cu:PA ratios of 1:0.1, 1:05, 1:1, 1:2, 1:5, 1:10, 1:50 are given in Appendix 2. Once again, all the EPR spectra reveal an axial environment at this operating frequency (X-band). At the lowest Cu:PA ratio studied here (1:0.1), the presence of the fully hydrated Cu(II) centre (Species 1) is clearly visible (shown in Appendix 2). At the stoichiometric Cu:PA ratio of 1:1, two Cu(II) centres are visible in the spectrum (Figure 3.4a) arising from a mix of Species 1 and an additional new centre hereafter labelled Species 4. We assign this latter Species 4 to the heteroleptic complex $[\mathrm{Cu^{II}(PA)(H_2O)}_m]$ arising from coordination of one

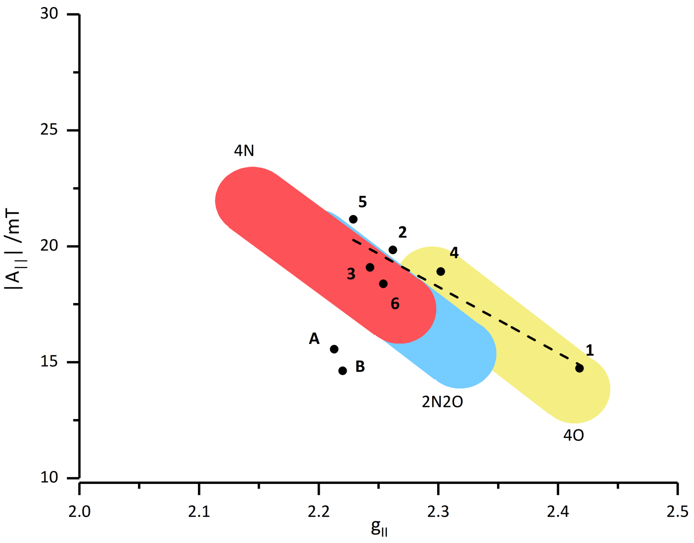

**Figure 3.6:** Peisach-Blumberg plot of the identified solution complexes.

PA ligand to Cu(II). At slightly higher ratios (1:2), another Cu(II) centre can be readily identified in the spectrum (Figure 3.4b), labelled Species 5. This Species can be easily assigned to the bis-adduct complex $[Cu^{II}(PA)_2(H_2O)_m]$formed by two PA ligands binding to the Cu(II) ion. A partly resolved $^{14}N$ super-hyperfine pattern is also evident in the perpendicular region of the spectrum, indicating nitrogen coordination, but lacking sufficient resolution to extract the number of coordinated $^{14}N$ nuclei (Figure 3.4b). At the highest Cu:PA ratios studied here (1:50), an additional signal is just apparent in the EPR spectrum (low intensity), most notably on the low field side of the $m_I$=+3/2 transition (Figure 3.4c). We assign this to the formation of the tris-adduct complex $[Cu^{II}(PA)_3]$ (Species 6), comparable to the isostructural $[Ni(PA)_3]^{2+}$ complex and observed for other first row transition metals.[23] However, it should be noted that the bis-adduct $[Cu^{II}(PA)_2(H_2O)_m]$ complex remains the more abundant Species even at these higher ratios (Figure 3.4c). Therefore, extraction of the exact spin Hamiltonian parameters for Species 6 is difficult owing to the overlapping features from Species 4 and 5, so only approximate values are given in Table 4.2. Furthermore, in support of these EPR findings, complimentary UV-Vis. measurements also indicate the presence of a third metal-ligand Species at high ligand ratios.

The spin Hamiltonian parameters obtained by simulation of the experimental spectra for Species 4, 5 and 6 (assigned to $[Cu^{II}(PA)](H_2O)_m$, $[Cu^{II}(PA)_2(H_2O)_m]$ and $[Cu^{II}(PA)_3]$) are listed in Table 4.2. Similar to the BPA adducts, the PA adducts can be easily distinguished based on the decreasing $g_{\|}$ and $^{Cu}A_{\|}$ values (relative to the hydrated $[Cu^{II}(H_2O)_6]$ complex) indicating an increasing degree of covelancy due to the strong interactions of the Cu(II) ion with the neutral, nitrogen donor sites on the PA ligands. In particular, the $g_{\|}$ and $^{Cu}A_{\|}$ values for Species 4 and 5 are indicative of a square-planar geometry, with PA ligands coordinating in the equatorial plane.[21] The slightly higher value of $g_{\|}$ for Species 4 is likely due to the asymmetric bonding interactions in the equatorial plane, due to the incomplete coordination sphere. The assignment of the largely square planar geometry, despite the high value for $g_{\|}$, is also supported by the progressively blue-shifted *d-d* band transitions observed with increasing ligand ratios in UV-Vis. titrations reported *vide infra.* Finally, the spin Hamiltonian parameters for Species 6 are consistent with a pseudo-octahedral geometry, generally unfavoured by Cu(II) due to its tendency to coordinate weakly in the axial positions. However, the decrease in magnitude of $^{Cu}A_{\|}$ and the increase in $g_{\|}$, compared to Species 5, is consistent with the lower spin delocalisation in the equatorial plane due to interactions in the axial positions. The proposed structures for Species 4-6 are shown in Figure

??.

### 3.2.3 UV-vis of metal titration with ligand

A similar experiment to that described above for the model Cu(II) complexes using EPR was repeated using UV-vis spectroscopy. These measurements were performed by Johnson Matthey. Initially, the $CuSO_4$ solution (0.01 M) was titrated with an increasing volume of a PA solution (0.1 M). As the PA is added, at 1 equivalent, a rapid change occurs in the spectrum with the appearance of a band at 710 nm. From two equivalents of ligand, the band shifts to 690 nm. The ligand itself shows no absorption above 500 nm (Figure 3.7)

Closer analysis of the data in Figure 3.7 shows that the titration can be broken down into at least two distinct processes (with associated isosbestic points) that occur from 0 to 1 equivalent and 1 to 2 equivalent of added ligand (see Appendix 2). The UV-vis data was then modelled to understand the underlying processes. A two-step model (i.e., $Cu^{+}L \rightarrow CuL$; $CuL^{+}L \rightarrow CuL_2$) was first used to process the titration data, but the fit was poor (see Appendix 2). Hence a three-step model, which included a third step (including formation of $CuL_3$), was used and a much better fit was obtained. The absorption spectra for the third species (*i.e.*, $CuPA_3$) was predicted to be very similar to the $CuL_2$ species (i.e., $CuPA_2$) in the 590 nm region with an additional shoulder at 890 nm. The log $K$ values (Table 3.3) reveal that the formation of CuPA and $CuPA_2$ are more favourable compared to formation of $CuPA_3$, in agreement with the EPR data where the species were identified at low ratios. The titration was also carried out in reverse, whereby a Cu(II) solution

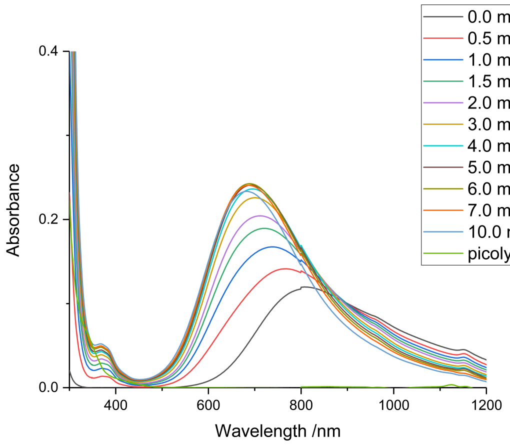

**Figure 3.7:** UV-vis spectra of a $CuSO_4$ solution bearing an increasing concentration of PA ligand.

was added to the PA solution, with a similar trend and observations obtained. The stability of the Cu(II) complexes in acidic environments was also tested. When a solution bearing a Cu:PA ratio of 1:2.25 was titrated with $H_2SO_4$, a clear change in chelation from $CuPA_2$ to $Cu(H_{2O})_6$ was evident in the UV-vis spectra (see Appendix 2). As the pH decreased below 4, the $CuPA_2$ Species rapidly diminished in intensity until at pH=2 no signal from this complex was detected. Similarly, the CuPA Species also diminished from pH=2.5 until at ca. pH=1 there is virtually no detectable chelated Cu(II) with the UV-vis spectra matching that of the $CuSO_4$ solution (Appendix 2). When a similar titration was carried out with the Cu:BPA complexes, the $CuBPA_2$ Species was found to gradually decreasfe in concentration with increasing pH. However, in this case, the CuBPA complex remains stable even up to pH=0.8 and can still be observed in the spectra at pH=0.5. This indicates that the BPA ligand forms an extremely stable complex with the Cu(II) ions which then cannot be easily displaced in acidic media (*i.e.*, *via* protonation of the amine nitrogen) whereas the Cu:PA complex is disrupted around pH=2, likely caused by the protonated amine ligand-copper complex being less favorable (i.e., the proton more favorably interacts with the ligand than Cu(II)).

A similar UV-vis study was performed for the titration of $CuSO_4$ with the BPA ligand. As with the PA addition, the titration was carried out by titrating a copper sulfate solution (10 mL, 0.01 M) with a solution of BPA (0.1 M). Initially, a two-step reaction model was used where the copper and ligand solution spectra were fixed, which resulted in a very poor fit. The model was adjusted with a fixed copper solution spectra and an unknown ligand spectra (Appendix 2, Figure S12). This gave an improved but still relatively poor fit with a similar issue to that previously indicated; whereby, a negative peak was required in the ligand spectra to fit at high ligand excess (at low wavelengths). The corresponding UV-Vis. spectra have been omitted due to the poor modelling. Nevertheless, the log $K$ values indicate a favourable formation of Cu(BPA), and $CuBPA_2$, in comparison to the values derived from the PA titrations.

| Step | Log K | Error |
|---|---|---|
| $Cu + PA \rightarrow CuPA$ | 7.853 | 0.067 |
| $CuPA + PA \rightarrow CuPA_2$ | 5.725 | 0.062 |
| $CuPA_2 + PA \rightarrow CuPA_3$ | 1.510 | 0.012 |
| $Cu + BPA \rightarrow CuBPA$ | 6.942 | 0.132 |
| $CuBPA + BPA \rightarrow CuBPA_2$ | 4.156 | 0.070 |

**Table 3.3:** Log K values obtained by UV-vis for the Cu(II)-BPA and -PA speciation study.

### 3.2.4 Assignment of Cu(II) Species on loaded resins

Once the model Cu(II) Species were characterised by EPR, and confirmed by UV-Vis. analysis and deconvolution of the experimental CuWRAM and Dowex EPR spectra (Figure 3.2) becomes more straight forward. The first point to note, is that there is no evidence for the hydrated $[Cu^{II}(H_2O)_6]$ complex (Species 1) in these spectra (Figure 3.3 and 3.4). This is not unexpected, particularly owing to the relatively hydrophobic framework on which the chelating groups are anchored.

In the Dowex case, Species 2 and 3 can be identified by simulation of the experimental spectrum (Figure 3.2d), although the poor resolution of the spectrum prevents an accurate quantitative estimate of the relative abundance of each Species. However, despite the identification of Species 2 and 3 in the EPR spectrum of the Cu loaded Dowex sample, an unidentified EPR signal remains. This is highlighted as Species A in Figure 3.3. An estimate of the spin Hamiltonian parameters for this unidentified Cu(II) centre (hereafter labelled Species A) are listed in Table 4.2. The $g_{\|}$ and $A_{\|}$ values of 2.21 and 436 MHz respectively, suggests a tetragonally perturbed square planar complex,[21] which would be consistent with a highly distorted, weakly bound environment that may arise due to the protonation equilibria of the ligand, or more likely an intermolecular coordination mode by neighbouring BPA ligands (Figure 3.1). In other words, two BPA ligands may interact with the Cu(II) ion, but involving different numbers of coordinating N-nuclei. Hence we assign this to a more weakly coordinating intermolecular $[Cu^{II}(BPA)_x(BPA)_y(H_2O)_m]$ complex, as opposed to the intramolecular $[Cu^{II}(BPA)](H_2O)_m$ and $[Cu^{II}(BPA)_2]$ complexes (Species 2 and 3). The presence of the coordinated water is evidenced from the dehydration studies *vide infra.*

For the CuWRAM sample, the experimental EPR spectrum (Figure 3.4d) could be simulated and deconvoluted knowing the spin Hamiltonian parameters for the model complexes Species 4-6. It is evident from the simulations that the spectrum is dominated by signals assigned to the bis- and tris-adducts (Species 5 and 6), with no evidence for any substantial contributions coming from $[Cu^{II}(H_2O)_6]$ or $[Cu^{II}(PA)](H_2O)_m$ complexes (Species 1 and 4). Similar to the Dowex case, an additional unassigned signal, not characterised by the $g/^{Cu}A$ values of the model complexes (Species 4-6), can be seen in the spectrum (labelled B in Figure 3.4d). An estimate of the spin Hamiltonian parameters for this Species are given in Table 4.2 (labelled Species B). Once again, the $g_{\|}$ and $A_{\|}$ values of 2.22 and 410 MHz are similar to that observed on the Dowex sample, and this Species can also be assigned either to coordination to the PA ligands with partially protonated chelating sites, dependent on pH and equilibrium acidities, or the different degrees of intermolecular N-coordination by neighbouring PA. In solution, one, two or three bi-dentate PA ligands coordinate to the Cu(II), but on the CuWRAM sample, it appears that mono- and bi-dentate coordination is possible (not reproduced in the model solution phase experiments). The geometry optimised structures for Species 2, 3, 4, 5 identified in the resin spectra for Dowex and CuWRAM are given in Figure 3.8.

### 3.2.5 Dehydration / Rehydration studies

According to the above findings, the loaded Cu(II) resins contain $[\mathrm{Cu^{II}(PA)}_x]$ and $[\mathrm{Cu^{II}(BPA)}_x]$ complexes, with intra- and inter-molecular coordination of the ligands anchored to the resins and likely bearing coordinated water molecules within the complex. To explore the latter point further, the resin samples were subjected to a series of dehydration and rehydration experiments. For CuWRAM, the sample was dried over silica gel for several hours and subsequently re-hydrated in a controlled atmosphere for several hours. The resulting EPR spectra are shown in Figure 3.9. Clear differences can be observed between the hydrated and dehydrated spectra, and the results were found to be completely reversible. This procedure was repeated several times, to ensure the observed reversibility was not associated with any changes in the polymer structure (*e.g.* framework degradation or shrink-swell changes) and instead are indeed associated with the loss of water. It is clear that only the signal assigned to Species B on the CuWRAM sample is affected, which suggests that this intermolecular $[\mathrm{Cu^{II}(PA)}_x\mathrm{(PA)}_y\mathrm{(H_2O)}_n]$ complex bears strongly coordinated $H_2O$ molecules in the inner sphere.

The EPR spectrum of the resulting dried sample (Figure 3.9b) is broadened, but contained observable signals associated with Species 5 ($[\mathrm{Cu^{II}(PA)_2}]$) and 6 ($[\mathrm{Cu^{II}(PA)_3}]$). Because the spin Hamiltonian parameters for these Species did not change upon drying, it suggests any coordinated water is only weakly bound and does not affect the EPR signals. Following dehydration of Species B, $[\mathrm{Cu^{II}(PA)}_x\mathrm{(PA)}_y\mathrm{(H_2O)}_n]$, the spin Hamiltonian parameters of the resulting $[\mathrm{Cu^{II}(PA)}_x\mathrm{(PA)}_y]$ must bear close resemblance to those of Species 5 and 6, since no new features were observed in the spectrum and the overall integrated Cu(II) signal intensity did not change. It is unlikely that the dehydrated $[\mathrm{Cu^{II}(PA)}_x\mathrm{(PA)}_y]$ rearranges into Species 5 or 6, since upon rehydration, the signal from Species B reappears, indicating a reversible $[\mathrm{Cu^{II}(PA)}_x\mathrm{(PA)}_y\mathrm{(H_2O)}_n] \leftrightarrow [\mathrm{Cu^{II}(PA)}_x\mathrm{(PA)}_y]$ process, and the more co-ordinatively saturated Species 5 and 6 will not be so

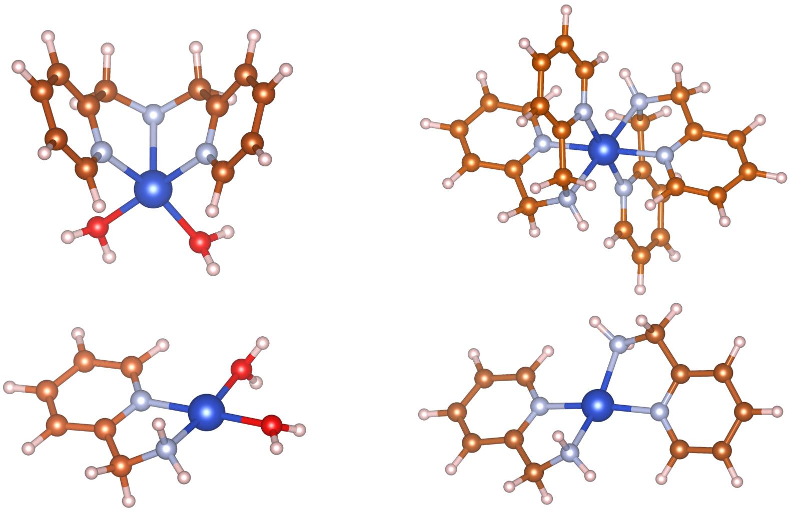

**Figure 3.8:** Geometry optimised structures of homoleptic and heteroleptic complexes, *Clockwise from top left:* 2, 3, 4, 5; identified as coordination modes within the CuWRAM (2, 3) and Dowex M4195 (4, 5) resins, respectively. Geometry optimisation calculations were performed by Johnson Matthey.

influenced by the hydration level. The above experiments were also repeated for the Dowex sample, wherein a similar Species A signal was identified in the EPR spectrum. The resulting dehydration / rehydration spectra are shown in Appendix 2. It should be noted, that in this case, it proved more difficult to dehydrate the sample and gentle thermal-evacuation was required to elicit a change in the spectra. Although the changes in the spectra were less pronounced compared to the CuWRAM sample (Figure 3.9), nevertheless an analogous reversible behaviour was once again identified, suggesting that Species A in the Dowex sample can also be assigned to a Cu(II) complex bearing coordinated water molecules, i.e., $[\mathrm{Cu^{II}(BPA)}_x\mathrm{(BPA)}_y\mathrm{(H_2O)}_n] \leftrightarrow [\mathrm{Cu^{II}(BPA)}_x\mathrm{(BPA)}_y]$.

### 3.2.6 Selective Cu(II) unloading studies

Typically, the adsorbed Cu(II) ions that are collected by the resins during the elution cycle, are subsequently released by washing with concentrated acid (1-2 M $H_2SO_4$) which protonate the nitrogen sites. Acid washing of the Dowex resin is insufficient to remove all of the Cu(II) ions and in such cases the sample requires washing with a concentrated ammonia solution (1-2 M $NH_4OH$) to fully release

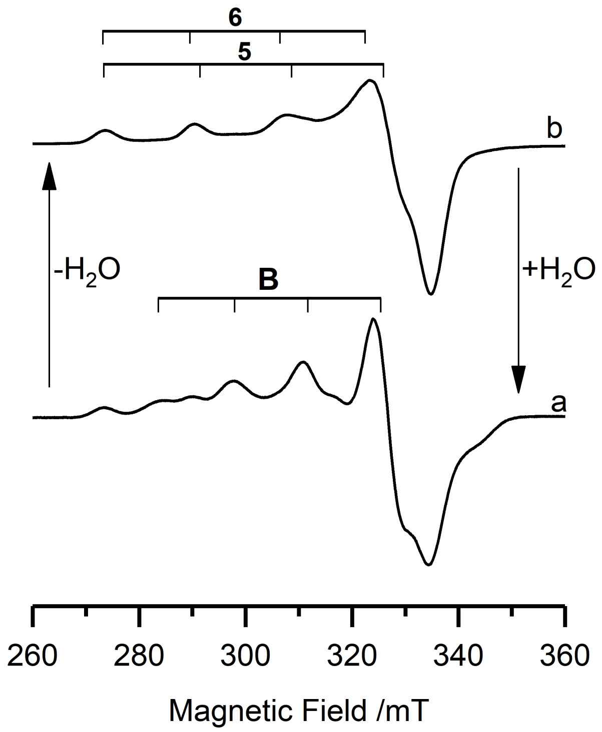

**Figure 3.9:** X-band CW EPR spectra (120 K) of the loaded CuWRAM sample (1 mg/g loaded resin) undergoing repeated dehydration – rehydration treatments: a) hydrated material, b) dehydrated material.

the metal. We therefore undertook a series of elution experiments using increasing concentrations of acid (or base) to explore any variation in binding strength, as monitored by changes in the EPR spectra. The resulting EPR spectra for the loaded CuWRAM sample before and after washing with increasing concentrations of $H_2SO_4$ are shown in Figure 3.10. The overall EPR signal intensity steadily decreases as the concentration of acid increases. At the highest concentrations studied here (2.5 M), virtually all of the Cu(II) ions have been removed from the sample. However, one striking observation from the spectra is the rapid and immediate loss of Species B from the CuWRAM sample at low $H_2SO_4$concentrations. At 0.5 M $H_2SO_4$ concentration, virtually all of Species B has been removed from the sample (Figure 3.10). At slightly higher concentrations (from 0.5 M to 1.5 M), the EPR spectra are reminiscent of the signals identified in the dehydrated sample (Figure 3.9b), and indicate that only the bis-adduct Species 5 and tris-adduct Species 6 remain. At 1.5 M $H_2SO_4$ concentration, a small shoulder emerges on one of the parallel hyperfine lines (labelled with a blue box in Figure 3.10, low field $m_I$=+1/2 transition at 312 mT) and based on the simulation, it appears that this feature is associated with Species 6. This result suggests that, following elution

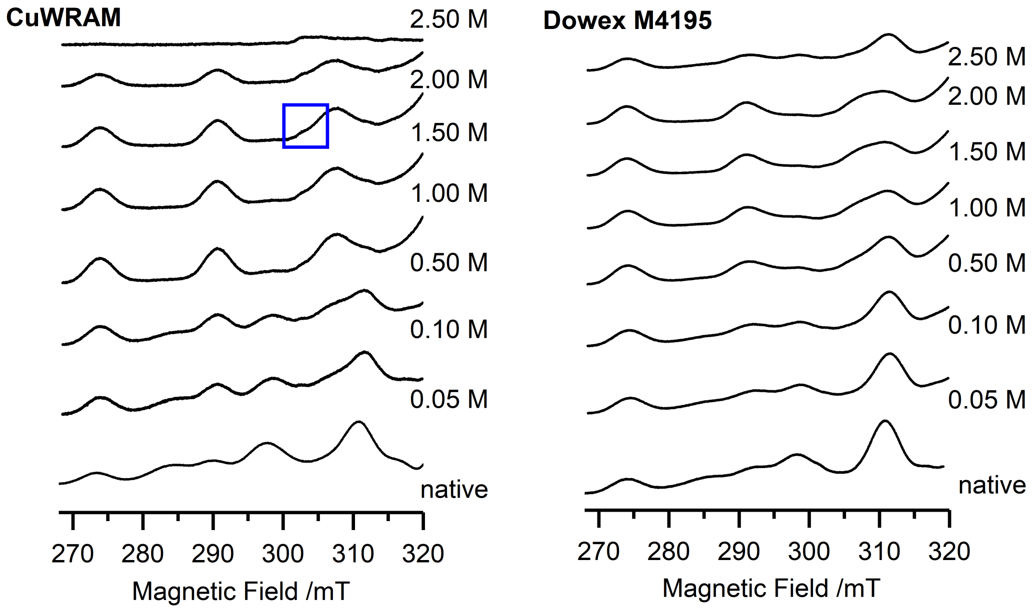

**Figure 3.10:** X-band CW EPR spectra (120 K) of the loaded CuWRAM and Dowex M4195 samples (1 mg $g^{-1}$ loaded resins), after washing with increasing concentrations of $H_2SO_4$: 0.05 M, 0.1 M, 0.5 M, 1 M, 1.5 M, 2 M, 2.5 M.

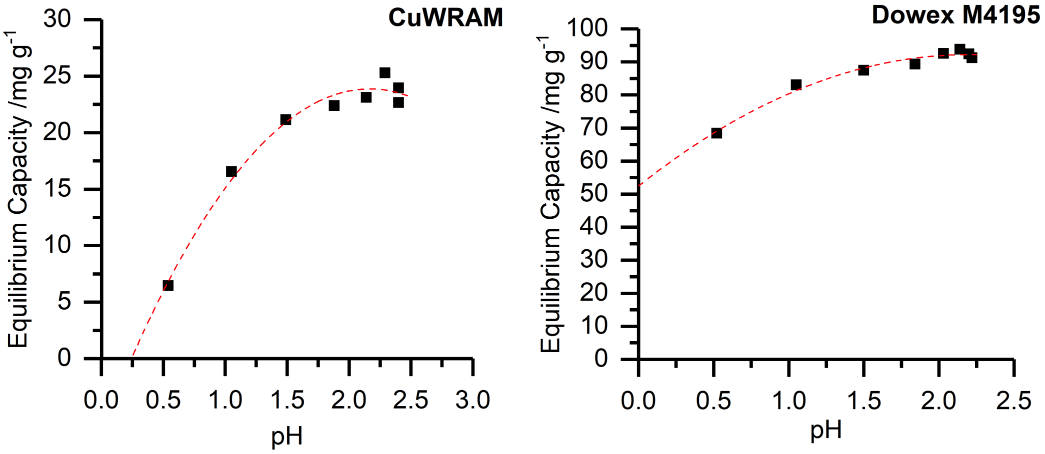

**Figure 3.11:** Copper capacity of CuWRAM, measured using 0.4 w/v% resin, and Dowex® M4195 measured using 0.2 w/v%. Initial solution of 500 ppm copper, pH adjusted using $H_2SO_4$. Error in equilibrium capacity measurements ±2 mg $g^{-1}$; Error in pH measurements ±0.01; $R^2$(CuWRAM) = 0.980; $R^2$(Dowex® M4195) = 0.978.

of the more labile Species B, the bis-adduct is then preferentially removed before the more highly coordinatively saturated tris-adduct Species 6 (although the resolution of the spectra were insufficient to accurately quantify this observation). Nevertheless, this observation would be a reasonable expectation associated with the Cu(II) speciation present on these sample and these results also fit with the assigned coordinations from solution measurements and UV-Vis data *vide infra*.

A similar series of experiments were performed by washing the Dowex sample with increasing concentrations of $H_2SO_4$. The resulting spectra are shown in Appendix 2. The results are very similar to the above findings observed for the CuWRAM sample. In particular, Species A was selectively and preferentially removed at the lower acid concentrations, whilst the appearance of a small shoulder at 312 mT (assigned to the fully coordinated Species 3) relative to the signal from Species 2 at higher concentrations, suggests that the heteroleptic complex 2 is eluted before the homoleptic complex 3. It should be noted, that even at the highest concentrations of acid used (2.5 M) residual Cu(II) ions remain attached to the resin (Appendix 2), in agreement with reported kinetics measurements on Dowex relative to CuWRAM.[3] This clearly indicates that protonation of the BPA chelate binding sites is insufficient to release Species 2 and 3 from the resin. Therefore, the Cu loaded resin samples were washed with an aqueous ammonia solution of increasing concentrations (0.05 – 2.5 M) and the resulting spectra are shown in Appendix 2. An identical trend to that observed above with acid washing was found in the ammonia washed samples, with the residual signal visible at 2.5 M $NH_4OH$(*aq.*) concentration having parameters typical of Species 3.

Equilibrium batch uptake measurements were carried out to determine the equilibrium Cu(II) capacity at varying pH. The resulting capacity data is shown in Figure 3.11. It is clear from the data, that the silica based CuWRAM material has a much lower capacity than the polymeric Dowex material, as expected. The Cu(II) capacity profile for the two resins is also different. The CuWRAM sample shows a rapid reduction in capacity as the pH is reduced below 2, with only 6 mg $g^{-1}$ capacity at pH=0.5 which is 28% of the capacity at pH=2. Below pH=0.5, the capacity rapidly decreases to zero, similar to the EPR data which revealed a facile loss in the Cu(II) signal as the acid concentration increased (Figure 3.10), and confirms the ready elution of copper from these materials. The Dowex material on the other hand, does not show such a rapid reduction in capacity with a capacity of 68 mg $g^{-1}$ achieved at pH=0.5 which is still 75% of the material capacity at pH=2. This result also confirms the earlier EPR observations on the difficulty of removing all the Cu(II) signal even at high acid concentrations.

## 3.3 Conclusions

CERs are currently an expensive, but efficient technology for metal uptake, with applications across a wide range of industrial, military, agricultural and waste disposal processes. A detailed understanding of local coordination sites and their interaction is critical in the understanding of functional properties and kinetics. Several typical transition metal impurities found in effluents are paramagnetic, and serve as native spin probes that can directly identify the nature and distribution of bound sites within the resins. EPR spectroscopy (and related hyperfine techniques) is therefore the ideal tool in their characterisation. Selective detection of metal Species, similar in electronic structure, is challenging with other spectroscopic techniques and therefore a direct relationship between binding distribution, local structure, and uptake/ removal kinetics can be identified. Similarly, a detailed understanding of structural properties, synthetic processes and their effects on binding capacities/ affinities under different operating conditions can be achieved.

A combined CW EPR, DFT and UV-vis study of local metal binding environments in the Dowex® and CuWRAM® resins, for Cu extraction from aqueous media was undertaken to provide a better understanding of previously reported uptake kinetics and operational properties. Three distinct binding environments (Species 2, 3 and A) were identified from the complex EPR spectrum of the "as received" Dowex® resin and a further three environments (Species 5, 6 and B) were identified in the CuWRAM® case. Comparison to model complexes in solution, containing the 'free ligand' Species, aided the characterisation of two Species out of three in each case.

An unknown Species was observed in each of the chelating exchange resins (Species A, B), which were not observed in solution and which were proposed to be based on weakly bound, inter-molecular type coordinations to the resin frameworks. The binding behaviour of the indicated Species was monitored during dehydration studies and elution with $H_2SO_4$ / $NH_4OH$, to better understand the nature and relative binding affinities of Cu Species adsorbed onto the surface. The EPR signals associated with unknown Species and the heteroleptic complexes (Species A and 2, and Species B and 6, respectively) were observed to diminish with dehydration of the resin, indicating the presence of water within the coordination sphere which may act to 'block' donor atoms. Selective unloading studies confirmed that the unknown Species, A and B, are weakly bound, and are first to be removed from the resin framework upon elution. A mixture of remaining Species are indicated in the intermediate eluent concentration ranges as non-regular line shapes in the parallel hyperfine region of the EPR spectra. The EPR investigations were supported by UV-vis measurements to determine equilibrium Cu(II) capacity versus pH, and estimated equilibrium formation constants for respective uptake mechanisms.

The characterisation of A and B remains challenging due to their nature and isolation; The distorted, intermolecular environment cannot be modelled in solution; and similarly cannot be easily isolated on the resin framework due to their relative binding affinity. Differences in anisotropic $g$ and $A$ tensors are relatively small Theoretical calculations are also challenging to define without further information about their local structure. These respective Species could be associated to either partially occupied or protonated chelating sites, by ionic association of lighter elements or covalent interactions with transition metal ions. Additionally, defective groups present on the resin structure may also be considered. It is clear that association of these distorted complexes is influenced by the occupied capacity of the resin pores.

In conclusion, EPR spectroscopy provides a direct, selective and sensitive method of probing magnetic structure in solid-state materials. IERs and CERs represent an important class of separation and catalytic technologies with application in several industries. This study represents an extensive and systematic characterisation of commercial materials of value for process control and materials development.

## 3.4 Experimental

**Materials:** Dowex® M4195, $CuSO_4$, and the free ligands 2-picolylamine (PA) and di-(2-picolylamine) (BPA) were sourced from Sigma-Aldrich. Silica gel, glycerol, $H_2SO_4$, and $NH_4OH$ (Reagent grade) were also purchased from Sigma-Aldrich, and used without further purification. CuWRAM® was supplied by Johnson Matthey.

**Loading procedure:** The copper loading procedure was performed on the resins Dowex® M4195 and CuWRAM® after an initial wash with water, followed by drying overnight in an oven at 70°C. A solution of $CuSO_4$ in water, of appropriate concentration for metal loadings (25 ppm, 40 mL g$^{-1}$(resin) for 1 mg g$^{-1}$ loading) were prepared and placed in a centrifuge tube with the appropriate mass of resin material. The slurry was mixed overnight, using a roller mixer, before collection under reduced pressure. The solid was rinsed with copious amounts of water, to yield the loaded, hydrated CuWRAM® and Dowex® samples. Excess water was removed on filter paper, and the samples were used, without further treatment, for EPR measurements. Accurate copper contents were measured by digestion analysis, and were determined to be within 10% of the target loading.

**Preparation of model complexes:** Stock solutions of $CuSO_4$ (80 mM), and the free ligands 2-picolylamine (hereafter abbreviated as PA) and di(2-picolylamine) (hereafter abbreviated as BPA) (4 M) were prepared in water. 1 mL samples of the Cu:PA and Cu:BPA complexes were prepared by mixing the 80 mM $CuSO_4$ solution (0.25 mL), with the appropriate volume of 4 M PA or BPA ligand solutions and diluted with water to achieve the desired molar ratios (Cu:L; L = PA, BPA) 1:0.1; 1:0.5; 1:1; 1:2; 1:5; 1:10; 1:50. The volume was made up with water, and glycerol (40% v/v), to achieve the desired concentration (20 mM $CuSO_4$). The mixtures were stirred for 30 minutes, and sonicated for 10 minutes to ensure homogeneity in the water-glycerol system for freezing. Prior to measurement, 0.2 mL samples were loaded into an EPR tube and flash-frozen in liquid nitrogen.

**Drying/ rehydration treatment:** The drying process for CuWRAM® was performed by placing the sample in a desiccator under ambient pressure for a period of 7 days, using silica gel as the desiccant. The rehydration was performed by placing the dried sample in a desiccator (without desiccant) with a vial of water to generate a humid environment. The sample was left for 7 days prior to measurement. For the Dowex® resin, desiccation was observed to have little change on the resultant EPR spectrum. Instead, the sample was subjected to gentle evacuation on a Schlenk line, at room temperature, for a period of 2 hours. The rehydration process was the same as described for the CuWRAM® sample. The degree of hydration was checked using EPR data (this work), and comparison with the "as received" samples.

**Selective unloading study:** Stock solutions of the $H_2SO_4$ and $NH_4OH$ eluents were prepared at varying concentrations, as required for the study (0.05 M; 0.1 M; 0.5 M; 1 M; 1.5 M; 2 M; 2.5 M). Samples of the respective resins (0.05 g) were weighed out and washed in a Büchner funnel with the chosen concentration of $H_2SO_4$ or $NH_4OH$ (20 mL). Finally, the samples were washed with water and collected ready for EPR measurement.

**CW EPR spectroscopy:** The X-band (9 GHz) CW-EPR spectra were recorded at 140 K on a Bruker EMX spectrometer operating at 100 kHz field modulation, 10 mW microwave power using an ER 4119HS cavity. Spectral simulations were performed using the EasySpin toolbox[24] in MATLAB, developed at ETH Zürich.

**UV titration experiments:** Stock solutions of $H_2SO_4$, $CuSO_4$, picolylamine and bis-picolylamine were made up in deionized water. An initial solution (20 mL) was measured in a 50 mL tube and varying aliquots of titrant solution were added. After mixing for 5 mins, an aliquot was taken to record the UV-vis spectra on a Cary 5000 UV-vis-NIR spectrometer, between 300-1200 nm at 5 nm intervals, and the pH was recorded of the solution. The spectra were processed using ReactLabTM Equilibria (JPlus Consulting Limited).

**Equilibrium uptake experiments:** Batch testing was carried out to determine the equilibrium adsorption capacity of the resins under varying pH. CuWRAM® or Dowex® resins were measured into a centrifuge tube to which 35 mL of $CuSO_4$ solution added; to this de-ionized water and $H_2SO_4$ was added (total 5 mL). After 18 h, a sample of solution was removed for analysis by ICP-OES and the pH of the remaining solution was measured. The metal concentration of the blank (untreated) sample was compared against the concentration of the treated sample to calculate the amount of metal adsorbed.

**Computations:** Geometries were optimised using GAMESS-US (Version 5 Dec 2014, R1)[25] at the DFT level of theory, in conjunction with the B3LYP functional[26–

29] (including the D3 empirical dispersion correction[30]), the Def2-SVP basis set,[31] and the aqueous SMD[32] implicit solvation model. Numerical frequencies were performed at the converged geometries to confirm stable energy-minima on the potential energy surface, as well as to obtain thermodynamic corrections to the electronic energies. More accurate energies were obtained by performing single-point energy calculations on the geometries obtained above, using the double-hybrid DSD-PBEP86 functional,[33, 34] the triple-zeta Def2-TZVP basis set,[31] and the SMD solvation model.[32] These calculations were performed using ORCA (Version 3.0.3),[35] implementing the RIJCOSX approximation[36] to speed up the calculations. The double-hybrid calculations required an additional auxiliary correlation basis set of triple-zeta quality;[37] additionally, the RIJCOSX approximation required a second Coulomb-fitting auxiliary basis set, also of triple-zeta quality.[38] Thermodynamic corrections obtained from the lower level of theory were added to the single-point energies obtained from the double-hybrid calculations to yield approximate aqueous Gibbs free energies ($G_{H_2O}$). Initial conformations of the free picolylamine (PA) and bis-picolylamine (BPA) ligands were obtained using Open Babel's[39] genetic algorithm based conformer searching functionality. For each ligand, a maximum of 50 random conformers were generated, and their energies scored with the MMFF94 force field,[40–44] as implemented in Open Babel. For each ligand, the lowest energy conformation was used as the starting point for DFT geometry optimisations.

**DFT calculation of EPR parameters:** The resulting geometries were used to estimate EPR parameters in ORCA,[35] using the hybrid PBE039 functional[45] and basis set of EPRII[46] for light atoms, and the Core Properties all electron basis set for Cu,[47] with spin-orbit effects accounted for in a mean field approach.[48]

# References

[1] Simon Glöser, Marcel Soulier, and Luis A. Tercero Espinoza. Dynamic analysis of global copper flows. global stocks, postconsumer material flows, recycling indicators, and uncertainty evaluation. *"Environmental Science & Technology"*, 47(12):6564–6572, 6 2013.

[2] Lawrence K. Wang, David A. Vaccari, Yan Li, and Nazih K. Shammas. Chemical precipitation. In *Physicochemical Treatment Processes*, Handbook of Environmental Engineering, pages 141–197. Humana Press, 2005.

[3] Y. J Hsu, M. J Kim, and T Tran. Electrochemical study on copper cementation from cyanide liquors using zinc. *Electrochimica Acta*, 44(10):1617–1625, 1 1999.

[4] Gordon M. Ritcey. Solvent extraction in hydrometallurgy: Present and future. *"Tsinghua Science & Technology"*, 11(2):137–152, 4 2006.

[5] Konrad Dorfner. *Ion Exchangers.* Walter de Gruyter, 1 1991.

[6] Sofia A. Cavaco, Sandra Fernandes, Margarida M. Quina, and Licínio M. Ferreira. Removal of chromium from electroplating industry effluents by ion exchange resins. *Journal of Hazardous Materials*, 144(3):634–638, 6 2007.

[7] Suresh K. Sahni and Jan Reedijk. Coordination chemistry of chelating resins and ion exchangers. *Coordination Chemistry Reviews*, 59:1–139, 9 1984.

[8] Mohsen Arbabi and Nazila Golshani. Removal of copper ions cu (ii) from industrial wastewater: A review of removal methods. *International Journal of Epidemiologic Research*, 3(3):283–293, 9 2016.

[9] F. Gode and E. Pehlivan. A comparative study of two chelating ion-exchange resins for the removal of chromium(iii) from aqueous solution. *Journal of Hazardous Materials*, 100(1):231–243, 6 2003.

[10] P. J. Hoek and J. Reedijk. Coordination of transition-metal ions by chelating cation-exchange resins; Co(II), Ni(II) and Cu(II) coordinated by the iminodiacetate group in chelex-100. *Journal of Inorganic and Nuclear Chemistry*, 41 (3):401–404, 1 1979.

[11] Taipeng Chen, Fuqiang Liu, Chen Ling, Jie Gao, Chao Xu, Lanjuan Li, and Aimin Li. Insight into highly efficient coremoval of copper and p-nitrophenol by a newly synthesized polyamine chelating resin from aqueous media: Competition and enhancement effect upon site recognition. *"Environmental Science & Technology"*, 47(23):13652–13660, 12 2013.

[12] Katri Sirola, Markku Laatikainen, Marko Lahtinen, and Erkki Paatero. Removal of copper and nickel from concentrated $ZnSO_4$ solutions with silica-supported chelating adsorbents. *Separation and Purification Technology*, 64 (1):88–100, 11 2008.

[13] Alaa S Abd-El-Aziz, Jr, Charles E. Carraher, Jr, and Charles U. Pittman. *Macromolecules Containing Metal and Metal-Like Elements Volume 4.* "John Wiley & Sons", Hoboken, 2005.

[14] D. Kołodyńska, W. Sofińska-Chmiel, E. Mendyk, and Z. Hubicki. Dowex m 4195 and lewatit™ monoplus tp 220 in heavy metal ions removal from acidic streams. *Separation Science and Technology*, 49(13):2003–2015, 9 2014.

[15] Katri Sirola, Markku Laatikainen, and Erkki Paatero. Effect of temperature on sorption of metals by silica-supported 2-(aminomethyl)pyridine. part ii: Sorption dynamics. *Reactive and Functional Polymers*, 70(1):56–62, 1 2010.

[16] Katri Sirola, Markku Laatikainen, and Erkki Paatero. Effect of temperature on sorption of metals by silica-supported 2-(aminomethyl)pyridine. part i: Binding equilibria. *Reactive and Functional Polymers*, 70(1):48–55, 1 2010.

[17] Mary R. Healy, Emma Carter, Ian A. Fallis, Ross S. Forgan, Ross J. Gordon, Eduardo Kamenetzky, Jason B. Love, Carole A. Morrison, Damien M. Murphy, and Peter A. Tasker. EPR/ENDOR and computational study of outer sphere interactions in Copper complexes of phenolic oximes. *Inorganic Chemistry*, 54(17):8465–8473, 9 2015.

[18] Jie Gao, Fuqiang Liu, Panpan Ling, Jintao Lei, Lanjuan Li, Chenghui Li, and Aimin Li. High efficient removal of cu(ii) by a chelating resin from strong acidic solutions: Complex formation and dft certification. *Chemical Engineering Journal*, 222:240–247, 4 2013.

[19] J. Peisach and W.E. Blumberg. Structural implications derived from the analysis of electron paramagnetic resonance spectra of natural and artificial copper proteins. *Archives of Biochemistry and Biophysics*, 165(2):691–708, 12 1974.

[20] W. Froncisz and J. S. Hyde. Broadening by strains of lines in the g-parallel region of $Cu^{2+}$ EPR spectra. *The Journal of Chemical Physics*, 73(7):3123–3131, 10 1980.

[21] Giovanni Tabbì, Alessandro Giuffrida, and Raffaele P. Bonomo. Determination of formal redox potentials in aqueous solution of Copper(II) complexes with ligands having nitrogen and oxygen donor atoms and comparison with their EPR and UV-Vis spectral features. *Journal of Inorganic Biochemistry*, 128:137–145, 11 2013.

[22] Mallayan Palaniandavar, Raymond J. Butcher, and Anthony W. Addison. "dipicolylamine complexes of Copper(II): Two different coordination geometries in the same unit cell of $Cu(Dipica)_2(BF_4)_2$". *Inorganic Chemistry*, 35 (2):467–471, 1 1996.

[23] Margaret L. Niven, (The Late)Gordon C. Percy, and David A. Thornton. The infrared spectra of 2-aminomethylpyridine complexes of metal(II) ions. *Journal of Molecular Structure*, 68:73–80, 11 1980.

[24] Stefan Stoll and Arthur Schweiger. Easyspin, a comprehensive software package for spectral simulation and analysis in EPR. *Journal of Magnetic Resonance*, 178(1):42–55, 1 2006.

[25] Michael W Schmidt, Kim K Baldridge, Jerry A Boatz, Steven T Elbert, Mark S Gordon, Jan H Jensen, Shiro Koseki, Nikita Matsunaga, Kiet A Nguyen, Shujun Su, Theresa L Windus, Michel Dupuis, and John A Montgomery. General atomic and molecular electronic structure system. *Journal of Computational Chemistry*, 14(11):1347–1363, 11 1993.

[26] Axel D Becke. Density-functional thermochemistry. iii. the role of exact exchange. *The Journal of Chemical Physics*, 98(7):5648–5652, 4 1993.

[27] Chengteh Lee, Weitao Yang, and Robert G Parr. Development of the colle-salvetti correlation-energy formula into a functional of the electron density. *Physical Review B*, 37(2):785–789, 1 1988.

[28] S H Vosko, L Wilk, and M Nusair. Accurate spin-dependent electron liquid correlation energies for local spin density calculations: a critical analysis. *Canadian Journal of Physics*, 58(8):1200–1211, 8 1980.

[29] P J Stephens, F J Devlin, C F Chabalowski, and M J Frisch. Ab initio calculation of vibrational absorption and circular dichroism spectra using density functional force fields. *The Journal of Physical Chemistry*, 98(45):11623–11627, 11 1994.

[30] Stefan Grimme, Jens Antony, Stephan Ehrlich, and Helge Krieg. A consistent and accurate ab initio parametrization of density functional dispersion correction (dft-d) for the 94 elements h-pu. *The Journal of Chemical Physics*, 132(15):154104, 4 2010.

[31] Florian Weigend and Reinhart Ahlrichs. Balanced basis sets of split valence, triple zeta valence and quadruple zeta valence quality for h to rn: Design and assessment of accuracy. *Physical Chemistry Chemical Physics*, 7(18): 3297–3305, 2005.

[32] V Aleksandr Marenich, Christopher J Cramer, and Donald G Truhlar. Universal solvation model based on solute electron density and on a continuum model of the solvent defined by the bulk dielectric constant and atomic surface tensions. *The Journal of Physical Chemistry B*, 113(18):6378–6396, 5 2009.

[33] Sebastian Kozuch and Jan M L Martin. Spin-component-scaled double hybrids: An extensive search for the best fifth-rung functionals blending dft and perturbation theory. *Journal of Computational Chemistry*, 34(27):2327–2344, 10 2013.

[34] Sebastian Kozuch and Jan M L Martin. Dsd-pbep86: in search of the best double-hybrid dft with spin-component scaled mp2 and dispersion corrections. *Phys. Chem. Chem. Phys.*, 13(45):20104–20107, 2011.

[35] Frank Neese. The orca program system. *Wiley Interdisciplinary Reviews: Computational Molecular Science*, 2(1):73–78, 1 2012.

[36] Frank Neese, Frank Wennmohs, Andreas Hansen, and Ute Becker. "efficient, approximate and parallel hartree–fock and hybrid dft calculations. a 'chain-of-spheres' algorithm for the hartree–fock exchange". *Chemical Physics*, 356 (1):98–109, 2009.

[37] Arnim Hellweg, Christof Hättig, Sebastian Höfener, and Wim Klopper. Optimized accurate auxiliary basis sets for ri-mp2 and ri-cc2 calculations for the atoms rb to rn. *Theoretical Chemistry Accounts*, 117(4):587–597, 2007.

[38] Florian Weigend. Accurate coulomb-fitting basis sets for h to rn. *Phys. Chem. Chem. Phys.*, 8(9):1057–1065, 2006.

[39] Noel M O'Boyle, Michael Banck, Craig A James, Chris Morley, Tim Vandermeersch, and Geoffrey R Hutchison. Open babel: An open chemical toolbox. *Journal of Cheminformatics*, 3(1):33, 2011.

[40] T Halgren. Merck molecular force field . i. basis, form, scope, parameterization, and performance of mmff94. *J Comput Chem*, 17:490–519, 1996.

[41] T Halgren. Merck molecular force field. ii. mmff94 van der waals and electrostatic parameters for intermolecular interactions. *J Comput Chem*, 17: 520–552, 1996.

[42] T Halgren. Merck molecular force field. iii. molecular geometries and vibrational frequencies for mmff94. *J Comput Chem*, 17:553–586, 1996.

[43] T Halgren. Merck molecular force field . v. extension of mmff94 using experimental data, additional computational data, and empirical rules. *J Comput Chem*, 17:616–641, 1996.

[44] T Halgren and R Nachbar. Merck molecular force field . iv. conformational energies and geometries for mmff94. *J Comput Chem*, 17:587–615, 1996.

[45] Carlo Adamo and Vincenzo Barone. Toward reliable density functional methods without adjustable parameters: The pbe0 model. *The Journal of Chemical Physics*, 110(13):6158–6170, 3 1999.

[46] Delano P. Chong, editor. *Recent advances in density functional methods*. Recent advances in computational chemistry. World Scientific, Singapore ; River Edge, N.J, 1995.

[47] Erik D. Hedegård, Jacob Kongsted, and Stephan P. A. Sauer. Improving the calculation of electron paramagnetic resonance hyperfine coupling tensors for d-block metals. *Physical chemistry chemical physics: PCCP*, 14(30):10669–10676, 8 2012.

[48] Frank Neese. Efficient and accurate approximations to the molecular spin-orbit coupling operator and their use in molecular g-tensor calculations. *The Journal of Chemical Physics*, 122(3):034107, 1 2005.

# Chapter 4

# An EPR Investigation of Red-Emitting CaS:Eu Phosphors: Rationalization of Local Electronic Structure

## 4.1 Introduction

Rare earth activated phosphors have long been of interest owing to their efficient luminescent properties and tuneability, making them ideal materials for a variety of applications including optoelectronics,[1] solid state lighting,[2, 3] persistent luminescence[4, 5] and scintillation devices.[6–8] Phosphors are luminescent solids consisting primarily of a host lattice and a photoluminescent activator species, typically a 3d or 4f metal which is responsible for the functional role of the material. Commonly used 4f metal activators are lanthanides, including $Eu^{2+}$/$Eu^{3+}$, $Ce^{3+}$, $Tb^{3+}$, $Gd^{3+}$, $Yb^{3+}$, $Dy^{3+}$.[9] It is the unique electronic structure of the f-block elements that is responsible for their desirable catalytic, magnetic and photophysical properties.

These phosphors can be broadly classified into two groups, based on the desired electronic transition and emission band width required; namely, broad band 5d→4f inter-electronic transitions possessing a short radiative lifetime ($\approx 1\mu$s) and sharp emission bands arising from 4f→4f intra-electronic transitions, that are Laporte forbidden, possessing a longer radiative lifetime ($\approx 1ms$).[10] The 4f subshell is relatively insensitive to the local environment, due to the screening of occupied 5s and 5p subshells which reduce the electrostatic potential of the ligand field. Therefore, the sharp f-f band transitions are usually weakly affected by an external bias, although the relative intensities can be perturbed significantly. The relative energy and degeneracy of the 5d orbitals are in contrast significantly influenced by the crystal field. Consequently, the relative energy between the 4f and 5d states, and thus the corresponding emissive wavelength, is readily tuned by the coordination environment.

After the Coulombic and crystal field effects, other important considerations include dopant concentration, particle size distribution, crystallinity and concentration of defects or impurities within the material which may compete with the lanthanide activator. As a result, the specific luminescent intensity of the broad band may be reduced via interaction with these impurities, either by competition for incident optical absorption, energy transfer processes, or quenching of luminescent emission at the desired wavelength.[11, 12] The luminescent efficiency of phosphors is also highly dependent on the relaxation properties of the activator during absorption and emission, i.e. the amount of energy lost to the lattice as heat,[9] which must be minimised to preserve the overall quantum yield.

$Eu^{2+}$-doped calcium sulphide (labelled hereafter as CaS:Eu) phosphors, have in particular recently generated considerable interest as solid state light sources for algae growth, owing to the broad band red emission near $\lambda = 645$ nm. Eu is readily found in the divalent oxidation state due to a half-filled 4f subshell and resulting stabilisation energy. Over 300 $Eu^{2+}$ compounds in different host matrices have been reported to date, where the emission colour of the 5d-4f transition has been tuned from near ultraviolet to deep red.[11] The CaS host lattice is an indirect band gap semiconductor with $E_g = 4.43$ eV possessing a NaCl-type cubic structure.[13] $Eu^{2+}$ is thought to substitute into regular octahedral $Ca^{2+}$ sites, with six $S^{2-}$ anions coordinated to the centre. Since the ionic radius of $Eu^{2+}$ is 1.17 Å (compared to 1.00 Å for $Ca^{2+}$),[14] substitution is not expected to cause a large distortion away from the high local symmetry environment.

Despite their desirable photoluminescent properties, and appreciable quantum yields in terms of their broad band emission near 645 nm, commercial CaS:Eu materials typically have a mean particle size which is too large for application as a light source, where they are typically incorporated into a film or coating. Therefore, an alternative synthetic route or appropriate post-synthesis treatment such as grinding, are necessary to reduce the mean particle size distribution. Clearly, due to the influence of particle size, morphology, and levels of defects or impurities on the photoluminescent properties of the material, the synthesis method and any subsequent treatments require careful consideration, since subtle changes in the experimental conditions can have a substantial effect on the final functional properties of the material. A number of studies have reported the presence of various intrinsic point defects in these alkaline earth sulphides,[12, 15–18] such as $S^{2-}$ vacancies, which can act as shallow electron traps ($\sim$0.26 eV) below the conduction band of CaS.[16] Other $S^{2-}$ vacancies, stabilised by $Ca^{2+}$ interstitial centres, were also evidenced by EPR and thermoluminescent measurements.[16] The specific luminescent intensity of the broad band emission near 645 nm may then potentially be reduced via interaction with these impurities.

Owing to the paramagnetic nature of the photoluminescent species, and also of the common impurities ($Mn^{2+}$, $Cr^{3+}$) and defects ($F^+$-centres) present in the material, Electron Paramagnetic Resonance (EPR) spectroscopy is a highly versatile and informative method to characterise such materials.[19] The EPR-derived spin Hamiltonian parameters of the likely defects and impurities present in the materials are well known,[12] and can be easily identified to elucidate structural information on the local environment. Furthermore, transition metals, such as $Mn^{2+}$, are highly sensitive to structure and disorder and can therefore be used as local order probes in the CaS lattice.[15] The magnetic resonance properties of lanthanides such as $Eu^{2+}$ are less well known, but their interest and utility is becoming more apparent.[4] EPR spectroscopy is therefore a useful tool to probe their identity, characterise their ground state electronic structure, relative concentrations, and local coordination environment within the system, and may provide a meaningful comparison to other characterisation methods.

The aim of this study was to provide a detailed characterisation of the important photoluminescent species in CaS:Eu phosphors following a series of synthetic steps, and post-synthetic treatments, including grinding and heating, using variable frequency EPR, XPS and photoluminescence spectroscopy. In the first instance, a series of doped CaS:Eu samples were characterised using EPR at X- and W-band frequencies to investigate the ground state electronic structure of the photoluminescent $Eu^{2+}$ species, and impurities such as $Mn^{2+}$ that may be used as structural probes, via zero field splitting (ZFS) interactions, where lower order interaction terms for S state ions are not susceptible to their local environment.

In addition to a detailed CW-EPR characterisation, supporting pulsed EPR relaxation measurements were also performed to probe dynamic properties of the localised spin states. The effect of post-synthetic treatments was rationalised based on the variation in magnetic properties. A series of undoped samples were also characterised to identify the presence of deactivating $F^+$ centre defects, and radicals related to oxidative processes upon treatment. A systematic EPR study of the cryo-milling treatment on doped CaS:Eu samples, at X-band frequency, was performed to further investigate the effect of local disorder and oxidative processes on the photoluminescent $Eu^{2+}$ species of interest. Finally, comparative XPS and photoluminescence studies were performed to underpin the primary EPR investigations, supporting findings determining the nature of local $Eu^{2+}$ sites identified, and their resultant luminescent properties after various treatments.

## 4.2 Results and Discussion

### 4.2.1 Treatment of the EPR spin Hamiltonian parameters for $Eu^{2+}$ and $Mn^{2+}$

The two isotopically abundant forms of Eu are $^{151}$Eu and $^{153}$Eu ($I = 5/2$). They are present in almost equal quantities and possess significantly different magnetic moments ($\mu/\mu_N = 3.4717$ and 1.5324 respectively[20]), which has a marked influence on the magnitude of the isotropic hyperfine component. The ground state electronic structure of $Eu^{2+}$, $^8S_{7/2}$, is paramagnetic and therefore EPR active ($S$=7/2). Since $Eu^{2+}$ has a half-filled 4f subshell, $L$=0 and therefore in the ground state $J = S$. The analysis of the $Eu^{2+}$ signal can then be treated in terms of an effective spin-only contribution, so higher level treatment of the spin system is not necessary to account for the large orbital interaction (i.e., $g \sim g_e$). Since the 4f subshell is insensitive to the crystal field environment, the $g$ and hyperfine values are not expected to vary significantly. On the other hand, $Eu^{3+}$ has a singlet $^7F_0$ ground state and is therefore EPR silent ($J$=0) as higher $J$ states are typically well separated by zero field splitting (ZFS) in non-Kramers (integer spin) systems.[21]

Although the ground state of $Eu^{2+}$ is $^8S_{7/2}$, and is therefore insensitive to crystal field effects, the $4f^65d^1$ configuration of $Eu^{2+}$ is far more susceptible to Coulombic and crystal field interactions, due to the d-orbital degeneracy which is lifted by interaction with the local ligand environment.[22] The first excited $4f^65d^1$ and $4f^7$ states ($^6P_{7/2}$) are significantly higher in energy and therefore relaxation back to the ground state is fast and not expected to contribute significantly to the EPR spectra. The magnitude of the isotropic hyperfine, $|A_{iso}|$, is reported to be approximately 91 and 40 MHz for $^{151}Eu^{2+}$ and $^{153}Eu^{2+}$ respectively,[12] with corresponding $g_{iso} = 1.9913$ for both isotopes. The spin Hamiltonian parameters for $Eu^{2+}$ and $Mn^{2+}$ centres observed in the EPR spectra of CaS:$Eu^{2+}$ samples reported here were calculated according to a spin Hamiltonian of the form:

$$\hat{H} = g\mu_B\vec{B}\cdot\vec{S} + A \cdot \vec{S} \cdot \vec{I} + \hat{H}_{ZFS} \tag{4.1}$$

where $g$ and $A$ are the $g$ and $A$ tensors, $\mu_B$ is the Bohr magneton, $\vec{B}$ is the external magnetic field and $\vec{S}$, $\vec{I}$ are the electron and nuclear spin operators, respectively. The $g$- and $A$ tensors were to first order assumed to be isotropic due to the cubic symmetry reasonable for S state ions such as $Eu^{2+}$.[21] In fact, non-isotropic $g$ tensor values are rarely observed within experimental error for S ground state ions.[23] The ZFS interaction is therefore a much more useful indicator of local site symmetry. For the other observed centres, not associated with transition or lanthanide metals, the spin Hamiltonian in equation 4.1 was used in the absence of the zero-field splitting (ZFS) term.

The line shape of high spin $\mathrm{Mn}^{2+}$ ($S$=5/2) was indicative of cubic symmetry fine structure, as has been observed previously,[15] therefore the upper limit for the magnitude for the ZFS Hamiltonian term was estimated, which was poorly resolved within the experimentally observed line width. For the high spin systems ($\mathrm{Eu}^{2+}$, $\mathrm{Mn}^{2+}$) , the ZFS Hamiltonian, $\hat{H}_{ZFS}$, was characterised in terms of extended Stevens operators of fourth- ($S \geq 2$) and sixth-order ($S \geq 3$), as described by Abragam and Bleaney.[24] The second-order operators, which relate to the more traditional $D$ and $E$ terms, vanish for cubic symmetry giving a simpler spin Hamiltonian of the following form, related to a four-fold axis, equation 4.2:

$$\hat{H}_{ZFS} = \frac{b_4}{60}\left(O_4^0 + 5O_4^4\right) + \frac{b_6}{1260}(O_6^0 - 21O_6^4) \tag{4.2}$$

where $O_k^q$ are the extended spin operators,[24] and $b_k^q$ are ZFS parameters for the fourth- and sixth- order terms. The ZFS Hamiltonian for cubic $\mathrm{Mn}^{2+}$ site is identical to the first part of equation 4.2, considering only the 4th order terms. The orientation of the principle axes of the higher order ZFS terms, which are anisotropic and therefore angularly dependent, were assumed to be coincident with the molecular axes.

For lower symmetry sites bearing high spin systems, the ZFS Hamiltonian also includes second order ($k = 2$) terms, relating to two-fold axis symmetry operators as given in equation 4.3, which are related to the traditional ZFS terms $D$ and $E$ (equations 4.4 and 4.5):

$$\hat{H}_{ZFS} = \frac{1}{3}\left(b_2^0 O_2^0 + b_2^2 O_2^2\right) + \frac{1}{60}\left(b_4^0 O_4^0 + b_4^2 O_4^2 + b_4^2 O_4^4\right) + \frac{1}{1260}(b_6^0 O_6^0 + b_6^2 O_6^2 + b_6^4 O_6^4) \tag{4.3}$$

$$D = b_2^0 \tag{4.4}$$

$$3E = b_2^2 \tag{4.5}$$

Typically, the second-order terms are much larger in magnitude and therefore the fourth and sixth order terms become less significant. In order to extract and resolve all ZFS parameters, it becomes necessary to perform single-crystal studies as a function of orientation, which has not been reported. The magnitude of the sixth order terms have thus been neglected in the simulation approach. Moreover, the relative sign of the ZFS terms is difficult to determine above 77 K and the parameters reported are therefore magnitudes rather than absolute values. In most cases, the traditional inhomogeneous line widths from distributions in $g$, $A$ or $D$ were acceptable to characterise line shapes in the spectra. However, for the cubic $Eu^{2+}$ and $Mn^{2+}$ sites, characterisation of line strains in the spectra were expressed in terms of a homogeneous peak-to-peak linewidth, and a Gaussian distribution of the $b_4$ terms which are largest in magnitude, since the traditional strains of $g$, $A$ or $D$ were inappropriate under the proposed conditions. It is expected that small perturbations from cubic symmetry would have a dominating effect on the $b_4$ term, unless the distortions were severe enough to reintroduce significant $b_2$ terms, in which case the cubic ZFS Hamiltonian would also be inappropriate. Since the observed fine structure is relatively weakly resolved, typical for a powder spectrum, it is challenging to separate the distribution of individual $b_4$ terms without appropriate single crystal measurements. A Gaussian distribution with the same FWHM was therefore assumed in both $b_4^0$ and $b_4^4$, to further simplify the model.

For the undoped samples, where multiple cubic $Mn^{2+}$ sites were observed, the fine structure is completely unresolved and therefore the line shape was approximated with a homogeneous Lorentzian line shape. This was suitable to extract the $g_{iso}$ and $A_{iso}$ values used to distinguish between the hosting phases.

### 4.2.2 CW X-band (9 GHz) EPR spectra of commercial CaS:Eu phosphors

The first series of samples (hereafter labelled CaSEu_1,2,3) analysed in this study were based on a commercially available material, investigated in its native as-received form (CaSEu_1), and after further treatments including cryo-milling (CaSEu_2), and thermal treatment in air (CaSEu_3). The EPR measurements were undertaken in order to identify the presence of any point defects, to monitor the changes in local environment of the structural paramagnetic probes ($Mn^{2+}$) and most importantly to analyse the profile of the $Eu^{2+}$ signals. Due to the number of defective centres, Kröger-Vink notation will be defined and referred to for the distinct sites characterised in the studies. The resulting low temperature CW X-band (9 GHz) EPR spectra are shown in Figure 4.1. An additional figure presenting the separated $Mn^{2+}$ and $Eu^{2+}$ simulations for CaSEu_2 and CaSEu_3 can also be found in Figure 4.2.

The spectra represent a composite and overlapping pattern from multiple paramagnetic centres. In the native sample, CaSEu_1 (Figure 4.1a), the two prominent

$Eu^{2+}$ isotopes are clearly visible, with hyperfine values of $|A_{iso}|$ = 91 MHz and $|A_{iso}|$= 40.2 MHz for $^{151}Eu^{2+}$ and $^{153}Eu^{2+}$ respectively, and with $g_{iso}$ = 1.9912 in both cases. The extracted parameters are almost identical to those reported previously in the literature,[15] and are indicative of $Eu^{2+}$ centres in a nearly cubic site, with only a small degree of local symmetry distortion. This is consistent with the proposal of a well isolated $Eu^{2+}$ ion, substitutionally exchanged for $Ca^{2+}$ in the cubic unit cell, in Kröger-Vink notation $\mathrm{Eu}_{\mathrm{Ca}}^{x}$. The intrinsic line width is relatively narrow, and hence the phase memory time, $T_m$, is expected to be slow, on the order of $\mu$s as evidenced by pulsed EPR measurements (*vide supra*, Figure 4.5). There is no clear evidence of any $Mn^{2+}$ signal initially present in the native sample, in contrast to previous reports.[12, 15] A magnified view of the low field $|m_I|$ =5/2 signal is provided in Appendix 3; Figure 1 for reference.

By comparison, the EPR spectra of the treated samples CaSEu_2 and CaSEu_3 (Figure 4.1b,c) show additional features that can be readily assigned to a high spin $Mn^{2+}$ centre ($S$=5/2, $I$=5/2), denoted $\mathrm{Mn}_{\mathrm{Ca}}^{x}$. This $Mn^{2+}$ signal is characterised by $g_{iso}$ = 2.0021 and $A_{iso}$ = 234 MHz, which is consistent with those expected for $Mn^{2+}$ located in the CaS lattice at a regular octahedral substitutional $Ca^{2+}$ site.[12] The fact that this signal is not observable in the ‘as received’ native sample, CaSEu_1 (Figure 4.1a)), indicates a broadening of the intrinsic line width, and reduction in the $Eu^{2+}$ signal intensity following cryo-milling due to oxidation, which prevented the observation of the weaker $Mn^{2+}$ signals. Oxidative processes, following cryo-milling, have been indicated in EPR measurements of undoped samples, the systematic cryo-milling study, and luminescence measurements *vide supra*. It is possible that some trace contamination from the milling process could also contribute, but this is not expected to be the sole reason due to the considerable concentration. Fine structure arising from the spin-spin interactions of $Mn^{2+}$ ($S$=5/2) is noticeable (Figure 4.2), indicating some disorder around the $\mathrm{Mn}_{\mathrm{Ca}}^{x}$ centre due to vacancies and dislocations.[12] The accumulation of these effects are expected to be responsible for the decreased luminescence observed from the treated sample.

A noticeable difference in spectral line width is also observed for the $\mathrm{Mn}_{\mathrm{Ca}}^{x}$ centres after thermal treatment in air, namely for sample CaSEu_3 (Figure 4.1c). Since inhomogeneous broadening due to the suppressed fine structure does not directly broaden the central ($|\Delta m_s|$ = +1/2 $\leftrightarrow$ -1/2) transition, due to the non-degenerate interaction of the Kramers doublets ($|m_s|$ =1/2, 3/2, 5/2), this is instead expected to correspond to an apparent decrease in relaxation time, $T_2$, and therefore a change in local environment that broadens the intrinsic line width,

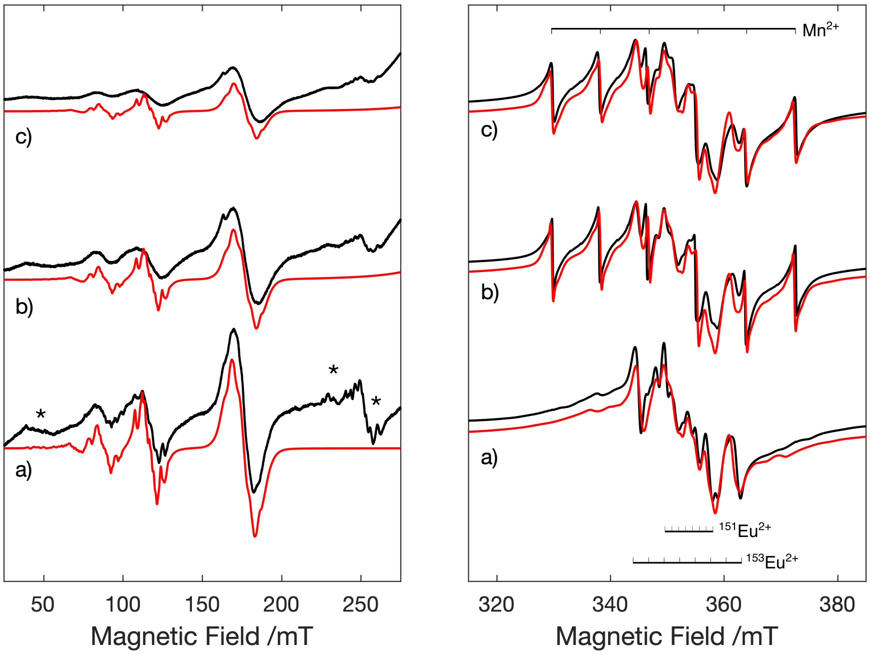

**Figure 4.1:** CW X-band (9 GHz) EPR spectra (120 K) of a) CaSEu_1, b) CaSEu_2 and c) CaSEu_3 samples. *Left:* low field measurement indicating the formally forbidden fine structure transitions. The asterisks indicate fine structure features not reproduced in the simulation of the cubic site Eu$^x_{\text{Ca}}$ species, and instead relate to the low symmetry Eu$^x_{\text{surface}}$ species (see Appendix 3; Figure 5). *Right:* high resolution spectra of the prominent features centred near $g_e$, including the $^{151,153}$Eu$^{2+}$ and Mn$^{2+}$ hyperfine patterns.

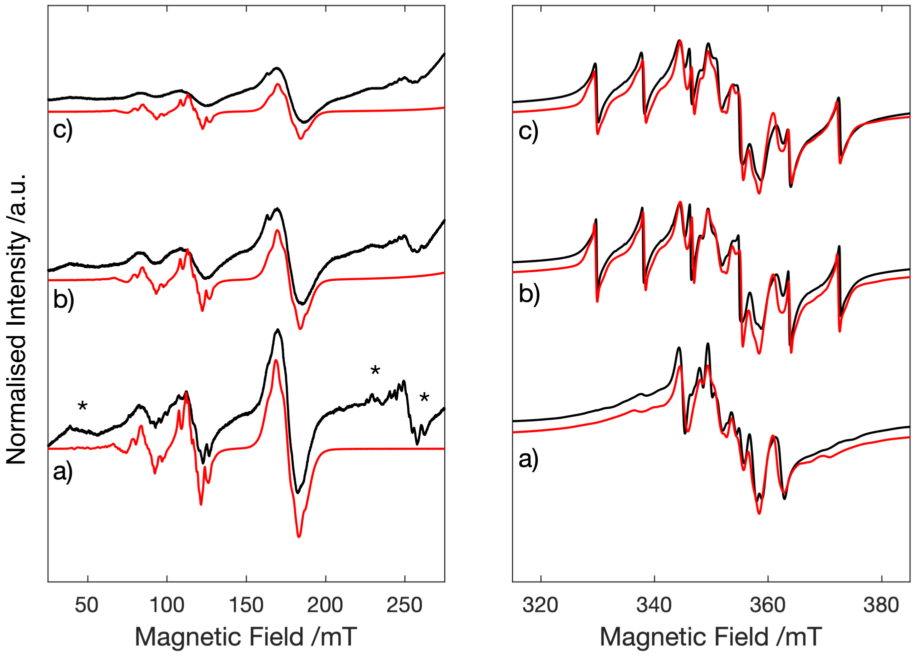

**Figure 4.2:** Deconvoluted simulations of CaSEu_2 and CaSEu_3 X-band EPR spectra, presented in Figure 4.1, containing two distinct species. *Black:* experimental trace; *Red:* simulation traces. The lower two red traces are the deconvoluted simulations, and the top red trace is the total simulation envelope, taking into account relative weights of the species.

*vide infra.* This will be discussed further *vide supra.* No other notable features are observed within this region, such as the expected $V_S^\bullet$ centres, metal impurities or additional sulphur radical species.

In the low magnetic field region of the EPR spectrum (Figure 4.1), another complex signal is observed for the samples which has not been previously reported in the literature, which corresponds to $Eu^{2+}$ fine structures. The simulated fine structure pattern is related to the cubic symmetry site with fourth and sixth order ZFS terms. The fine structure patterns that do not appear in the simulation indicate the observation of another $Eu^{2+}$ environment occupying a lower symmetry site, which was resolved by comparison with the higher frequency W-band EPR measurement discussed later. The ZFS parameter values for this species are reported in Table 4.1. The relative abundance of this second $Eu^{2+}$ environment compared to the main $Eu_{Ca}^{x}$ signal observed at centre field, 335 mT, is considerably smaller ( $<$ 1:10), and may be responsible for part of the unresolved features to low and high field of the isolated $Eu_{Ca}^{x}$ hyperfine pattern, where the corresponding simulation of ${Eu_{surface}}^{x}$ was not included.

### 4.2.3 CW W-band (95 GHz) spectra of commercial and prepared CaS:Eu phosphors

In order to improve the resolution of the comparatively larger ZFS arising from this second $Eu^{2+}$ species in a lower symmetry environment, CW W-band (95 GHz) EPR spectra were recorded (Figure 4.3). When the ZFS parameters are comparable to or larger than the microwave quanta, complex EPR spectra are observed which can be very difficult to accurately rationalise due to the presence of formally forbidden transitions.[25] When $D$ (or higher order terms) $\ll h\nu$, all allowed transitions are possible and a fine structure pattern is observed from transitions between the respective Kramers doublets. Simulation of the resulting spectrum readily allows simulation of the ZFS parameters thus providing an informative view of the symmetry environment. A number of transitions are observed in the low field region of the X-band spectrum. Higher frequency measurements aid in resolving this structure and can also improve field resolution to assist in deconvolving the signals appearing at similar $g$ values. A comparison of the W-band CW EPR spectra for the native commercial sample, CaSEu_1, and another sample prepared by a solid-state reduction synthesis method, labelled CaSEu_SSR, are shown in Figure 4.3. The signal intensities have been normalised for ease of comparison. A further magnified comparison of the experimental and simulated hyperfine pattern can be found in Appendix 3, Figure 2.

With respect to the CaSEu_SSR sample, the hyperfine structure associated with the high symmetry $\mathrm{Eu}_{\mathrm{Ca}}^{x}$ environment, which is clearly visible in CaSEu_1 (Figure 4.3, left hand side), is now barely perceptible, buried within the most intense central peak pertaining to the $m_S$ = -1/2 ↔ +1/2 transition. The resolution of this signal is obscured by the dominant fine structure in the spectrum, which is also observed in the X-band spectra for these samples (see Appendix 3; Figures 3 and 4 for the X-band spectra of CaSEu_SSR), with estimated ZFS values reported in Table 4.1. This additional structure is a clear indication of the second low symmetry $\mathrm{Eu}^{2+}$ environment suggested earlier, denoted as $\mathrm{Eu}_{\mathrm{surface}}^{x}$. In the commercial sample, CaSEu_1, very weak shoulders to low and high field of the central resonance indicates that this lower symmetry environment is also present here, albeit in much lower concentration. By simulation of the $\mathrm{Eu}_{\mathrm{surface}}^{x}$ species at X-band, using the spin Hamiltonian parameters obtained from fitting at W-band, the forbidden fine structure transitions in the low field region not reproduced by the $\mathrm{Eu}_{\mathrm{Ca}}^{x}$ model (Figure 4.1, *left*, denoted by asterisks) are now simulated reasonably well (see Appendix 3: Figure 5). Finally, the $\mathrm{Mn}^{2+}$ hyperfine pattern which was not observed in CaSEu_1, is now resolved from the $\mathrm{Eu}_{\mathrm{Ca}}^{x}$ signal at higher frequency, indicating the presence of the high symmetry octahedral $\mathrm{Mn}^{2+}$ species $\mathrm{Mn}_{\mathrm{Ca}}^{x}$ (1).

### 4.2.4 CW X-band EPR of prepared undoped CaS phosphors

In order to detect the presence of any underlying defect signals within the material, which are not visible owing to the intense Eu signals, a series of undoped CaS samples were also analysed. In the native undoped sample, the presence of multiple $\mathrm{S}_x\mathrm{O}_y^{\,-}$ type radicals can be clearly detected (Figure 4.4a). These species are presumably formed as by-products from the partial oxidation of CaS → $\mathrm{CaSO}_4$. Further analysis of the EPR spectra reveals the presence of two distinct sulphur based radicals, specifically assigned to $\mathrm{S_2O^-}$ and $\mathrm{S_2O_2^-}$ centres (see Appendix 3: Figure 7 for details of the simulations).[26] The spin Hamiltonian parameters (Table 1) for these two sulphur radicals are slightly different compared to those reported previously in CaS powders,[15] and this may be an artefact of the different synthesis methods employed. No sharp isotropic signal due to any $\mathrm{V}_{\mathrm{S}}^{\bullet}$ centres were observed, which could indicate that such species are stabilised by cationic $\mathrm{Eu}^{3+}$ defects, $\mathrm{Eu}_{\mathrm{Ca}}^{\bullet}$ , as suggested in previous EPR studies.[15]

After heating this sample in an $\mathrm{N_2/H_2}$ atmosphere, a complete loss of signals

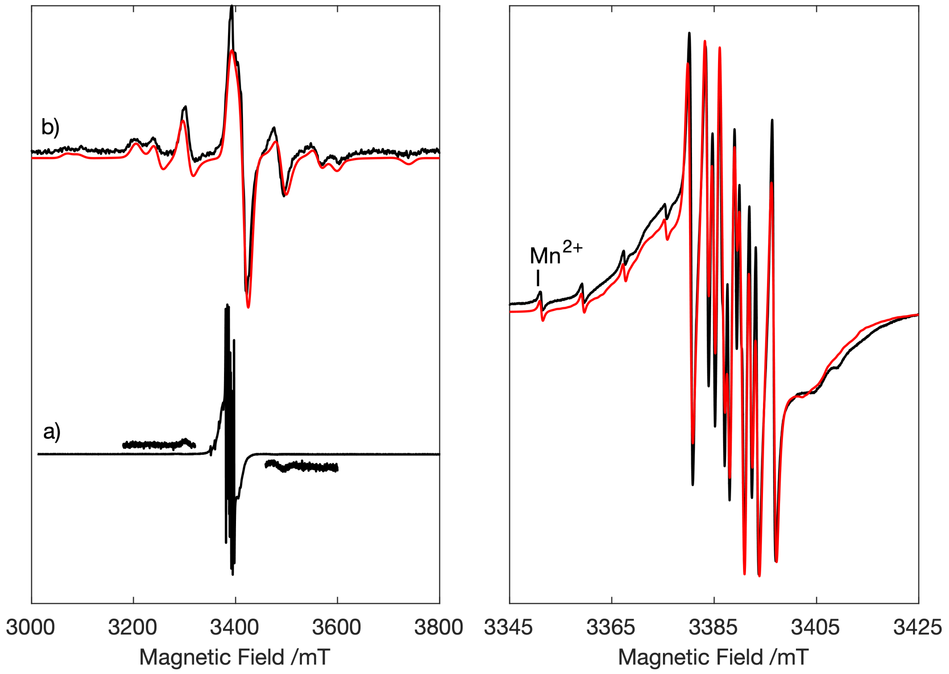

**Figure 4.3:** *Left:* Comparative CW W-band (95 GHz) EPR spectra (300K) of a) the native commercial sample CaSEu_1, and b) sample prepared by solid-state reduction synthesis method, labelled CaSEu_SSR. *Right:* High resolution spectrum of the native CaSEu_1 sample in a). *Black:* experimental spectrum; *Red:* simulated spectrum.

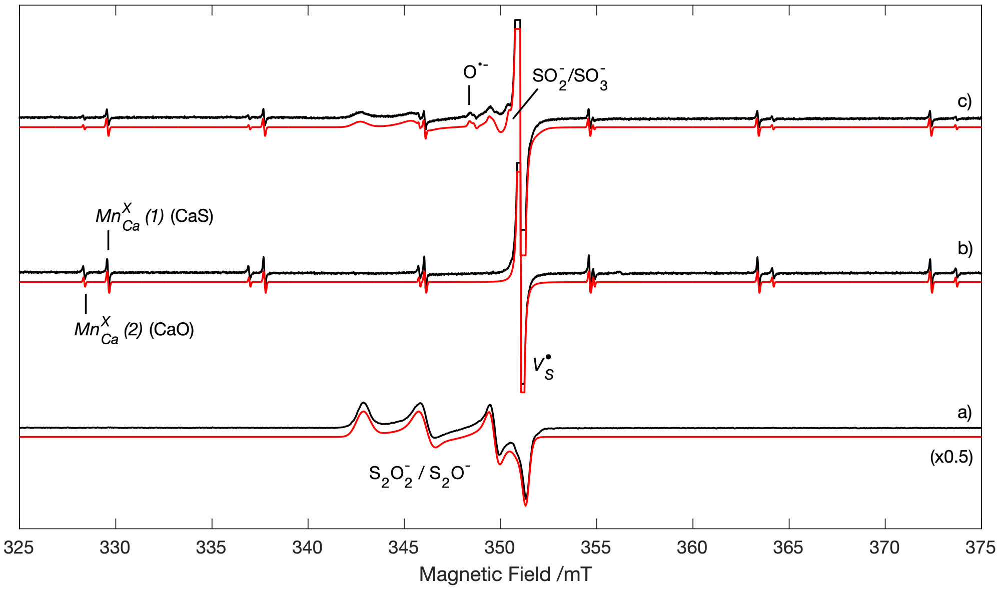

**Figure 4.4:** CW X-band (9 GHz) EPR spectra (120K) of a) undoped CaS sample (see Appendix 3: Figure 7 for simulation breakdown), and the same sample after treatment including b) heated to 973 K in $N_2/H_2$, and c) cryo-milled sample from b) (see Appendix 3; Figure 7 for simulation breakdown). The $V_S^\bullet$ signal in b) and c) is clipped for better resolution of weak signals. *Black:* experimental spectrum; *Red:* total simulated spectrum.

associated with the $S_xO_y^-$ radicals is observed, indicating a reduction of $S_xO_y^-$ to $S_x^-$ species in the highly reducing atmosphere (Figure 4.4b). Simultaneously, two new signals become visible in the spectrum, including a sharp isotropic signal which can be easily attributed to an $F^+$ centre, $V_S^\bullet$ , as well as the clear features arising from two distinct $Mn^{2+}$ species in an approximate 1:2 intensity ratio. In this case, a simpler line broadening model with a homogeneous Lorentzian linewidth was sufficient to reproduce the Mn signals. The hyperfine values for these $Mn_{Ca}^x$ species (${}^{Mn(1)}A_{iso}$ = 239.6 MHz and ${}^{Mn(2)}A_{iso}$ = 254.5 MHz) are consistent with the known values reported for $Mn^{2+}$ embedded within a CaS and CaO phase respectively.[12, 27] This indicates the presence of a CaO phase in the sample, formed through oxidation of the sample during synthesis. The slightly larger $A_{iso}$ value for the $Mn_{Ca}^x$ (2) centre is expected to result from the increased covalency in CaO due to the crystal field effect of $O^{2-}$ *vs.* $S^{2-}$. No fine structure is resolved for $Mn^{2+}$ in this case, around the two isolated $Mn^{2+}$ environments, $Mn_{Ca}^x$ (1) and $Mn_{Ca}^x$ (2), and the 6-line pattern is due to a hyperfine interaction with the nuclear dipole of $Mn^{2+}$ ($I$=5/2). It is expected that $Mn^{2+}$ would occupy similar cubic sites to $Eu^{2+}$ in the CaS lattice,[28] $Mn_{Ca}^x$ (1), and also in the CaO phase,[27] $Mn_{Ca}^x$ (2), i.e. in octahedral substitutional sites replacing $Ca^{2+}$. Therefore, these different $Mn^{2+}$ signals may indirectly evidence the possibility of two $Eu^{2+}$ environments, in CaS and CaO phases, although their spin Hamiltonian parameters are unlikely to vary significantly to be resolved from one another due to screening of the 4f ground state electrons.

Finally, after annealing and cryo-milling of the sample, little additional change can be seen in the spectrum (Figure 4.4c). A weak signal associated with the $S_xO_y^-$ species is visible, indicating that mechanical stress, induced by cryo-milling, can readily oxidise some of the diamagnetic sulphur radicals into paramagnetic sulphur-oxygen based radicals. Another weak signal also appears to the low field of the $V_S^\bullet$ signal, as discussed below.

The extracted spin Hamiltonian parameters for distinct species in the native undoped sample, CaS_1, and after heating at 500°C, may be compared to the complex spectrum observed in CaS_3. Most of the weakly resolved features, at low field of the $V_S^\bullet$ centre, may now be identified as a mixture of $S_2O^-$ and $S_2O_2{}^-$ species, after partial oxidation of the buried diamagnetic $S^{2-}$ centres indicated vide infra (see Appendix 3; Figure 6). In addition, another unidentified species is also present at a field value of $B_0$ = 334 mT. The species appeared to be characterised by an orthorhombic signal, with the $g$ values of 2.0167, 2.0184 and 2.0025, and can be tentatively assigned to a trapped hole centre, generated by heat treatment.[15]

It is reported that these defects can be stabilised by cations such as $Na^+$ which could be present as impurities, but cannot be detected directly using CW EPR.[15]

| Species | | $b_2^0$ | $b_2^2$ | $b_4^0$ | $b_4^2$ | $b_4^4$ | $b_6^0$ | $b_6^2$ | $b_6^4$ |
|---|---|---|---|---|---|---|---|---|---|
| $\mathrm{Eu}_{\mathrm{Ca}}^{x}$ | Isolated (CaS)$^{\mathrm{c}}$ | - | - | 47.1 | - | 235.3 | 16.0 | - | -336.0$^{\mathrm{a}}$ |
| $\mathrm{Eu}_{\mathrm{surface}}^{x}$ | Surface (‘EuO’) | 2442.7 | 416.3 | 37.8 | -184.4$^{\mathrm{a}}$ | 51.4 | N.R.$^{\mathrm{b}}$ | N.R.$^{\mathrm{b}}$ | N.R.$^{\mathrm{b}}$ |
| $\mathrm{Mn}_{\mathrm{Ca}}^{x}$ (1) | Isolated | - | - | 12.6 | - | 63.0 | - | - | - |

**Table 4.1:** Experimental ZFS spin Hamiltonian parameters for $\mathrm{Eu}^{2+}$ and $\mathrm{Mn}^{2+}$ species identified in the CaS:Eu samples.All $b_k^q$ parameters were determined by least-squares fitting procedures and are reported in MHz. The absolute sign of the parameters was not determined and therefore the magnitude of values is reported. The additional spin Hamiltonian parameters used in the simulation are given in Table 2. $^{\mathrm{a)}}$ The negative sign denotes an opposite relative sign to the additional ZFS parameters, not an absolute sign. $^{\mathrm{b)}}$ Not resolved due to the magnitude of the $b_2$ and $b_4$ terms. $^{\mathrm{c)}}$ These values were obtained by simultaneous fitting of the X- and W-band spectra.

| Species | | $g_1^a$ | $g_2^a$ | $g_3^a$ | $\lvert A_{iso}\rvert^b$ |
|---|---|---|---|---|---|
| $\mathrm{Eu}_{\mathrm{Ca}}^{x}$ (CaS)$^{\mathrm{c}}$ | Isolated | 1.9912 | 1.9912 | 1.9912 | 40.2 |
| $\mathrm{Eu}_{\mathrm{surface}}^{x}$ | Surface (‘EuO’) | 1.9921 | 1.9921 | 1.9921 | 41.0$^{\mathrm{d}}$ |
| $\mathrm{Mn}_{\mathrm{Ca}}^{x}$ (1) | CaS | 2.0021 | 2.0021 | 2.0021 | 239.6 |
| $\mathrm{Mn}_{\mathrm{Ca}}^{x}$ (2) | CaO | 2.0015 | 2.0015 | 2.0015 | 254.5 |
| $\mathrm{V}_{\mathrm{S}}^{\bullet}$ | | 2.0031 | 2.0031 | 2.0031 | - |
| $S_xO_y^-$ radicals | $S_2O^-$ | 2.0035 | 2.0129 | 2.0328 | - |
| | $S_2O_2^-$ | 2.0045 | 2.0334 | 2.0529 | - |
| | $SO_2^-$ | 2.0030 | 2.0030 | 2.0125 | - |
| | $SO_3^-$ | 2.0049 | 2.0065 | 2.0063 | - |

**Table 4.2:** Experimental $g$ and $A$ spin Hamiltonian parameters for the paramagnetic species observed in doped and undoped CaS samples. All $A$ values reported in MHz; $^{\mathrm{a)}}$ ±0.003; $^{\mathrm{b)}}$ ±5 MHz; For $\mathrm{Eu}^{2+}$, the hyperfine values are quoted for major isotope $^{151}\mathrm{Eu}$. Hyperfine values for $^{153}\mathrm{Eu}$ correspond to $^{151\mathrm{Eu}}A$ multiplied by the ratio of nuclear $g$ factors $g_n$ for the isotopes ~2.26 giving 91 MHz; $^{\mathrm{c)}}$ These values were obtained by simultaneous fitting of the X- and W-band spectra; $^{\mathrm{d)}}$ Hyperfine structure not resolved, assumed to be the same as for isolated species.

### 4.2.5 Pulsed relaxation measurements of $\mathbf{Eu_{surface}}^x$ and $\mathbf{Mn_{Ca}}^x$

For the CW EPR investigations reported *vide infra*, variation in the spin relaxation properties with sample treatments were indirectly attributed by comparison of the peak-to-peak line widths. Pulsed EPR experiments facilitate direct measurement of the $T_1$ and $T_2$ relaxation times and therefore provide a direct means of comparison for relaxation effects to complement the reported findings. Pulsed EPR measurements were initially performed on the CaSEu_SSR sample in order to determine estimates for the relaxation times of the $Eu^{2+}$ species. Relaxation measurements recorded at two field positions ($B_0$ = 252.1 and 350 mT, shown by the arrow, *top*) are presented in Figure 4.5 by means of an example.

It was necessary to fit both the $T_1$ and $T_M$ relaxation profiles with a bi-exponential function in order to extract the rate constants (and linear combination coefficients), of the form:

$$f(x) = c_0 + c_1 \cdot e^{-k_1 x} + c_2 \cdot e^{-k_2 x} \tag{4.6}$$

where $k_i$ is the rate constant (which is equivalent to the inverse of the relaxation times) and $c_i$ are the linear combination coefficients. The fact that a double exponent was necessary could arise from multiple sources, complicated by the superposition of two species: i) possible contributions of both $Eu^{2+}$ sites, $Eu_{Ca}^x$ and $Eu_{surface}^x$, which were identified using CW EPR at W-band frequency; ii) spectral diffusion rate due to nuclear spin flip-flops and molecular motion or rotation. Given that the relative concentration of $Eu_{surface}^x$ is much larger compared to $Eu_{Ca}^x$, it is expected to dominate the echo response. Additional measurements were also performed at a different field position, $B_0$ = 252.1 mT, which corresponds purely to the $Eu_{surface}^x$ site ($|\Delta m_S| = 1/2 \leftrightarrow 3/2$), also possessed bi-exponential character indicating a spectral diffusion contribution was likely. Considering the second exponent time constant is also substantially smaller than the first in both cases (6.68% for $T_1$; 15.95% for $T_M$), the smaller values can be tentatively attributed to spectral diffusion, and the larger values to the spin-lattice and spin-spin relaxation processes for $Eu_{surface}^x$. The fitted parameters are provided in Tables 4.3 and 4.4.

In addition to the comparison of relaxation times for the $|\Delta m_S| = 1/2 \leftrightarrow 3/2$ and $|\Delta m_S| = 1/2 \leftrightarrow$ -1/2 transitions for $Eu_{surface}^x$, a comparison of the relaxation times for $Mn_{Ca}^x$ at $T$ = 10K was performed for the CaSEu_2 and CaSEu_3 samples; after cryo-milling treatment and subsequent heat treatment in $N_2/H_2$, respectively. It was determined that, upon heating treatment, a broadening in the EPR linewidth for the $\mathrm{Mn}_{\mathrm{Ca}}^{x}$ signal was observed, that was attributed to a change in the $T_2$ spin relaxation time (which is typically the dominant relaxation contribution). Pulsed EPR therefore directly allows the relative changes in $T_1$ and $T_2$ to be distinguished. Again, it was necessary to fit both the $T_1$ and $T_M$ relaxation profiles with a bi-exponential function *vide infra* to obtain a reasonable fit of the echo decay and inversion recovery experiments, indicating the possible contributions of spectral diffusion and/ or spin packets from $Eu_{surface}^{x}$ or $\mathrm{Eu}_{\mathrm{Ca}}^{x}$ that contribute to the echo intensity at the measured field positions. The experimental data and fitted curves are shown in Figure 4.6; and the best-fit rate constants $k_i$ and linear combination coefficients $c_i$ in Tables 4.5 and 4.6, respectively. It is clear from the FSED-EPR spectra that the $\mathrm{Mn}_{\mathrm{Ca}}^{x}$ signal cannot be completely separated from the broad $Eu_{surface}^{x}$ species, which may therefore contribute to the relaxation profile of the detected echo. Given the narrow intrinsic line width for the $\mathrm{Mn}_{\mathrm{Ca}}^{x}$ signal, this is expected to be the dominant contribution to the echo growth/ decay at the measured field positions, despite the superimposed $Eu_{surface}^{x}$ and $\mathrm{Eu}_{\mathrm{Ca}}^{x}$ species.

Starting with the fitted $T_1$ parameters, the calculated curves are slightly distinguishable from the experimental traces that indicates another potential contribution to the response, however, this was not included in the calculation as the separation of contributions with similar rate constants is not clear. Concerning the reported values in Table 4.5 the 'fast' component is again different by an order of magnitude to the 'slow' component. Considering a reasonable estimate of the $T_1$ time constant was measured for $Eu_{surface}^{x}$ (Table 4.3), which is of the same order of magnitude as the 'slow' component, the $T_{1f}$ value is again attributed to spectral diffusion contributions. The $T_{1s}$ values reported here are also significantly slower than those for $Eu_{surface}^{x}$ reported *vide infra* in Table 4.3. This component is thus attributed to the $\mathrm{Mn}_{\mathrm{Ca}}^{x}$ site. Upon treatment of the sample in a reducing atmosphere (CaSEu_3), the fitted $T_1$ value increases from approximately $224.4\mu$s to $301.6$ $\mu$s, which is consistent with the proposed increase in disorder around the substitutional $\mathrm{Mn}_{\mathrm{Ca}}^{x}$ position. With less efficient pathways for the coupling of the spin to the phonon modes of the lattice, the induced decay of the magnetisation will thus evolve more slowly. It has been shown in other studies[12] that heating treatment does not facilitate restoration of local order about these paramagnetic sites.

The $T_M$ relaxation profiles are also presented in Figure 4.6 for comparison. In this case, a bi-exponential function provided an excellent fit with the experimental decay curves for the respective CaSEu_2 and CaSEu_3 samples. The 'fast' component is also an order of magnitude smaller than the 'slow' component and this is therefore attributed to the spectral diffusion, as in the previous instances. The 'slow' component, $T_{2s}$, is therefore attributed to the $\mathrm{Mn}_{\mathrm{Ca}}^{x}$ species. Upon heat treatment, a small increase in the $T_{2s}$ value is actually observed, which would account for a decrease in the efficiency of the spin-spin relaxation pathways (and therefore longer relaxation time). Indeed, it has been shown that during heating treatment (which partly restores the luminescent intensity of the material) the diffusion of bulk $\mathrm{F}^{+}$-centres occurs to the surface, where they can rapidly capture oxygen (or in this case other gases). [12] This finding is therefore attributed to a decreased local spin concentration relative to the bulk $\mathrm{F}^{+}$-centre defects. Additionally, the partial reduction of oxidised $\mathrm{Eu}_{\mathrm{Ca}}^{x}$ upon grinding is able to occur, however, these sites have been shown to be well isolated in the bulk, and their contribution is therefore expected to be minor.

To conclude, an apparent increase in the $T_1$ and $T_M$ times was observed for the $\mathrm{Mn}_{\mathrm{Ca}}^{x}$ site upon heating treatment, contrary to the observed increase in line width. This observed broadening is instead attributed to an inhomogeneous contribution. Of the most likely influences, due to a distribution in $g$, $A$, or the distribution of the unresolved $b_4$ term, which was observed in both samples (Figure 4.2). A broadening was also noted in the central line, pertaining to the $\Delta m_s = 1/2 \leftrightarrow m_s = -1/2$ transition, which remains unperturbed by effects of the ZFS terms for Kramers ions. One of the former cases is therefore considered responsible. Distributions in the $g$ and $A$ tensor values are related to micro-structural variations in the bond lengths, orientations and local environment of the ensemble of spins within the polycrystalline samples. Considering the cubic nature of the CaS host lattice, strain effects also represent an indicator of disorder within the local structure. Both $\mathrm{Mn}_{\mathrm{Ca}}^{x}$ and $\mathrm{Eu}_{\mathrm{Ca}}^{x}$ are effective spin-only ions ($L = 0$) with isotropic $g \approx g_{free}$ and $A \approx a_{iso}$ ($T = 0$). With a quenching of the orbital angular momentum and symmetric nature of the line shapes, it is believed more likely to result from a distribution in $A$. The isotropic hyperfine component, for coupling to the respective Mn ($I = 5/2$) and Eu ($I = 7/2$) ions, is proportional to the unpaired spin density and represents the effective $s$-character of the wave function, *i.e.* the narrow statistical distribution of the localised states.

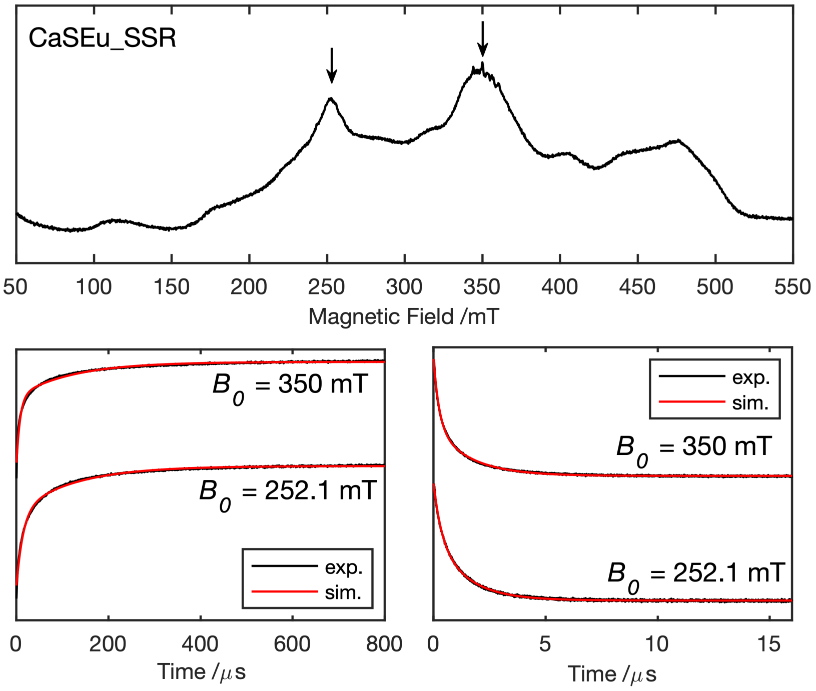

**Figure 4.5:** Pulsed EPR measurements of CaSEu_SSR, recorded at 10K and X-band microwave frequency. *Top:* field-swept echo decay (FSED-EPR) spectrum of CaSEu_SSR. The arrows indicate field positions at which relaxation measurements were performed; *Bottom left:* Inversion recovery experiments for the determination of $T_1$; *Bottom right:* Hahn echo decay experiments for the determination of $T_M$. *Black:* experimental spectra; *Red:* simulated spectra.

| $B_0$ | $c_0$ | $T_{1s}$ | $c_1$ | $T_{1f}$ | $c_2$ |
|---|---|---|---|---|---|
| 252.1 | 0.981 | 122.4 | -0.447 | 14.39 | -0.772 |
| 350 | 0.982 | 120.7 | -0.336 | 8.066 | -0.665 |

**Table 4.3:** Best fit parameters from the least-squares fitting routine for $T_1$ measurements, using a bi-exponential function, for CaSEu_SSR at $T = 10$ K. field units are in mT; all time constants are reporting in $\mu$s. '$f$' and '$s$' subscripts denote *fast* and *slow* for distinction.

| $B_0$ | $c_0$ | $T_{2s}$ | $c_1$ | $T_{2f}$ | $c_2$ |
|---|---|---|---|---|---|
| 252.1 | 0.0639 | 1.408 | 0.523 | 0.3486 | 0.420 |
| 350 | 0.0593 | 1.586 | 0.401 | 0.2530 | 0.541 |

**Table 4.4:** Best fit parameters from the least-squares fitting routine for $T_2$ measurements, using a bi-exponential function, for CaSEu_SSR at $T = 10$ K. field units are in mT; all time constants are reporting in $\mu$s. '$f$' and '$s$' subscripts denote *fast* and *slow* for distinction.

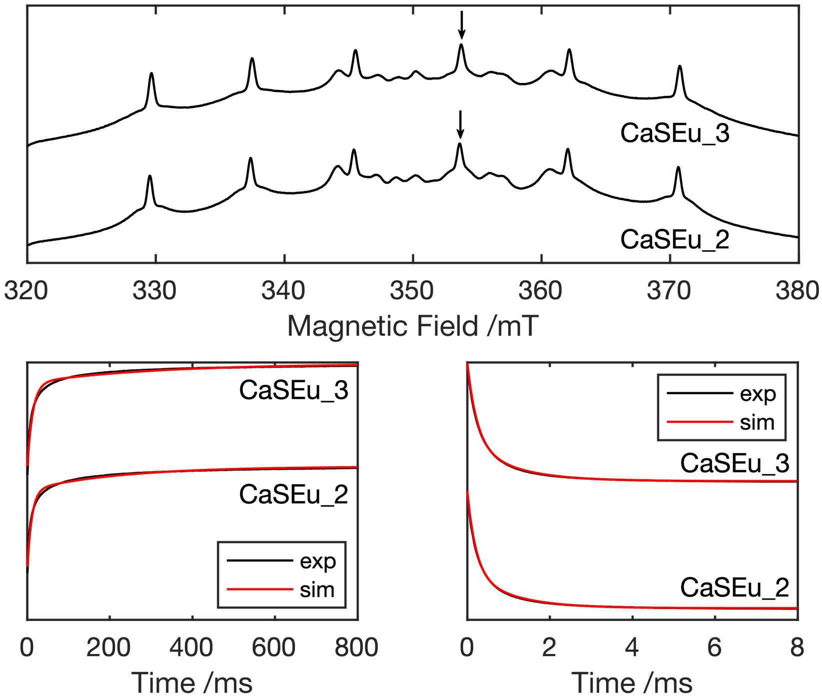

**Figure 4.6:** Pulsed EPR measurements of CaSEu_2 and CaSEu_3, recorded at 10K and X-band microwave frequency. *Top:* field-swept echo decay (FSED-EPR) spectrum of CaSEu_2 and CaSEu_3. The arrows indicate field positions at which relaxation measurements were performed; *Bottom left:* Inversion recovery experiments for the determination of $T_1$; *Bottom right:* Hahn echo decay experiments for the determination of $T_M$. *Black:* experimental spectra; *Red:* simulated spectra.

| *Sample* | $c_0$ | $T_{1s}$ | $c_1$ | $T_{1f}$ | $c_2$ |
|---|---|---|---|---|---|
| CaSEu_2 | 0.991 | 224.4 | -0.232 | 10.9 | -0.772 |
| CaSEu_3 | 0.991 | 301.6 | -0.190 | 13.0 | -0.832 |

**Table 4.5:** Best fit parameters from the least-squares fitting routine for $T_1$ measurements, using a bi-exponential function, for CaSEu_2 and CaSEu_3 at 10 K. field units are in mT; all time constants are reporting in $\mu$s. '$f$' and '$s$' subscripts denote *fast* and *slow* for distinction.

| *Sample* | $c_0$ | $T_{2s}$ | $c_1$ | $T_{2f}$ | $c_2$ |
|---|---|---|---|---|---|
| CaSEu_2 | 0.089 | 1.027 | 0.278 | 0.210 | 0.616 |
| CaSEu_3 | 0.077 | 1.063 | 0.298 | 0.233 | 0.605 |

**Table 4.6:** Best fit parameters from the least-squares fitting routine for $T_2$ measurements, using a bi-exponential function, for CaSEu_2 and CaSEu_3 at 10 K. field units are in mT; all time constants are reporting in $\mu$s. '$f$' and '$s$' subscripts denote *fast* and *slow* for distinction.

The preliminary findings facilitated by relaxation measurements suggest three main implications, which support the characterisation afforded by CW EPR, *i.e.*, i) The characterised $\mathrm{Eu}^{x}_{\mathrm{surface}}$, and by inference, $\mathrm{Eu}^{x}_{\mathrm{Ca}}$ sites have characteristically long $T_1$ and $T_M$ relaxation times due to negligible spin-orbit interactions; ii) The $\mathrm{Mn}^{x}_{\mathrm{Ca}}$ relaxation times indicate an increase in $T_1$ and $T_M$, in part due to the diffusion of bulk $\mathrm{F}^{+}$ - centres and preserved disorder upon heating treatment; iii) the dominating line width effect, upon heating treatment, is likely related to a distribution in $A$, relating to disorder, rather than a relaxation-dominated process. An understanding of the underlying spin dynamics, and relaxation effects due to local disorder give an informative insight into the effect of post-synthetic treatments of the material, and in this case, partial reactivation of the phosphor from milling induced effects.

### 4.2.6 Cryo-milling study of prepared CaS:Eu(Na) sample

To determine the effect of local disorder in the sample upon cryo-milling, and to identify the presence of any intrinsic $\mathrm{V}^{\bullet}_{\mathrm{S}}$ centres in the doped sample, a systematic study of the effects of consecutive cryo-milling cycles on the samples were performed. Therefore, a CaS:Eu sample, prepared via a solid-state reduction method using a carbon reductant and source of $\mathrm{Na}^{+}$ impurities, was used in order to manipulate the redox state of $\mathrm{Eu}^{2+}$ in the sample *via* charge compensation and thus reduce the signal intensity. This sample has been labelled as CaSEu_Na and the subsequent cryo-milled samples CaSEu_Na_C$x$ ($x$=1,2,3) respectively where $x$ is the number of consecutive cycles.

Figure 4.7 presents the X-band CW EPR spectra of this CaSEu_Na sample, after one, two and three consecutive cycles. For clarity, the spectra are shown in 1st and 2nd derivative mode. In the native sample, a hyperfine pattern indicative of the isolated $\mathrm{Eu}^{2+}$ species was observed (Figure 4.7a), similar to the commercial samples discussed earlier (Figure 4.1a). After the first cryomilling cycle (Figure 4.7b), an increase in $\mathrm{Eu}^{x}_{\mathrm{Ca}}$ signal intensity is observed which is attributed to reduction of the unreacted Eu precursor by the carbon reductant. In the 2nd derivative mode, an additional sharp isotropic signal is clearly observed with $g = 2.0031$ and which can be attributed to the $\mathrm{V}^{\bullet}_{\mathrm{S}}$ centre. After an additional cryo-milling cycle (Figure 4.7c), the $\mathrm{Eu}^{x}_{\mathrm{Ca}}$ signal decreases further, presumably due to oxidation to $\mathrm{Eu}^{\bullet}_{\mathrm{Ca}}$ , whilst simultaneously the $\mathrm{V}^{\bullet}_{\mathrm{S}}$ center signal intensity increases. In the 1st derivative spectrum, a change in the line shape within the $\mathrm{Eu}^{x}_{\mathrm{Ca}}$ hyperfine multiplet indicates the appearance of the $\mathrm{V}^{\bullet}_{\mathrm{S}}$ centre signal which was not resolved.

Finally, after the 3rd consecutive cryo-milling cycle (Figure 4.7d), the $\mathrm{Eu}_{\mathrm{Ca}}^{\bullet}$ concentration reduces further, accompanied by a significant broadening in the line width. This change to the line width is likely due to the increased spin concentration around the $\mathrm{Eu}_{\mathrm{Ca}}^{x}$ site, which reduces the $T_2$ relaxation time and thereby increases the homogeneous line width contribution. Additional strain effects, such as distribution of the $b_4$ terms included in the broadening model, due to disorder within the sample, is also likely to contribute to the broadening.

### 4.2.7 XPS studies of commercial and prepared CaS:Eu phosphors

In order to provide a comparison between the distinct paramagnetic $\mathrm{Eu}^{2+}$ environments as identified by EPR, additional XPS measurements were performed on the commercial treated samples CaSEu_1, 2 and 3, as well as the solid-state reduced sample CaSEu_SSR. The Eu 3d XPS region is shown for these four samples in Figure 4.8. The XPS measurements were performed by Dr. David Morgan.

For the treated commercial samples, CaSEu_1,2 and 3, no well resolved signals were observed in the Eu 3d region for either $\mathrm{Eu}^{2+}$ or $\mathrm{Eu}^{3+}$, indicating Eu is either

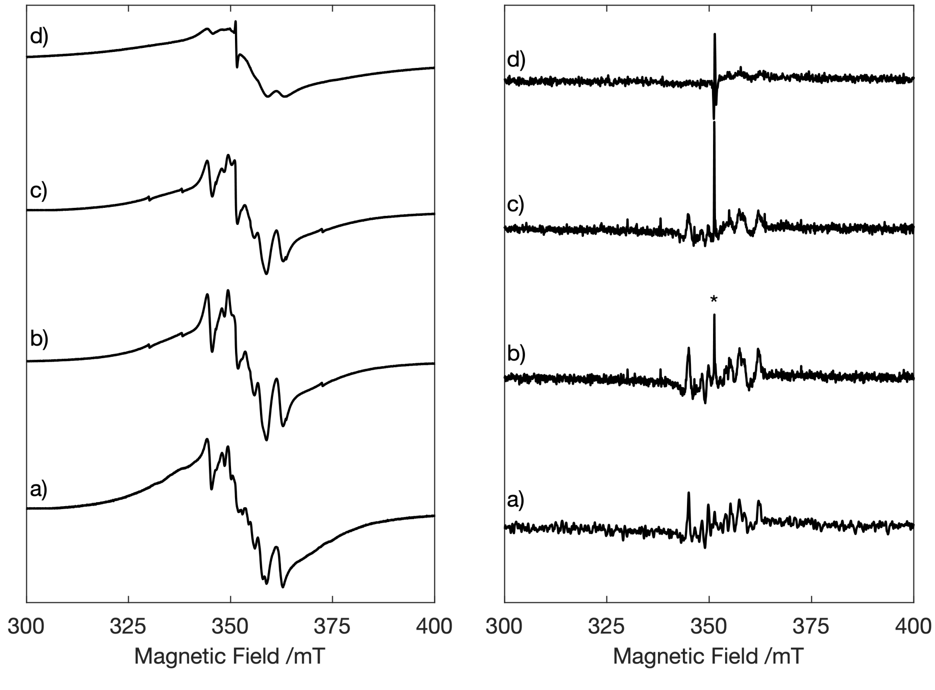

**Figure 4.7:** CW X-band (9 GHz) EPR spectra (120 K) of a) the native CaSEu_Na sample after b) one, (CaSEu_Na_C1) c) two (CaSEu_Na_C2), and d) three (CaSEu_Na_C3) consecutive cryo-milling treatments. *Left:* Standard 1st derivative measurements; *Right:* 2nd derivative measurements indicating onset of $V_S^{\bullet}$ centre signal, labelled by an asterisk.

below the limits of detection, or absent from the surface region, and are therefore distributed within the bulk of the material as expected from the EPR data. However, for CaSEu_SSR, Figure 4.8(d), broad peaks were observed at binding energies of 1134.6 eV and 1164.6 eV along with weakly resolved satellite features, which correspond to the Eu $3d_{5/2}$ and $3d_{3/2}$ regions typical of oxygen containing $Eu^{3+}$ species.[29] The binding energies of the observed signals are comparable to those reported for $Eu(OH)_3$, present at 1134.4 eV and 1164.2 eV for the $3d_{5/2}$ and $3d_{3/2}$ regions respectively.[30] The binding energies for $Eu^{2+}$, the EPR-active state, are typically reported to be around 1125 and 1155 eV for the $3d_{5/2}$ and $3d_{3/2}$ core levels[31, 32] and would be well removed from the observed spectral lines. We can therefore be confident that the XPS signals do not directly correspond to paramagnetic $Eu^{2+}$ (within the limits of detection). By comparison to the native sample, CaSEu_1, these broad peaks are also observed to be very weakly resolved from the baseline.

In the O 1s region, a major peak was observed in all samples at 531.4 eV which was attributed to a CaO or $CaSO_4$ type phase (O 1s binding energy reported as 531.2 eV for CaO and 531.5 eV for $CaSO_4$)[33] resulting from the oxidation of CaS, The line shape and peak height is not observed to change significantly upon treatment of the sample from CaSEu_1 to 3. The presence of these phases was also evidenced by the spin Hamiltonian parameters for the $Mn^{2+}$ impurity for the undoped samples CaS_2 and CaS_3. For CaSEu_SSR, an asymmetry is evident to higher binding energy of the larger peak observed in all samples, corresponding to the presence of another distinct signal at 533.1 eV. This could indicate a surface hydroxyl species, such as that attributed to the broad Eu 3d signal and has been tentatively assigned to $Eu(OH)_3$. Such adsorbed hydroxyl species have been reported in $Eu_2O_3$ host materials (532.7 eV).[34]

The findings reported for the Eu 3d and O 1s regions of the CaSEu_SSR sample indicate that Eu is present at the surface, which has not been successfully doped into the material. This indirectly corroborates the observation of a low symmetry $Eu^{2+}$ species from W-band EPR measurements of CaSEu_SSR and CaSEu_1, which was attributed to the $Eu^{x}_{\text{surface}}$ species in an 'EuO' type phase, for which the exact composition was not determined. The Ca and S 2p regions for all samples (see Appendix 3; Figures 9 and 10) consisted of multiple signals expected to relate to various phases containing Ca, S and O. The similarity of the binding energies, and lack of corroborating literature values, was not conclusive of any significant findings with respect to the characterisation of the luminescent $Eu^{2+}$ environments.

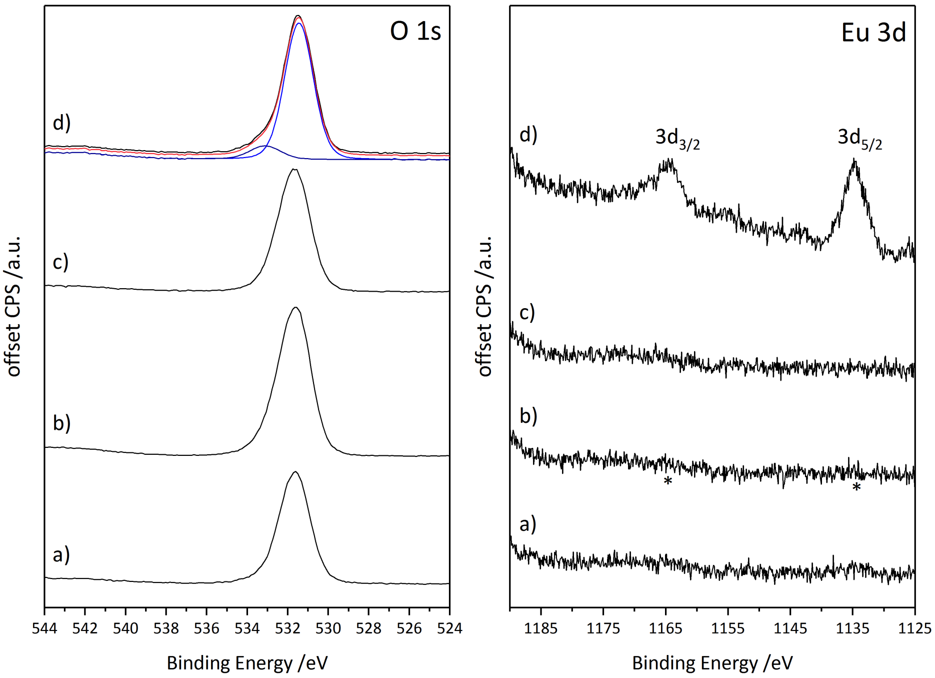

**Figure 4.8:** XPS spectra for commercial CaSEu_1, 2 and 3 samples, compared to the sample prepared *via* solid state reduction method (CaSEu_SSR). Experimental traces are shown in black. *Left:* O 1s region with simulations for CaSEu_SSR. *Red trace:* simulation envelope; *Blue traces:* simulation components. *Right:* Eu 3d region. See Appendix 3: Figure 8 for survey spectra.

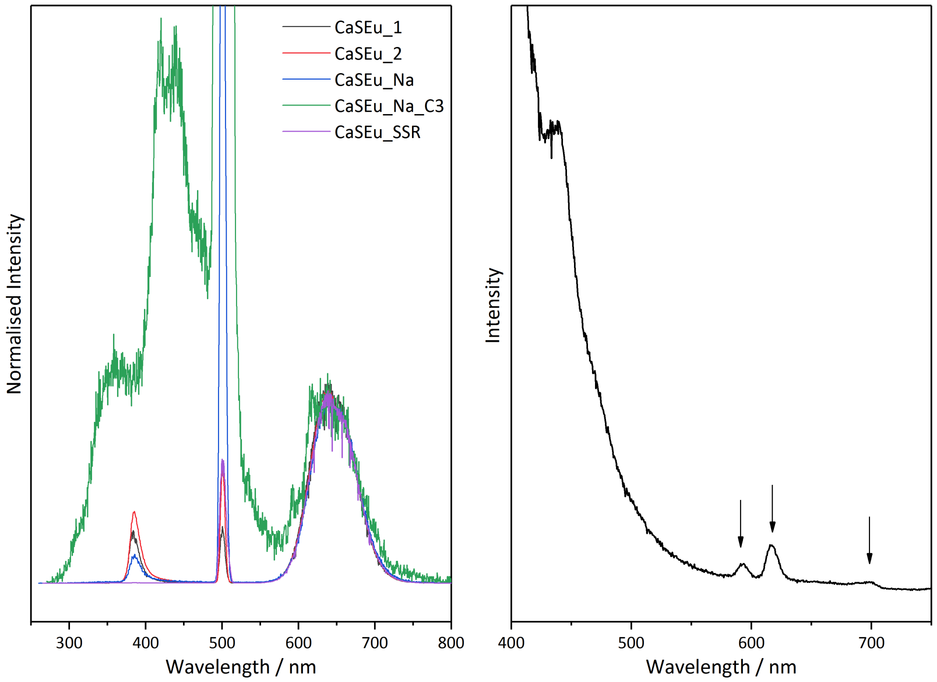

**Figure 4.9:** *Left:* A comparison of the emission spectra of the samples using $\lambda_{ex}$ = 250 nm (note double harmonic feature at 500 nm), normalised to the intensity of the peak around 645 nm; *Right:* The emission spectra of CaSEu_Na_C3 obtained using $\lambda_{ex}$ = 395 nm. The arrows indicate the $Eu^{3+}$ centred $^5D_0 \rightarrow {}^7F_J$ transitions where $J = 1$, $J = 2$ and $J = 4$.

### 4.2.8 Luminescence studies of CaS:Eu phosphors

The photoluminescent properties of the different phosphors were also assessed using steady state luminescence spectroscopy on solid samples. Since the characteristic phosphorescence emission wavelengths of $Eu^{3+}$ are likely to overlap with the broad emission spectrum that is typically attributed to the $Eu^{2+}$ doped phosphor species, it can be challenging to establish the presence of a $Eu^{3+}$ contaminant/by-product in such species. Therefore, the photophysical properties of the different samples were investigated using a range of excitation wavelengths. In particular, the possibility that $Eu^{3+}$ may be present in the samples was interrogated using an excitation wavelength of 395 nm, as this provides direct promotion of the spin forbidden $^7F_0 \rightarrow {}^5L_6$ transition which can then rapidly relax to the emitting $^5D_0$ excited state of $Eu^{3+}$.

The photoluminescence measurements were performed by Danielle Merrikin and Prof. Simon Pope. Firstly, all samples were investigated using an excitation wavelength of 250 nm and displayed the expected broad emission peak peaking around 640 nm, which is consistent with the previously reported $Eu^{2+}$-based (5d-4f transition) emission that is commonly observed for this class of $Eu^{2+}$-doped phosphor (Figure 4.9, *left*). The excitation acquisition ($\lambda_{em} = 645$ nm) revealed a longest wavelength feature at 450-550 nm. When analysing sample CaS:Eu_Na_C3 (after 3 cryo-milling cycles) this emission feature, although present, appeared to be much weaker. In addition, weak shorter wavelength emission bands between $\lambda_{em} = 300$-$550$ nm were also noted although these were absent in all other samples.

Each of the samples were also investigated using an excitation wavelength of 395 nm. In only one case, CaSEu_Na_C3, was the broad 645 nm peak not observed. Instead, we noted a very weak set of peaks superimposed upon the tail of a shorter wavelength emission feature (Figure 4.8, *right*). These weaker bands were consistent with the luminescence spectroscopic signature of $Eu^{3+}$: from this spectrum there was unequivocal evidence for the $^5D_0 \rightarrow {}^7F_J$ transitions at around 590 nm, 615 nm and 700 nm (for $J = 1$, $J = 2$ and $J = 4$, respectively) was found. A corresponding excitation spectrum ($\lambda_{em} = 592$ nm) also revealed a weak, but sharply distinctive band at 395 nm again corroborating the assignment of these features to the presence of $Eu^{3+}$ in the sample. Therefore, the 3rd consecutive cryo-milling cycle not only reduced the $Eu^{2+}$ concentration, but was also accompanied by an increased concentration of $Eu^{3+}$, due to an oxidative process, which was not possible to detect directly using EPR characterisation due to its singlet ground state.

## 4.3 Conclusions

EPR investigations, supported by XPS and photoluminescence measurements, have been utilised in order to better understand the nature of local $\mathrm{Eu}^{2+}$ sites, defects and impurities in CaS:Eu red-emitting phosphors. The effect of synthetic and post-synthetic treatments was also rationalised in terms of activating and de-activating species that directly affect the luminescent properties. EPR measurements of the native sample showed a complex hyperfine structure at $g < g_e$ indicative of a well isolated $\mathrm{Eu}^{2+}$ site, $\mathrm{Eu}_{\mathrm{Ca}}^{x}$, located in a cubic substitutional site ($\mathrm{Ca}^{2+}$).

Upon treatment, $\mathrm{Mn}^{2+}$ impurities, $\mathrm{Mn}_{\mathrm{Ca}}^{x}$, became evident which are expected to be present also in substitutional $\mathrm{Ca}^{2+}$ sites. The $\mathrm{Eu}_{\mathrm{Ca}}^{x}$ signal intensity was also observed to decrease following oxidation to $\mathrm{Eu}^{3+}$, $\mathrm{Eu}_{\mathrm{Ca}}^{\bullet}$ . Upon application of heating treatment, the signal intensity was partially improved and the change in line shape of $\mathrm{Mn}_{\mathrm{Ca}}^{x}$ (1) is indicative in the change of local order within the cubic lattice due to unresolved fine structure. $\mathrm{F}^{+}$ centre defects, $\mathrm{V}_{\mathrm{S}}^{\bullet}$ , were observed in the prepared undoped materials, and also after several cryo-milling cycles, which are well known to reduce the efficacy of the material.

In the prepared CaSEu_SSR sample, W-band EPR measurements and XPS indicated the presence of an additional 'EuO' type surface species, $\mathrm{Eu}_{\mathrm{surface}}^{x}$, not incorporated into the lattice, which was also weakly resolved in the W-band measurements of the native commercial sample, CaSEu_1. This species is responsible for the fine structure not observed within the simulations for the $\mathrm{Eu}_{\mathrm{Ca}}^{x}$ site.

Preliminary relaxation studies were also performed to underpin the nature of line broadenings and their relation to structural disorder. The characterised $\mathrm{Eu}_{\mathrm{surface}}^{x}$, and by inference, $\mathrm{Eu}_{\mathrm{Ca}}^{x}$ sites were determined to have characteristically long $T_1$ and $T_M$ relaxation times due to negligible spin-orbit interactions. Comparison of the $\mathrm{Mn}_{\mathrm{Ca}}^{x}$ relaxation times after cryo-milling (CaSEu_2) and heating (CaSEu_3) under a reducing atmosphere indicated an increase in $T_1$ and $T_m$, which was attributed to the to the diffusion of bulk $\mathrm{F}^{+}$ - centres and preserved disorder upon heating treatment. The dominating line width effect, upon heating treatment, was assigned to a distribution in $A$, relating to disorder, rather than a relaxation-dominated process.

The findings from EPR measurements were rationalised using photoluminescence spectroscopy to give a qualitative account of their effect on the luminescent properties. The photophysical properties of various solid samples were investigated using a range of excitation wavelengths in order to probe the electronic transitions of both the $\mathrm{Eu}^{2+}$ and $\mathrm{Eu}^{3+}$ sites (where $\mathrm{Eu}^{3+}$ is EPR silent). At excitation wavelength $\lambda_{ex} = 395$ nm the characteristic broad emission feature at $\lambda_{em} = 645$ nm was observed in most samples which corresponds to directly to the 4f-5d emission of interest. The emission was not observed CaSEu_Na_C3 sample (after 3 cryomilling cycles) due to oxidation of $\mathrm{Eu}_{\mathrm{Ca}}^{x}$ sites to $\mathrm{Eu}_{\mathrm{Ca}}^{\bullet}$ , and defect formation in the solid. A set of shorter wavelengths corresponding to the $^{5}\mathrm{D}_{0} \rightarrow {}^{7}\mathrm{F}_{\mathrm{J}}$ transitions of $\mathrm{Eu}_{\mathrm{Ca}}^{\bullet}$ were instead observed.

In conclusion, EPR spectroscopy and related techniques are a fundamental tool in the characterisation of semiconductors, point defects and paramagnetic ions, and is recognised as such by its extensive application. The mechanism of charge carrier promotion and trapping processes (particularly rare earth metals) are applicably complex and in some cases, poorly understood.[35] transition metal and rare-earth activated phosphors are responsible for a rich and diverse set of materials with tuneable optical and electronic properties, which affords them application across bio-labelling, photocatalysts, sensors and lighting.[36–41]

## 4.4 Experimental

**Materials:** The commercial sample, CaS:Eu in its native form (CaSEu_1) was purchased from Phosphor Technologies Ltd. and used as received without further purification or treatment.

**Sample Preparation:**

**Co-precipitation method for undoped samples:** The procedure used for the preparation of the undoped samples was modified from a method previously reported by Rekha et al.[42] who used 2-propanol as the solvent. Solution A was prepared by dissolving anhydrous $CaCl_2$ (3.077 g, 28 mmol) in 56 ml of ethanol. Nitrogen was then bubbled continuously through the solution. Solution B was prepared by dissolving anhydrous $Na_2S$ (2.164 g, 28 mmol) in 56 ml of ethanol. A yellow, slightly cloudy solution resulted. Solution B was then added dropwise over 10 minutes to solution A with stirring to form a white suspension.

This suspension was warmed to approximately 60°C and left stirring overnight with nitrogen bubbling to produce a faintly yellow fine powder. This powder was then transferred quickly under nitrogen to an alumina boat in a tube furnace previously flushed with $N_2$/2% $H_2$ and left under this gas for several hours. The sample was then annealed at 700°C (10°C min$^{-1}$ ramp up, dwell two hours, 20°C min$^{-1}$ to R.T.).

**Solid state reduction method for doped samples:** The method used was that described by Hubacek et al.[43] Urea (45 g 0.749 mol) was mixed with $CaSO_4$ (6 g, 44.07 mmol) and $Eu(NO_3)_3{\cdot}6H_2O$ (0.22 g 0.651 mmol) and initially heated in an open alumina crucible on a hot plate to °C where the mixture became liquid. The mixture was then stirred briefly, and the temperature raised. At 160°C, gas evolution was seen to occur. After an hour at ∼200°C, solidification occurred, A white lumpy product was obtained, which was easily crushed to a powder. The product was ground with a pestle and mortar and heated to 550°C (30 min, 30 min, 20 min) in a loosely covered crucible in air. the powder was then heat-treated at 700°C under 5% $H_2/N_2$ (10°C min$^{-1}$ ramp up, 120 min dwell, 20°C min$^{-1}$ ramp down). A very pale pink product was obtained. This was only weakly fluorescent under long wave UV (pinky bluish white), but quite strongly red under short wave UV irradiation.

**Solid state reduction method for CaSEu_Na:** The Na co-doped sample was prepared via a method similar to that previously reported by Guo et al.[44] A flux composed of $CaSO_4$ (25.21g, 0.18 mol), $Na_2S_2O_3$ (4.40g 27.8 mmol), $Eu(NO_3)_2 \cdot 5H_2O$ (0.59 g, 1.37 mmol) and a carbon black reductant (4.38g, 0.364 mol) were mixed in a planetary ball mixer with ceramic beads for 30 minutes to obtain a well-mixed powder. The powder was sieved, packed into a ceramic crucible and covered with a graphite foam to limit oxidation of the sample. The crucible was subsequently fired at 950°C, with a 20°C min$^{-1}$ ramp rate, for 2 hours before leaving overnight to cool. The sample was obtained as a black powder due to residual carbon. A red emission was observed under a UV torch confirming the presence of luminescent $Eu^{2+}$ sites and the sample was used without further treatment.

**Sample Treatments:**

The sample treatments were performed by JM staff.

**Cryo-milling treatment:** The samples CaSEu_1, CaS_2 and CaSEu_Na were milled in a Retsch Cryo-mill with an initial 8-minute cooling stage at 5 Hz. This was followed by three consecutive milling stages at 30 Hz, with inter-stage cooling periods of 3 minutes at 5 Hz to normalise any temperature increase from the grinding action. Heating treatment in air and $N_2/H_2$: For heating treatments in $N_2/H_2$, the samples were treated as described in the co-precipitation synthesis method For heat treatments in air, the sample was contained in an alumina boat and placed into a Nannetti fast-fire furnace for a dwell time of 30 minutes.

**Characterisation Techniques:**

**CW EPR spectroscopy:** The samples for EPR measurements were used either as prepared or as received, and approximately 50 mg of the powders were packed into a standard 4mm quartz tube. The X-band (9 GHz) CW-EPR spectra were recorded at 140 K on a Bruker EMX spectrometer, and unless otherwise stated, operating at 100 kHz field modulation frequency; 2 mW microwave power; 1 G modulation amplitude using an ER 4119HS cavity. For W-band measurements, the samples were packed in a 0.5 mm I.D. quartz cell The W-band (95 GHz) CW-EPR spectra were recorded at 300K on a Bruker E600 spectrometer operating at 100 kHz field modulation frequency; 0.005 mW microwave power; 1 G modulation amplitude, using a E600-1021H TeraFlex resonator. Field calibration was performed using a BDPA standard at X-band, and the microwave frequency for spectra at W-band were adjusted accordingly by simultaneous fitting at the two microwave frequencies. Spectral simulations were performed using the EasySpin toolbox in MATLAB developed at ETH Zurich.[45] The second derivative spectra in Figure 4.7 were smoothed using a spline modelling approach with the MATLAB curve fitting toolbox to improve the signal resolution.

**Pulsed EPR measurements:** Measurements were performed on a Bruker E580 spectrometer equipped with an Oxford Instruments cryostat at 10K, with a microwave frequency of approximately 9.82 GHz. The primary echo was generated using a standard $\pi/2 - \tau - \pi - \tau - echo$ pulse sequence ($\pi/2$=16 ns), with a time delay ($\tau$) of 220 ns for the field-swept echo decay experiment *(top).* The absorption spectrum was obtained by integration of the echo. The $T_2$ (or $T_M$) relaxation time was measured by Hahn echo decay (i.e. echo intensity mapping by variation of the time delay, $\tau$), with the same sequence and pulse length. The $T_1$ relaxation time was measured using an inversion recovery experiment, with the typical $\pi - T - \pi/2 - \tau - \pi - \tau - echo$ pulse sequence, with the same pulse length and time constant, $\tau$ (= 400 ns), by varying the time delay $T$. Simulations were also performed using the EasySpin toolbox in MATLAB developed at ETH Zürich.[45]

**X-ray Photoelectron (XPS) Spectroscopy:** A Kratos Axis Ultra DLD system was used to collect XPS spectra using monochromatic Al K$\alpha$ X-ray source operating at 120 W (10 mA x 12 kV). Data was collected with pass energies of 160 eV for survey spectra, and 20 eV for the high-resolution scans with step sizes of 1 eV and 0.1 eV respectively. The system was operated in the Hybrid mode of operation utilising a combination of magnetic and electrostatic lenses for electron collection over an analysis area of approximately 300 x 700 $\mu$m$^2$. A magnetically confined electron-only charge compensation system was used to minimise charging of the sample surface, and all spectra were taken with a 90° take-off angle. A pressure of *ca.* 1x10$^{-9}$ Torr was maintained during collection of the spectra, with base pressure of the system 5x10$^{-10}$ Torr. All data was calibrated to the C(1s) line of adventitious carbon, taken to have a value of 284.8 eV, and quantified using CasaXPS (v2.3.23) using modified Wagner sensitivity factors as supplied by the manufacturer, after subtraction of a two parameter Tougaard background defined as a “U2 Tougaard” background in the analysis software.

**Photoluminescence Spectroscopy:** All photophysical data were obtained on a Jobin-Yvon Horiba Fluorolog-3 spectrometer fitted with a JY TBX picosecond photodetection module. Solid samples were used in all cases and a front face accessory was used for light collection. Emission spectra were uncorrected and excitation spectra were instrument corrected.

# References

[1] Yang Zhang and Jianhua Hao. Metal-ion doped luminescent thin films for optoelectronic applications. *Journal of Materials Chemistry C*, 1(36):5607–5618, 8 2013.

[2] de Ana Bettencourt-Dias. Lanthanide-based emitting materials in light-emitting diodes. *Dalton Transactions*, 0(22):2229–2241, 5 2007.

[3] Ye Lu and Bing Yan. Lanthanide organic–inorganic hybrids based on functionalized metal–organic frameworks (mofs) for a near-uv white led. *Chemical Communications*, 50(97):15443–15446, 11 2014.

[4] Koen Van den Eeckhout, Philippe F. Smet, and Dirk Poelman. Persistent luminescence in $Eu^{2+}$-doped compounds: A review. *Materials*, 3(4):2536–2566, 4 2010.

[5] Yanjie Liang, Feng Liu, Yafei Chen, Xianli Wang, Kangning Sun, and Zhengwei Pan. Extending the applications for lanthanide ions: efficient emitters in short-wave infrared persistent luminescence. *Journal of Materials Chemistry C*, 5(26):6488–6492, 7 2017.

[6] P. Dorenbos, R. Visser, van C. W. E. Eijk, N. M. Khaidukov, and M. V. Korzhik. Scintillation properties of some $Ce^{3+}$ and $Pr^{3+}$ doped inorganic crystals. *IEEE Transactions on Nuclear Science*, 40(4):388–394, 8 1993.

[7] Carel W. E van Eijk. Development of inorganic scintillators. *Nuclear Instruments and Methods in Physics Research Section A: Accelerators, Spectrometers, Detectors and Associated Equipment*, 392(1):285–290, 6 1997.

[8] Carel W. E. van Eijk. Inorganic scintillators in medical imaging. *Physics in Medicine and Biology*, 47(8):R85–106, 4 2002.

[9] V. B. Pawade, H. C. Swart, and S. J. Dhoble. Review of rare earth activated blue emission phosphors prepared by combustion synthesis. *Renewable and Sustainable Energy Reviews*, 52:596–612, 12 2015.

[10] Joel Garcia and Matthew J. Allen. Developments in the coordination chemistry of europium(ii). *European journal of inorganic chemistry*, 2012(29): 4550–4563, 10 2012.

[11] Xian Qin, Xiaowang Liu, Wei Huang, Marco Bettinelli, and Xiaogang Liu. Lanthanide-activated phosphors based on 4f-5d optical transitions: Theoretical and experimental aspects. *Chemical Reviews*, 117(5):4488–4527, 3 2017.

[12] D. Caurant, D. Gourier, N. Demoncy, I. Ronot, and J. Pham-Thi. Paramagnetic defects induced by mechanical stress in calcium sulfide phosphor. *Journal of Applied Physics*, 78(2):876–892, 1995.

[13] R. L. Nyenge, H. C. Swart, and O. M. Ntwaeaborwa. Luminescent properties, intensity degradation and x-ray photoelectron spectroscopy analysis of $CaS:Eu^{2+}$ powder. *Optical Materials*, 40:68–75, 2 2015.

[14] R. D. Shannon. Revised effective ionic radii and systematic studies of interatomic distances in halides and chalcogenides. *Acta Crystallographica Section A: Crystal Physics, Diffraction, Theoretical and General Crystallography*, 32 (5):751–767, 9 1976.

[15] D. Caurant, D. Gourier, N. Demoncy, and M. Pham-thi. Point defects produced by grinding of CaS phosphors: An electron spin resonance study. *Radiation Effects and Defects in Solids*, 135(1-4):115–119, 12 1995.

[16] P. K. Ghosh and R. Pandey. Thermoluminescence due to intrinsic point defects in polycrystalline calcium sulphide. *Journal of Physics C: Solid State Physics*, 15(28):5875–5885, 10 1982.

[17] Ravindra Pandey, A. Barry Kunz, and John M. Vail. Study of point defects in alkaline-earth sulfides. *Journal of Materials Research*, 3(6):1362–1366, 12 1988.

[18] P. K. Ghosh, H. P. Narang, and Harish Chander. Thermoluminescence of an X-ray induced defect in CaS:Ce. *Journal of Luminescence*, 35(2):99–106, 5 1986.

[19] Victor Chechik and Damien M Murphy, editors. *Electron Paramagnetic Resonance: Volume 26*, volume 26 of *SPR - Electron Paramagnetic Resonance*. The Royal Society of Chemistry, 2019.

[20] N.J. Stone. Table of nuclear magnetic dipole and electric quadrupole moments.

[21] J. W. Jewett and P. E. Wigen. EPR of $Tb^{3+}$, $Pr^{3+}$, $Gd^{3+}$, and $Eu^{3+}$ ions in single crystal $La_2O_2S$. *The Journal of Chemical Physics*, 61(8):2991–2995, 10 1974.

[22] N. Sabbatini, M. Ciano, S. Dellonte, A. Bonazzi, F. Bolletta, and V. Balzani. Photophysical properties of Europium(II) cryptates. *The Journal of Physical Chemistry*, 88(8):1534–1537, 4 1984.

[23] A. Abragam and B. Bleaney. *Electron Paramagnetic Resonance of Transition Ions*. Oxford Classic Texts in the Physical Sciences. Oxford University Press, Oxford, 2012.

[24] A. Abragam and B. Bleaney. *Electron paramagnetic resonance of transition ions*. Oxford classic texts in the physical sciences. Oxford University Press, Oxford, 2012.

[25] Roman Boča. Zero-field splitting in metal complexes. *Coordination Chemistry Reviews*, 248(9):757–815, 5 2004.

[26] İlkay Yildirim, Bünyamin Karabulut, Esat Bozkurt, and Fevzi Köksal. EPR study of gamma-irradiated $Na_2S_2O_3{\cdot}5H_2O$ single crystals. *Radiation Physics and Chemistry*, 78(3):165–167, 3 2009.

[27] J. Rubio O., E. Muñoz P., J. Boldú O., Y. Chen, and M. M. Abraham. EPR powder pattern analysis for $Mn^{2+}$ in cubic crystalline fields. *The Journal of Chemical Physics*, 70(2):633–638, 1 1979.

[28] B. Ray, Mirzai P. A., Monskf, and Brightwell J. W. Fluorescence and ESR in $CaS:Mn^{2+}$. *physica status solidi (a)*, 100(1):233–237, 3 1987.

[29] Y. Uwamino, T. Ishizuka, and H. Yamatera. X-ray photoelectron spectroscopy of rare-earth compounds. *Journal of Electron Spectroscopy and Related Phenomena*, 34(1):67–78, 1 1984.

[30] Ping Li, Hanyu Wu, Jianjun Liang, Zhuoxin Yin, Duoqiang Pan, Qiaohui Fan, Di Xu, and Wangsuo Wu. "sorption of Eu(III) at feldspar/water interface: effects of ph, organic matter, counter ions, and temperature". *Radiochimica Acta*, 105(12):1049–1058, 11 2017.

[31] R. "Vercaemst, D. Poelman, L. Fiermans, R. L. Van Meirhaeghe, W. H. Laflère, and F." Cardon. A detailed XPS study of the rare earth compounds eus and $EuF_3$. *Journal of Electron Spectroscopy and Related Phenomena*, 74 (1):45–56, 9 1995.

[32] T. Maruyama, S. Morishima, H. Bang, K. Akimoto, and Y. Nanishi. Valence transition of Eu ions in GaN near the surface. *Journal of Crystal Growth*, 237-239:1167–1171, 4 2002.

[33] C. D. Wagner, D. A. Zatko, and R. H. Raymond. Use of the oxygen KLL auger lines in identification of surface chemical states by electron spectroscopy for chemical analysis. *Analytical Chemistry*, 52(9):1445–1451, 8 1980.

[34] John P. Baltrus and Murphy J. Keller. Rare earth oxides $Eu_2O_3$ and $Nd_2O_3$ analyzed by XPS. *Surface Science Spectra*, 26(1):014001, 2 2019.

[35] Yang Li, Mindaugas Gecevicius, and Jianrong Qiu. Long persistent phosphors—from fundamentals to applications. *Chem. Soc. Rev.*, 45(8):2090–2136, April 2016.

[36] Thomas Maldiney, Aurélie Lecointre, Bruno Viana, Aurélie Bessière, Michel Bessodes, Didier Gourier, Cyrille Richard, and Daniel Scherman. Controlling Electron Trap Depth To Enhance Optical Properties of Persistent Luminescence Nanoparticles for *in vivo* Imaging. *J. Am. Chem. Soc.*, 133(30): 11810–11815, August 2011.

[37] Shicheng Yan, Jiajia Wang, Honglin Gao, Nanyan Wang, He Yu, Zhaosheng Li, Yong Zhou, and Zhigang Zou. Zinc Gallogermanate Solid Solution: A Novel Photocatalyst for Efficiently Converting $CO_2$ into Solar Fuels. *Advanced Functional Materials*, 23(14):1839–1845, 2013.

[38] Shuzo Hirata, Kenro Totani, Junxiang Zhang, Takashi Yamashita, Hironori Kaji, Seth R. Marder, Toshiyuki Watanabe, and Chihaya Adachi. Efficient

Persistent Room Temperature Phosphorescence in Organic Amorphous Materials under Ambient Conditions. *Advanced Functional Materials*, 23(27): 3386–3397, 2013.

[39] Zhigao Yi, Xiaolong Li, Zhenluan Xue, Xiao Liang, Wei Lu, Hao Peng, Hongrong Liu, Songjun Zeng, and Jianhua Hao. Remarkable NIR Enhancement of Multifunctional Nanoprobes for In Vivo Trimodal Bioimaging and Upconversion Optical/T2-Weighted MRI-Guided Small Tumor Diagnosis. *Advanced Functional Materials*, 25(46):7119–7129, 2015.

[40] Thomas Maldiney, Aurélie Bessière, Johanne Seguin, Eliott Teston, Suchinder K. Sharma, Bruno Viana, Adrie J. J. Bos, Pieter Dorenbos, Michel Bessodes, Didier Gourier, Daniel Scherman, and Cyrille Richard. The *in vivo* activation of persistent nanophosphors for optical imaging of vascularization, tumours and grafted cells. *Nature Materials*, 13(4):418–426, April 2014.

[41] Yongyang Gong, Gan Chen, Qian Peng, Wang Zhang Yuan, Yujun Xie, Shuhong Li, Yongming Zhang, and Ben Zhong Tang. Achieving Persistent Room Temperature Phosphorescence and Remarkable Mechanochromism from Pure Organic Luminogens. *Advanced Materials*, 27(40):6195–6201, 2015.

[42] S. Rekha, Arturo I. Martinez, T. A. Safeera, and E. I. Anila. Enhanced luminescence of triethanolamine capped calcium sulfide nanoparticles synthesized using wet chemical method. *Journal of Luminescence*, 190:94–99, 10 2017.

[43] Milan Hubacek, JP, Kenji Takahashi, and JP. United states patent: 7378038 - process for producing phosphors.

[44] Chongfeng Guo, Dexiu Huang, and Qiang Su. Methods to improve the fluorescence intensity of CaS:Eu$^{2+}$ red-emitting phosphor for white led. *Materials Science and Engineering: B*, 130(1):189–193, 6 2006.

[45] Stefan Stoll and Arthur Schweiger. Easyspin, a comprehensive software package for spectral simulation and analysis in EPR. *Journal of Magnetic Resonance (San Diego, Calif.: 1997)*, 178(1):42–55, 2006.

# Chapter 5

# An EPR Investigation of Defect Structure and Electron Transfer Mechanism in Mixed-Conductive $LiBO_2-V_2O_5$ Glasses

## 5.1 Introduction

The tuneable multi-functional properties of $V_2O_5$-based materials have led to their usage in a variety of energy storage, optical and electrocatalytic applications (especially as a water-splitting cathodes).[1–4] Amorphous vanadate glasses are also attractive for use as solid state electrolytes,[5–10] cathodes for Li-ion batteries,[11, 12] and alternative alkali-ion battery technologies,[13–15] due primarily to the content-dependent mixed ionic-electronic conductivity of the materials. Vanadium possesses multiple accessible redox couples, which provides a subsequent high theoretical capacity and energy density, that can incorporate up to 3 Li per $V_2O_5$ unit.[11] Crystalline $V_2O_5$ materials have had limited commercial application due to the poor capacity retention, which results from irreversible phase changes (amorphisation) and volume expansion upon Li incorporation. On the other hand, amorphous vanadate materials have been shown to reduce some of these challenges and therefore offer a highly attractive route to overcome performance-limiting properties upon intercalation.

The functional properties of these glassy materials are highly dependent on the nature and content of the precursors used in their preparation. A great deal of literature is available that focuses on the structural characterisation of $V_2O_5$-based glassy materials for a variety of applications.[14, 16–19] For example, when $V_2O_5$ behaves as a network modifier, *i.e.* at low contents, its incorporation into a borate network can be accompanied by a modification of the regular (trigonal) structure as diborate, chain-type metaborate and tetrahedral $BO_4$ units.[20] The presence of trigonal and tetrahedral borate sites was also confirmed in other studies of $xV_2O_5(1\text{-}x)[2\,B_2O_3-Li_2O]$ glasses[21] closely analogous to the glass samples to be reported in this study.

Glasses containing high $V_2O_5$ content (up to $x = 0.8$; $xV_2O_5(1\text{-}x)B_2O_3$) were also described in the literature,[20] where $V_2O_5$ acts as a network former, and revealed that borate was only present as tetrahedral $BO_4^-$ units in network modifying positions. At $V_2O_5$ contents greater than the $LiBO_2$ contents, vanadium can also be considered the primary network former and therefore, to local order,

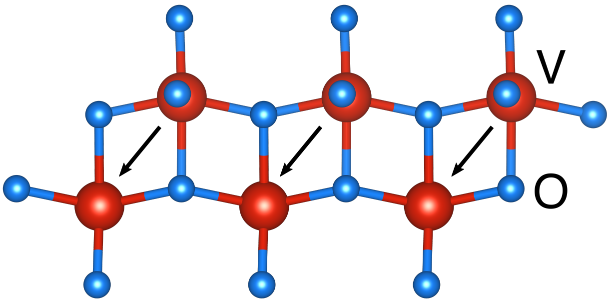

**Figure 5.1:** Schematic of polaron hopping direction (arrows) in the $V_2O_5$ type phase.

can be a useful model in the characterisation of the $V^{4+}$ defects in amorphous materials. The electronic interactions between $V^{4+}$ defects actually mediate the polaron hopping mechanism of electron transfer for conductivity (Figure 5.1).The local defect structure, primarily vacancies and cationic impurities (such as Li), are then generally responsible for the formation of the $V^{4+}$ sites.

The introduction of oxygen vacancies into $V_2O_5$ can also induce ferromagnetism between sites of the form $V_2O_5$-x (where x $<$ 0.13 and 0.19 $<$ x $<$ 0.45), with the electron spin density occupying the $3\,d_{xy}$ orbital in the ground state.[22] These electrons are then spin polarised due to intra-atomic exchange interactions giving rise to half-metallic ferromagnetism. Other theoretical and experimental studies have shown that for higher oxygen vacancy concentrations (x $>$ 0.45), antiferromagnetic ordering can dominate.[23]

This presents a straight-forward model upon which the effect of incorporation of network modifying defects, such as Li and B, in addition to intrinsic defects such as oxygen vacancies, can be understood in terms of their resulting magnetic properties. The formation of intrinsic oxygen vacancies that can lead to $V^{4+}$ defects through charge compensation according to:[24]

$$2V_V^X + O_O^X \leftrightarrow 2V'_V + \Box_O^{\bullet\bullet} + \frac{1}{2}O_2 \tag{5.1}$$

and in this case, the intrinsic concentration of oxygen vacancies is approximately equal to half the concentration of $V^{4+}$.[24] A useful comparison for the vanadate glass network is the understanding of lithium defect chemistry in the $V_2O_5$ network, particularly the electrochemical insertion of Li-ions.[25], Introduction of $Li^+$ into a $V_2O_5$ intercalation site is accompanied by the reduction of a single $V^{5+}$ site to $V^{4+}$ and association to the adjacent oxygen site forming a coupled electron-hole pair:

$$V_V^X + O_O^X + Li^+ + e' \leftrightarrow V_V' + OLi_O^\bullet \tag{5.2}$$

Where $V_V^X$ denotes the $V^{5+}$ site, $O_O^X$ is an $O^{2-}$ site, $V_V'$ is an effective $V^{4+}$ defect site and $OLi_O^\bullet$ is the associated oxygen site with net positive charge.

It is clear that the electrochemical stability, and performance of electrode materials is directly related to the local electronic structure of the redox-active vanadium sites, additional to defects, vacancies, dislocations *etc.* as a result of the disordered glassy network. Amorphous glasses can hence present challenges in understanding the local structure of the material due to short-range order and localised ordering. Information from conventional techniques for structural determination, such as XRD, can often be challenging in providing a comprehensive structural view of the material.

By comparison, EPR spectroscopy can be readily exploited as a powerful characterisation technique when studying such glassy materials bearing paramagnetic vanadium states, notably $V^{3+}$ ($S = 1$; $^3F_4$) and $V^{4+}$ ($S = 1/2$; $^2D_{5/2}$).[26] The coordination environment is critical in determining the relative ordering of the 3d states and hence the orbital occupancy of the unpaired electron. Due to the orbital contribution to the total angular momentum, the $g$ tensor is also highly sensitive to the its coordination environment. Further more, hyperfine and super-hyperfine interactions with neighbouring nuclei, offer a wealth of information on the local site symmetry, and coordination geometry.

It is important to note that in the glassy materials, two distinctly different and observable $V^{4+}$ environments can be expected, with the vanadium acting as a network forming or network modifying phase. At low contents, in the network modifying phase, $V^{4+}$ defects are formed via charge compensation for Li and B, and can be considered well isolated in the bulk $LiBO_2$ network compared to other substitutional vanadium sites. On the other hand, in network forming phases, the structure is akin to defective $V_2O_5$ (to short range order), whereby $V^{4+}$ sites are formed via incorporation of Li, B and oxygen vacancy defects. In this case, the spin delocalisation and spin concentration is much greater, and the $V^{4+}$ defects can no longer be considered as isolated, localised species. This environment is then attributed to an extended lattice of interacting spins, responsible for the super-exchange behaviour associated with polaron hopping conductivity. The dimensionality of the lattice is thus highly dependent on the local structure, and bonding to nearby spins, and hence the magnitude of the electronic interactions are sensitive to this. Both of these environments can be readily interrogated by

EPR spectroscopy.

In this study we have therefore employed continuous wave (CW) EPR spectroscopy to investigate the electronic structure of $V^{4+}$ sites and the inter-site interactions of relevance to electronic conductivity. A series of $LiBO_2$–$V_2O_5$ (VLB) glasses, varying in $V_2O_5$ content, were studied in order to identify the distinct $V'_V$ and other defective sites present. Careful analysis of the line width broadening in the EPR spectra, provides insights into the exchange mechanism, and in turn an estimate of the thermodynamic and electronic properties pertaining to the polaron hopping mechanism, including the polaron hopping activation energy, the Curie-Weiss temperature and the isotropic exchange integral. The EPR linewidth analysis model adopted here, can thus be used to directly probe redox-sensitive sites and rationalise their local environment and functional properties in $V_2O_5$-based glassy materials.

## 5.2 Results and discussion

### 5.2.1 CW EPR study of glasses at varying $V_2O_5$ content

In the first instance, a series of $LiBO_2$:$V_2O_5$ glass samples with varying $V_2O_5$ to $LiBO_2$ ratios including VLB1 (70:30 ratio), VLB2 (36:64) and VLB3 (20:80), were prepared and characterised by X-band CW EPR spectroscopy. The resulting experimental and simulated spectra for these three representative samples are shown in Figure 5.2.

At low $V_2O_5$ content, the spectrum is characterised by a well resolved 8-line hyperfine structure arising from the interaction of the electron spin ($S = 1/2$) with that of the $^{51}$V nucleus ($I = 7/2$). The spin Hamiltonian parameters extracted from the simulation for the $V^{4+}$ network modifying position were found to be $g$ = [1.9775 1.9819 1.9471] ± 0.003 and $^{51V}A$ = [152.1 180.5 520.1] ± 5 MHz (Table 5.1).

The relative magnitudes of the $g$ and $A$ tensor components $g_e > g_{xx}, g_{yy} > g_{zz}$ and $A_{zz} > A_{xx}, A_{yy}$ are typical for a $3\,d^1$ $VO^{2+}$ species occupying a distorted (tetragonally compressed) octahedral environment of $C_2$ type symmetry or lower, with a $3\,d_{xy}$ ground state. These $g$ and $A$ values are consistent with other vanadium doped glass systems,[21, 27–32] although the symmetry is typically reported to be axial in the literature. We assume (in the absence of single crystal or quantum chemical calculations) that the principle axis frames for the $g$ and $A$ tensors are collinear. The shifts in $g$ values ($\Delta g$), usually represented as $\Delta g_{\parallel}/\Delta g_{\perp}$, is frequently reported for vanadyl species,[21, 33–35] as the degree of tetragonal distortion in the system after Kivelson and Lee.[36] Considering the relatively small deviation in the $g_1$ and $g_2$ values ($\approx$0.0025), an average value may be used to approximate $\Delta g_\perp$ for simple comparison with similar vanadyl systems. $\Delta g_\parallel / \Delta g_\perp =$ 2.44 and $\Delta g_\parallel / \Delta g_\perp =$ 2.90 for VLB1 and VLB2, respectively, agree reasonably with other reported glasses containing similar phases.[21, 33, 37] A considerable increase in the value for $VO^{2+}$(2) is consistent with a comparative increase in tetragonal distortion at the defect sites.

The full quasi-axial $^{51V}A$ hyperfine tensor determined from simulation of the CW EPR spectrum for VLB1 (Table 5.1) may be further decomposed into an isotropic component, $a_{iso}$, and the sum of two traceless axial dipolar hyperfine tensors following schemes related to the angular radial components for $d_{xy}$ and $d_{nz}$ ($n = x, y$) orbitals reported by Morton and Preston:[38]

$$A_{ij} = a_{iso} + \begin{bmatrix} T & & \\ & \text{T} & \\ & & -2T \end{bmatrix} + \begin{bmatrix} T' & & \\ & -2T' & \\ & & T' \end{bmatrix} /MHz \tag{5.3}$$

In this case, one may obtain values of the anisotropic dipolar hyperfine terms, $T$ and $T'$, which correspond to $3\,d_{xy}$ and $3\,d_{nz}$ (n = x,y; the relative ordering cannot

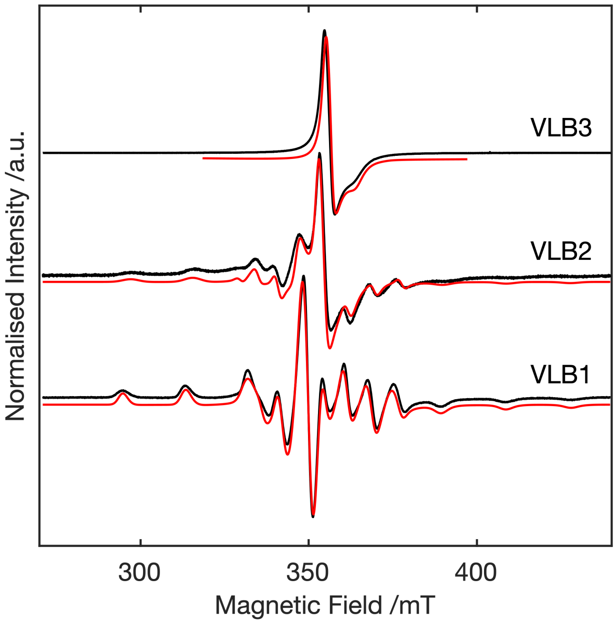

**Figure 5.2:** Low temperature (120 K) X-band CW EPR spectra of VLB1, VLB2, and VLB3 at varying $V_2O_5$ contents. *Black:* experimental spectrum; *Red:* simulated spectrum.

| Species | $g_{iso}$ | $g$ | $\frac{\Delta g_{\parallel}}{\Delta g_{\perp}}$ | $a_{iso}$ | $A$ | $T^c$ |
|---|---|---|---|---|---|---|
| VO$^{2+}$ (1) | 1.9688 | $g_1$ 1.9775 | 2.44 | 284.2 | $A_1$ 152.1 | $T(d_{xy})^d$ 113.2,122.7 |
| (VLB1) | ± 0.003 | $g_2$ 1.9819 | | ±5 | $A_2$ 180.5 | $T'(d_{nz})$ 9.45 |
| | | $g_3$ 1.9471 | | | $A_3$ 520.1 | |
| VO$^{2+}$ (2) | 1.9679 | $g_1$ 1.9773 | 2.90 | 277.1 | $A_1$ 134.8 | $T(d_{xy})^d$ 106.3,124.3 |
| (VLB2) | ± 0.003 | $g_2$ 1.9852 | | ±5 | $A_2$ 188.7 | $T'(d_{nz})$ 18.0 |
| | | $g_3$ 1.9411 | | | $A_3$ 507.7 | |
| V$_2$O$_5$[a] | 1.9720 | $g_1$ 1.9925 | 4.13 | | | |
| (VLB3) | ± 0.001 | $g_2$ 1.9825 | N.R.[b] | N.R.[b] | N.R.[b] | N.R.[b] |
| | | $g_3$ 1.9445 | | | | |

**Table 5.1:** Spin Hamiltonian parameters for the V$^{4+}$ species identified in amorphous vanadyl glasses, extracted by simulation of the experimental spectrum. All hyperfine related terms are given in MHz and are reported as magnitudes rather than absolute values. The full hyperfine tensor can be reconstructed using the identity matrices defined in equation 5.2.1. Note: [a] $g$ tensor results were obtained from the simultaneous fitting of LBV3 at multiple frequencies (X, Q, W) and $T = 10$ K (X, Q) $T = 20$ K (W). [b] Not resolved. [c] Calculated solutions to the tensor decomposition, assuming $A_3$ coincides with the compressed axial direction. The values reported here are magnitudes (the relative sign cannot be determined). [d] Two solutions for $T$ are given for completeness, dependent on the relative sign of $T'$.

be determined) orbital states which admix *via* spin-orbit coupling. These relations reflect the localised electron spin density partially occupies the next lowest lying $3\,\mathrm{d_{nz}}$ orbital and suggests a destabilisation in the $n$-character orbitals through compression and/or strain.

In the absence of quantum chemical calculations, one may compare experimental values to the calculated atomic parameters,[38] to extract and estimate further information about the ground state electronic structure and spin density at the vanadium centre. The reported values for vanadium correspond to $A_0 = 4165$ MHz and $P = 437.6$ MHz,[†] in addition to the anisotropic angular factors required for the occupied orbital (2/7 for $\mathrm{d_{xy}}$ and $\mathrm{d_{nz}}$). The $A_3$ component was assumed to be coincident with the compressed $D_{2h}$ axis, which allows one to extract estimated magnitudes for T' for the VO$^{2+}$ defects. For the $\mathrm{d_{xy}}$ orbital, there are two solutions to the tensor decomposition, dependent on the relative sign of T', which cannot be determined from the powder EPR measurement. Nevertheless this gives a reasonable insight into the orbital character of the electron spin density at the vanadium site.

The isotropic hyperfine term, dominated by the Fermi contact interaction, is proportional to the spin density at the nucleus (s-character). $\rho_s \approx A_{iso}/A_0 = 0.0682$. Similarly an estimate of the $3\,\mathrm{d_{xy}}$ and $3\,\mathrm{d_{xz}}$ orbital occupancy can also be extracted from the hyperfine values, resulting in values of $\rho_{3d_{xy}} \approx T/({}^{51V}P \cdot 2/7) =$ 0.905 and 0.981, and $\rho_{3d_{nz}} \approx T'/({}^{51V}P \cdot 2/7) = 0.0756$. The value for $\rho_{3d_{xy}}$ indicates that the unpaired spin density is almost completely localised on the vanadium site ($\sum_i \rho_i = 1.05$ and 1.12) with the majority occupying the expected $3\,\mathrm{d_{xy}}$ orbital.

In the case of the high $V_2O_5$ content sample, VLB3, a distinct axial signal is observed lacking any hyperfine structure (Figure 5.2).The absence of a visible hyperfine arises from a dynamic effect characteristic of the strong exchange narrowing regime, as described by Anderson.[39] In this situation, the exchange (or hopping) frequency is much greater than the rate of modulation caused by the hyperfine or anisotropic (dipolar) exchange interactions. As a result, the time frame of the electron spin relaxation process is sufficiently rapid that the surrounding magnetic framework is seen as an effective static field, and therefore the weak perturbation of the energy levels by these effects are effectively averaged. This is further exacerbated by the polaron hopping mechanism, expected in amorphous $V_2O_5$ materials,[40] due to the delocalisation of unpaired spin density across extended network.

The local network can be approximated as a distorted $V_2O_5$- type phase, containing network-modifying $LiBO_2$ units which manifest as defects. The nature of electron transfer for the partially localised spins may be identified by the magnitude of exchange, with respect to the nearest neighbour $\mathrm{V^X}_\mathrm{V}$ units, and the activation barrier for hopping conductivity to occur. The dimensionality of the lattice may be determined by the magnitude of exchange coupling between different lattice dimensions. No resolved structures related to the network modifying $VO^{2+}$ sites found in VLB1 and VLB2 were observed for the VLB3 sample.

The simulated $g$ values in the strong exchange limit ($J \gg \ \Delta g \mu_B B$), are characteristic of the mean deviation from $g_e$, assuming a distribution of magnetic sites arising from distortions in the amorphous framework are present due to variations in the bonding, distance and orientation. The mean tetragonality parameter obtained from an average of $g_1$, $g_2$ is very high (4.13) indicating a more significant distortion at the $V_V'$ site compared to that observed for VLB1 and VLB2. The value is much higher compared to the reported values found for isolated $V^{4+}$ species.[30, 31] Clearly, the consequence of the screening of hyperfine and anisotropic exchange interactions is therefore a subsequent loss of information regarding the ground state electronic structure and local environment.

Finally, in the intermediate content sample, a complex line shape is observed corresponding to a superposition of signals attributed to the network forming ($V_2O_5$) and network modifying ($VO^{2+}$) sites identified in VLB3 and VLB1, respectively. An increased broadening of the $VO^{2+}$ signal is consistent with an increased disorder about the isolated sites due to the mixed network-forming phases in the material. Similarly, for the intermediate content glass, VO2+ (2) $\rho_s = 0.0665$, $\rho_{3d_{nz}} = 0.144$ giving solutions $\rho_{3d_{xy}}$= 0.850 and 0.994. The value for $3\,\mathrm{d_{xy}}$ indicates that the unpaired spin density is again almost completely localised on the vanadium site ($\sum_i \rho_i = 1.06$ and 1.20), in the ground state $3\,\mathrm{d_{xy}}$ orbital. A noteable increase in the $\mathrm{d_{nz}}$ contribution was determined in comparison to $VO^{2+}(1)$, which indicated a more significant distortion at the vanadium site in the equatorial plane as the $V_2O_5$ content increases. The majority of the unpaired spin density was still attributed to the ground $3\,\mathrm{d_{xy}}$ orbital.

### 5.2.2 Variable Temperature study of high content sample

The high $V_2O_5$ content sample, VLB3, was investigated further using variable temperature (VT) CW EPR between $T$ = 4 - 370 K, to indirectly probe the electron-electron exchange interactions, and transfer mechanisms responsible for the electronic conductivity. The $g$ anisotropy (and subsequent line shape) is indicative of the inequivalence between exchange and hopping dimensions of the disordered lattice. Ideally, single crystal measurements are necessary to resolve different contributions to the system. Nevertheless valuable information can still be extracted from the powder spectrum despite the loss of directional/ angular information.

In order to partially recover information on orientational resolution, a phenomenological broadening model was applied to reproduce the changes in line shape as a function of temperature. For cases where the $g$ anisotropy is non-negligible, it follows that the relaxation time is also orientation-dependent with respect to $B_z$, the $z$ component of the external magnetic field, which can be approximated by an anisotropic Lorentzian line shape function in the strong-exchange narrowing limit. This likely arises due to the dimensionality of the lattice (distinct $J$ values), and/or potential antisymmetric Dzyaloshinskii–Moriya (DM) exchange terms ($d_{12}$) which would have a correlation frequency comparable to the isotropic integral. This additional term would arise due to the local distortions of the amorphous phase. In the regular, ordered $V_2O_5$ lattice, the vanadium nuclei possess an inversion centre (assuming no distortion due to Li intercalation or oxygen vacancy formation) which causes the antisymmetric terms to vanish.

These interactions are rarely resolved within the powder EPR spectrum and single crystal measurements, in addition to variable frequency is often necessary to interrogate this exchange term fully. Although there is tangible anisotropy between the $g_1$ and $g_2$ components, this is comparatively small compared to the $g_3$ term. This small anisotropy can therefore be neglected in order to obtain orientational information from the rhombic system with respect to electronic motion and inter-electronic interactions.

In systems with strong isotropic exchange in comparison to magnetic anisotropy, deviations in the wings of the Lorentzian line shape can occur, resulting in a line shape that can be approximated by the superposition of broad Gaussian and Lorentzian line shape functions.[41] The observed line shape in the case of VLB3 was suitably approximated by a pure Lorentzian function.

The amorphous nature of the glass requires treatment in order to obtain a good fit to the experimental data. The orientational distribution of the paramagnetic ensemble is non-isotropic and therefore a biased distribution must be calculated. Due to the nature of the varying line widths and/or other possible spin Hamiltonian parameters following a change in temperature, each measurement was simulated consecutively by least-squares fitting to obtain approximate parameter fits for the $g$ values and anisotropic Lorentzian line shape. An ordering potential, $\lambda$,

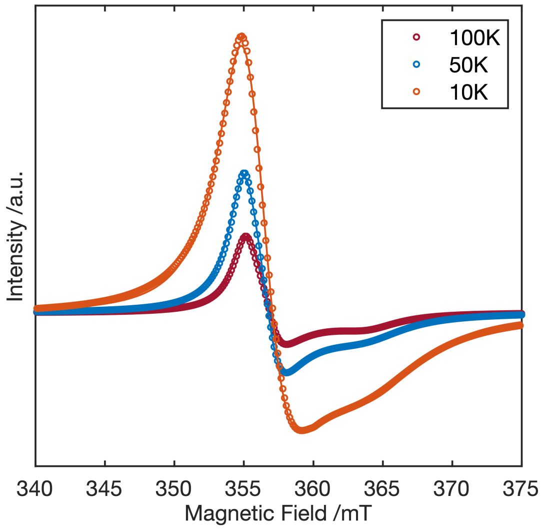

**Figure 5.3:** Example simulations of EPR anisotropic linewidth modelling at single temperature points, indicating goodness of fit. The hollow circles correspond to the experimental trace (only 1/8 of the recorded points are shown for clarity). The solid lines correspond to the fitting results using the anisotropic Lorentzian model. The values of the line width and $g$ tensor were obtained from a least-squares fitting routine as a function of temperature.

was allowed to vary during the initial routine, of the form:

$$P\left(\theta\right) = exp\left(-U\left(\theta\right)\right) \tag{5.4}$$

$$U(\theta) \; = \; -\lambda(3cos^2(\theta) \; - \; 1)/2 \tag{5.5}$$

where $\theta$ is the rotation from the z axis, and *lambda* is the ordering potential. *lambda* was then taken as an average and fixed for the second run of the least-squares fitting routine. Values of $\lambda$ = -0.7725 and -0.087 were obtained, respectively, for the temperature ranges $T$ = 4-100 K and 120-370 K, due to the change in orientation of the sample upon switching between spectrometers. These values represent a comparatively weak orientational bias for the amorphous glass within the approximation of a powder sample (where the orientational dependence is not resolved) and was thus a reasonable approximation for the line shape simulations upon variation of the temperature. Several contributions to the line width can arise in such complex systems, including, most importantly, the distribution of the $g$ tensor values due to inter-site distortions.

In the strong exchange limit, the relative difference in Zeeman energies represents only a small perturbation to the exchange energy and therefore this effect is expected to be averaged out from the observed line shape. Similarly, the hyperfine and anisotropic exchange interactions that may contribute to unresolved structure within the line width are treated as non-perturbing effective fields and also averaged out. It is possible for the partial resolution of these interactions approaching low temperatures ($T$ < 50 K) to occur due to the increase in the spin lifetime, characteristic of the spin-lattice relaxation time, $t_{1e}$, however no evidence of this was observed within the studied temperature ranges.

Examples of the fitting results for VLB3 at various temperatures are shown in Figure 5.3, and the full set of single point measurements and simulations including residual analysis can be found in Appendix 4, Figures 1-5. From these simulations, the variation of the average $g$ values, in addition to the peak-to-peak linewidth, $\Delta B_{pp}$, for the exchange-averaged signal components (where $\Delta B_{pp}$ is equivalent to $\Delta B_{pp} \; = \; \Delta B_{FWHM}/\sqrt{3}$ for the $g_3$ component), taking into account anisotropic Lorentzian broadening due to the dominant spin relaxation contribution to the line width and $g$ anisotropy.

A relatively small error was obtained for the direct fitting of the line shape at each temperature, with the root mean square deviation on the order of $10^{-3}$. The main source in deviation from the observed trace was within the wings of the signal due to the exchange-narrowed line shape which is approximated as a broad

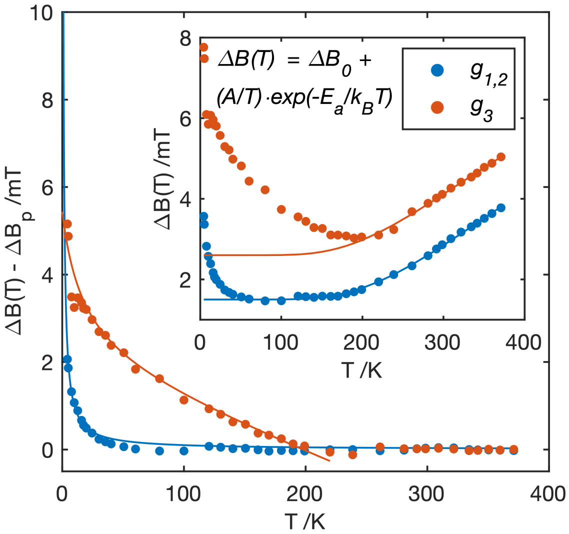

**Figure 5.4:** Line width analysis after subtraction of the polaron hopping contribution to the line width. The fits for the $g_{1,2}$ and $g_3$ components are defined in equations 5.9 and 1.3. Inset: Results for the fit of the Arrhenius law to the total EPR line width temperature dependence, defined in equation 5.8.

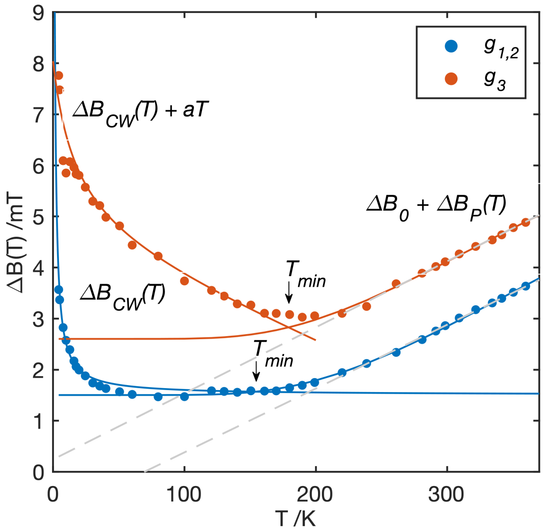

**Figure 5.5:** Results of the line width analysis for the $g_{1,2}$ and $g_3$ components. The lines for the temperature region $T > T_{min}$ are the results of the fitting to an Arrhenius law. The lines for the temperature region $T < T_{min}$ are the result of fitting of the superposition model to the line width dependence, after subtracting the contribution from the high temperature Arrhenius type behaviour (Figure 5.4). The dashed grey lines provide a representative linear fit. The individual fits are presented in Figure 5.4. The parameters obtained from the fits are presented in Table 5.2.

Gaussian in the wings of the spectrum, and minor deviations within the unresolved $g_1$, $g_2$ components. This observation is considered to be either of the following: orientational bias not accounted for in the relatively simple model (equations 5.4 and 5.5); inequivalent localised defect states, due to variation of the degree of polarisation due to spin-orbit coupling between sites. Approaching $T = 4$ K, the fit diverges more considerably, which indicate an additional structure due to unresolved interactions or distinct defect states.

The Curie-Weiss behaviour of the EPR magnetic susceptibility is considered by the following equation:

$$\chi_{EPR} \approx C/(T - \Theta_{CW})^{\gamma} \tag{5.6}$$

where $\chi_{EPR}$ is the effective EPR magnetic susceptibility, $C$ is the Curie constant, and $\Theta_{CW}$ the Curie-Weiss (CW) temperature. $\gamma$ is a constant usually taken as $\gamma = 1$ in a mean field approach. The EPR temperature dependent line width can be related to the effective magnetic susceptibility:[42]

$$\Delta B(T) = [\chi_0(T)/\chi(T)]\Delta B_{pp}^{\infty} \tag{5.7}$$

where $\chi_0\,(T)$ is the Curie susceptibility; $\chi(T)$ is the effective susceptibility; and $\Delta B_{pp}^{\infty}$ is the temperature independent contribution to the intrinsic line width. The

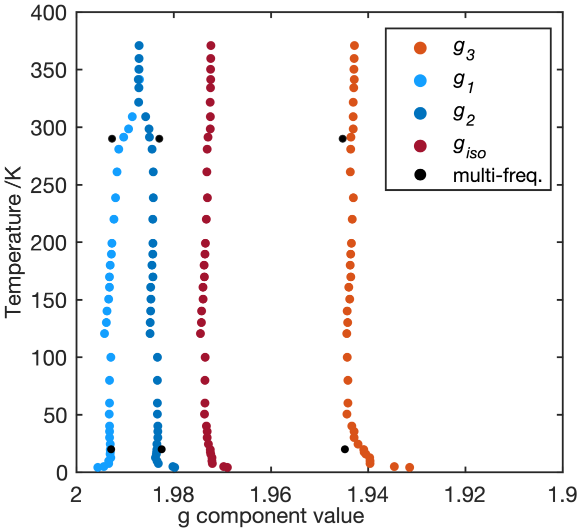

**Figure 5.6:** Results of $g$ tensor monitoring obtained from the variable temperature modelling. The filled black circles are the results from simultaneous multiple frequency fitting at $T = 20$ K and $T = 290$ K.

EPR line width can be phenomenologically modelled as a linear combination of decomposed components, where $\Delta B_P(T)$ is a function describing the contribution to the line width from polaron hopping, and $\Delta B_{CW}(T)$ is a function describing the Curie-Weiss behaviour:

$$\Delta B(T) = \Delta B_0(T) + \Delta B_P(T) + \Delta B_{CW}(T) \tag{5.8}$$

The quantity $\Delta B_0(T)$ encompasses the temperature-independent term, $\Delta B_0^{\infty}$, in addition to a temperature-dependent term, which for short $t_{1e}$ is comparable to:

$$\Delta B_0(T) \propto (1/t_{1e}(T) + 1/t_{2e}(T)) \tag{5.9}$$

thus including contributions from spin-spin and spin-lattice relaxation mechanisms. The spin-lattice contribution to the linewidth was expected to be characteristic of the polaron-hopping motion in the system due to the localisation of spin density at the defect sites, and the associated phonon coupling to the lattice.

Values for the line widths were obtained as a function of temperature for a wider range ($T$ = 4-370 K). The results are presented in Figure 5.5. Both components of the model are represented by distinct temperature regions that characterise the magnetic properties, and charge carrier dynamics.

At high temperatures, the line width dependence is approximately linear for both the $g_{1,2}$ and $g_3$ components respectively, with a similar gradient observed in both cases. Approaching $T = 200$ K, a deviation away from linearity was observed at a minimum line width value and corresponding temperature, $T_{min}$, followed by a plateau over a comparatively long temperature range. Approaching $T = 4$ K, the line width was observed to increase monotonically for both modelled components, albeit *via* different rates. It is not immediately clear as to the contributions to this region due to the competing magnetic and transfer processes as a function of temperature.

It has been reported that, in systems known to undergo polaron hopping, the line width exhibits a dependence on the hopping frequency and thus the conductivity.[43] The portion of the experimental data above $T_{min}$ was therefore fitted to an Arrhenius equation which describes the $\Delta B_P(T)$ term:[42]

$$\Delta B(T) = \Delta B_0^{\infty} + (A/T) \cdot exp(-E_a/k_BT) \tag{5.10}$$

where $A$ is a pre-exponential factor, and $E_a$ is the activation energy for the

| Component | $E_a$ /eV | $\Delta B_0^{\infty}$ /mT | $\Theta_{CW}$ /K | J /cm$^{-1}$ | $a$ /mT K$^{-1}$ |
|---|---|---|---|---|---|
| $g_3$ | 0.0805 | 2.255 | -16.8 | -0.7928 | -0.0161 |
| $g_{1,2}$ | 0.0940 | 1.390 | -0.005 | -0.0002 | - |

**Table 5.2:** fitting parameters and quantities obtained from linewidth analysis of LBV3.

hopping process. An excellent fit was afforded for the $g_{1,2}$ components, which accurately reproduced the plateau observed below $T = 200$ K. The linear portion of the plot and deviation was well reproduced for the $g_3$ component. However, the line width deviated below $T_{min}$ indicating a further contribution. The fitting afforded values $\Delta B_0 = 1.390$ mT and $E_a = 0.0940$ eV for the $g_{1,2}$ components, and $\Delta B_0 = 2.255$ mT and $E_a = 0.0805$ eV for the $g_3$ component, providing a comparable value for the hopping energy barrier, in agreement with the dependence of the line width on the hopping rate.

The line width behaviour was then probed at low temperatures, by subtracting the contribution from the polaron hopping conductivity and the intrinsic line width, leaving only contributions expected from the Curie-Weiss behaviour, Figure 5.4. For the $g_{1,2}$ components, the subtracted line width is effectively nil across most of the temperature range, before increasing asymptotically approaching $T = 0$ K, consistent with paramagnetic Curie-Weiss behaviour where the exchange interaction is zero.

The behaviour of the $g_3$ component, however, is less straight forward, and exhibits a composite behaviour, which we attribute to two competing processes: (i) an additional apparent linear increase in the line width approaching $T = 0$ K; (ii) an antiferromagnetic exchange ordering contribution, which results in a monotonic increase in the line width response. We believe that the former corresponds to the transfer of spin density, and its subsequent change in relaxation properties due to the gradual localisation of spin density with decreasing temperature. The low temperature regions were fitting with the following equations for the $g_{1,2}$ and $g_3$ components, respectively:

$$\Delta B_{CW}(T) = C/(T - \Theta_{CW}) \tag{5.11}$$

$$\Delta B(T) = \Delta B_{CW}(T) + a{\cdot}T \tag{5.12}$$

where $C$ is a constant analogous (but not equal) to the Curie constant; $\Theta_{CW}$ is the Curie-Weiss temperature; and $a$ is a constant describing the gradient of the superposed linear dependence. Both models reproduced the observed behaviour well for the $g$ components, and provided values $\Theta_{CW}$ = -0.005 ± 5 K for $g_{1,2}$ (effectively nil within experimental error); and $\Theta_{CW}$ = -16.8 K, $a$ = -0.01061 $\mathrm{mT\,K^{-1}}$ for $g_3$. The isotropic exchange integral may be estimated from the Curie temperature using the following equation:[39]

$$3k_B\Theta_{CW} \;=\; 2JZS(S+1) \tag{5.13}$$

where $Z$ is the number of nearest-neighbour spins, which was kept constant (assuming 2-fold coordination along the hopping dimension) for comparison. The estimated CW temperature values provide values $J$ = -0.7928$\mathrm{cm}^{-1}$ for the $g_3$ component, and $J'$ = -0.0002 $\mathrm{cm}^{-1}$ for the $g_{1,2}$ components (effectively nil within error). The observed CW behaviour is therefore convincing proof that the VLB3 glass is a one-dimensional hopping pathway (and hence one-dimensional exchange lattice), with a moderate antiferromagnetic coupling, and a virtually paramagnetic (uncoupled) behaviour along the other dimensions. We may consider that the broad, $g_3$ component is aligned to the dimension of the hopping conduction which would correspond with a decrease in the spin relaxation time due to the antiferromagnetic coupling.

The spin-lattice relaxation time $t_{1e}$ is expected to be comparable to the order of $t_{2e}$ along the hopping dimension due to the strong coupling of the spin-phonon modes. The orientation of the $g_3$ component with respect to the crystallographic domain was therefore expected to coincide with the shortest V-V distance and the hopping dimension. The fit of the Arrhenius law (Figure 5.4) showed that the effective hopping frequency, below the critical temperature, tends towards a linear dependence as the temperature was decreased.

In this situation, the phonon modulation of the lattice is coincident not only with the spin-lattice relaxation processes, but also the localisation of spin density at the trapping defect sites.[44] We propose that for the region $T < T_{min}$, the polarisation of the conduction electron spin density increases substantially due to the introduction of orbital angular momentum into the spin-orbit coupling and subsequent effective magnetic moment, in addition to spin-spin relaxation contributions that are proportional to the spin density at the site, due to the Fermi contact, isotropic and anisotropic exchange contributions. The effect of spin localisation is therefore observed as an increase in the effective magnetic moment at the electronic site due to spin-orbit and spin-spin coupling contributions. Assuming that this effect is dominated by $t_{1e}$, the linear behaviour suggests the contribution is associated with a one-phonon relaxation process, which usually dominates at high temperatures and has the opposite gradient. We therefore tentatively propose that the apparent linear contribution corresponds to the effective spin density at the $\mathrm{V}_{\mathrm{V}}'$ trapping sites, where spin-orbit coupling is non-negligible.

The behaviour of the $g$ tensor over the temperature range $T = 4$-370 K was also investigated and is presented in Figure 5.6. The apparent $g$ values are shifted away from free-spin via spin orbit coupling, and therefore any change in these values is characteristic of a change of the local electronic environment. At high temperatures, a quasi-axial symmetry is observed with two inequivalent components. However, upon lowering of the temperature, the $g_{1,2}$ components diverge, exhibiting an asymmetry that is central to the averaged value at high temperatures. This averaging is attributed to the effective screening of the magnetic anisotropy due to the hopping transfer, which occurs on a timescale greater or comparable to $t_{1e}$.[45] Across most of the temperature range, the values remain effectively constant, until they diverge significantly approaching $T = 4$ K. The anisotropy between the $g_1$ and $g_2$ components, and additionally between the $< g_1 + g_2 >$ and $g_3$ components, increases dramatically.

This divergence provides further convincing evidence of the localisation of spin density, and subsequent increase in the spin-orbit and spin-spin coupling interactions, which was attributed to the linear dependence in the line width at low temperatures. The isotropic $g$ value deviates also to a slightly lower value, which is expected to be characteristic of the increasing population of the $\mathrm{V}_{\mathrm{V}}'$ sites formed via Li incorporation/ oxygen vacancy formation.

The effect of anisotropic exchange can similarly shift the $g$ value as a function of temperature due to the mixing of excited states via spin-orbit coupling.[46] This effect also likely contributes an important role in the inter-electronic coupling mechanism, however this is difficult to probe in the situation of a disordered system. Finally, the observed deviation of the $g$ values illustrates the averaging of disorder within the system due to the exchange and hopping processes.

Concerning the nature of the exchange coupled states, comparing back to the schemes presented in equations 5.1 and 5.2, the $\mathrm{V}_{\mathrm{V}}'$ site observed in VLB3 is attributed to the redistribution of charge carriers due to the incorporation of primary oxygen vacancy defects (1), rather than by Li incorporation from the minor phase, although these are likely to contribute significantly to the electronic conductivity also.

### 5.2.3 Variable Frequency study of high content sample

The line shape and structure of the VLB3 sample was further investigated at multiple microwave frequencies, in order to better resolve the $g$ tensor components. The resulting X-, Q- and W-band EPR spectra, recorded at $T$ = 20 K (X-,W-) and $T$ = 10 K (Q-), are presented in Figure 5.7. The variation of the line width, and values of g, was determined to be less than 5% (within error) at the two temperatures. At Q- and W-band frequencies, a rhombic $g$ tensor can be readily identified, as expected from the inequivalent equatorial directions depicted earlier in Figure 5.1.

A dominant Lorentzian line shape persists in these spectra, particularly at X-band. This can be attributed to the anisotropic spin relaxation processes resulting from magnetic anisotropy in the strong exchange limit. The X-, Q- and W-band EPR measurements were simulated and fitted simultaneously by taking into consideration the line width anisotropy and averaged resonant field positions for the exchange-coupled $V^{4+}$ site. The spin Hamiltonian used for simulation of the single dimension with two nearest neighbours, was of the following form:

$$\hat{H} = \sum_i g_i \mu_B B \hat{s}_i - 2J \hat{s}_i \cdot \hat{s}_j \tag{5.14}$$

Using this equation, any possible nuclear, hyperfine, anisotropic or antisymmetric exchange contributions, which were not resolved from the spectrum, were neglected in the simulation. Even the difference in Zeeman energies is effectively averaged along the hopping dimension, and therefore the inter-site disorder was not considered. For the W-band spectrum, it was necessary to include an additional simulation parameter to correct for the microwave phase, which is non-zero, although this was comparatively small.

The $g_1$ and $g_2$ anisotropy was already clearly resolved in the Q-band spectrum, thereby confirming the modelling results presented earlier based on the X-band spectra alone, where this anisotropy was not immediately resolved. The $g$ tensor parameters obtained from the simulations (those presented in Table 5.1 and Figure 5.2) were in good agreement with similar amorphous systems possessing a square pyramidal $V^{4+}$ symmetry.[31, 47] While the deviation away from the central values above $T$ = 20 K may be overestimated, this is nevertheless an indication of the increase in anisotropy. An analogous fitting at X and W band frequencies and $T$ = 290 K was also performed for comparison, Appendix 4, Figure 8, which are also presented in Figure 5.2.

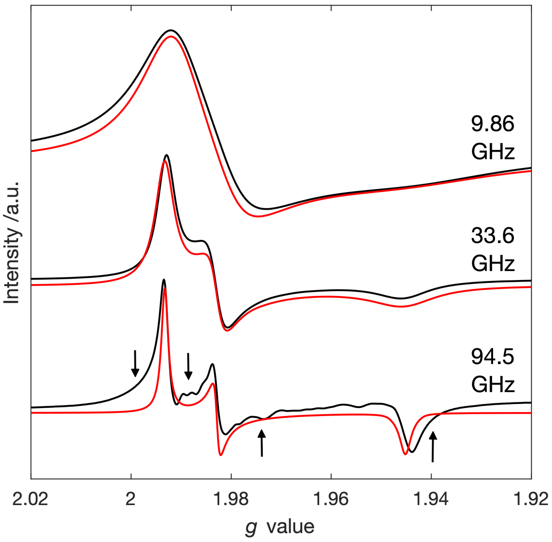

**Figure 5.7:** CW EPR spectra of VLB3 collected at X- (9.5 GHz) Q- (35 GHz) and W-band (95 GHz) frequencies, plotted on a $g$ scale for ease of comparison. The simulations presented are the result of simultaneous fitting at each microwave frequency. The black arrows indicate regions of the W-band spectrum not reproduced by the simulation, which are thought to arise due to disorder at the vanadium trapping sites.

A series of weakly resolved features were observed between the $g_1$ and $g_3$ components in the W-band spectrum. The origin of these features is not clear, and could arise from a number of factors, including distortions of the exchange-coupled sites away from co-linear orientations, residual hyperfine structure arising from trace concentrations of $VO^{2+}$ phases (observed in VLB1 and VLB2), and distinct, exchange-coupled species relating to unpaired electrons at the vanadium, oxygen, or vacancy sites.

The apparent line width of the $g_3$ component was observed to decrease on a $g$ scale (similar to the $g_1$, $g_2$ components) with increasing frequency. The fact that a frequency-independent line width was observed is also consistent with the explanation that the line broadening is relaxation-dominated. Several additional (frequency-independent) sources of broadening are possible for real, low dimensional systems such as unresolved hyperfine coupling, anisotropic and antisymmetric exchange contributions; $g$ anisotropy and crystal field effects.[48] The fact that angularly resolved measurements to a defined coordinate frame is not possible here, complicates the the process of determining which broadening mechanism occurs. None of these interactions were resolved across the entire temperature range studied here. Therefore, we suggest that the anisotropic line width arising from spin relaxation is a suitable model for the observed line broadening effects in the

VLB3 sample.

Another interesting feature not reproduced by the simulation are the asymmetric shoulders to low and high field of the $g_1$ and $g_3$ components (Figure 5.7. At $T$ = 20 K, increased anisotropy in the signal is apparent. The simulated Lorentzian line shape corresponds well to the centre of the turning points of the spectrum, and in contrast diverges asymmetrically within the wings of the line shape. This anisotropic line shape is attributed to the orientational disorder due to variations in the bond angle and length between random defect sites within the disordered network. As the hopping frequency tends to zero, this orientational strain would become more apparent, which would modulate the value of $g$ with a probability distribution rapidly vanishing towards the wings of the signal. For the room temperature spectrum at W-band, Appendix 4, Figure 8, a well defined Lorentzian line shape was observed for each of the tensor components indicating an averaging of the inter-site disorder due to the effect of the hopping process.

## 5.3 Conclusions

A series of $V_2O_5$–$LiBO_2$ mixed conductive glasses (abbreviated VLB1-3) were investigated using EPR spectroscopy. Understanding the local electronic structure, and its effect on the functional properties is critical in the understanding and design of more efficient materials, which is a critical driver in battery material research.

At low contents, an isolated $S = 1/2$ vanadium defect centre was observed at a network modifying position within the $LiBO_2$ matrix. The observed spin Hamiltonian parameters were consistent with a $V^{4+}$ centre possessing a distorted octahedral configuration, where the spin density primarily localised in the $d_{xy}$ ground state orbital. At high $V_2O_5$ content, a distinct exchange-narrowed signal was observed. This observation is consistent with the presence of a strongly polarised CESR/ one-dimensional exchange-coupled lattice with a distorted square pyramidal geometry (*i.e.* can be considered *ca.* $V_2O_5$ to short-range order). The species responsible for this site likely arises from defects formed from intrinsic oxygen vacancies in the disordered network, although the Li intercalation defect site is also likely a significant contribution.

Linewidth and $g$ tensor analysis of the EPR signals in VLB3 evidenced a marked temperature-dependent behaviour, consistent with the polaron hopping mechanism of electron transfer and inter-electronic exchange along the $g_3$ direction, which was proposed to be coincident with the electron transfer axis. At temperatures approaching the minimum observed linewidth, $T_{min}$, a deviation away from linear behaviour was observed, coincident with a dominant contribution from the hopping process. The activation energy was estimated as $E_a = 0.0805$ eV from the temperature dependence, which is consistent with other conducting glass systems. Separation of the underlying line width contributions were achieved based on a superposition model (including the Curie-Weiss law). The analysis identified contributions from the exchange interactions and an additional process for the $g_3$ component, which was attributed to the spin-orbit and spin-spin contributions to the relaxation upon transition to a localised state.

Finally, a relaxation-dominated line broadening mechanism was further supported by multi-frequency EPR measurements, which also identified unresolved features at high frequencies due to unaccounted for anisotropic exchange/ speciation within the disordered network. This analysis presents a straight-forward method for the use of EPR to investigate solid-state glassy materials and to understand their functional properties.

## 5.4 Experimental

**Materials and Methods:** All precursors were used as-received without further purification.

**Synthesis:** The $V_2O_5$ - $LiBO_2$ glass materials studied in this work were prepared via a melt-quench method. Analytical pure grade raw materials i.e. $V_2O_5$ (>99.6%, Aldrich) and $LiBO_2$ (99.9%, Alfa Aesar) were weighed according to the corresponding ratios of $V_2O_5$ to $LiBO_2$. The weighed raw material mixtures were thoroughly mixed using a Turbula Mixer for 45 minutes before they were placed in Pt crucibles and heated in a muffle furnace to 900°C for 60 minutes. To prevent the crystallisation due to the slow cooling rate, homogeneous melts were poured directly into baskets containing liquid nitrogen. The produced ingots were then crushed and dry-milled using a high energy planetary mill. The whole milling process consisted of 20 minutes using 20 mm diameter YSZ milling balls and consequently 3mm diameter beads for 40 minutes respectively, which gave rise to powders of suitable particle sizes characterised by EPR spectroscopy.

**Continuous-Wave (CW) EPR spectroscopy:**
**X-band measurements:** The X-band (9 GHz) CW-EPR spectra were recorded at 120 K on a Bruker EMX spectrometer, operating at 100 kHz field modulation frequency; 0.6325 mW microwave power; 1 G modulation amplitude using an ER 4119HS cavity. Approximately 50 mg of each sample was packed in a 3.8mm I.D. quartz cell.
**Q-band measurements:** The Q-band (35 GHz) CW-EPR spectra was recorded at 20 K on a Bruker E500 spectrometer operating at 100 kHz field modulation frequency; 0.005 mW microwave power; 1 G modulation amplitude, using a Bruker ER5106 QT-E resonator. The samples were individually packed into a 1.2 mm I.D. quartz cell.
**W-band measurements:** The W-band (95 GHz) CW-EPR spectra were recorded at 20 K and 300 K on a Bruker E600 spectrometer operating at 100 kHz field modulation frequency; 0.005 mW microwave power; 1 G modulation amplitude, using a E600-1021H TeraFlex resonator. Field calibration was performed using a BDPA standard at X-band, and the microwave frequency for spectra at W-band were adjusted accordingly by simultaneous fitting at the three microwave frequencies. The samples were packed in a 0.5 mm I.D. quartz cell.

**Variable Temperature (VT) study:** VT X-band EPR measurements were performed on the VLB3 sample, using a Bruker E500 spectrometer equipped with a ER 4119HS resonator and an Oxford instruments cryostat for the temperature range $T$ = 4-100 K. A saturation study was recorded to ensure that the operating microwave power was not within saturation. Field calibration was performed using a BDPA standard. The operating parameters were 100 kHz field modulation frequency, 0.6325 mW microwave power, and 1 G modulation amplitude. EPR measurements in the temperature range $T$ = 120-370 K were recorded on a Bruker EMX spectrometer equipped with a ER 4119HS resonator, as stated *vide infra*, with the same operating parameters used for $T$ = 4-100 K. The $Q$ value was checked to ensure a similar environment for the separate temperature ranges.

**Simulations and fitting:** Spectral simulations were performed using the EasySpin toolbox in MATLAB developed at ETH Zurich.[49] The simulation models used to reproduce the experimental data were as described in the text *vide infra*.

# References

[1] Leigang Li, Qi Shao, and Xiaoqing Huang. Amorphous Oxide Nanostructures for Advanced Electrocatalysis. *Chemistry – A European Journal*, 26(18):3943–3960, March 2020.

[2] Sengeni Anantharaj and Suguru Noda. Amorphous Catalysts and Electrochemical Water Splitting: An Untold Story of Harmony. *Small*, 16(2):1905779, 2020.

[3] Yuan-Chao Hu, Chenxiang Sun, and Chunwen Sun. Functional Applications of Metallic Glasses in Electrocatalysis. *ChemCatChem*, 11(10):2401–2414, May 2019.

[4] Se-Hee Lee, Hyeonsik M. Cheong, Maeng Je Seong, Ping Liu, C. Edwin Tracy, Angelo Mascarenhas, J. Roland Pitts, and Satyen K. Deb. Microstructure study of amorphous vanadium oxide thin films using raman spectroscopy. *Journal of Applied Physics*, 92(4):1893, July 2002.

[5] Kang Ill Cho, Sun Hwa Lee, Ki Hyun Cho, Dong Wook Shin, and Yang Kuk Sun. $Li_2O$-$B_2O_3$-$P_2O_5$ solid electrolyte for thin film batteries. *Journal of Power Sources*, 163(1):223–228, December 2006.

[6] Kihyun Cho, Teawon Lee, Jangwon Oh, and Dongwook Shin. Fabrication of $Li_2O$-$B_2O_3$-$P_2O_5$ solid electrolyte by aerosol flame deposition for thin film batteries. *Solid State Ionics*, 178(1):119–123, January 2007.

[7] M. Helena Braga, Andrew J. Murchison, Jorge A. Ferreira, Preetam Singh, and John B. Goodenough. Glass-amorphous alkali-ion solid electrolytes and their performance in symmetrical cells. *Energy & Environmental Science*, 9 (3):948–954, 2016.

[8] Nicholas B. Wyatt and Matthew W. Liberatore. The effect of counterion size and valency on the increase in viscosity in polyelectrolyte solutions. *Soft Matter*, 6(14):3346–3352, 2010.

[9] Ryoichi Komiya, Akitoshi Hayashi, Hideyuki Morimoto, Masahiro Tatsumisago, and Tsutomu Minami. Solid state lithium secondary batteries using an amorphous solid electrolyte in the system $(100\text{-}x)(0.6Li_2S \cdot 0.4\,SiS_2) \cdot xli_4sio_4$ obtained by mechanochemical synthesis. *Solid State Ionics*, 140(1):83–87, March 2001.

[10] C. H. Lee, K. H. Joo, J. H. Kim, S. G. Woo, H. J. Sohn, T. Kang, Y. Park, and J. Y. Oh. Characterizations of a new lithium ion conducting $Li_2O$-$SeO_2$-$B_2O_3$ glass electrolyte. *Solid State Ionics*, 149(1):59–65, July 2002.

[11] Semih Afyon, Frank Krumeich, Christian Mensing, Andreas Borgschulte, and Reinhard Nesper. New High Capacity Cathode Materials for Rechargeable Li-ion Batteries: Vanadate-Borate Glasses. *Scientific Reports*, 4:7113, November 2014.

[12] Yoji Sakurai, Toshiro Hirai, Shigeto Okada, Takeshi Okada, Jun-ichi Yamaki, and Hideaki Ohtsuka. Lithium battery including vanadium pentoxide base amorphous cathode active material. *U.S. Patent*, 1(US4675260A), June 1987.

[13] Masashi Inamoto, Hideki Kurihara, and Tatsuhiko Yajima. Electrode Performance of Vanadium Pentoxide Xerogel Prepared by Microwave Irradiation as an Active Cathode Material for Rechargeable Magnesium Batteries. *Electrochemistry*, 80(6):421–422, 2012.

[14] Timothy S. Arthur, Keiko Kato, Jason Germain, Jinghua Guo, Per-Anders Glans, Yi-Sheng Liu, Daniel Holmes, Xudong Fan, and Fuminori Mizuno. Amorphous $V_2O_5$-$P_2O_5$ as high-voltage cathodes for magnesium batteries. *Chemical Communications*, 51(86):15657–15660, October 2015.

[15] Aishuak Konarov, Hee Jae Kim, Jae-Hyeon Jo, Natalia Voronina, Yongseok Lee, Zhumabay Bakenov, Jongsoon Kim, and Seung-Taek Myung. High-Voltage Oxygen-Redox-Based Cathode for Rechargeable Sodium-Ion Batteries. *Advanced Energy Materials*, 10(24):2001111, 2020.

[16] Jenny Faucheu, Elodie Bourgeat-Lami, and Vanessa Prevot. A Review of Vanadium Dioxide as an Actor of Nanothermochromism: Challenges and Perspectives for Polymer Nanocomposites. *Advanced Engineering Materials*, 21 (2):1800438, 2019.

[17] Nicole Johnson, Gene Wehr, Eric Hoar, Siyu Xian, Ugur Akgun, Steve Feller, Mario Affatigato, Jose Repond, Lei Xia, Burak Bilki, and Yasar Onel. Electronically Conductive Vanadate Glasses for Resistive Plate Chamber Particle Detectors. *International Journal of Applied Glass Science*, 6(1):26–33, 2015.

[18] Jerome H. Perlstein. A dislocation model for two-level electron-hopping conductivity in $V_2O_5$: Implications for catalysis. *Journal of Solid State Chemistry*, 3(2):217–226, May 1971.

[19] A. K. Bandyopadhyay, J. O. Isard, and S. Parke. Polaronic conduction and spectroscopy of borate glasses containing vanadium. *Journal of Physics D: Applied Physics*, 11(18):2559–2576, December 1978.

[20] D. Maniu, T. Iliescu, I. Ardelean, I. Bratu, and C. Dem. Studies of borate vanadate glasses using Raman and IR spectroscopy. *Stud. Univ. Babes-Bolyai, Phys*, pages 366–371, 2001.

[21] O Cozar, I Ardelean, I Bratu, S Simon, C Craciun, L David, and C Cefan. IR and EPR studies on some lithium-borate glasses with vanadium ions. *Journal of Molecular Structure*, 563-564:421–425, May 2001.

[22] Zhi Ren Xiao, Guang Yu Guo, Po Han Lee, Hua Shu Hsu, and Jung Chun Andrew Huang. Oxygen Vacancy Induced Ferromagnetism in $V_2O_{5-x}$. *Journal of the Physical Society of Japan*, 77(2):023706, February 2008.

[23] D. Dreifus, M. P. F. Godoy, A. C. Rabelo, A. D. Rodrigues, Y. G. Gobato, P. C. Camargo, E. C. Pereira, and A. J. A. de Oliveira. Antiferromagnetism induced by oxygen vacancies in $V_2O_5$ polycrystals synthesized by the Pechini method. *Journal of Physics D: Applied Physics*, 48(44):445002, October 2015.

[24] Kit McColl, Ian Johnson, and Furio Corà. Thermodynamics and defect chemistry of substitutional and interstitial cation doping in layered $\alpha$-$V_2O_5$. *Physical Chemistry Chemical Physics*, 20(22):15002–15006, June 2018.

[25] Karen E. Swider-Lyons, Corey T. Love, and Debra R. Rolison. Improved lithium capacity of defective $V_2O_5$ materials. *Solid State Ionics*, 152-153: 99–104, December 2002.

[26] J. Krzystek, Andrew Ozarowski, Joshua Telser, and Debbie C. Crans. High-frequency and -field electron paramagnetic resonance of vanadium(IV, III, and II) complexes. *Coordination Chemistry Reviews*, 301-302:123–133, October 2015.

[27] J.E. Garbarczyk, L. Tykarski, P. Machowski, and M. Wasiucionek. EPR studies of mixed-conductive glasses in the $AgIAg_2O$-$V_2O_5$-$P_2O_5$ system. *Solid State Ionics*, 140(1-2):141–148, March 2001.

[28] N. S. Saetova, A. A. Raskovalov, B. D. Antonov, T. V. Yaroslavtseva, O. G. Reznitskikh, E. V. Zabolotskaya, N. I. Kadyrova, and A. A. Telyatnikova. Conductivity and spectroscopic studies of $Li_2O$-$V_2O_5$-$B_2O_3$ glasses. *Ionics*, pages 1–10, January 2018.

[29] O. Cozar, I. Ardelean, and Gh. Ilonca. EPR and magnetic susceptibility studies of vanadium lead-borate glasses. *Materials Chemistry*, 7(6):755–765, November 1982.

[30] Young Hoon Kim, Tae Ho Noh, Jae Peel Kang, Sung Duk Hong, Deok Choi, and Seung Kee Song. Epr investigation of $V^{4+}$ions in $GeO_2$-$B_2O_3$-$V_2O_5$ glasses and polycrystalline compounds. *Journal of the Korean Physical Society*, 62 (6):906–911, March 2013.

[31] C. S. Sunandana and A. K. Bhatnagar. An ESR study of hopping conduction in the glass system $V_2O_5$-$MO_2$ (M=Ge, Se, Te). *Journal of Physics C: Solid State Physics*, 17(3):467, 1984.

[32] A. Sheoran, A. Agarwal, S. Sanghi, V. P. Seth, S. K. Gupta, and M. Arora. Effect of $WO_3$ on epr, structure and electrical conductivity of vanadyl doped $WO_3 \cdot M_2O \cdot B_2O_3$ (m = li, na) glasses. *Physica B: Condensed Matter*, 406(23): 4505–4511, December 2011.

[33] V. P. Seth, A. Yadav, and Prem Chand. ESR of vanadyl ions in borate glasses. *Journal of Non-Crystalline Solids*, 89(1):75–83, 1987.

[34] G. L. Narendra, J. Lakshmana Rao, and S. V. J. Lakshman. Esr and optical absorption spectra of $VO^{2+}$ ions in $Na_2SO_4$-$ZnSO_4$ glasses. *Solid State Communications*, 77(3):235–237, 1991.

[35] D. Sreenivasu, N. Narsimlu, G. S. Sastry, and V. Chandramouli. Epr study of $VO^{2+}$ ions in lithium-lanthanum borate glasses. *physica status solidi (a)*, 143(2):K107–K110, June 1994.

[36] Daniel Kivelson and Robert Neiman. ESR Studies on the Bonding in Copper Complexes. *The Journal of Chemical Physics*, 35(1):149–155, July 1961.

[37] Daniel Kivelson and Sai-Kwing Lee. ESR Studies and the Electronic Structure of Vanadyl Ion Complexes. *The Journal of Chemical Physics*, 41(7):1896, 2004.

[38] J. R Morton and K. F Preston. Atomic parameters for paramagnetic resonance data. *Journal of Magnetic Resonance (1969)*, 30(3):577–582, 1978.

[39] P. W. Anderson and P. R. Weiss. Exchange Narrowing in Paramagnetic Resonance. *Reviews of Modern Physics*, 25(1):269–276, January 1953.

[40] L. Murawski, C. Gledel, C. Sanchez, J. Livage, and J.P. Audières. Electrical conductivity of $V_2O_5$ and $Li_xV_2O_5$ amorphous thin films. *Journal of Non-Crystalline Solids*, 89(1-2):98–106, January 1987.

[41] A. Zorko, F. Bert, A. Ozarowski, J. van Tol, D. Boldrin, A. S. Wills, and P. Mendels. Dzyaloshinsky-Moriya interaction in vesignieite: A route to freezing in a quantum kagome antiferromagnet. *Physical Review B*, 88(14):144419, October 2013.

[42] Sushil K. Misra, Sergey I. Andronenko, Saket Asthana, and Dhirendra Bahadur. A variable temperature epr study of the manganites $(La_{(1/3}Sm_{2/3})_{2/3}Sr_xBa_{0.33-x}MnO_3$ (x = 0.0, 0.1, 0.2, 0.33): Small polaron hopping conductivity and Griffiths phase. *Journal of Magnetism and Magnetic Materials*, 322(19):2902–2907, October 2010.

[43] Hazime Mori. Transport, Collective Motion, and Brownian Motion. *Progress of Theoretical Physics*, 33(3):423–455, March 1965.

[44] V. I. Krinichnyi, P. A. Troshin, and N. N. Denisov. The effect of fullerene derivative on polaronic charge transfer in poly(3-hexylthiophene)/fullerene compound. *The Journal of Chemical Physics*, 128(16):164715, April 2008.

[45] Aránzazu Aguirre, Peter Gast, Sergey Orlinskii, Ikuko Akimoto, Edgar J. J. Groenen, Hassane El Mkami, Etienne Goovaerts, and Sabine Van Doorslaer. Multifrequency EPR analysis of the positive polaron in I2-doped poly(3-hexylthiophene) and in poly[2-methoxy-5-(3,7-dimethyloctyloxy)]-1,4-phenylenevinylene. *Physical Chemistry Chemical Physics*, 10(47):7129–7138, December 2008.

[46] Andrej Zorko. Determination of Magnetic Anisotropy by EPR. In Ahmed M. Maghraby, editor, *Topics From EPR Research*. IntechOpen, February 2019.

[47] E. Gillis and E. Boesman. E. P. R.-Studies of $V_2O_5$ Single Crystals. I. Defect Centres in Pure, Non-stoichiometric Vanadium Pentoxide. *physica status solidi (b)*, 14(2):337–347, 1966.

[48] Alessandro Bencini and Dante Gatteschi. *Electron Paramagnetic Resonance of Exchange Coupled Systems*. Springer-Verlag, 1990.

[49] Stefan Stoll and Arthur Schweiger. EasySpin, a comprehensive software package for spectral simulation and analysis in EPR. *Journal of Magnetic Resonance (San Diego, Calif.: 1997)*, 178(1):42–55, January 2006.

# Chapter 6

# *ex situ* EPR characterisation of electrode materials for Li-ion batteries

## 6.1 Introduction

Rechargeable batteries are currently an intensive area of research, not only for developing new technological solutions for renewable feedstocks and pollution reduction, but also in the field of advanced energy storage devices.[1] The discovery of the $LiCoO_2$ (LCO) electrode material, which enabled the advent of commercial rechargeable batteries, was in part based on the work of Whittingam on Li intercalation hosts,[2] in addition to Goodenough's work on the *electronic* and *magnetic* behaviour of transition metal oxides.[3–6]

Furthermore, another important consideration in the optimisation of materials for Li-ion battery (LIB) electrodes is the control of the defect chemistry. This further regulation of the electronic structure, through structural features such as cationic, anionic vacancies and heteroatom doping, has been intensively researched recently, not only for LIB,[7, 8] but also in the field of electrocatalysis.[9] As exemplified in earlier Chapters in this Thesis, EPR spectroscopy is one of the essential tools that can be used for direct interrogation of defects in the solid state.[9]

A critical aspect of the magnetic interactions of transition metal (TM) based electrode materials are the extended exchange coupling pathways, which can mediate the localisation and electron transfer processes associated with the paramagnetic centres. An example of this effect is illustrated in Figure 1.1. Since many open-shell sites are often present, this in turn can lead to the formation of a percolating network of exchange interactions,[10] which can be strong compared to the Zeeman energies. This in turn can lead to an averaging of site disorder, and hence a loss of information about the system under investigation.

The intrinsic and perturbed electronic structure is therefore interconnected with the bulk properties of the material, for which EPR and magnetometry become ideal techniques for screening and understanding.[11] The application of EPR into research of battery materials is therefore attracting increasing attention.[10, 12–14] An overview of some of the recent research developments in this area, specifically, the application of EPR spectroscopy in the interrogation of these battery materials, was presented in Chapter 1.

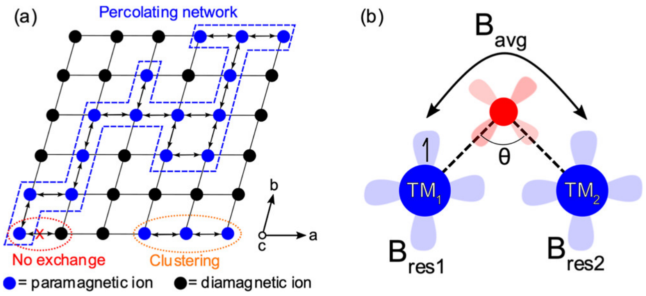

**Figure 6.1:** (a) Cationic lattice of paramagnetic battery electrode material, illustrating the formation of an extended network of exchange couplings between transition metal centres in a matrix of diamagnetic cations. Clustering of magnetic moments is also an important consideration in these materials (*Lower Right*). (b) Schematic illustration of the typical super-exchange pathways, involving d orbitals on the transition metals (TM), and formation of overlap on a diamagnetic bridging atom (O). Figure reprinted with permission from reference [10]. ©Copyright 2020 American Chemical Society.

In this Chapter, a systematic investigation of Li-ion cathode (labelled LFP) and anode (labelled LTO, NTO) materials was therefore undertaken to better understand the relationship between preparation and performance. EPR spectroscopy was to directly probe the nature of the redox sites, defects and impurities in the materials, in order to correlate the electronic properties with their local magnetic structure. The investigation was supported with multi-frequency EPR analysis (to resolve inaccessible transitions), variable temperature measurements (to indirectly probe their magnetic properties) and finally electrochemical measurements (to underpin the EPR investigation, and to further correlate their structure-function relationship).

## 6.2 Results and Discussion

### 6.2.1 Background to the $LiFePO_4$ (LFP) cathode materials

$LiFePO_4$ (hereafter labelled LFP) is a widely used commercialised cathode material for Li-ion batteries due to its high theoretical capacity ($\approx$ 170 $mAh\,g^{-1}$), acceptable operating potential window (2 - 4.1 V *v.s.* $Li/Li^+$), long cycle life, excellent stability and widely available precursors.[15] LFP possesses an olivine-type orthorhombic structure containing $LiO_6$ and $FeO_6$ octahedral units, and $PO_4$ tetrahedra (Figure 1.2). The Li ions intercalate along the 1D pathways. The $FeO_6$ octahedra are significantly distorted, with axial bond lengths of 2.204 and 2.2108 Å, and equatorial bond lengths of 2.251 and 2.064 Å.[16] The LFP material also possesses a relatively low electronic conductivity, and therefore requires the addition of carbon coatings and conductive additives in the electrode formulation, in order to reduce the resistivity of the cell.[17].

The predominant form of iron in the cathode material is $LiFe^{2+}PO_4$, which is in principle detectable with EPR in the high-spin state ($S = 2$). However, signals pertaining to $Fe^{2+}$ are rarely observed at conventional microwave frequencies ($\nu_{MW} = 9$ GHz, X-band) due to several considerations, including large ZFS interactions (which increase quadratically in non-Kramers ions), quenching of the total angular momentum by the orbital moment ($L = S = 2$; $J = 0$),additional exchange couplings to other electronic moments in the lattice, and subsequent fast spin relaxation times, leading to broadening beyond detection.

The combination of these effects typically raises the transition energies above the accessible microwave frequencies, and contributes to fast relaxation times, which broadens the line width beyond detection. To add to these complications, the intrinsically conductive nature of these materials, acts to exacerbate these effects. Firstly, the relative mobility of the unpaired spin density leads to a short $T_{1e}$ time. In addition, the penetration depth of the microwave quanta is limited due to the microwave skin depth (on the order of $\mu m$ at X-band), which in turn limits the sensitivity of the EPR technique to the surface of the material, thus limiting the effective spin density accessible to probe.

Iron is also present as high-spin $Fe^{3+}$ ($S = 5/2$, ground state ${}^6S_{5/2}$), in the delithiated form, $Fe^{3+}PO_4$, and in impurities such as $Fe_2O_3$. In contrast, $Fe^{3+}$ is often readily observable by EPR, but suffers from very broad signals (due to the interactions outlined above), and an absence of hyperfine coupling due to the low abundance of spin active nuclei (≈2% ${}^{57}$Fe, $I = 1/2$). The ZFS parameters of these systems is often greater than the quantum limit (*i.e.* $\nu_{MW} \ll D/\hbar$), the weak field condition is met and the only allowed transition originates from within

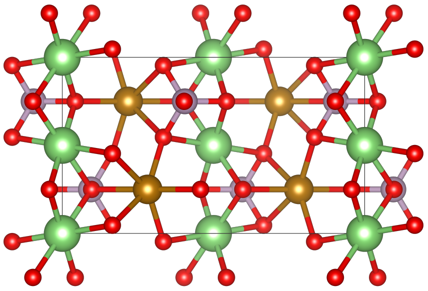

**Figure 6.2:** Schematic illustration of the LFP unit cell along the c axis. Reproduced using neutron diffraction data from reference [18], available on the Crystallography Open Database (COD)[19–22] *Red:* O; *Orange:* Fe; *Pink:* P; *Green:* Li.

the $|S, m_s\rangle = |5/2, \pm 1/2\rangle$ doublet ($\Delta m_s = +1/2 \leftrightarrow -1/2$). The examination of high spin systems at conventional microwave frequencies is therefore often treated as an effective $S_{eff}$ =1/2 system and the full electronic structure is not accessed. In contrast, low spin Fe$^{3+}$ ($S = 1/2$) has a large orbital contribution with ground state $^2$D$_{5/2}$ and therefore a significant $g$ anisotropy, and a considerably narrower line width. These two spin states are therefore readily distinguished using EPR.

Since the main phase of LFP, LiFe$^{2+}$PO$_4$ is effectively 'EPR silent', then the presence of any signal in the steady state (*ca.* the unperturbed material) will be attributed to impurities and defects present in the sample as Fe$^{3+}$ for example. Several impurities ($Fe_2O_3$, $Fe_2P$ (silent), $FePO_4$, as well as $Li_3PO_4$, $Fe_2P_2O_7$, $Li_4P_2O_7$ and $Li_3Fe_2(PO_4)_2$) have been reported in the literature, which are highly sensitive to the preparative method employed.[23]

The LFP materials therefore represent an interesting class of compounds for study by EPR, to correlate the local electronic structure, to the bulk magnetic properties from magnetometry research, in addition to the electrochemical performance. A series of LFP materials, varying with the 'FeO' precursor used, were therefore initially investigated to determine the sensitivity of the impurity phases in the as-received samples depending on the preparative method (see Section 1.4 for details). The samples include LFP1 (bearing the $Fe_2O_3$ precursor), LFP2 (bearing the $Fe_3O_4$ precursor), LFP3 (bearing the FeO precursor) and finally LFP4 (bearing the $Fe(OH)_2$ precursor).

### 6.2.2 CW EPR analysis of the LFP starting materials

The series of carbon-coated LFP samples were measured at X-band ($\nu_{MW}$9 GHz), with $T$ = 120 K and 300 K, Figure 1.3. A distinct broadening of the observed EPR signals was generally observed at lower temperature, which is characteristic of both the magnetic ordering within the material and the fast spin relaxation times. The line broadening of the observed Fe$^{3+}$ signals was discussed earlier, and any signal observed readily confirms the presence of Fe$^{3+}$-type impurities of some form within the samples, either arising from unreacted precursors, or from undesired oxidation at the surface.

Each sample showed a very broad isotropic resonance, characteristic of high spin Fe$^{3+}$. Some of the signals were so broad that they could not be readily characterised at this frequency, and only the negative part of the first derivative signal is observed (*e.g.* LFP2 and LFP4, Figure 1.3). Additional weakly anisotropic signals at low field were also noticeable in some cases, indicative of a high spin Fe$^{3+}$

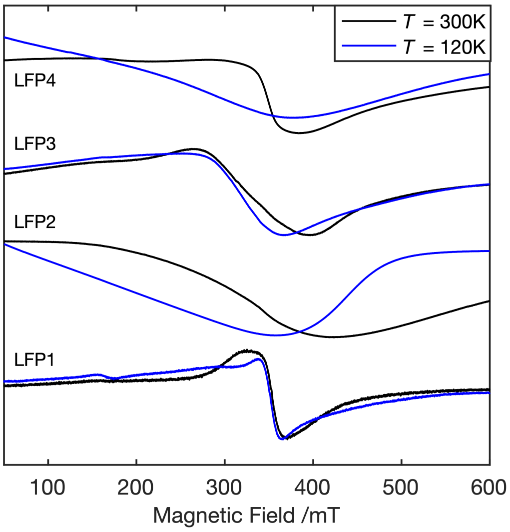

**Figure 6.3:** X-band EPR spectra, at $T$ = 120 K (blue) and 300 K (black), of the carbon-coated LFP samples (LFP1-4), synthesised using different Fe precursors.

species in a strong ($g_{eff}$ =4.3-9), low symmetry environments. The features were barely visible due to the dominating broad resonance arising from the near-cubic $Fe^{3+}$ site. The variance in line shape is characteristic of the varying local site distortion (ZFS), and exchange structure (to both "silent" $Fe^{2+}$ and "active" $Fe^{3+}$) which are indicative of the nature of the impurities formed in the materials and their local environment. Broader components about the central line shape likely arise from unresolved fine structure.

Some information on the site symmetry is provided by the observed effective $g$ value. In the samples investigated here, the dominating EPR feature is the broad signal of various line widths (varying according to preparative method and temperature) at $g_{eff} \approx 2.0$, extending to about $g_{eff} \approx 2.2$ for LFP3. In the weak field limit, This effective value is characteristic of a weakly distorted ligand field ($E/D = 0$), often found for Fe-oxide type environments.[24] The site symmetry of $LiFePO_4$ is orthorhombic, and therefore any impurity phase associated with $FePO_4$ is inconsistent with the apparent values. Additional structure, observed in the shoulders of the EPR signal, may be attributed to distinct impurity phases, and most certainly unresolved ZFS interactions. The only clear indication of an additional distinct phase is observed for the sample LFP1 at $T$ = 120K, bearing a feature at $g_{eff} \approx 4.3$ ($B_0 \approx 150$ mT), labelled by an arrow in Figure 1.3. This additional feature is characteristic of a low symmetry site with large axial dipolar interaction and $E/D = 1/3$, which is commonly seen for $Fe^{3+}$ containing materials.[25, 26] A lack of any resolved structure, such as that arising from hyperfine, ZFS or anisotropic exchange, prevents a clear distinction between coordination environments at X-band frequencies (9.5GHz), and thus any distinction between impurity phases is therefore challenging.

As a result, W-band EPR measurements was then performed on LFP3 at $T = 300$K in order to investigate the unresolved fine structure of the broad isotropic signal further. The frequency matching and coupling proved challenging at these high microwave frequencies. The measurement of the LFP3 sample was undertaken as a cut electrode strip for X-band, and as the scraped material from the film for W-band measurement (Figure 1.4).

The X-band spectrum of the printed film indicated some further unresolved features in the spectrum of LFP3, which were observed as a 'shoulder' in the middle of the broad resonance around $g_{eff} \approx 2$, characteristic of an additional phase in the material with $2 > g_{eff} > 4.3$ and an intermediate distorted environment ($0 < E/D < 1/3$).[25] There are comparatively few EPR examples of LFP materials published in the literature. Similar line shapes were observed in $LiCo_{(1-2x)}Ni_xMn_xO_2$ (NCM) electrode materials, which at high frequencies ($\nu_{MW} = 285$ GHz and $T = 5$ K), were resolved into two distinct metal sites at low doping concentrations.[27] Despite the different chemistry of the NMC material, the electron transport mechanism, and large ZFS parameters (compared to the Zeeman energies afforded by S-O coupling) are somewhat comparable. Within the free-spin region, $B_0 \approx 350$ mT, a narrow isotropic resonance is clearly resolved from the broader $Fe^{3+}$ line shape with $g = 2.002$. The narrow line width, indicative of comparatively long $T_{1e}$ and $T_{2e}$, is characteristic of a localised site which is attributed to a carbon additive-related defect.[28] Such signals are commonly observed in graphite materials and effect a pseudo-capacitive behaviour (non-Faradaic current) through the polarisation and storage of charge-carriers.

At W-band frequency, the observed EPR response is considerably different (Figure 1.4. Although the signal quality was poor, nevertheless an apparent fine structure across the field range $0.5 < B_0 < 4$ T was observed. Features at $g_{eff} \approx 2.066$, 3.289 and 5.784 were observed which likely arise from the presence of $Fe^{3+}$ impurities with weak, intermediate and strongly distorted environments respectively, with $D \gg h\nu_{MW}$ even at this higher frequency. However, due to the relatively poor resolution it was challenging to accurately simulate these species, and the possibility that this signal arises from a trace impurity in the resonator cannot be excluded. Additional EPR measurements of the unloaded resonator identified some weak features across the magnetic field range studied, however these were

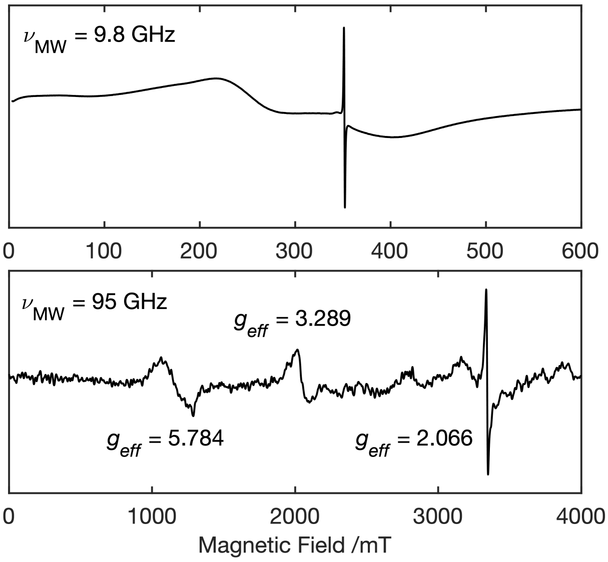

**Figure 6.4:** X-band (9.8 GHz) and W-band (95 GHz) CW EPR spectra of the carbon-coated LFP3 starting material at $T$ = 300K.

completely unresolved, and therefore it was not possible to provide a categorical distinction between these two possibilities.

Scanning electron microscopy (SEM) measurements, performed by staff at Johnson Matthey (JM), indicated the presence of iron-rich surface phases (see Appendix 5, Figure 2) on the surface of the LFP3 sample, that were not identified by XRD measurements of the material (Also performed by JM staff, Appendix 5, Figure 3). Assuming the apparent features observed at W-band arise from the sample, it is expected to be associated with this surface phase, which can be attributed to the non-incorporated Fe precursor, although the relative stoichiometry is challenging to determine as a result of the large $D$, $E$ values and lack of other identifying interactions such as $g$-anisotropy, or hyperfine structure.

### 6.2.3 Comparison of LFP printed electrode films at varied potential *v.s.* Li/Li$^+$

The magnetic properties were determined to be highly sensitive to the nature of the electrochemically perturbed material, and are further moderated by impurity phases such as those indicated *vide infra*, which can contribute room-temperature ordering transitions to the magnetic behaviour. Electrochemical cycling was therefore performed on assembled 2032 coin cells *ex situ* with the LFP3 printed film, to determine the sensitivity of the magnetic properties of upon perturbation of the electronic structure, and to potentially identify the associated lithiated phase $FePO_4$. After a standard testing protocol, the cells were stopped at varied circuit potentials, corresponding to the degree of delithiation at the WE. The electrodes were subsequently extracted from the cells to undertake the EPR measurements.

Figure 1.5 presents the GCD data from the final discharge step in the protocol, indicating the potential (and corresponding reversible capacity) at which the cells were stopped. Figure 1.6 then presents the corresponding EPR measurements at stopped potential. The EPR spectra are characterised by three main features, including: i) a signal at $g_{eff} \approx 4.3$, indicative of $Fe^{3+}$ in a low symmetry environment ( $E/D \approx 1/3$, $D \neq 0$); ii) a broad signal at $g_{eff} \approx 2$, characteristic of a near-cubic site symmetry and attributed to an 'FeO' impurity phase; iii) a narrow, isotropic resonance at $g \approx g_e$ which was attributed to a carbon additive related defect. The low symmetry $Fe^{3+}$ site was considerably better resolved after cycling than that observed in Figure 1.4 for the as-prepared film, which is attributed to the formation of surface $FePO_4$ *via* the irreversible loss of Li and subsequent reduction of the lattice site during the initial cycle. The broadening is expected to result from distributions in the $b_k^q$ parameters, in addition to the spin relaxation properties with respect to inter-site homogeneity, spin correlation, and electron transfer processes.

Comparing the spectra with respect to their cell potential, reveals that the three features are observed to be comparatively invariant within experimental error (See

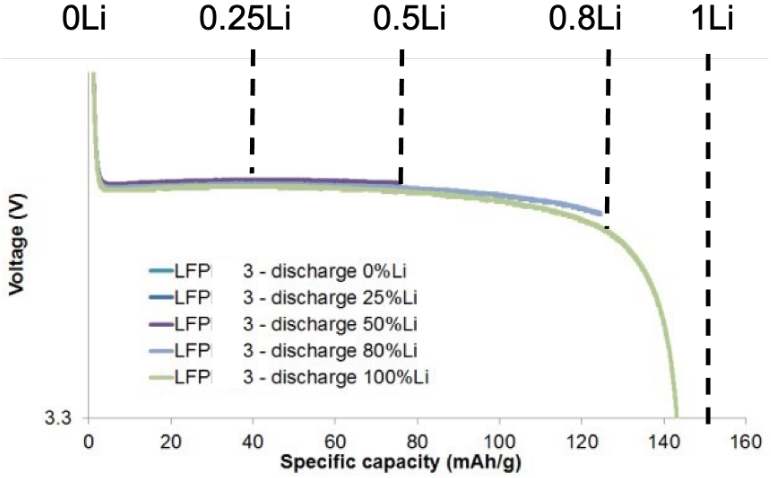

**Figure 6.5:** Stacked potential capacity plot of the final discharge step in the GCD protocol for the five LFP3 coin cells, cycled at low current rates (0.1C and 0.1D, respectively). The dashed lines indicate the potential values at which the cells were stopped, corresponding to the degree of delithiation in the LFP material (assuming 1 $e^-$ reduction).

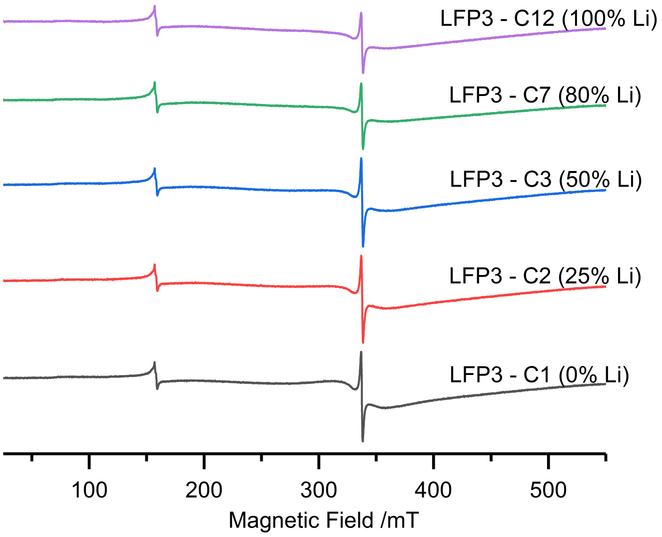

**Figure 6.6:** X-band CW EPR (120K) measurements of extracted LFP3 electrodes with varying degrees of lithiation. The active material was removed (scraped) from the surface of the foil and packed into a Q-band EPR tube. The sample height was ensured to be constant across the samples, due to the imprecision in mass correction ($m \approx 1 - 2mg$).

Appendix 5, Figure 5 for comparison of their integrated intensity). While the sensitivity of EPR is relatively high, the quantitative understanding of dynamic electrochemical processes are challenging. The sample mass was also relatively small which contributed a considerable error to the analysis of the integrals and signal intensities. Furthermore, the skin effect causes a lowering of the Q factor (despite the fact this was minimised), which also limits the available spins for sensitive detection. While this appears to support the assignment of an irreversible surface defect, this cannot be unambiguously assigned. It is also possible that the relaxation properties of the reversibly exchanged lattice site are too fast to detect, or that the spin density at the site is simply distributed *via* electron transfer. This illustrates the motivation for the development of *in situ* capabilities for the on-line generation and monitoring of such species.

### 6.2.4 $Li_4Ti_5O_{12}$ (LTO) and $TiNb_2O_7$ (NTO) anode materials

Graphite anode materials have been used since the first commercialisation of Li-ion batteries. However, they remain a challenging material to use, in part due to the considerable volume change upon intercalation/ deintercalation (≈ 10%),[29] low ionic conductivity[30] and propensity for lithium dendrite formation.[31] One of the critical limitations occurs under fast charging (high current density) conditions, where these effects are exacerbated significantly due to degradative processes. To address these considerations, alternative materials such as $Li_4Ti_5O_{12}$ (LTO) have been investigated intensively.

LTO is widely regarded as a "zero-strain" material due to its negligible volume change upon intercalation/ deintercalation. It therefore possesses excellent cycling stability and high redox potential which inhibits lithium dendrite formation. LTO has a defective spinel structure with a cubic space group, and is insulating due to the large band gap between the empty d-orbitals and filled oxygen p-states.[32]

Three Li ions can be incorporated per unit, providing a theoretical specific capacity of $Q_{theory}$ =175 mAh g$^{-1}$.[32] However, compared to graphite, the capacity is relatively low ($Q_{theory}$ = 372 mAh g$^{-1}$.[33] $TiNb_2O_7$ (NTO) is another possible anode candidate material as a result of its much higher capacity ($Q_{theory}$ = 387.6 mAh g$^{-1}$)[34] accommodating up to five Li ions per unit cell due to the action of Ti and Nb redox couples, including $Ti^{3+}/Ti^{4+}$ and $Nb^{3+}/Nb^{4+}/Nb^{5+}$. A comparison of the experimental specific capacity as a function of the $C$- (Charging) rate for LTO and two NTO half cells, varying in preparation, is presented in Figure 1.7. This data was collected by JM staff. This illustrates the challenge with the possible NTO materials, which also suffers from poor conductive properties, but also the capacity retention at high cycling rates diminishes significantly.

Concerning the redox couples for LTO and NTO, both $Ti^{3+}$ ($S = 1/2$, $I = 0$ for major isotope) and $Nb^{4+}$ ($S = 1/2$, $I = 9/2$) are paramagnetic, for which the

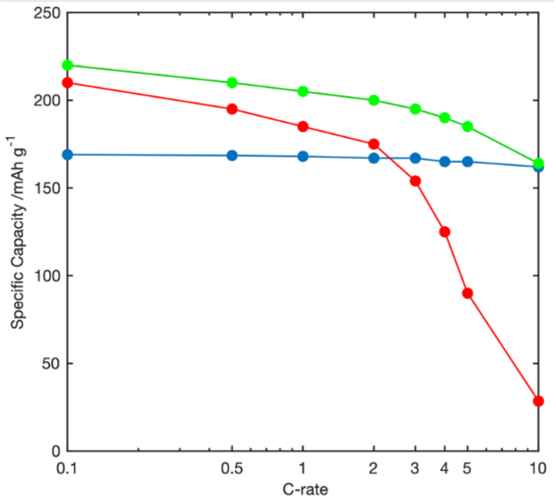

**Figure 6.7:** Specific capacity as a function of C-rate for LTO, NTO1 and NTO2, illustrating the reduced capacity for NTO at high cycling rates.

former is well characterised within the literature, particularly for $TiO_2$ materials in photocatalytic applications.[35–39] $Nb^{4+}$ on the other hand is observable using EPR, although only a few reports of this species have appeared in the literature to date.[36, 40] Due to fast spin relaxation kinetics, $Nb^{4+}$ is however rarely observed above $T$ = 20K and measurement of its magnetic properties can often be challenging.[41]

Therefore, in order to explore the role of EPR in the characterisation of these materials, and to correlate the local electronic structure, to the degradative and rate limiting elements of the electrode material from a steady-state perspective, a series of LTO and NTO samples, prepared from different precursors, were therefore investigated *ex situ*. These materials include:

1. $Li_4Ti_5O_{12}$ (hereafter labelled LTO), is a commercial material from Targray;
2. $TiNb_2O_7$ (labelled NTO1) is a JM material, prepared *via* flame spray pyrolysis from a niobium ethoxide precursor;
3. $TiNb_2O_7$ (labelled NTO2) is a JM material, prepared *via* flame spray pyrolysis from a niobium oxalate precursor.

In addition, NTO1 and NTO2 were found to have significantly different performances when cycled at high C rates (as shown in Figure 1.7). These materials were studied in particular to understand the structural changes involving defects generated under stress, and thereby determine the cause of capacity loss within the materials.

### 6.2.5 Comparison of LTO and NTO starting materials

The CW EPR spectra ($T$ = 120 K) for the LTO, NTO1 and NTO2 starting materials are presented in Figure 1.8 for comparison.

In the NTO1 sample, a sharp isotropic signal is observed near free spin at $g$ = 2.0035 with a well resolved Lorentzian line shape (Figure 1.8). The measured $g$ value indicates that the signal is likely a defect from the carbon additive. Some carbon-based radicals could be expected from the flame spray preparation method. For NTO2, Another sharp isotropic signal is also observed although not as well resolved due to the broad overlying signal. $g$ = 2.0024 indicates that this also likely arises carbon-based radical, however there is considerable uncertainty in the $g$ factor measurement at such small shifts from the free spin value.

The more dominant feature in the EPR spectrum is centred at $g$ = 1.954, which can be assigned to $Ti^{3+}$ aggregates in the sample. A similar assignment

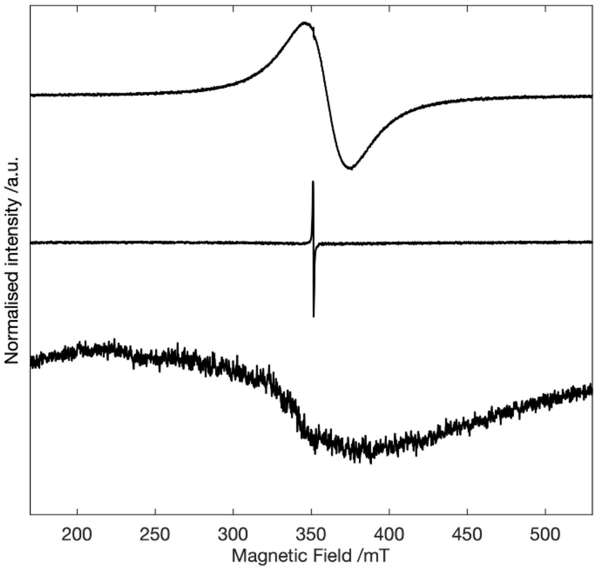

**Figure 6.8:** X-band CW EPR spectra ($T$ = 120 K) of the as-received LTO (*Bottom*), NTO1 and NTO2 (*Top*) starting materials. Signal intensities have been normalised for comparison.

of an analogous signal in lithum intercalated anatase has been proposed.[42] It is possible that the $Ti^{3+}$ aggregates is the cause of the reduced cell capacity when compared to NTO1. The broad signal line width of the signal may be attributed to one of two spin-spin interactions the anisotropic dipolar interaction from nearby $Ti^{3+}$ sites or alternatively, the strongly correlated exchange interactions of reduced lattice sites and disordered clusters within the material.

Finally, the LTO sample displays no observable EPR signals at the measurement temperatures employed (Figure 1.8). Only a weakly resolved signal is observed which may arise from transition metal impurities in the precursor materials. The screening of these starting materials provides a useful reference to present phases in the active material due to choice of preparation method, and in the understanding of perturbations effected by electrochemical cycling.

### 6.2.6 Reduction of LTO and NTO materials

In the native form of LTO, most of the Ti centres exist in the diamagnetic $Ti^{4+}$ form. Paramagnetic $Ti^{3+}$ surface species can therefore be readily generated by vacuum annealing, in order to compare the spectra of the $Ti^{3+}$ centres.The generation of oxygen vacancies at the particle surface causes charge trapping and compensation, resulting in the $Ti^{3+}$ sites in relatively isolated environments with a lack of nearby magnetic nuclei and spin-phonon coupling modes that influence relaxation. The X-band CW EPR spectrum ($T$ = 300 K) for the vacuum annealed LTO is therefore shown in Figure 1.9 (b).

Comparing the vacuum annealed sample in Figure 1.9 (b) to the native material, shown earlier in Figure 1.8, a clear change is observed in the EPR spectrum, with a well resolved axial signal of the order $g_1 = g_2 > g_3$ ($g_\perp > g_\parallel$). A good fit of the signal was obtained *via* simulation revealing the $g$ values of [1.989, 1.989, 1.964] which is typical for distorted octahedral $Ti^{3+}$ species reported in $TiO_2$ with $D_{4h}$ symmetry due to a tetragonal compression along the z-axis. The Ti-O bonds in the $x, y$-plane are almost identical as expected, presumably corresponding to the Ti-O-Ti lattice direction although this cannot be confirmed by powder measurements.[43, 44] As significantly higher vacuum annealing temperatures were required for NTO ($T > 1000$ K), it was not possible to repeat this experiment for the NTO sample.

Chemical reduction of the material, using a strong reducing agent such as *n*-BuLi, can also be used to generate reduced $Ti^{3+}$ centres in these materials.[45] Since n-BuLi has a potential of *ca.* 1 V vs. Li/$Li^+$,[46] it can efficiently reduce Nb and Ti centres without an applied bias, and also provides a source of $Li^+$ for intercalation and charge compensation. This approach has been used previously for spinel lithium titanate materials.[46] The incorporation of Li into NTO can be

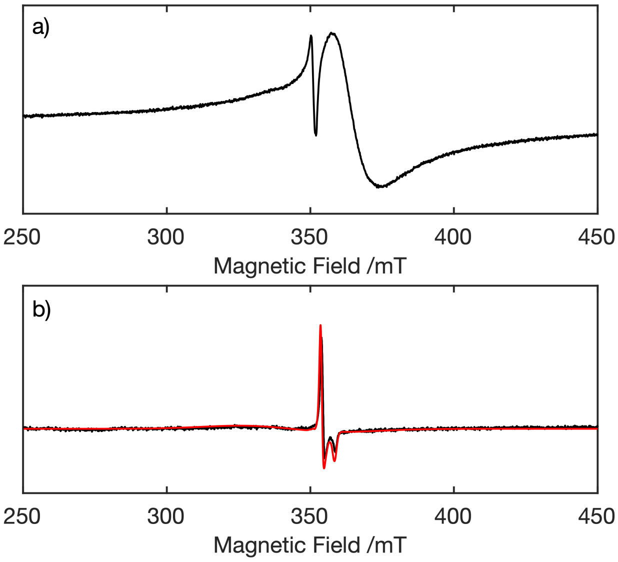

**Figure 6.9:** a) X-band CW EPR spectra ($T$ = 120 K) of NTO1 sample, after reaction with 3 *eq.* n-BuLi. The tube was sealed under an Argon atmosphere; b) X-band CW EPR spectrum ($T$ = 300 K) of LTO, vacuum annealed in a vacuum quartz tube ($P = 10^{-4}$ mbar; $T$ = 800K). *black:* experimental spectrum; *red:* simulated spectrum.

represented by the following equations:

$$Ti_{Ti}^{X} + O_{O}^{X} + Li^{+} + e' \rightleftharpoons Ti'_{Ti} + OLi^{\bullet} \tag{6.1}$$

$$Nb_{Nb}^{X} + O_{O}^{X} + Li^{+} + e' \rightleftharpoons Nb'_{Nb} + OLi^{\bullet} \tag{6.2}$$

at oxygen framework positions adjacent to the respective Nb and Ti redox sites. Two notable signals were present within the sample which changed upon n-BuLi addition. Firstly, a broad resonance (indicated A) appears at $B_0 = 360$ mT which was not observed in the reference sample. The signal intensity increases upon further addition of n-BuLi, and also undergoes a slight broadening. Secondly, a sharp isotropic signal (indicated B) is observed at $B_0 = 350$ mT which also increases in intensity upon n-BuLi addition.

The broad signal, A, appears to possess axial symmetry with perpendicular and parallel components that are not clearly resolved due to the line width. The $g$ values obtained were $g = [1.940\ 1.940\ 1.810]$ and have been attributed to tetragonally compressed octahedral $Ti^{3+}$ defect sites within the bulk of the material. Similar values have also been obtained for $Ti^{3+}$ in $LiTi_{1-x}(Nb_x)O_3$ materials.[40] The sharp isotropic signal B is similar to the most intense feature of the reference sample, which was assigned to an $OLi^{\bullet}$ centre, due to intercalation of Li at the framework oxygen sites. The observed $g$ value was found to be $g = 2.0035$, which is consistent with the reference material. The cause of these defect sites upon reduction with n-BuLi, and their significance is currently unclear. However, further studies monitoring the change in EPR signals upon addition of air to the sample (Appendix 5) indicated a dependence between the $OLi^{\bullet}$ signal, B, and the $Ti^{3+}$ signal, A, through defect formation and charge trapping at the local sites. Upon addition of air, a consecutive decrease in signal B was observed in addition to an increase in signal A, was attributed to the gradual reaction of Li at the $OLi^{\bullet}$ site with air (or moisture). The Li ion is abstracted from the site, and forms a seperate '$Li_2O$' or 'LiOH' type phase at the surface of the material. This process has been observed by XRD measurements previously.[46] The trapped electron at the $OLi^{\bullet}$ site is redistributed to form an additional $Ti'_{Ti}$ (or $Nb'_{Nb}$) site, thus accounting for the increase in signal A.

**Table 6.1:** Simulated $g$ tensor values for the observed defects and impurities in LTO, NTO1 and NTO2. All $g$ values are reported with a precision of ±0.001.

| Material | Species | Formation | $g_1$ | $g_2$ | $g_3$ |
|---|---|---|---|---|---|
| LTO | $\mathrm{Ti}'_{\mathrm{surface}}$ | annealing | 1.989 | 1.989 | 1.964 |
| | $\mathrm{V}_{\mathrm{O}}^{\bullet}$ | intrinsic | 2.0029 | 2.0029 | 2.0029 |
| | $\mathrm{OLi}^{\bullet}$ | electrochemical | 2.0032 | 2.0032 | 2.0032 |
| | carbon $\mathrm{O}^{\bullet}$ | intrinsic | 2.0025 | 2.0025 | 2.0025 |
| NTO1 | $\mathrm{Ti}'_{\mathrm{Ti}}$ | n-BuLi | 1.940 | 1.940 | 1.810 |
| | $\mathrm{OLi}^{\bullet}$ | n-BuLi | 2.0035 | 2.0035 | 2.0035 |
| | carbon $\mathrm{O}^{\bullet}$ | intrinsic | 2.0035 | 2.0035 | 2.0035 |
| NTO2 | $\mathrm{Ti}'_{\mathrm{imp}}$ | preparation | 1.954 | 1.954 | 1.954 |
| | $\mathrm{Ti}'_{\mathrm{Ti}}$ | electrochemical | 1.961 | 1.961 | 1.920 |
| | $\mathrm{OLi}^{\bullet}$ | electrochemical | 2.0025 | 2.0025 | 2.0025 |
| | carbon $\mathrm{O}^{\bullet}$ | intrinsic | 2.0031 | 2.0031 | 2.0031 |

### 6.2.7 Comparison of LTO and NTO printed electrode films at varied potentials

A series of LTO and NTO samples were also investigated after GCD cycling in the 2032 coin cells. The samples were stopped at cell potentials along the final charge step, and subsequently extracted for EPR measurement as in the case of LFP. The X-band CW EPR spectra (120 K) of the LTO samples, stopped at different 'states of charge' (SOC) are shown in Figure 1.11.

A well resolved isotropic signal centred near $g = 2.0029$ is observed in the spectrum for the cell 1 sample in the fully discharged state ("0Li"). Upon charging

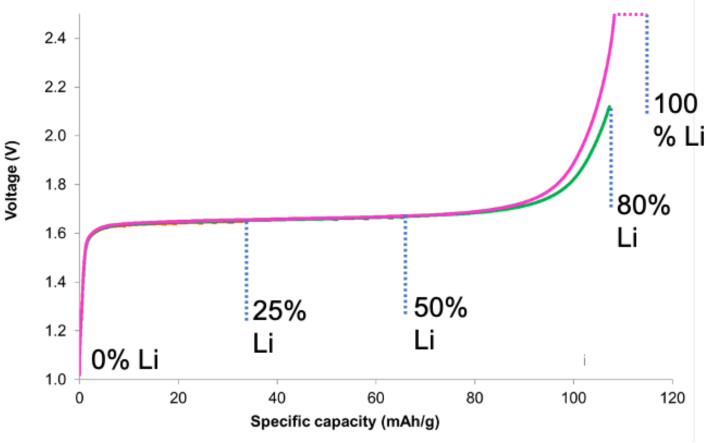

**Figure 6.10:** GCD measurements of LTO 2032 coin cells, final charge step indicating potentials at which cells were stopped and extracted for EPR measurements.

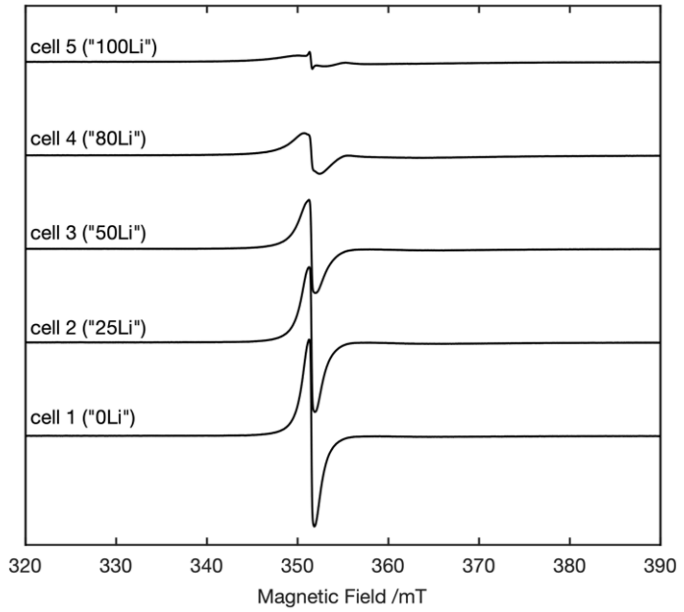

**Figure 6.11:** X-band CW EPR (120K) spectra of the harvested LTO coin cell samples (1-5), stopped at different states of charge.

of the cell, the observed isotropic signal at $g = 2.0029$ decreased in intensity as the cell potential was increased. This was attributed as a trapping oxygen vacancy site, $V_O^\bullet$, which is reduced to a diamagnetic state with increasing electron density in the conduction band of the material (and subsequent relaxation into the intra-band gap state). As the isotropic signal decreases further in intensity, the resolution of an increasing, broader signal at similar $g$ ($= 2.0032$) was observed from cell 1 to cell 3.

Finally, in the fully charged state (“100Li”), cell 5, another distinct isotropic signal with much smaller line width is observed in the centre of the superposed signals.This is assumed to remain constant upon change of cell potential. It also appeared that a weak shoulder to high field of the central resonance was observed beneath the more intense central line. In order to better resolve and identify the multiple signals identified, the EPR spectrum for this final sample (cell 5) along with the corresponding simulations can be found in Appendix 5.

The broader isotropic signal at $g = 2.0032$, which increased in intensity, was attributed to a trapped electron on an associated Li site, labelled $OLi^\bullet$, which was indicated to potentially play a role in charge compensation of the $Ti^{3+}$ lattice sites for NTO1 with n-BuLi. The narrower isotropic signal identified at higher cell potentials (cells 4 and 5) also appears at approximately $g = 2.0025$, and is attributed to the intrinsic carbon related defect from the carbon coating, labelled

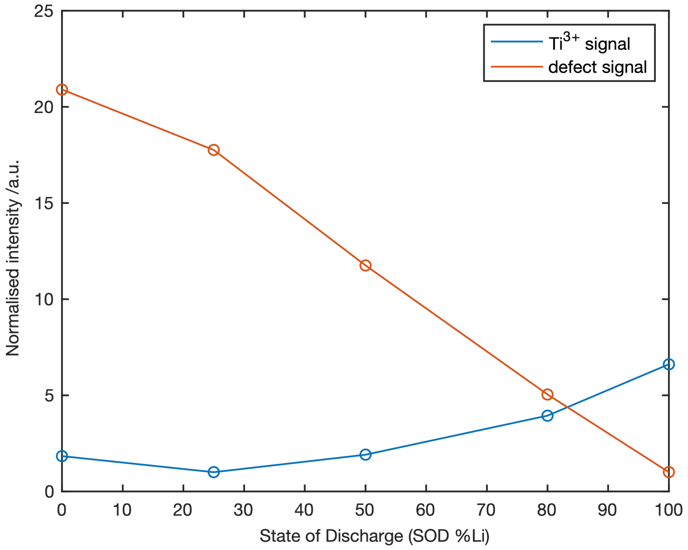

**Figure 6.12:** Normalised integrated EPR signal intensities of the LTO coin cell samples at varying states of charge (SOC). The connecting lines are presented as a guide for the eye.

C-O$^\bullet$ since this is not expected to change significantly during the variation of the applied bias. A minor perturbation in the baseline of the spectra (to higher field of the defect signals) was also observed, apparently increasing with the degree of charge. The origin of this feature is currently unknown due to the poor resolution. It appears at $g < g_e$, possessing approximate $g$ values of $g$ = [1.990 1.990 1.955], which could potentially be attributed to bulk Ti$^{3+}$ sites ($\mathrm{Ti}'_{\mathrm{Ti}}$), as seen for NTO. However, a clearly resolved signal for $\mathrm{Ti}'_{\mathrm{Ti}}$ was not observed at any temperature within the ranges investigated *vide supra*. The integrated signal intensities are shown in Figure 1.12, which indicate the variation in intensity for the identified signals.

An analogous experiment was performed on the NTO2 printed film sample in order to further investigate changes in redox state and defect structure upon cycling. The corresponding final charge step in the GCD measurements is presented in Figure 1.13. The X-band CW EPR spectra ($T$ = 120 K) of the NTO2 cell samples, stopped at different 'states of charge' (SOC) are shown in Figure 1.14.

For each sample, a similar set of features were observed in all spectra, including: i) a narrow isotropic signal close to free spin (around $B_0$ = 350 mT), either due to localised defects resulting from the n-type band structure for NTO, and ii) a broader, weakly anisotropic signal to slightly higher field attributed to the reduced Ti$^{3+}$ ($S = 1/2$) lattice sites. In the latter case, the simulated $g$ values of $g_1 = g_2 =$ 1.961 and $g_3$ = 1.920 are similar in each sample, which indicated an axial local spin environment, and a compressed octahedral coordination geometry with a $d_{xy}$ ground state ($g_{1,2}, > g_3$). The variation is relatively subtle in the line widths (related to relaxation processes). However, a consistent increase in signal intensity (proportional to spin concentration) was observed for the $\mathrm{Ti}'_{\mathrm{Ti}}$ site.

This increasing signal intensity was therefore characteristic of the lithiation and subsequent reduction of the bulk lattice sites. Finally, simulations performed on measurements indicated an approximate linear increase for the $\mathrm{Ti}'_{\mathrm{Ti}}$ site upon charging of the cell.

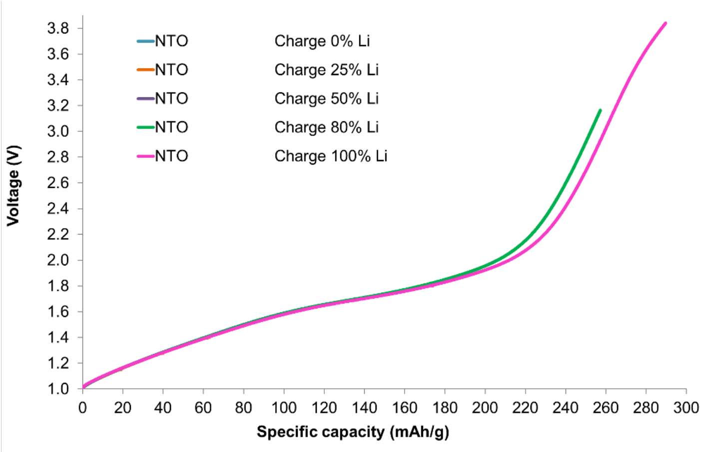

**Figure 6.13:** GCD measurements of the NTO2 2032 coin cells, final charge step indicating potentials at which cells were stopped and extracted for EPR measurements.

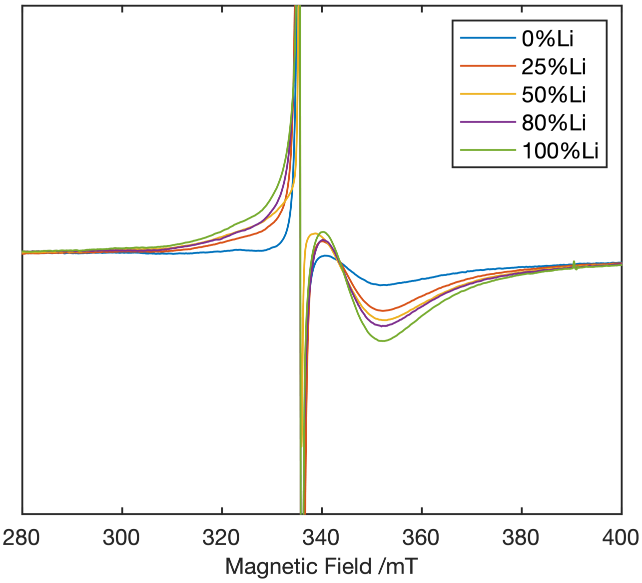

**Figure 6.14:** X-band CW EPR ($T$ = 120 K) spectra of harvested NTO2 coin cell samples, stopped at different states of charge.

### 6.2.8 Variable temperature EPR studies of LTO and NTO

The LTO material was further investigated at variable temperatures ($T$ = 4-100 K) in order to understand the bulk magnetic properties of the attributed $\text{OLi}^\bullet$ signal. The LTO sample was examined using EPR after stopped potential measurements, and reduced to approximately 80% of the capacity; hereafter this is labelled LTO80. The EPR spectra, and calculated integrated intensity as a function of temperature, are presented in Figure 1.15.

Upon decreasing of the temperature, a marked decrease in the signal intensity is observed, coinciding with the subsequent broadening of the signal, which reaches a minimum at *ca.* $T$ = 20 K, before subsequently increasing in intensity at $T$ = 4 K. The $g$ value of the signal was monitored across the temperature range, and was observed to be invariant within experimental error. Mapping the integrated signal intensity as a function of temperature reveals an exponential decrease in signal intensity approaching the minimum, before a sharp increase is observed for the last temperature point ($T$ = 4.3 K). The trend was identified to exponentially increase with temperature, and therefore was attributed to an Arrhenius type process (equations 1.3 and 1.4):

$$I(T) = I_0 + I_{ET} \tag{6.3}$$

$$I_{ET} \cdot T = A \cdot exp(-E_a/k_B T) \tag{6.4}$$

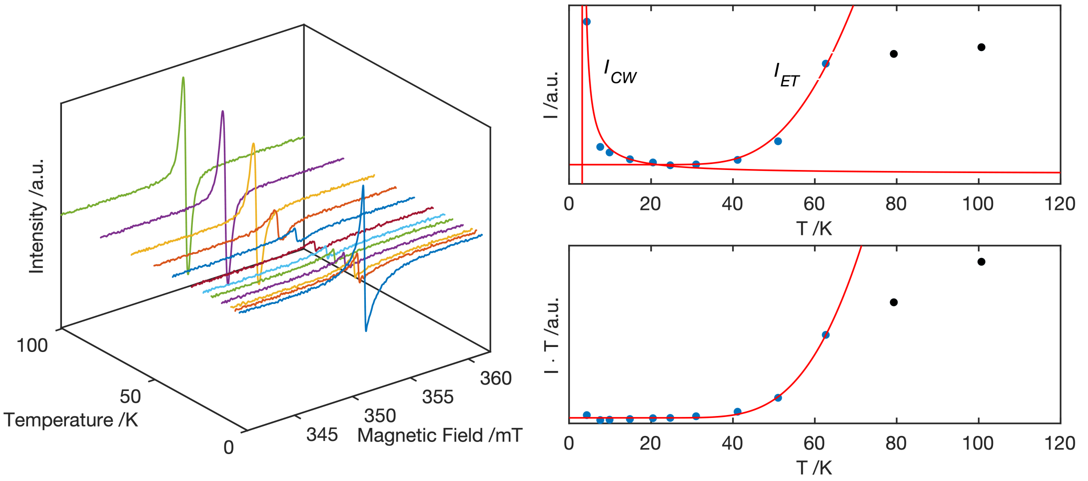

**Figure 6.15:** *Left:* X-band CW EPR spectra of the LTO80 sample measured at various temperatures; *Right:* Fitting of the calculated integral intensity (*Top*) and the product $I \cdot T$) as a function of temperature. *Blue circles:* experimental points; *Black circles:* excluded points from the least-squares fitting; *Red line:* Fitting results using equations 1.3 and 1.4.

where $E_a$ is the activation energy for the electron transfer process. For the OLi$^\bullet$ defects near the conduction band edge, charge carriers associated with the formation of extrinsic defects (due to the intercalation of Li) in the material may be thermally excited into the conduction band if the thermal energy $k_BT$ is sufficiently high. Upon decreasing the temperature, as the thermal energy available becomes much less than the associated energy barrier, the spin density will be localised at the trapping states, which results in interactions with the neighbouring spins, through dipolar and exchange interactions, in addition to spin orbit coupling, all of which in turn affect the spin-spin and spin-lattice relaxation properties. The observed behaviour at $T > 20$ K is therefore expected to be characteristic of this electron transfer process, and the parameters extracted from least-squares fitting to the product $I{\cdot}T$ from the experimental points gives an estimate of $E_a = 0.0324$ $\pm$ 0.005 eV, which is characteristic of the energy gap between the trapping state and the conduction band edge. A deviation from the model was noted at $T >$ 60 K, which may be due to the onset of an additional relaxation process. At low temperatures ($T < 20K$), a monotonic increase in signal intensity is observed approaching $T = 0$ K. This temperature region was fitted to the Curie-Weiss law, taking into account a temperature-independent contribution, $I_0$:

$$I_{CW} = I_0 + \frac{C}{T - \Theta_{CW}} \tag{6.5}$$

which can then be related to the isotropic exchange integral providing the number of nearest neighbours ($z$) and the effective spin ($S(S+1)$) is known:

$$3k_B\Theta_{CW} = 2JZS(S+1) \tag{6.6}$$

where $Z$ is the number of nearest-neighbour spins, which was kept constant (assuming 6-fold coordination, consistent with the octahedral arrangement in LTO and NTO) for comparison. The fitting of equation 1.5 to the integrated intensity *v.s.* $T$ provided values $\Theta_{CW} = +3.2$ K and an estimate of the isotropic exchange integral, $J = 0.278$ cm$^{-1}$ which suggested a weak ferromagnetic interaction between partially localised charge carriers in the material.

Finally, at temperatures approaching $T = 4$ K, the pronounced increase in signal intensity is accompanied by a notable asymmetry of the signal at approximately $g = 2.0012$. The origin of this signal is not immediately clear due to the superposition of the broad, unresolved isotropic signal identified at temperatures $T > 10$ K. This distinct signal may be associated with two considerations: i) polarisation of the unpaired spin density due partial localisation at the $\mathrm{Ti}_{\mathrm{Ti}}^{x}$ sites, resulting in a subsequent spin-orbit coupling contribution; ii) a Dyson line with A/B $\neq 1$, due to fast relaxing spins within the skin depth of the material, resolved due to the effect of lowering temperature on the spin relaxation processes. It is not straight forward to seperate these contributions without a more extensive examination of the EPR response approaching $T = 4$ K.

Variable temperature measurements between $T = 4$ - 125 K were also performed on an NTO2 electrode sample cycled ex situ and charged to a potential corresponding to approximately 80% of the reversible capacity (a reduction to $\mathrm{Ti}^{3+}$ and $\mathrm{Nb}^{4+}$ /$\mathrm{Nb}^{3+}$ redox states), hereafter labelled NTO80. An illustrative plot of the overlaid spectra taken at temperatures between $T = 4$ - 125 K can be found in Appendix 5, together with corresponding simulations. Upon decreasing the sample temperature, a steady increase in the signal intensity and subsequent broadening is observed for the defect signals, located around $B_0 = 320$ mT, and the $\mathrm{Ti}^{3+}$ trapping site, located to high field of the isotropic signals. The combination of these effects is a clear indicator of multiple spin relaxation processes possibly including exchange, and electron transfer.

In order to separate the contributions to the spectrum, a simulation model was applied to understand the nature of inter-electronic processes and their behaviour as a function of temperature. A simulation of the EPR spectrum for the NTO2 sample at a single temperature point is presented in Figure 1.16. A good fit to the experimental trace was achieved after taking into account three distinct species with Lorentzian line shapes, where the line width is dominated by relaxation effects. The broad $\mathrm{Ti}_{\mathrm{Ti}}'$ feature can be readily distinguished at high field, which is characteristic of compressed octahedral geometry and in agreement with previous EPR measurements. Superimposed onto this signal is a much narrower asymmetric line shape, which is the product of two distinct species. The narrower and more intense feature to slightly higher field (top) was attributed to the carbon additive-related defect (labelled $\mathrm{C\text{-}O}^{\bullet}$) with $g = 2.0031$. Finally, a minor component to lower field ($g = 2.0025$) and slightly broader line width is also apparent, which was attributed to an $\mathrm{OLi}^{\bullet}$ defect in the NTO80 sample.

Taking this model as a starting point, the three components of the simulations were fitted to the spectra at each temperature using a least-squares fitting routine in order to extract the line width of each component. The results for the three fitted components are presented in Figure 1.17. The line width for the Lorentzian signals, as mentioned *vide infra*, is characteristic of fundamental spin relaxation processes associated with the spin-lattice, exchange, and electron transfer relax-

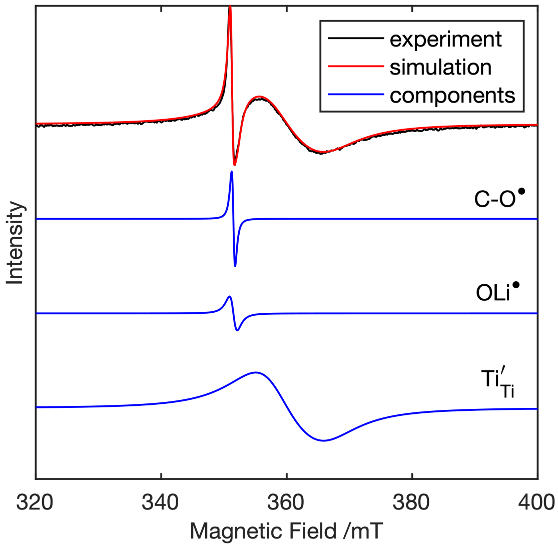

**Figure 6.16:** Decomposed EPR simulation for the NTO2 electrode sample, charged to 80% capacity *ex situ*. *Black:* experimental trace; *Red:* total simulation envelope, taking into account three distinct paramagnetic sites. *Blue:* deconvoluted simulation components, summed and weighted to produce the total envelope.

ation processes. Furthermore, analysis of the line width affords a selective analysis of contributing signals to the total line shape. The line width is proportional to the relative spin susceptibility of the system (*c.f.* magnetometry measurements) according to the following equation:

$$\Delta B(T) = [\chi_0(T)/\chi(T)]\cdot\Delta B_0^\infty \tag{6.7}$$

Where $\chi_o(T)$ is the Curie susceptibility, $\chi(T)$ is the effective susceptibility and $\Delta B_0^\infty$ is the temperature independent contribution to the intrinsic line width. The behaviour of the observed EPR line width, $\Delta B(T)$, shows a distinctly different behaviour as a function of temperature, which is characteristic of the multiple relaxation processes contributing to the effective Lorentzian line width.

The estimated line width for each simulated component shows a monotonic increase approaching $T = 0$ K, which can be phenomenologically modelled using the Curie-Weiss law:

$$\Delta B(T) = \Delta B_0^\infty + \Delta B_{CW}(T) \tag{6.8}$$

$$\Delta B_{CW}(T) = C/(T - \Theta_{CW}) \tag{6.9}$$

where $C$ is a constant, and $\Theta_{CW}$ is the observed Curie-Weiss temperature. This equation accurately described the observed line width behaviour for the attributed

OLi$^\bullet$ site (Table 1.2) without the need for any additional contributions to the line width term. The fitting obtained $\Theta_{CW}$ = -1.71 K which indicated a weak antiferromagnetic interaction, which may be estimated (assuming $Z = 6$) as $J$ = -0.149 cm$^{-1}$. This is consistent with the proposed defect formation due to the intercalation of Li and subsequent redistribution of spin density across a neighbouring $\mathrm{Ti}'_{\mathrm{Ti}}$ or $\mathrm{Nb}'_{\mathrm{Nb}}$ lattice site, respectively.

For the other identified components, $\mathrm{Ti}'_{\mathrm{Ti}}$ and C-O$^\bullet$, the line width behaviour was considerably less straightforward and required further contributions to be considered . Beginning with the C-O$^\bullet$ defect, a reasonable fit was obtained for the low temperature region ($T$ = 20 K) to the Curie Weiss law which provided $\Theta_{CW}$ = 0.003 K (zero within error) which identified a distinct paramagnetic behaviour. This further reinforced the attribution that C-O$^\bullet$ is a well-isolated, localised point defect and is thus agreeable with an oxygen containing carbon defect arising from the carbon additive.

Approaching $T$ = 20K, the measured line width deviated linearly away from the Curie-Weiss fit indicating another contribution to the line width. Considering the localised paramagnetic behaviour and linear trend observed, the contribution was attributed to a one phonon spin-lattice relaxation process of the form:

$$\Delta B(T) = \Delta B_0^{\infty} + bT \tag{6.10}$$

where $b$ is a constant describing the linear gradient. Fitting of equation 1.10 to the data provided $b$ = 0.0078 mT K$^{-1}$. Approaching higher temperatures ($T >$ 60 K), the line width deviates again at a critical temperature which identified the introduction of a further contribution to the line width term. This was not accounted for in the modelling due to the relatively small number of experimental points in this region.

For the broader $\mathrm{Ti}'_{\mathrm{Ti}}$ lattice site in Figure 1.17, another composite line width dependence as a function of temperature was determined. Firstly, fitting of the Curie-Weiss law indicated another weak antiferromagnetic interaction with $\Theta_{CW}$ = -4.11 K and estimated $J$ = -0.357 cm$^{-1}$ using $Z$ = 6. At higher temperatures, $T >$ 20 K, the model deviated away from the Curie-Weiss fit and the additional line width contribution was determined to be non-linear, due to the relatively long plateau across the temperature range 5 < $T$ <30 K. Above the critical temperature, additional contributions were attributed to the thermal activation of charge carriers from the trapping state $\mathrm{Ti}'_{\mathrm{Ti}}$, below the conduction band edge, and was

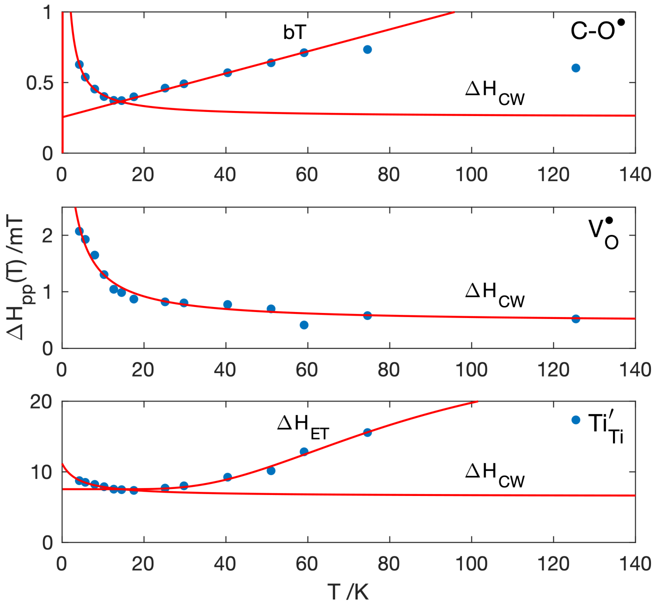

**Figure 6.17:** Extracted peak-to-peak Lorentzian line widths for the simulated components of the EPR spectrum shown in Figure 1.16. A phenomenological model was applied to these simulation components, as defined in the figure, taking into account a temperature independent intrinsic line width, and additional temperature dependent terms, $\Delta B_{CW}(T)$, $\Delta B_{ET}(T)$ and $bT$.

thus fitted to an Arrhenius law:

$$\Delta B(T) = \Delta B_0^{\infty} + \Delta B_P(T) \tag{6.11}$$

where the term $\Delta B_{ET}(T)$ expands to:

$$\Delta B_{ET}(T) = A{\cdot}exp(-E_a/k_BT) \tag{6.12}$$

and $E_a$ is the activation energy for the electron transfer process, analogous to equation 1.3 used for LTO80. The fitted expression provided an apparent activation energy of $E_a = 0.0126$ eV, which was expected to be characteristic of the energy difference between the local $\text{Ti}'_{\text{Ti}}$ defect and the conduction band edge. Some deviation away from the fit was again observed at $T > 100$ K, nonetheless the line width behaviour below this was reproduced well. These contributions were consistent with a partially localised site which may be directly associated with the attributed $\text{OLi}^{\bullet}$ defect species through the intercalation of Li into the network.

**Table 6.2:** Parameters obtained from least-squares fitting to the integrated intensity and line width modelling for the observed defects in LTO80 and NTO80, respectively. The terms are defined in the text, and the line width contributions labelled in Figures 1.15 and 1.17 for LTO80 and NTO80, respectively. $^{a}$ value is nil within error.

| Material | Species | $\Delta B_0^{\infty}$ /mT | $\Theta_{CW}$ / K | $b$ /mT K$^{-1}$ | $J$ cm$^{-1}$ | $E_a$ /eV |
|---|---|---|---|---|---|---|
| LTO80 | $\text{OLi}^{\bullet}$ | - | 3.20 | - | 0.278 | 0.0324 |
| NTO80 | $\text{C-O}^{\bullet}$ | 0.254 | 0.003 | 0.0078 | nil$^{a}$ | - |
| | $\text{OLi}^{\bullet}$ | 0.453 | -1.71 | - | -0.149 | - |
| | $\text{Ti}'_{\text{Ti}}$ | 6.515 | -4.11 | - | -0.357 | 0.0126 |

## 6.3 Conclusions

In summary, a series of LFP cathode and LTO, NTO anode materials for Li-ion batteries were investigated using EPR. The characterisation of the LFP materials, a widely commercialised material for Li-ion batteries, illustrated the application of EPR to understand the defects and impurities in the active material. At X-band, broad signals were observed for $\text{Fe}^{3+}$ impurities, due to the fast spin relaxation times from exchange coupled nearest neighbour spins, spin-lattice relaxation pathways and additional unresolved ZFS structure. Distinct magnetic environments are therefore typically unresolved at these employed conventional frequencies. Due to the partial accessibility and unresolved information, further variable temperature measurements only provided a limited amount of further information about the magnetic properties of the materials. The characterisation of intrinsic high spin centres is therefore appropriate at high frequencies. In particular, for $S$ state ions, the full resolution and discrimination of the ZFS parameters is of importance due to the relatively insensitive $g$ tensor shift due to spin-orbit coupling.

The investigation of the LTO and NTO anode materials illustrated a rich array of defect states observable in these materials, that were dependent on their preparative conditions and environment. Some of these states are important in inferring the electronic properties to the system, by perturbing the local band structure, or contributing to the charge carrier density in the system. Variation of the states of charge (SOC) for the LTO and NTO materials indicated a perturbation in the bulk magnetic properties, as the Fermi energy is varied within the system. The population of defect states was readily monitored in order to understand the progress of these complex processes. The $\text{Nb}^{4+}$ centre, which was expected to be observed in the NTO system, and the $\text{Ti}^{3+}$ centre in the LTO system, were not resolved across the temperature ranges investigated.

Variable temperature EPR measurements were also performed, which revealed markedly different magnetic behaviour for LTO80 and NTO80. For the LTO80 material, an effective insulator in the unperturbed state, was found to be highly sensitive to the thermal activation of charge carriers that provided some electronic conductivity to the system. The electron transfer process dominated the spin relaxation properties of the system at low temperatures ($T < 120$ K). An Arrhenius model was fitted to provide a value of $\mathrm{E}_a = 0.0324$ eV between the trapping state and the conduction band edge. Fitting of the Curie Weiss law at low temperatures approaching $T = 4$ K identified a weak ferromagnetic interaction with estimated $J = 0.0278$ cm$^{-1}$. For the NTO material, a series of contributions to the line width were identified for the simulation components $\mathrm{C{-}O^{\bullet}}$, $\mathrm{OLi^{\bullet}}$ and reduced $\mathrm{Ti'_{Ti}}$ lattice sites upon lithiation of the material. The $\mathrm{C{-}O^{\bullet}}$ species was attributed to a localised point defect arising from the carbon additive due to the paramagnetic behaviour and monotonic increase approaching $T = 0$ K. An additional linear contribution was identified which was thought to arise from a one-phonon spin-lattice relaxation process. For the $\mathrm{OLi^{\bullet}}$ and $\mathrm{Ti'_{Ti}}$ sites, fitting to the Curie-Weiss law identified weak AFM interactions and the isotropic exchange integral was estimated as $J$ = -0.149 and $J$ = -0.357 cm$^{-1}$, respectively. The relatively long plateau for the $\mathrm{Ti'_{Ti}}$ species, and non-linear temperature dependence, indicated another possible contribution due to the thermal excitation of charge carriers from the partially localised state. The activation energy was estimated to be $E_a = 0.0126$ eV *via* fitting to an Arrhenius law.

Investigation into the electronic structure and interactions as a function of temperature was found to offer a valuable means of monitoring electron transfer processes and magnetic correlation of paramagnetic states. The study also highlights the challenges of operating at room temperature: metal sites may not be significant populated in semiconductor materials, and spin relaxation properties are typically fast in such materials where exchange pathways (with neighbouring spins) are present. The characterisation of TM sites with increasingly quenched angular momentum, and lower spin states, in addition to point defects, is more straight-forward.

## 6.4 Experimental

**Materials:** All materials were bought from Alfa Aesar unless otherwise stated. The electrode starting materials, and printed electrode films, were prepared by Johnson Matthey and were checked by XRD and standard GCD cycling protocols prior to study. The LFP starting materials were prepared as described in patent EP2969938B1 using the iron oxide precursors described in the text.[47] The LTO-2s starting material was purchased from *Targray.* The material was used as received to incorporate into the cast film using the general procedure below. The NTO1 and NTO2 starting materials were prepared *via* the flame spray pyrolysis technique in a single step, from a Ti(2-ethylhexanode) precursor, a niobium oxalate precursor or niobium ethoxide precursor (NTO1 and NTO2), respectively. Xylene was used as a solvent in both cases. The temperature used was 3000°C in both cases. The material was used, as prepared, for incorporation into a cast film.

**Reductive Annealing of LTO:** The LTO powder ($m$ = 50 mg) was placed into a custom-build sealed quartz cell, with a fused tap sealed with UHV grease, and lower grade glass heating chamber for attachment to a vacuum line. The cell was evacuated to $P \approx 10^{-3}$ mbar and left at room temperature for an hour. An upright tube furnace was heated to 600 °C and placed around the cell under dynamic vacuum. The powder was heated for 2 hours before sealing the tube and dismounting for recording the EPR spectra. A distinctive blue colour was observed in the sample following annealing.

**Chemical reduction of NTO:** The NTO powder ($m$ = 100mg) was placed into a Schlenk flask and subsequently evacuated ($P \approx 10^{-3}$ mbar) and purged with Argon for 4 to 5 cycles. In a nitrogen-filled glovebox, the appropriate amount of *n*-BuLi (0.5 M in toluene) was diluted with dry toluene, and transferred into the evacuated Schlenk flask containing the NTO material. An immediate colour change from white to black was observed, and the slurry was stirred under argon for 12 hours. The material was washed twice with dry toluene, and then filtered *via* a cannula and Whatman glass fibre filter paper. The material was left to dry under vacuum for an hour, and the sample transferred to a glovebox for storage. The material was transferred into a quartz EPR tube in a glovebox, and sealed with PTFE tape and a 3mm subaseal for EPR measurements.

**Preparation of the working electrodes (WE):** The starting materials were prepared *via* the methods indicated above (NTO), or used as received (LTO, Targray) for incorporation into an electrode film. A general procedure for the preparation of an electrode film *via* slurry casting is as follows:[48]

1. The prepared starting material (90 wt.%), a polyvinylidene fluoride binding agent (PVDF) (5%) and a carbon additive (5%, TIMCAL Super C65) were mixed by milling with a small amount of N-methyl-2-pyrrolidone (NMP) to form a slurry;
2. The slurry is uniformly spread onto a cleaned foil (which serves as the current collector) using a notch bar;
3. The film is dried and then pressed to obtain a laminated, homogeneous film;
4. The printed film is punched into discs of appropriate diameter (14mm for coin type cells);
5. Finally, the prepared electrodes are dried under vacuum prior to assembly.

**Coin cell Assembly/ Disassembly:** The working electrode (WE) typically consisted of 90 wt.% active material, 5 wt.% carbon additive and 5 wt.% binder. Li metal foil (Alfa Aesar, $d$ = 0.7mm) was used as the counter electrode (CE). The electrodes were separated with a Whatman glassy fibre (GF-D) separator, wetted with 80 $\mu$L of 1M $LiPF_6$ salt in equal quantities of EC:DMC (ethylene carbonate:dimethylcarbonate).

The printed and calendared electrodes, and other cell components (2032 coin cell casing, springs, spacers, separators), were dried under vacuum at 60 °C overnight. The components were assembled in a glovebox under an Argon atmosphere ($< 0.1$ ppm $O_2, H_2O$). The assembled cells were left for 1-2 hrs to allow wetting of the electrode surface prior to removal for electrochemical testing.

To collect samples for EPR characterisation, the cycled coin cells were disassembled in a glovebox, the WE was extracted from the cell and washed several times in DMC. The electrode was left to dry, before heat-sealing in plastic under an Ar atmosphere for transport. The samples were stored and sealed in a glovebox between experiments.

**Sample Preparation for EPR spectroscopy:** For the cut electrode films for measurements, a strip of the WE (approximately 0.8 x 10 $mm^2$) was cut to the appropriate size in an Ar glovebox, for the tested samples, or in air, for the as received samples. The strip was placed into a quartz Q-band EPR tube sealed at one end. The Q-band EPR tube was then placed into a standard X-band 4 mm O.D. quartz tube, sealed with PTFE tape and a 3 mm suba-seal. When opened in air, the tube was degassed with nitrogen for 30 - 60 mins prior to measurement.

For the starting materials, a constant volume was achieved by packing into a quartz Q-band EPR tube which was then placed into a standard X-band 4mm O.D. quartz tube, sealed with PTFE tape and a 3mm suba-seal. The tube was degassed with nitrogen for 30 -60 minutes prior to measurement.

For the W-band measurement, a small amount of the LFP/C powder was dispersed in acetone and placed in an ultrasonic bath for 5-10 minutes, until a fine suspension was formed. A glass pipette was stretched to approximately 0.6 mm diameter (to fit into a standard quartz suprasil W-band tube), ensuring the section of tubing was of appropriately homogeneous thickness. The suspension was introduced by capillary force, and the capillary was gently dried in the oven at 70 °C to remove the solvent. The process was repeated until an opaque black coating was formed on the inside of the capillary. The capillary was inserted into a standard W-band EPR tube, sealed at one end, and closed with PTFE tape prior to measurement.

**X-band EPR spectroscopy:** The X-band (9 GHz) CW-EPR spectra were recorded at 120 K on a Bruker EMX spectrometer, operating at 100 kHz field modulation frequency; 0.6325 mW microwave power; and 1 G modulation amplitude using an ER 4119HS cavity.

**W-band EPR spectroscopy:** The W-band (95 GHz) CW-EPR spectra were recorded at 20 K and 300 K on a Bruker E600 spectrometer operating at 100 kHz field modulation frequency; 0.005 mW microwave power; and 1 G modulation amplitude, using a E600-1021H TeraFlex resonator. Field calibration was performed using a BDPA standard at X-band, and the microwave frequency for spectra at W-band were adjusted accordingly by simultaneous fitting at the two microwave frequencies.

**Variable temperature study:** The temperature ranges $T$ = 4-100 K were recorded on a Bruker E500 spectrometer equipped with a ER 4119HS resonator and an Oxford instruments cryostat. A saturation study was recorded to ensure that the operating microwave power was not within saturation limits. Field calibration was performed using a BDPA standard. The operating parameters were as follows; 100 kHz field modulation frequency; 0.6325 mW microwave power; 1 G modulation amplitude. EPR measurements in the temperature range $T$ = 120-370 K were recorded on a Bruker EMX spectrometer equipped with a ER 4119HS resonator, as stated *vide infra*. The Q value was checked to ensure a similar environment for the separate temperature ranges. The sample was marked to ensure a similar height and angle to the external field between temperature ranges also.

**Galvanostatic charge-discharge (GCD) cycling measurements:** Electrochemical cycling was performed on the coin cells using a Maccor battery testing station, incubated at 23°C. LFP electrodes were cycled between a potential window of 2 - 4.2 V. The LTO and NTO electrodes were cycled between a potential window of 1 - 2.5 V. The applied current density was determined from the active mass of the electrode and the theoretical specific capacity.

For the SOC cycling experiments, the cell was charged at 0.1C (current applied to reach fully charged state in 10 hours) for 2 cycles. The cells were subsequently charged at the same rate to the appropriate stopped potential values, corresponding to %Li intercalated at the WE.

# References

[1] George Crabtree. Perspective: The energy-storage revolution. *Nature*, 526 (7575):S92–S92, October 2015.

[2] M. Stanley Whittingham and Fred R. Gamble. The lithium intercalates of the transition metal dichalcogenides. *Materials Research Bulletin*, 10(5):363–371, May 1975.

[3] J. B. Goodenough and A. L. Loeb. Theory of ionic ordering, crystal distortion, and magnetic exchange due to covalent forces in spinels. *Physical Review*, 98 (2):391–408, April 1955.

[4] John B. Goodenough. Theory of the role of covalence in the perovskite-type manganites [la, m(ii)]$\text{MnO}_3$. *Physical Review*, 100(2):564–573, October 1955.

[5] John B. Goodenough. An interpretation of the magnetic properties of the perovskite-type mixed crystals $\text{La}_{1-x}\text{Sr}_x\text{CoO}_{3-\lambda}$. *Journal of Physics and Chemistry of Solids*, 6(2):287–297, August 1958.

[6] John B. Goodenough. On the influence of 3d4 ions on the magnetic and crystallographic properties of magnetic oxides. *Journal de Physique et le Radium*, 20(2-3):155–159, February 1959.

[7] Gongming Wang, Yi Yang, Dongdong Han, and Yat Li. Oxygen defective metal oxides for energy conversion and storage. *Nano Today.*

[8] Karen E. Swider-Lyons, Corey T. Love, and Debra R. Rolison. Improved lithium capacity of defective $\text{V}_2\text{O}_5$ materials. *Solid State Ionics*, 152-153: 99–104, December 2002.

[9] Xuecheng Yan, Yi Jia, and Xiangdong Yao. Defective Structures in Metal Compounds for Energy-Related Electrocatalysis. *Small Structures*, n/a(n/a): 2000067.

[10] Howie Nguyen and Raphaële J. Clément. Rechargeable Batteries from the Perspective of the Electron Spin. *ACS Energy Letters*, 5(12):3848–3859, December 2020.

[11] Natasha A. Chernova, Gene M. Nolis, Fredrick O. Omenya, Hui Zhou, Zheng Li, and M. Stanley Whittingham. What can we learn about battery materials from their magnetic properties? *Journal of Materials Chemistry*, 21(27): 9865–9875, June 2011.

[12] Jun Lu, Tianpin Wu, and Khalil Amine. State-of-the-art characterization techniques for advanced lithium-ion batteries. *Nature Energy*, 2(3):1–13, March 2017.

[13] Hapuarachchi Sashini N. S., Sun Ziqi, and Yan Cheng. Advances in In Situ Techniques for Characterization of Failure Mechanisms of Li-Ion Battery Anodes. *Advanced Sustainable Systems*, 0(0):1700182, February 2018.

[14] Yiqiong Zhang, Li Tao, Chao Xie, Dongdong Wang, Yuqin Zou, Ru Chen, Yanyong Wang, Chuankun Jia, and Shuangyin Wang. Defect Engineering on Electrode Materials for Rechargeable Batteries. *Advanced Materials*, 32(7): 1905923, 2020.

[15] Feng Yu, Lili Zhang, Yingchun Li, Yongxin An, Mingyuan Zhu, and Bin Dai. Mechanism studies of $LiFePO_4$ cathode material: Lithiation/delithiation process, electrochemical modification and synthetic reaction. *RSC Advances*, 4(97):54576–54602, October 2014.

[16] V. A. Streltsov, E. L. Belokoneva, V. G. Tsirelson, and N. K. Hansen. Multipole analysis of the electron density in triphylite, $LiFePO_4$, using X-ray diffraction data. *Acta Crystallographica Section B: Structural Science*, 49(2): 147–153, April 1993.

[17] N. Ravet, Y. Chouinard, J. F. Magnan, S. Besner, M. Gauthier, and M. Armand. Electroactivity of natural and synthetic triphylite. *Journal of Power Sources*, 97-98:503–507, July 2001.

[18] Yuri Janssen, Dhamodaran Santhanagopalan, Danna Qian, Miaofang Chi, Xiaoping Wang, Christina Hoffmann, Ying Shirley Meng, and Peter G. Khalifah. Reciprocal salt flux growth of $LiFePO_4$ single crystals with controlled defect concentrations. *Chemistry of Materials*, 25(22):4574–4584, November 2013.

[19] Saulius Gražulis, Daniel Chateigner, Robert T. Downs, A. F. T. Yokochi, Miguel Quirós, Luca Lutterotti, Elena Manakova, Justas Butkus, Peter Moeck, and Armel Le Bail. Crystallography Open Database an open-access collection of crystal structures. *Journal of Applied Crystallography*, 42(4): 726–729, August 2009.

[20] Saulius Gražulis, Adriana Daškevič, Andrius Merkys, Daniel Chateigner, Luca Lutterotti, Miguel Quirós, Nadezhda R. Serebryanaya, Peter Moeck, Robert T. Downs, and Armel Le Bail. Crystallography Open Database (COD): An open-access collection of crystal structures and platform for worldwide collaboration. *Nucleic Acids Research*, 40(D1):D420–D427, January 2012.

[21] Miguel Quirós, Saulius Gražulis, Saulė Girdzijauskaitė, Andrius Merkys, and Antanas Vaitkus. Using SMILES strings for the description of chemical connectivity in the Crystallography Open Database. *Journal of Cheminformatics*, 10(1):23, December 2018.

[22] Andrius Merkys, Antanas Vaitkus, Justas Butkus, Mykolas Okulič-Kazarinas, Visvaldas Kairys, and Saulius Gražulis. COD::CIF::Parser : An error-correcting CIF parser for the Perl language. *Journal of Applied Crystallography*, 49(1):292–301, February 2016.

[23] Natasha A. Chernova, Gene M. Nolis, Fredrick O. Omenya, Hui Zhou, Zheng Li, and M. Stanley Whittingham. What can we learn about battery materials from their magnetic properties? *Journal of Materials Chemistry*, 21(27): 9865–9875, June 2011.

[24] D. Goldfarb, M. Bernardo, K. G. Strohmaier, D. E. W. Vaughan, and H. Thomann. Characterization of Iron in Zeolites by X-band and Q-Band ESR, Pulsed ESR, and UV-Visible Spectroscopies. *Journal of the American Chemical Society*, 116(14):6344–6353, July 1994.

[25] Theodore Castner, George S. Newell, W. C. Holton, and C. P. Slichter. Note on the Paramagnetic Resonance of Iron in Glass. *The Journal of Chemical Physics*, 32(3):668–673, March 1960.

[26] Natalia Domracheva, Valerya Vorobeva, Andrew Pyataev, Rui Tamura, Katsuaki Suzuki, Matvey Gruzdev, Ulyana Chervonova, and Arkadij Kolker. Magnetic properties of novel dendrimeric spin crossover iron(III) complex. *Inorganica Chimica Acta*, 439:186–195, January 2016.

[27] R. Stoyanova, A.-L. Barra, M. Yoncheva, E. Zhecheva, E. Shinova, P. Tzvetkova, and S. Simova. High-Frequency Electron Paramagnetic Resonance Analysis of the Oxidation State and Local Structure of Ni and Mn Ions in Ni,Mn-Codoped $LiCoO_2$. *Inorganic Chemistry*, 49(4):1932–1941, February 2010.

[28] Bin Wang, Alistair J. Fielding, and Robert A. W. Dryfe. In situ electrochemical electron paramagnetic resonance spectroscopy as a tool to probe electrical double layer capacitance. *Chemical Communications*, 54(31):3827–3830, 2018.

[29] Martin Winter, Gerhard H. Wrodnigg, Jürgen O. Besenhard, Werner Biberacher, and Petr Novák. Dilatometric Investigations of Graphite Electrodes in Nonaqueous Lithium Battery Electrolytes. *Journal of the Electrochemical Society*, 147(7):2427, July 2000.

[30] S. S. Zhang, K. Xu, and T. R. Jow. Study of the charging process of a $LiCoO_2$-based Li-ion battery. *Journal of Power Sources*, 160(2):1349–1354, October 2006.

[31] Sheng Shui Zhang. The effect of the charging protocol on the cycle life of a Li-ion battery. *Journal of Power Sources*, 161:1385–1391, 2006.

[32] Hailei Zhao. Lithium Titanate-Based Anode Materials. In Zhengcheng Zhang and Sheng Shui Zhang, editors, *Rechargeable Batteries: Materials, Technologies and New Trends*, Green Energy and Technology, pages 157–187. Springer International Publishing, Cham, 2015.

[33] J.-M. Tarascon and M. Armand. Issues and challenges facing rechargeable lithium batteries. *Nature*, 414(6861):359–367, November 2001.

[34] Kazuki Ise, Sayaka Morimoto, Yasuhiro Harada, and Norio Takami. Large lithium storage in highly crystalline $TiNb_2O_7$ nanoparticles synthesized by a hydrothermal method as anodes for lithium-ion batteries. *Solid State Ionics*, 320:7–15, July 2018.

[35] Andrea Folli, Jonathan Z. Bloh, Eva-Panduleni Beukes, Russell F. Howe, and Donald E. Macphee. Photogenerated Charge Carriers and Paramagnetic Species in (W,N)-Codoped $TiO_2$ Photocatalysts under Visible-Light Irradiation: An EPR Study. *The Journal of Physical Chemistry C*, 117(42):22149–22155, October 2013.

[36] Andrea Folli, Jonathan Z. Bloh, Anaïs Lecaplain, Rebecca Walker, and Donald E. Macphee. Properties and photochemistry of valence-induced-$Ti^3$ enriched (Nb,N)-codoped anatase $TiO_2$ semiconductors. *Physical Chemistry Chemical Physics*, 17(7):4849–4853, February 2015.

[37] Jacob Spencer, Andrea Folli, Emma Richards, and Damien M. Murphy. Chapter: Applications of electron paramagnetic resonance spectroscopy for interrogating catalytic systems. In *Electron Paramagnetic Resonance*, pages 130–170. November 2018.

[38] Jakub Biedrzycki, Stefano Livraghi, Elio Giamello, Stefano Agnoli, and Gaetano Granozzi. Fluorine- and Niobium-Doped $TiO_2$: Chemical and Spectroscopic Properties of Polycrystalline n-Type-Doped Anatase. *The Journal of Physical Chemistry C*, 118(16):8462–8473, April 2014.

[39] Mario Chiesa, Maria Cristina Paganini, Stefano Livraghi, and Elio Giamello. Charge trapping in $TiO_2$ polymorphs as seen by Electron Paramagnetic Resonance spectroscopy. *Physical Chemistry Chemical Physics*, 15(24):9435–9447, May 2013.

[40] H. Müller and O. F. Schirmer. ESR analysis of $Nb^{4+}$ and $Ti^{3+}$ in $LiNbO_3$. *Radiation Effects and Defects in Solids*, 119-121(2):693–698, November 1991.

[41] Peter H. Zimmermann. Temperature Dependence of the EPR Spectra of Niobium-Doped $TiO_2$. *Physical Review B*, 8(8):3917–3927, October 1973.

[42] Vittorio Luca, Brett Hunter, Boujemaa Moubaraki, and Keith S. Murray. Lithium Intercalation in Anatase Structural and Magnetic Considerations. *Chemistry of Materials*, 13(3):796–801, March 2001.

[43] Ryoji Inada, Tomoya Mori, Rei Kumasaka, Ryuta Ito, Tomohiro Tojo, and Yoji Sakurai. Characterization of vacuum-annealed $TiNb_2O_7$ as high potential anode material for lithium-ion battery. *International Journal of Applied Ceramic Technology*, 16(1):264–272, January 2019.

[44] Navaratnarajah Kuganathan, Apostolos Kordatos, and Alexander Chroneos. $Li_2SnO_3$ as a Cathode Material for Lithium-ion Batteries: Defects, Lithium Ion Diffusion and Dopants. *Scientific Reports*, 8, August 2018.

[45] M. Stanley Whittingham and Martin B. Dines. n-butyllithium - an effective, general cathode screening agent. *Journal of The Electrochemical Society*, 124 (9):1387–1388, sep 1977.

[46] M. Wagemaker, D. R. Simon, E. M. Kelder, J. Schoonman, C. Ringpfeil, U. Haake, D. Lützenkirchen-Hecht, R. Frahm, and F. M. Mulder. A Kinetic Two-Phase and Equilibrium Solid Solution in Spinel $Li_{4+x}Ti_5O_{12}$. *Advanced Materials*, 18(23):3169–3173, 2006.

[47] Forbert Rainald, Gerhard Nuspl, Nicolas Tran, and Guoxian Liang. Lithium Transition Metal Phosphate Secondary Agglomerates and Process for its Manufacture.

[48] Thomas Marks, Simon Trussler, A. J. Smith, Deijun Xiong, and J. R. Dahn. A Guide to Li-Ion Coin-Cell Electrode Making for Academic Researchers. *Journal of The Electrochemical Society*, 158(1):A51, 2011.

# Chapter 7

# *in situ* EPR characterisation of Li-ion battery materials

## 7.1 Introduction

The combination of EPR spectroscopy and electrochemistry has been widely used to study the metal/ solution interface, not only because of its selectivity towards paramagnetic species, but also due to unprecedented mechanistic resolution that can be obtained through the characterisation of paramagnetic elements within electron transfer processes. The prevalence of single electron transfer reactions in several areas of chemistry has become increasingly apparent.[1–5] Furthermore, the electrolysis and sensitive on-line detection of generated paramagnetic species *via* EPR is fast becoming a powerful and convenient tool towards their direct interrogation.

In their review, Wadhawan and Compton described the application of EPR spectroscopy for electrochemistry,[6] and summarised a variety of *in situ* cell designs for radical generation at the metal solution interface. Many of these designs integrate a flat cell,[7, 8], capillary structures,[9, 10] or even novel resonator designs[11] to overcome the challenge of inductive behaviour from the metallic components and lossy electrolytes, which has a deleterious effect on the sensitivity of EPR.

However, this considerable amount of research was focused around the characterisation and understanding of radical species generated in solution. Lithium intercalation and conversion compounds traditionally used for Li-ion batteries rely on the surface reactions (through a two-phase process) or bulk conversion (*via* solid solution behaviour) of rather more complex semiconductor materials for energy storage. The majority of the developed cell designs are therefore not often optimised for monitoring critical elements of the Li-ion battery chemistry. The exploration of new cell designs for EPR has only received attention more recently, in line with other *in situ* spectroscopic techniques,[12, 13] to probe degradation mechanisms and structure-function properties of such systems.

From the outset it should be mentioned that a number of aspects of the Li-ion battery system are not ideal for EPR spectroscopic measurements, and are definitive in the design of efficient and useful cell designs:

- The cell components should be EPR silent and not produce a signal in the

EPR spectrum;

- An air-tight seal must be achieved to protect the cell components from air and moisture;
- The cell housing should be microwave transparent, and inert towards the conditions within the cell (mainly derived from the electrolyte);
- The dimensions of the cell should be oriented to minimise the interaction of the electric field component of the microwave source;
- Electrode volume (due to the skin effect) should be maximised for sample sensitivity;
- The cell assembly should be designed such that the internal resistance of the electrochemical cell is minimised, and a stable potential response is given.

It is apparent that some of these considerations are contradictory, and a compromise between them is often necessary. A key element of the challenges result from the commercial resonator designs, which are optimised towards the sensitivity of samples without conductive or dielectric properties, and thus have their own limitations for such studies. The outlook for the development of systems that meet these requirements is however optimistic. Several designs for EPR *in situ* applications to Li-ion battery chemistry,[14–16] and next generation technologies,[14, 17, 18] have been recently reported. A summary of these applications was reported in Chapter 1.

The development of a home-built *in situ* EPR cell with a half-cell design was therefore undertaken in this work to enable the monitoring of electron transfer processes and kinetics. The potential benefits of *in situ* EPR underpin the careful characterisation, and more ready optimisation of steady state measurements. The technique therefore can potentially provide a closer correlation to the electrochemical processes that may be monitored on-line.

The design of the *in situ* electrochemical EPR cell is examined more closely with respect to the considerations discussed *vide supra*. Comparative measurements were provided by the reference electrode materials (LTO, NTO, LFP) investigated in the previous Chapter 6. A quantitative examination of the redox processes during perturbation of the cell potential *ex situ* was challenging due to the necessity of the sample preparation. The application of *in situ* techniques was intended to address this by conducting the perturbation of the sample under identical conditions between measurements, and to interrogate the formation of the paramagnetic sites throughout the course of the reaction.

## 7.2 Results and Discussion

### 7.2.1 *in situ* cell design

The starting point for the design of the electrochemical cell was based on the earlier work reported by Sathiya *et al.*,[15] due to its apparent compatibility with commercial (Bruker) resonator designs and ease of assembly. The general principle of the design closely corresponds to the Swagelok cell system; *i.e* a two electrode cell with parallel disc electrodes. A printed electrode on an Al foil was used for the working electrode (WE), isolated by a glass fibre separator wetted with electrolyte, against a Li metal foil counter electrode (CE). The cell design is presented in Figure 7.1. The cell housing was made from PCTFE which was inert towards the battery components, including HF formation (hydrolysis of $LiPF_6$ salt), and able to withstand a reasonable temperature.This material was also shown to be microwave transparent. The highly plasticised nature of the material lends well to its self-sealing, to maintain anaerobic conditions within the cell. The electrical contacts were fitted in the centre of respective PCTFE screws embedded upon the PTFE tape and sealed with beeswax, to ensure good isolation from the cell chamber. The screw allows variable pressures to be enacted upon the cell components to maintain contact. Using this design, different cell component thicknesses were also easily incorporated into the system. The electrical contacts were metal discs soldered (using EPR inactive materials) onto 1 mm diameter wires which were constrained to the centre of the cell. Finally, PCTFE gaskets were used to ensure a good seal between the screws and the cell body.

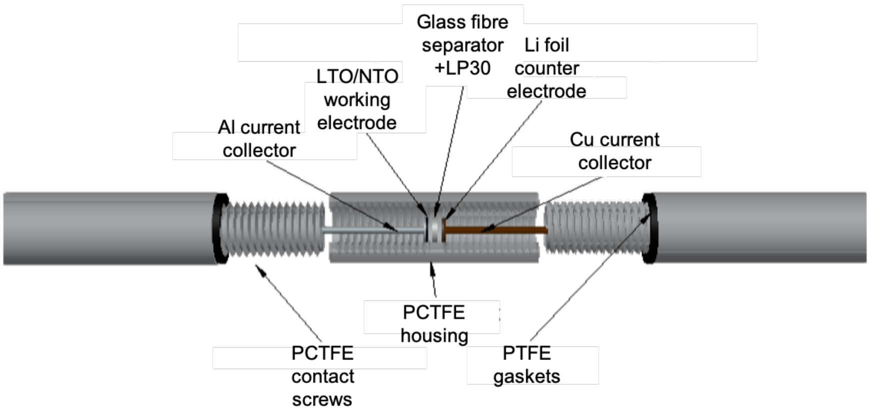

**Figure 7.1:** Schematic illustration of home-built *in situ* cell design for the online EPR monitoring of Li-ion batteries. The cell is sealed and constrained to the resonator dimensions.

The housing was constrained to the maximum width of the resonator bore (10 mm), incorporating the 4.76 mm electrodes ($\approx$ 3-5 mg of sample at varying densities). The restrictions of the cell dimensions and antiparallel arrangement of the electrical contacts restricted measurements to $T = 300$ K, which introduces a challenge in terms of sensitivity due to the spin lifetime, and thermal population of electronic states.

The signal of $Fe^{3+}$ for the LFP sample was nevertheless resolved, and clearly comparable to that observed for the *ex situ* measurement. This indicated that monitoring of the signal was possible with careful comparison to the steady state measurements, whilst recognising that some subtle changes in the anisotropy or line width of the system could be lost.

The *in situ* EPR cell was then investigated to qualitatively determine its relative sensitivity to comparative steady state measurements. The effect of the cell components on the $Q$ factor of the resonator and thus the measurement conditions prevents a direct, quantitative comparison of the two environments. An example is presented for the LFP electrode material, Figure 7.2, investigated also in Chapter 6. The *ex situ* measurement was performed on a cut electrode strip for comparison at $T = 300$ K, degassed within a standard 4 mm quartz tube. An unusual signal, (approximating a phase shifted Lorentzian line shape) arising from a defect in the resonator wall (black arrows) provides a useful indicator of the cell sensitivity where measurement conditions were maintained as close as possible. In the *ex situ*

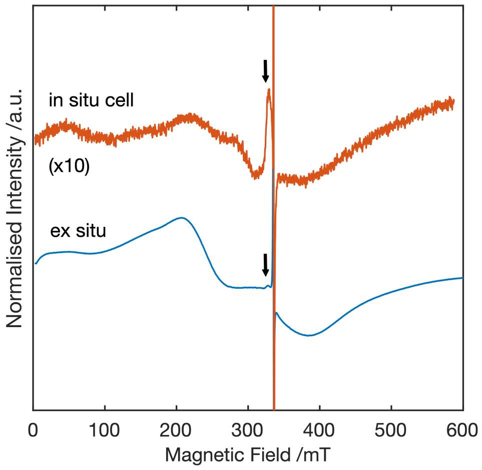

**Figure 7.2:** Comparison of $T = 300$ K X-band EPR measurements *ex situ* of the cut electrode strip, and a 4.76 mm cut electrode assembled within the *in situ* cell under steady state conditions. The cut electrode strip was determined to be approximately the same surface area as the electrode sample. The black arrow indicates a signal originating from the sample cavity, which is a useful indicator of the comparative sensitivity.

sample, the broad FeO phase is well resolved and the broad peaks clearly defined from the noise. For the unperturbed *in situ* cell, under closed circuit conditions, the resolution of this signal is considerably lower and some weak distortions in the line shape occur as a result.

### 7.2.2 Comparison of electrochemical measurements

Preliminary chronopotentiometry measurements of the *in situ* cell, with the LTO and NTO materials as WE's, were performed to determine the electrochemical response in comparison to a reference coin cell. The *in situ* cells were constructed from LTO and NTO 4 mm electrodes, printed onto Al foil, v.s. $Li/Li^+$ (4 mm diameter), and containing approximately 5 $\mu$L of LP30 electrolyte. The electrical contacts were Cu foil disks at both electrodes, soldered to 1 mm diameter Cu wires. The GCD measurements for the NTO1 material v.s. $Li/Li^+$ in the assembled *in situ* cell, are shown in Figure 7.3. For the *in situ* cell, a reasonable capacity of above 300 $mAh\,g^{-1}$ was observed at C/2. The capacity decreased to around 275 $mAh\,g^{-1}$ after 3 cycles, an approximately 8% loss. Although a relatively large internal resistance was observed, the *in situ* cell was found to be comparatively reproducible, and showed similar electrochemical behaviour to the coin cell.

A small plateau at around 2V was attributed to the $Ti^{4+}/Ti^{3+}$ redox couple, followed by a relatively flat plateau at around 1.7 V, which was attributed to the $Nb^{5+}/Nb^{4+}$ redox couple. Finally, a small plateau around 1.2 V was observed and suggested to be associated with the $Nb^{4+}/ Nb^{3+}$ redox couple. The electrochemical response agreed reasonably well with reported values for $TiNb_2O_7$ materials.[19]

For the LTO material, the initial discharge curve for the 2032 coin cell with LTO v.s. $Li/Li^+$ showed that the cell was also unintentionally overcharged to around 4 V where side reactions may begin to occur. For the *in situ* cell, the 1st cycle shows an initial discharge capacity of around 56 $mAh\,g^{-1}$ at C/2, which increases to around 76 $mAh\,g^{-1}$ in the second sample, which is likely the result of the difference between the initial OCP ( 1.55 V) and the upper terminal potential of 2.5 V not accessed during the initial discharge. The internal resistance was observed to be quite high in this case also, as determined by the potential drop between charge / discharge curves. This is expected to be the underlying reason why the reduction / oxidation plateaus apparently take place at differing potential ranges (*ca.* 0.4 V difference). A long, flat plateau is observed at around 1.55 V for the second discharge, which is attributed to the commonly accepted two phase process involving the $Ti^{4+}/ Ti^{3+}$ redox couple, which agrees well with reported values for $Li_4Ti_5O_{12}$.[20] A

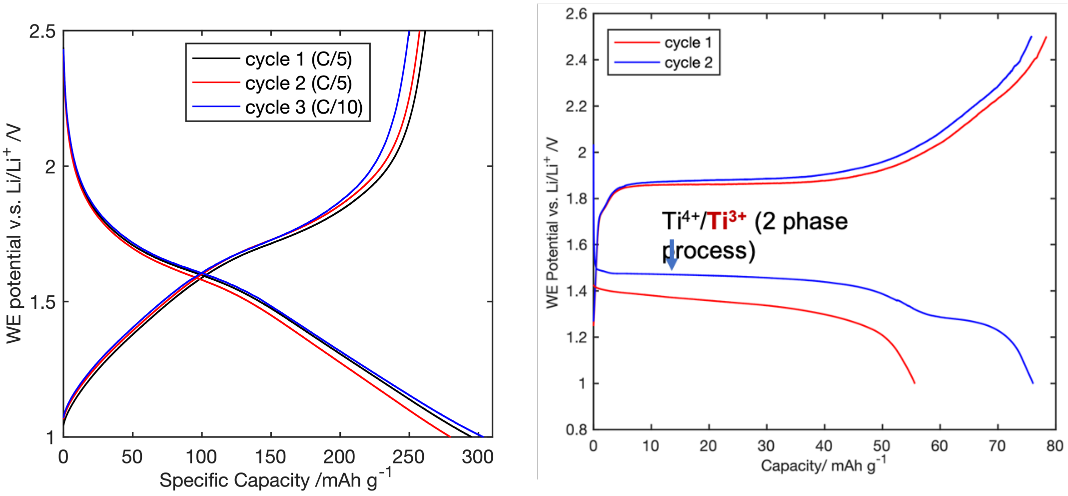

**Figure 7.3:** Galvanostatic charge-discharge (GCD) profile of the NTO1 half cell v.s. Li/Li$^+$, assembled in the *in situ* EPR cell. Two consecutive 0.2C / 0.2D cycles and one subsequent 0.1C/ 0.1D cycle were performed on the cell, cycled between cutoff potentials of 1 and 2.5 V. *Right:* GCD profile of LTO half cell v.s. Li/Li$^+$, assembled in the *in situ* EPR cell. Two consecutive 1C/ 1D cycles were performed on the cell, cycled between cutoff potentials of 1 and 2.5V .

prominent 2nd plateau is observed around 1.3 V in the discharge curve, which is decidedly less pronounced in the subsequent charging cycle. This suggests a difference in diffusion kinetics upon charging and discharging of the cell. Again, reasonably reproducible results were obtained which were acceptable for the *in situ* EPR measurements.

### 7.2.3 *in situ* EPR measurements

A comparison of the room-temperature EPR measurements of the assembled NTO sample in the *in situ* electrochemical cell, directly after assembly (blue), and after the three consecutive cycles is shown in Figure 7.4. A marked difference in the EPR spectrum is apparent between these measurements. The blue signal is composed of two species; i) a broad line and (ii) a narrower anisotropic line at slightly higher field which were both very weak in intensity (magnified for comparison). The broader underlying signal is assigned to an intrinsic oxygen vacancy defect, with a slightly positively shifted $g$ value, by comparison with *ex situ* measurements. The narrower signal to slightly high field has a characteristic Dyson line shape ($A/B \neq 1$); a conduction electron signal likely originating from a trace impurity of Li metal. This has been reported in several studies, with the shape, line shift and asymmetry being characteristic of the particle size.[21] Figure 7.4 *Left* illustrates this effect on the line shape, when the particle size is much larger than the microwave skin depth. After cycling, an intense narrow signal is evident at slightly lower $g$ value and any signals from the pre-measurements are obscured. The origin of this signal is clearly associated with a conduction electron spin resonance component, although two likely sources could be responsible: namely a small Li dendritic structure from alloying processes occurring during charge;[22] or polarised conduction electrons from the semiconductor oxide material. Clearly the latter would be more informative and diagnostic. However greater precision in $g$ factor measurements are necessary to achieve such a resolution, which is challenging in this cell design.

Following the cycling protocol, the stopped potential measurements were performed at approximately 0.2 V steps along the discharge curve, using the method explained earlier and an applied current of 10 $\mu$A. The results of these measurements, recorded at two microwave powers, are presented in Figures 7.5 and 7.6. A narrow sweep EPR measurement was taken at low microwave power to probe the intense conduction signal observed, as seen in Figure 7.4 (and previously shown in the pre-measurement in 7.5). Assuming the signal arises from the semiconductor material, changes in polarisation of the electron spin resonance should occur which manifests as a $g$ shift. Upon gradual discharge of the cell, a very slight variation of the $g$ value is observed between 2.50 and 1.80 V, and 1.40 to 1.10 V respectively. The difference is of the order $10^{-4}$ and therefore likely within experimental error, however, a shift in $g$ appears to accompany the passage through the electrochemical oxidation processes. This would relate to the available unpaired spin density (or the bulk susceptibility), and nearby interacting spins, which act to polarise the

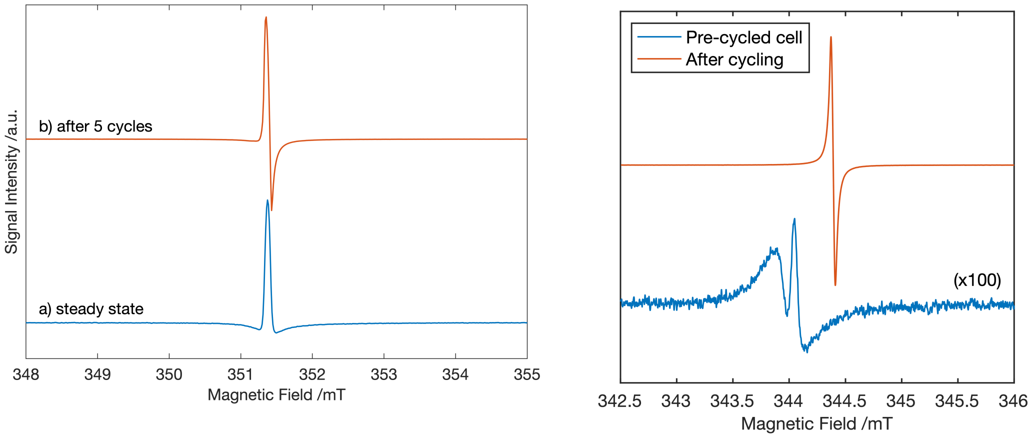

**Figure 7.4:** X-band CW EPR spectra ($T$ = 298K) of the NTO1 electrode sample v.s. Li/Li$^+$assembled in the home-built *in situ* cell. Blue: EPR measurement after assembly of the cell; Orange: After three consecutive C/D cycles at 0.1C.

unpaired spin density. Small variations in the line width and double integral were also noted.

Figure 7.6 presents the high microwave power *in situ* EPR measurements recorded at the same potentials as in Figure 7.5. The narrow, very intense signal is several times larger and obscures the weaker underlying signals. As a result, an appropriate smoothing treatment was applied to the data. The small perturbation in the line shape, just below $B_0 = 350$ mT (the minimum of the broad signal),

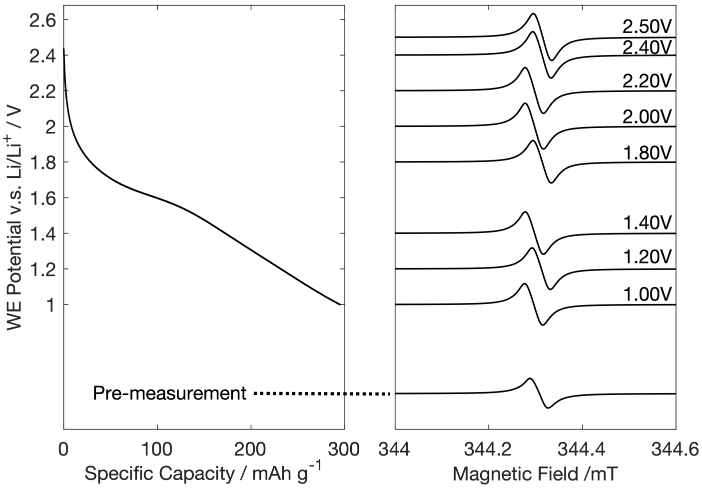

**Figure 7.5:** *in situ* EPR measurements of the NTO1 half cell; *Left:* Plot of the GCD curve, for reference; and *Right:* correlated EPR measurements at stopped potential values of approximately 0.2 V steps. Low microwave powers were used to probe the broad narrow signals near free spin.

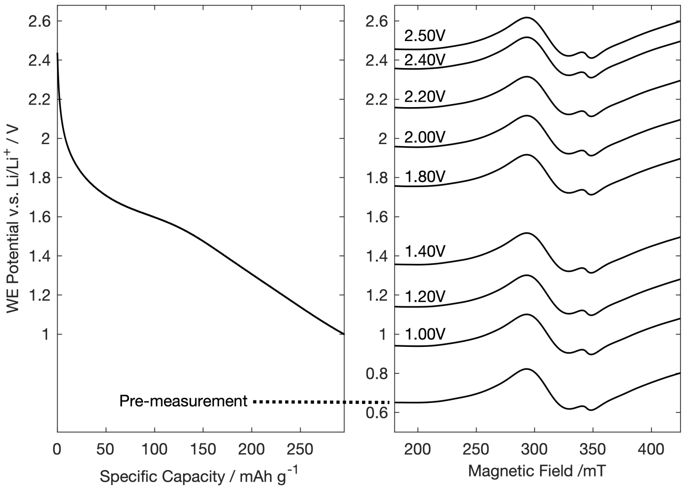

**Figure 7.6:** *in situ* EPR measurements of the NTO1 half cell; *Left:* Plot of the GCD curve, for reference; and *Right:* correlated EPR measurements at stopped potential values of approximately 0.2 V steps. High microwave powers were used to probe the broad signals near free spin. The narrow signal was removed using a spline modelling approach.

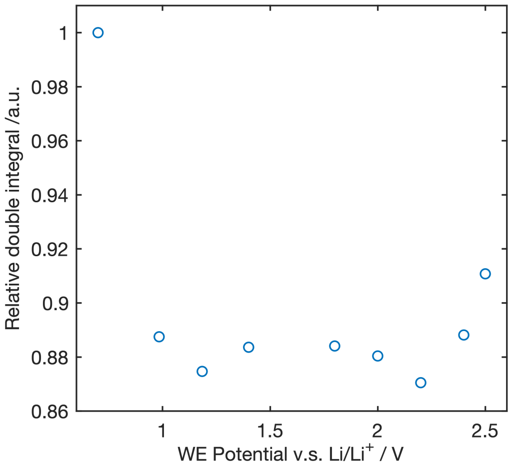

**Figure 7.7:** Calculated double integral for the broad signal shown in Figure 7.6 , relative to the pre-measurement signal.

arises from an artefact from a spline smoothing process, which was applied in kind to each potential measurement. Upon discharge, no clear change in the signal becomes apparent visually. This broad signal is composed partly by trace impurities of CuO. Even after intensive cleaning of the electrical contacts, the same signal appears. Other contributions may arise from trace impurities in the starting material, or broadened $Ti^{3+}$ sites that are barely resolved from the baseline. A relative double integral was calculated for each potential measurement which is presented in Figure 7.7. A variation in the total double integral is apparent, with apparent minima at around 1.2 V and 2.2 V respectively. It is difficult to separate possible contributions at this stage and all three are likely to be redox active. However, this appears at potential edges for the expected redox couples for the NTO materials. This provides a possible indication of the indirect quantification of redox processes *via* the sensitive monitoring of the double integrated intensity.

## 7.3 Conclusions

A home-built *in situ* electrochemical EPR design was developed and tested, in order to study the Li-ion battery system. Critical elements of the design were required to ensure compatibility with the EPR resonator, and a series of preliminary measurements were performed to demonstrate the feasibility of the cell design. The observed electrochemical behaviour in this cell was compared to standard coin cell measurements.

As stated earlier, many of the considerations for optimised electrochemical and

EPR measurements are somewhat contradictory. One of the biggest challenges for the application of EPR is obtaining an appreciable sensitivity, on a relatively small sample mass in order to meet these requirements. This is further exacerbated by the microwave skin effect, arising from the conductive components. This was demonstrated in a comparative measurement under *ex situ* conditions, and recorded within the assembled *in situ* cell. It was concluded that a further limitation was placed on the nature of samples investigated. The samples required an appropriately long spin lifetime at $T = 300$ K, high concentrations, narrow line widths, and an appreciable SNR in order to detect an unperturbed line shape. The characterisation of metal sites for most electrode materials is challenging at room temperature due to inter-electronic interactions, fast relaxation times, and spin delocalisation which all collectively contribute to the poor signal resolution. However, a series of localised point defects (and CESR signals from Li) showed an appreciable resolution using the cell. It was concluded that room temperature measurements were most suited to the direct detection and interrogation of such species.

Another key consideration which adds to the challenge of performing such measurements, is the performance of the commercial resonator when studying particularly lossy samples. In order to reduce the inductive coupling of the conductive components to the $E_1$ field, the cell components were required to be constrained to the cavity dimensions. This limited the available sample mass for measurement (which is surface-area dependent), and introduced a comparatively high internal resistance across the circuit, which influenced the available potential window for electrochemical perturbation of the material. The consideration of the resonator design was therefore as critical as the cell design itself in measurement optimisation. Of particular note is the loop-gap resonator, introduced into EPR spectroscopy by Froncisz and Hyde.[11] The resonator involves the application of an inductive coupling loop, and gaps that provide a capacitative element to influence the separation of the $B_1$ and $E_1$ components of the microwave field. They reported a sensitivity gain of up to 30 times that of a standard cavity, and a negligible reduction in the $Q$ factor drop due to these effects. This in turn allows a larger sample to be incorporated, and a greater freedom of the cell dimensions. This allows both of these considerations to be addressed in principle.

Finally, a low temperature *in situ* cell capability would offer a powerful tool in characterising metal sites, bulk solid properties and defects in such materials. This would move away from the *in situ* measurement, but still provide a ready perturbation of the material to generate redox species of interest for further characterisation. The electrochemical process could still be somewhat correlated to the observed EPR response, but the benefits of low temperature measurements towards sensitivity, and spin-relaxation, are undeniable.

## 7.4 Experimental

**Materials and methods:** The metals (Al, Cu) used for preparation of the electrical contacts were purchases from Fisher Scientific with a purity of $> 99.98\%$ and were used without further treatment. The general method of electrode preparation was described in Chapter 6. The electrical contacts were prepared by soldering (using Cu and Sb free solder) respective metal discs, with a thickness of 1mm and area of 5mm, to 1mm diameter metal wires of the same type and purity. The seperators and electrolyte were the same as described in Chapter 6.

**Preparation of electrical contacts:** After making the new Cu metal electrical contacts, a deposited CuO layer was observed on the surface of the contacts. The metal was sonicated in an ultrasound bath in acetic acid (99%) at RT for 30 mins which was observed to remove the dull layer from the surface of the contacts. The metals was then washed with water and ethanol before drying in an oven at 80°C. The assembled cell was left in the glovebox for 2-3 days prior to measurement to ensure the cell was totally dry.

**Sealing of the cell:** The *in situ* cell with cleaned electrical contacts was sealed with PTFE and melted beeswax in air to support the contacts and provide an air-tight seal to the terminal screws. The wires at the soldered electrical contacts were wrapped with PTFE tape, and embedded into the column of the PCFTE screws. Beeswax was then introduced from the external site in order to prevent contamination of the internal surfaces.The cell was then placed in an Ar glovebox for a minimum of 1-2 days to ensure all components were dry prior to use.

The *in situ* cell was tested prior to starting the preliminary *in situ* electrochemical cell and EPR measurements. An air-sensitive solution of bis-(cyclopentadienyl)titanium(III) chloride in toluene/THF (the Nugent–Rajanbabu reagent) was used for this purpose.[23] The dimer rapidly oxidises in the presence of air, which is accompanied by a colour change from green to yellow, and a consequent change in spin state ($S = 1/2$ to $S = 0$) that could be monitored by EPR. A separator was placed in the cell and wetted with the solution and the double integral of the signal was monitored at intervals over several days (the results are presented in Appendix 5, Figures 17 and 18). A change in double integral to approximately 96% was recorded after 2 days, which was coincident with the reference measurement within precision. A decrease to 89% was noted in the sample after 4 days in the cell, which indicated a good seal and therefore that the cell was therefore suitable for relatively short-term cycling and perturbation experiments.

**Cell assembly:** The *in situ* cell was assembled in an argon filled glovebox. Smaller diameter electrodes (4.76 mm) were cut using a hole punch for sheet metal, which was checked to not damage the surface of the film. The OCP potential was checked for the assembled cell within the glovebox, and several times after assembly, determined to be at the appropriate OCP potential *v.s.* $Li/Li^+$. The cell potential was checked to be stable to small knocks or stresses to the cell prior to removal.

The assembled cell was then removed from the glovebox and cycled using a two-electrode set up, at C/5 for two cycles, and one additional cycle at C/10 using an applied, constant current of approximately 20 $\mu$A and 10 $\mu$A, respectively. The cell was left overnight before positioning in the EPR cavity for the *in situ* measurements. A 10 $\mu$A constant current was applied to the cell, which was stopped at systematic potentials along the charge-discharge curves corresponding to the effect reversible specific capacity. At the desired potential, the cell was switched off and disconnected from the circuit for EPR measurements to be performed. Once the EPR measurements were complete, the magnetic field was turned off and the cell reconnected, which was left under open circuit conditions for 30 seconds before continuing the protocol to the next potential. Rapid drops in the potential were noted after multiple cycles, which was attributed to polarisation of the cell due to kinetic effects.

***in situ* EPR spectroscopy:** The *in situ* EPR measurements were performed on a Bruker E500 spectrometer equipped with a ER4102ST resonator. This was chosen due to a slightly lower $Q$ factor, in order to enable better tuning at higher microwave powers. The $Q$ factor was recorded and monitored during the course of the measurement. No quartz insert was present in the resonator due to the constraints of the *in situ* cell dimensions. The measurement conditions were as follows: 6 mW microwave power, 5 G modulation amplitude (metal signals); 0.01 mW microwave power (narrow, easily saturated signals), 0.3 G line width, which was checked not to be over-modulated or saturated during the course of the experiment.

During EPR acquisition, the cell was kept under closed circuit conditions to avoid induction that is able to shift the resonance frequency, microwave phase and thus influence the sensitivity. Furthermore, for the electrochemical cycling, the magnetic field was switched off and the microwave power attenuated to the minimum.

# References

[1] Michel H. Devoret, Daniel Esteve, and Cristian Urbina. Single-electron transfer in metallic nanostructures. *Nature*, 360(6404):547–553, December 1992.

[2] R. P. G. McNeil, M. Kataoka, C. J. B. Ford, C. H. W. Barnes, D. Anderson, G. A. C. Jones, I. Farrer, and D. A. Ritchie. On-demand single-electron transfer between distant quantum dots. *Nature*, 477(7365):439–442, September 2011.

[3] Jin Xie, Qi Dong, Ian Madden, Xiahui Yao, Qingmei Cheng, Paul Dornath, Wei Fan, and Dunwei Wang. Achieving low overpotential $LiO_2$ Battery Operations by $Li_2O_2$ Decomposition through One-Electron Processes. *Nano Letters*, 15(12):8371–8376, December 2015.

[4] Edward M. Arnett, L.G. Whitesell, J.-P. Cheng, and Etienne Marchot. An “all-organic” battery: Single electron transfer in an electrochemical cell. *Tetrahedron Letters*, 29(13):1507–1508, 1988.

[5] Ch Fabjan, J Garche, B Harrer, L Jörissen, C Kolbeck, F Philippi, G Tomazic, and F Wagner. The vanadium redox-battery: An efficient storage unit for photovoltaic systems. *Electrochimica Acta*, 47(5):825–831, December 2001.

[6] Jay D. Wadhawan and Richard G. Compton. EPR Spectroscopy in Electrochemistry. In *Encyclopedia of Electrochemistry*. Wiley-VCH Verlag GmbH & Co. KGaA, 2007.

[7] Ira B. Goldberg and Allen J. Bard. Simultaneous electrochemical-electron spin resonance measurements. I. Cell design and preliminary results. *The Journal of Physical Chemistry*, 75(21):3281–3290, October 1971.

[8] Ira B. Goldberg and Allen J. Bard. Simultaneous electrochemical-electron spin resonance measurements. II. Kinetic measurments using constant current pulse. *The Journal of Physical Chemistry*, 78(3):290–294, January 1974.

[9] W. John Albery and Richard G. Compton. Tube electrode and electron spin resonance transient signals. *Journal of the Chemical Society, Faraday Transactions 1: Physical Chemistry in Condensed Phases*, 78(5):1561, 1982.

[10] W. J Alberty, R. G Compton, and C. C Jones. A novel electrode for electrochemical ESR and its application to modified electrodes. *Journal of the American Chemical Society*, 106(3):469–473, 1984.

[11] W Froncisz and James S Hyde. The loop-gap resonator: A new microwave lumped circuit ESR sample structure. *Journal of Magnetic Resonance (1969)*, 47(3):515–521, May 1982.

[12] Jun Lu, Tianpin Wu, and Khalil Amine. State-of-the-art characterization techniques for advanced lithium-ion batteries. *Nature Energy*, 2:17011, March 2017.

[13] Hapuarachchi Sashini N. S., Sun Ziqi, and Yan Cheng. Advances in In Situ Techniques for Characterization of Failure Mechanisms of Li-Ion Battery Anodes. *Advanced Sustainable Systems*, 0(0):1700182, February 2018.

[14] Johannes Wandt, Cyril Marino, Hubert A. Gasteiger, Peter Jakes, Rüdiger-A. Eichel, and Josef Granwehr. Operando electron paramagnetic resonance spectroscopy – formation of mossy lithium on lithium anodes during charge-discharge cycling. *Energy & Environmental Science*, 8(4):1358–1367, April 2015.

[15] M. Sathiya, J.-B. Leriche, E. Salager, D. Gourier, J.-M. Tarascon, and H. Vezin. Electron paramagnetic resonance imaging for real-time monitoring of Li-ion batteries. *Nature Communications*, 6:ncomms7276, February 2015.

[16] Mingxue Tang, Annalisa Dalzini, Xiang Li, Xuyong Feng, Po-Hsiu Chien, Likai Song, and Yan-Yan Hu. Operando EPR for Simultaneous Monitoring of Anionic and Cationic Redox Processes in Li-Rich Metal Oxide Cathodes. *The Journal of Physical Chemistry Letters*, 8(17):4009–4016, September 2017.

[17] Peter G. Bruce, Stefan A. Freunberger, Laurence J. Hardwick, and Jean-Marie Tarascon. Li-$O_2$ and Li-S batteries with high energy storage. *Nature Materials*, 11(1):19–29, January 2012.

[18] Chibueze V. Amanchukwu, Hao-Hsun Chang, Magali Gauthier, Shuting Feng, Thomas P. Batcho, and Paula T. Hammond. One-Electron Mechanism in a Gel–Polymer Electrolyte $LiO_2$ Battery. *Chemistry of Materials*, 28(19):7167–7177, October 2016.

[19] Yong-Seok Lee and Kwang-Sun Ryu. Study of the lithium diffusion properties and high rate performance of $TiNb_6O_{17}$ as an anode in lithium secondary battery. *Scientific Reports*, 7(1):16617, December 2017.

[20] M. Selvamurugan, C. Natarajan, Y. Andou, and S. Karuppuchamy. Synthesis and characterization of lithium titanate ($li_4ti_5o_{12}$) nanopowder for battery applications. *Journal of Materials Science: Materials in Electronics*, 29(20): 17826–17833, October 2018.

[21] Thomas Waldmann, Björn-Ingo Hogg, and Margret Wohlfahrt-Mehrens. Li plating as unwanted side reaction in commercial Li-ion cells - A review. *Journal of Power Sources*, 384:107–124, April 2018.

[22] Charles-Emmanuel Dutoit, Mingxue Tang, Didier Gourier, Jean-Marie Tarascon, Hervé Vezin, and Elodie Salager. In Situ Electron Paramagnetic Resonance Correlated Spectroscopy and Imaging: A Tool for Lithium-Ion Batteries to Investigate Metallic Lithium Sub-Micrometric Structures Created by Plating and Stripping. *Energy Storage*, September 2020.

[23] María Castro Rodríguez, Ignacio Rodríguez García, Roman Nicolay Rodríguez Maecker, Laura Pozo Morales, J. Enrique Oltra, and Antonio Rosales Martínez. $Cp_2TiCl$: An Ideal Reagent for Green Chemistry? *Organic Process Research & Development*, 21(7):911–923, July 2017.

# Chapter 8

# Conclusions

Electron Paramagnetic Resonance (EPR) spectroscopy is a powerful, but often under-utilised tool in the characterisation and development of advanced functional materials. The work reported in this Thesis illustrates the application of EPR in order to provide a deeper understanding of the nature of paramagnetic sites, local electronic structure and resulting functional properties.The optimisation of solid-state functional materials towards the desired redox activity, optical or magnetic properties is fundamental in rationalising the performance, and in turn facilitating the development of more efficient advanced materials. The outcomes of this work are now briefly summarised in consideration of the aims of this work.

The application of EPR across a range of solid state functional materials was extensively reviewed in Chapter 1, in order to demonstrate the common theme in the local electronic structure, and defect chemistry, of these materials. Several areas where significant developments could be made in research areas were considered. An overview of EPR theory was then presented with a focus on high spin systems, which featured in several of the chapters. A number of other characterisation techniques were also outlined which are complementary to the information provided by EPR.

IERs and CERs represent an important class of separation and catalytic technologies with application in several industries. Two commercial chelating exchange resins (CER), CuWRAM and Dowex M4195 were investigated in terms of their efficiency and selectivity for $Cu^{2+}$ uptake from aqueous media. Surprisingly, it was not well understood how these metals bind to the chelating groups attached to the resin framework. A combined CW EPR, DFT and UV-Vis study of the local metal environments was therefore undertaken to provide a detailed understanding of this mechanism. Multiple binding environments containing one or more chelating units were identified, in addition to unknown, inter-molecular coordination groups that were not formed by the ligand titration experiments with a partially hydrated coordination sphere. The joint EPR - UV-vis study indicated that the intermolecular sites were weakly bound and easily removed from the framework. EPR spectroscopy provides a direct, selective and sensitive method of probing magnetic structure in solid-state materials. This study represents an extensive and systematic characterisation of commercial materials of value for process control and materials development.

Rare earth activated phosphors have attracted considerable attention for various optical, upconversion and scintillation applications owing to the readily tuneable luminescent emission, and structural diversity of these materials. The optical band gap is well known to be highly sensitive to the local symmetry and crystal field, which in turn can be interrogated using EPR spectroscopy. A series of red-emitting CaS:$Eu^{2+}$ phosphors were investigated which were of interest as a light source for algae growth. A joint EPR, XPS and PL investigation was applied in order to understand the local electronic structure through a series of different synthetic and post-synthetic treatments. The local structure, symmetry, and disorder of $Eu^{2+}$ environments in the material were directly characterised in terms of their zero-field splitting. A series of other defects (such as $V_S^{\bullet}$ centres) were also identified and characterised, which are known to deactivate the material *via* competitive absorption/ emission. Their effect on the luminescent properties were evaluated in order to correlate the functional properties of the material. EPR was a powerful tool in understanding process control, and the formation of a rich and diverse array of paramagnetic defects that directly influence their optical properties.

Glasses and glass-ceramics are a huge glass of disordered (or partially ordered) materials with complex local structures, and in turn properties that are unique to their crystalline counterparts due to the interplay between phase composition and network disorder. The understanding of local paramagnetic sites provides a ready means of understanding the functionalisation of glasses, and the distribution of unpaired spin density within the material. A series of $LiBO_2 - V_2O_5$ glasses with content-dependent ionic and electronic conductivity were investigated, which were of interest for application as electrode/ electrolyte materials in solid state Li ion batteries. At low contents, an isolated $S = 1/2$ vanadium defect was identified in a 'network-modifying' position of the major $LiBO_2$ phase. The defect was identified to have a distorted octahedral configuration with most of the unpaired spin density occupying the ground $d_{xy}$ orbital. In the high content glasses, which possess electronic conductivity, a distinct species was observed indicative of $V^{4+}$ sites in a 'network-forming' position (a majority $V_2O_5$ phase). This species has a characteristic strong exchange-narrowed signal which showed a marked temperature dependence. The signal was characteristic of a 1D extended lattice of spins, with an exchange coupling along the hopping plane, and at low temperatures the CESR was observed to localise onto the vanadium sites, identified by a corresponding increase in the spin-orbit interaction ($g$ tensor shift). The investigation provided a detailed insight into the local electronic structure of defect sites responsible for the conductive properties of the system. This, in turn, provides an insight into the disordered structure and underpins the design of more efficient and selective materials.

The characterisation of Li-ion battery materials is an important aspect of the development of energy storage systems, where EPR is a considerably underemployed technique. A systematic *ex situ* EPR investigation of Li-ion cathode (LFP) and anode (LTO, NTO) materials for secondary rechargeable batteries was presented. The magnetic properties of the LFP system were characteristic of an impurity 'FeO' type phase, and the local electronic structure was shown to be highly sensitive to its preparation. It was concluded that high frequency EPR measurements are necessary for further information on these high spin systems. LTO and NTO anode materials are of interest as an alternative for the traditional graphite electrode, particularly for fast charging applications. These materials exhibited a rich array of defect states which were readily monitored using EPR. The nature and concentration of these defects were again preparation and environment sensitive. Variable temperature measurements indicated markedly different magnetic behaviour between the two materials. For the LTO material, it was dominated by the thermal activation of charge carrier states that increased exponentially with temperature. On the other hand, the NTO material was characterised by weak exchange between defect states.

EPR and electrochemistry have historically been used in conjunction for the generation and detection of radical species at the metal/electrolyte interface. For that reason, *in situ* cell designs are generally not optimised for the characterisation of semiconductor electrode materials for Li-ion batteries. A home-built *in situ* electrochemical cell for the purpose of EPR monitoring was described, and examples were presented for the LFP, LTO and NTO materials. The challenges associated with the sensitive detection of fast-relaxing defect states were outlined, in addition to considerations for further development, and outlook.

The application of EPR was demonstrated to better rationalise the performance of several advanced materials, and to underpin the design and manufacture of next generation systems. The outcomes of this work have illustrated a rich diversity of paramagnetic states, which are critical for the function of many industrially relevant materials. Through careful investigation, EPR is able to provide a detailed understanding of single electron transfer processes, and through the detection of a range of magnetic interactions between spin active states, therefore a mechanistic understanding often not available *via* other techniques. This information is generally complementary to more widely employed characterisation techniques such as XRD, IR, UV-Vis and NMR spectroscopy, in order to provide a deeper understanding of the local structural features that infer its bulk properties. Furthermore, the full potential of EPR spectroscopy is therefore afforded by the inclusion of complementary spectroscopic or analytical techniques. The final important outlook for the study of systems such as Li-ion batteries reported in this thesis, is the cutting-edge application of *in situ* spectroscopic methods. This facility allows further correlation of the local electronic structure and magnetic properties to the functional properties (*ca.* optical, or electronic transitions) of the material for real-time monitoring, and an additional means of control for perturbation of the electronic structure.

# Appendix 1 to Chapter 2

### Higher order Zero field Splittings

For $S > 2$, an additional fine structure (splitting of the energy levels) is often observed due to indirect effects of the crystal field. The preceding expressions $D$ and $E$, are usually suitable for $S < 3/2$ systems. However, $S > 5/2$ systems are possible (*c.a.* lanthanides), and sometimes the description by these terms only, is inappropriate. This situation arises in particular for cases of high symmetry, *i.e.* near-cubic symmetry. The ZFS can be more generally incorporated into the spin Hamiltonian by higher-order spin Hamiltonian operators, where each operator is the equivalent of a combination of spherical harmonics, *i.e.* the orbital basis. The higher order terms must then reflect the symmetry of the crystal field, of greater than two-fold symmetry, and are restricted by spin operators less than $2S$. These higher order interactions are often only applicable in two situations: (i) when ZFS terms are comparatively large (particularly when single crystal measurements are performed); (ii) when (second-order) ZFS terms are comparably small, *i.e.* cases of cubic symmetry. The general spin Hamiltonian of the higher order ZFS terms can then be defined in terms of the extended Stevens operators:

$$\hat{H}_{ZFS} = \sum_{k,q} B_k^q O_k^q \tag{A1.1}$$

where $O_k^q$ are the spin operators, which are defined in terms of the total angular momentum, $J$, tabulated by various sources.[1] the labels $k$ and $q$ denote the order, and rank (related to the symmetry), of the operator respectively. The relevant operators are as follows:[2]

$$O_2^0 = 3S_z^2 - S(S+1) \tag{A1.2}$$

$$O_2^2 = \frac{1}{2}(S_+^2 + S_-^2) \tag{A1.3}$$

$$O_4^0 = 35S_z^4 - (30S(S+1) - 25)S_z^2 - 6S(S+1) + 3S^2(S+1)^2 \tag{A1.4}$$

$$O_4^2 = \frac{1}{4}\{7S_z^2 - S(S+1) - 5\}(S_+^2 + S_-^2) + \frac{1}{4}(S_+^2 + S_-^2)\{7S_z^2 - S(S+1) - 5\} \tag{A1.5}$$

$$O_4^4 = \frac{1}{2}(S_+^4 + S_-^4) \tag{A1.6}$$

and the raising and lowering operators, $S_+$ and $S_-$, are defined as:

$$S_+ = S_x + iS_y \tag{A1.7}$$

$$S_- = S_x - iS_y \tag{A1.8}$$

where $i$ is the imaginary number. When the symmetry is less than cubic, the second order operators, *i.e.* the more familiar $D$ and $E$ terms are generally dominant and may be related to the Stevens operators:

$$\hat{H}_{ZFS} = B_2^0 O_2^0 + B_2^2 O_2^2 \tag{A1.9}$$

$$D = 3B_2^0; E = B_2^2 \tag{A1.10}$$

Where the $B_k^q$ parameters are the ZFS parameters of respective order and rank. An additional set of parameters, $b_k^q$, are also often used with $B_k^q \equiv b_k^q{\cdot}f_k$ where $f_k$ are scaling parameters ($f_2 = 2; f_4 = 60; f_6 = 1260$). It should be noted than several inconsistencies in the definition of the higher order ZFS terms are present within the literature, as described in detail by Rudowicz.[3, 4]

For spin systems with $S < 3$, fourth-order terms may be incorporated:

$$\hat{H}_{ZFS} = B_2^0 O_2^0 + B_2^2 O_2^2 + B_4^0 O_4^0 + B_4^2 O_4^2 + B_4^4 O_4^4 \tag{A1.11}$$

where the more conventional cubic and axial terms, $a$ and $F$, are defined as:

$$B_4^0 = \frac{a}{120} + \frac{F}{180}; B_4^4 = \frac{a}{24} \tag{A1.12}$$

In general, for tetragonal symmetry, the ZFS term is described by all operators of order $k < 2S$, and all even-rank terms may contribute (typically these are only *all* resolved for single crystal measurements). However, a special case arises for cubic symmetry, which *e.g.* for $S = 7/2$ (up to $k = 6$ terms), the second-order terms vanish and the provides the following expression:

$$\hat{H}_{ZFS} = B_4(O_4^0 + 5O_4^4) + B_6(O_6^0 - 21O_6^4) \tag{A1.13}$$

where for $S = 5/2$, the same expression is true (omitting the $k$=6 terms). This allows the ZFS parameters to be calculated implicitly from two (or one) fitted ZFS parameters to the experimental spectrum in this special case. Situations of cubic symmetry are especially important for metal ions with half-filled subshells, *i.e.* possessing singlet ground state terms with totally quenched orbital angular momentum ($J = S$); and therefore isotropic $g$ values close to free-spin due to the absence of SOC. Well-known examples include $Mn^{2+}$; $Fe^{3+}$ ($^6S_{5/2}$); $Eu^{2+}$; $Gd^{3+}$ ($^8S_{7/2}$).

**Antisymmetric Dzyaloshinskii–Moriya exchange, $d_{12}$**

$$\hat{H}_{DM} = d_{12}\cdot\hat{s}_1\times\hat{s}_2 \tag{A1.14}$$

The antisymmetric $d_{12}$ term is a vector arising from the cross product of the $\hat{s}_1$ and $\hat{s}_2$ states. This favours a perpendicular alignment of the spins, which can facilitate canted antiferromagnetism in extended lattices.[5] The quantification of the $d_{12}$ term is not trivial; however, it is governed by symmetry rules which often simplify the situation, and reduce the number of terms necessary to describe the interaction: [5]

1. $d_{12} = 0$ if $s_1$ and $s_2$ are related by an inversion centre;
2. $d_{12,i}$ (where $i = x, y, z$) is non-zero if $s_1$ and $s_2$ lie on an $n$-fold axis;
3. $d_{12,z} \neq 0$ if $s_1$ and $s_2$ lie on a mirror plane (xy)
4. $d_{12,x,z} \neq 0$ if $s_1$ and $s_2$ are bisected by a mirror plane (xz)
5. $d_{12,y,z} \neq 0$ if $s_1$ and $s_2$ are bisected by a $C_2$-axis (x)

Finally, the exchange terms have been described in terms of the simplest case, $s_1 = s_2 = 1/2$. In real systems, interactions from $g$, $A$, $D$ *etc.* are possible, in addition to non-coincidence of the coordinate frame orientations (for the respective interaction terms). The situation becomes increasingly complex as the number of interactions increases, or if a divergence from coincidence is observed.

This is especially true when the isotropic exchange interaction term $J$ is of the order of these additional interactions, and often multi-frequency EPR measurements (in addition to single crystal measurements) may then be necessary to fully characterise the resulting situation.

**Conduction electron spin resonance**

So far, most of the discussion has considered localised spin density at well-defined sites in a crystalline lattice. This need not be the case; for metallic systems, and for semiconductors with excess unpaired spin density (*ca. n-type* doping), unpaired electrons in the conduction band may be delocalised across the sites, only weakly interacting with localised centres; a phenomenon known as *conduction electron spin resonance* (CESR). The motion of conduction electrons, and its interaction with the lattice has a profound effect on the observed EPR signal.

The resonance condition of CESRs is analogous to that described *vide infra*; resulting in the polarisation of delocalised electrons due to interaction with the external magnetic field. The observed $g$ factor is often isotropic, and close to $g_e$ due to weak interactions with the orbital moments at localised sites. The spin relaxation behaviour, however, is often markedly different; In metallic systems, relaxation mechanisms are often so efficient that $T_1 = T_2$ and therefore the resonance may be described by a single lifetime. Furthermore, the principle spin relaxation process in metals is due to the scattering of electrons from lattice vibrations or imperfections, and therefore the relaxation rate is strongly correlated to the electrical resistivity.[6] The relaxation rate is frequently so fast that these signals are broadened beyond detection. Additionally, only electronic states of the order of $k_B T/E_F$ (where $E_F$ is the Fermi energy) are sensitive to microwave excitation despite the total number of conduction electrons being much higher.

This is also a characteristic case of exchange narrowing; where hyperfine (with localised nuclear moments) and dipolar interactions (with localised electron moments) are effectively screened due to the magnitude of the exchange frequency.

It follows that the unpaired spin density in the sample does not experience the same microwave field; interactions of the microwave field $\vec{B_1}$ with eddy currents, due to the fast diffusing electron density, causes a perturbation in the phase, and rapid attenuation of the magnitude, which is related to the microwave frequency, $\nu_{MW}$, by the skin depth, $\delta$:

$$\delta = (\frac{c^2 \varepsilon_0 \rho}{\pi \nu_{MW}})^{1/2} \tag{A1.15}$$

where $\varepsilon_0$ is the vacuum permittivity; $\rho$ the electrical resistivity; and $\nu_{MW}$ the microwave frequency. The effective penetration depth of the microwave field is therefore inversely proportional to the $\nu_{MW}^{1/2}$. One of the effects of this is that, for comparatively small skin depths when compared to the particle size, $d$ ($d/\delta \gg 1$), EPR becomes effectively a *surface-sensitive* technique. The spin density that contributes to the spectrum in this situation is therefore *surface area* dependent as opposed to *mass* or *volume.*

Another effect of this is the observation of an asymmetric line shape, the *Dyson* line, which is often approximated by a phase-shifted Lorentzian function. The ratio of the intensity for the positive and negative parts of the first derivative signal determines the ratio $A/B$. Dyson proposed that the asymmetric line shape arises from a combination of two effects; (i) attenuation of the microwave field $\vec{B_1}$ within the skin depth which perturbs the amplitude and phase; (ii) fast diffusion of the conduction electrons compared to the relaxation rate $T_2$, which causes further modulation of the $\vec{B_1}$ field. The resonance line asymmetry is therefore an important parameter which is dependent on the skin depth, $\delta$, the electron mean free path

$\Lambda$, the spin relaxation time, $T_2$, and the diffusion lifetime, $T_D$, which as defined as (for a free electron metal):

$$T_D = \frac{3}{2}\frac{\delta^2}{\nu_F \Lambda} \tag{A1.16}$$

which is associated with the average time taken for electrons to travel through the skin depth.

For semiconductor systems, the observation of CESR is somewhat more complicated, and is dependent on its band structure. For metallic systems, as described *vide infra*, the Fermi energy lies within the conduction band of the material, and therefore the unpaired intrinsic spin concentration is constant that may contribute to a CESR signal. For semiconductors, the Fermi energy lies within the band gap, and therefore the unpaired spin concentration is temperature-dependent due to promotion (which must be of the order $k_BT$). The charge carrier concentration in a pristine material is therefore zero (or close to, due to intrinsic defects in the lattice). CESRs are however commonly observed in n-type doped materials, due to the increased electron density promoted into the conduction band, and subsequently raised Fermi energy towards the conduction band edge. The relaxation times, however, are generally much higher than the metallic case ($T_1 \gg T_2$), and therefore CESR signals can be more straightforward to detect and to characterise effectively.

### Photoluminescence (PL) spectroscopy

EPR spectroscopy is a highly informative technique for the study of ground state electronic structure in paramagnetic systems, however, it lacks the ability to directly probe the excited states of such systems without additional stimuli. Furthermore, the optical properties are commonly of great interest to the function of the material, and its application. Such properties can be complemented, but not replaced, by the understanding of the ground state electronic structure.

Photoluminescence spectroscopy is therefore a useful technique in rationalising the photophysical properties and excited state structure of defects, charge carriers, metals and impurities that may act as chromophores in solid state systems, and provides an additional insight to support the understanding of the magnetic and optical properties. Conversely to optical absorption spectroscopies, photoluminescence spectroscopy relies on the absorption and subsequent emission of photons due to relaxation of electronic transitions to the equilibrium state.

The wavelength at which emission bands occur are characteristic of the energy gap between the ground and excited states; taking into account radiative and

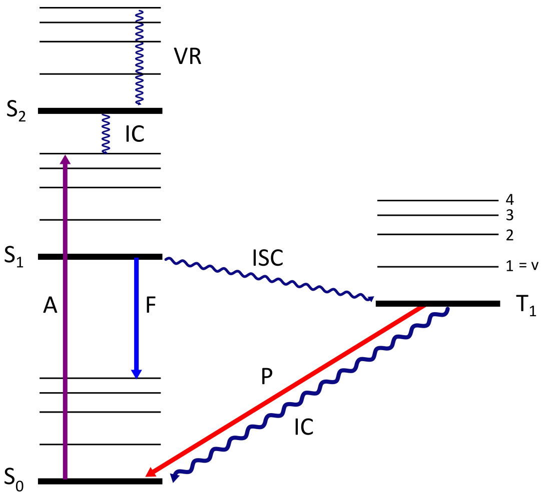

**Figure A1.1:** Jablonski diagram illustrating the radiative (solid, coloured lines) and non-radiative (curved lines) processes that occur upon photoemission. VR = vibronic relaxation; IC = internal conversion; A = absorption; F = fluorescence; P = phosphorescence; ISC = intersystem crossing.

non-radiative processes that act to relax the electronic transition. The emission spectrum is a mirror image of the absorption spectrum; the transition associated with the emission process is shifted to lower energy when compared to the absorption process, before the excited state has relaxed to the ground vibrational level. The difference between the absorption and emission bands is the Stokes shift, which is calculated as:

$$\Delta\lambda = \lambda_e^{max} - \lambda_a^{max} \tag{A1.17}$$

The subsequent emission due to the absorption of light can be broadly classified into three areas, all of which are illustrated in Figure A1.1:

- **Resonant emission:** the equivalent absorption and emission of a photon, where the internal energy change is minimal to the system ($\tau \approx 10ns$)

- **Fluorescence:** Excitation from singlet ground state $S_0$ to vibrational levels of singlet excited state $S_1$ with subsequent vibrational relaxation (VR) and emission of a photon ($\tau \approx 10^{-8}$ to $10^{-4}s$). The fluorescent intensity, $I_f$ is related to the fluorescence quantum yield, $\Phi_f$:

$$I_f = k\Phi_f(P_0 - P_t) \tag{A1.18}$$

which can then be related to the concentration of the fluorescing species:

$$I_f = k\Phi_f P_0(1 - 10^{-\varepsilon bC}) \tag{A1.19}$$

- **Phosphorescence:** Excitation from singlet ground state $S_0$ to vibrational levels of singlet excited state $S_1$, which undergoes intersystem crossing (ISC) to the La Porte-forbidden triplet state $T_1$ before subsequent emission with a characteristically longer lifetime ($\tau \approx 10^{-4}$ to $10^{-2}s$).

Similarly for the phosphorence processes:

$$I_p = k\Phi_p P_0(1 - 10^{-\varepsilon bC}) \tag{A1.20}$$

and therefore the intensity (or peak area) can be used as a quantitative measure of the concentration of the emitting species.

### X-ray photoelectron spectroscopy (XPS)

One aspect of the utility of EPR is the possibility to characterise the ground state electronic structure of both *bulk* and *surface* species. However, solid samples will commonly manifest as a complex superimposed spectrum, where it may be difficult to deconvolve and assign respective species; or resolution may be insufficient to discern differences in the magnetic properties between sites. XPS is then a powerful surface technique, which can assist in the deconvolution and rationalisation of electronic sites.

XPS relies on the photoelectric effect: incident X-ray absorption onto a sample results in the ejection of a core shell electron in the form of a photoelectron, which is subsequently detected. The kinetic energy afforded to the photoelectron is equivalent to the characteristic binding energy that may be used to determine the nature of the atom, its electronic structure and local environment. While incident light can penetrate on the order of microns into a solid sample; the inelastic scattering of electrons in the solid mean that only scattered electrons from the first few nanometers are able to escape.

$$E_k = h\nu - E_B - \phi_s \tag{A1.21}$$

where $E_k$ is the kinetic energy of the photoelectron; $\nu$ is the incident frequency; $E_B$ is the binding energy and $\phi_s$ is the work function of the sample.

The ionisation process that occurs at the sample surface can be broken down into three fundamental steps:

1. incident ionising light is absorbed by the analyte in its electronic ground (initial) state;
2. a core level photoelectron is ejected with binding energy $E_k$ leaving an ionised excited state;
3. subsequent relaxation and/ or reorganisation of the excited ionised (final) state.

Koopman's theorem approximates that no change in the atom after photoemission occurs, and that the binding energies are related to the electronic structure. However, initial and final state effects cause a shift in the measured binding energy, $E_B$. This allows identification of the excited atom and its local environment for chemical fingerprinting. There are various contributions to this; including such as Auger emission, fluorescence, spin orbit coupling and multiplet splitting (interaction of the ionised core hole to unpaired electron valence states).

For quantitative analysis of the surface concentration, the peak area of the XPS response can be related to the atomic density of analyte in the sample, $n_x$:

$$n_x = \frac{I_x}{k{\cdot}\sigma{\cdot}\lambda{\cdot}T} = \frac{I_x}{S} \tag{A1.22}$$

where $k$ is a constant resulting from various instrumental factors (area, photon flux, *etc.*); $\sigma$ is the ionisation cross-section; $\lambda$ is the inelastic mean free path, the average distance an electron travels between successive inelastic collisions; and $T$ is the transmission function. These corrections are usually approximated by the elemental sensitivity factor, $S$, and therefore the relative concentration of elements, $C_x$ can be expressed:

$$C_x = \frac{n_x}{\sum_i n_i} \tag{A1.23}$$

XPS has detection sensitivity (for the surface) close to that of EPR (approximate ppm scale) and is therefore a useful comparative technque in the quantitative understanding of speciation and local electronic structure. Furthermore, splitting effects such as spin-orbit coupling and multiplet splitting can provide further rationalisation of the ligand field effects at the ionised site. The technique is, however, destructive towards the sample and care must be taken to avoid oxidative effects that may change the nature of the sample under extended exposure.

# References

[1] A. Abragam and B. Bleaney. *Electron Paramagnetic Resonance of Transition Ions*. Oxford Classic Texts in the Physical Sciences. Oxford University Press, Oxford, 2012.

[2] Hideto Matsuoka, Ko Furukawa, Kazunobu Sato, Daisuke Shiomi, Yoshitane Kojima, Ken Hirotsu, Nobuo Furuno, Tatsuhisa Kato, and Takeji Takui. Importance of Fourth-Order Zero-Field Splitting Terms in Random-Orientation EPR Spectra of Eu(II)-Doped Strontium Aluminate. *J. Phys. Chem. A*, 107 (51):11539–11546, December 2003.

[3] C. Rudowicz. On the relations between the zero-field splitting parameters in the extended Stevens operator notation and the conventional ones used in EMR for orthorhombic and lower symmetry. *J. Phys.: Condens. Matter*, 12 (25):L417–L423, June 2000.

[4] C. Rudowicz and C. Y. Chung. The generalization of the extended Stevens operators to higher ranks and spins, and a systematic review of the tables of the tensor operators and their matrix elements. *J. Phys.: Condens. Matter*, 16 (32):5825–5847, August 2004.

[5] Eric J. L. McInnes and David Collison. EPR Interactions – Coupled Spins. In *eMagRes*, pages 1445–1458. American Cancer Society, 2016. _eprint: https://onlinelibrary.wiley.com/doi/pdf/10.1002/9780470034590.emrstm1502.

[6] R. N. Edmonds, M. R. Harrison, and P. P. Edwards. Chapter 9. Conduction electron spin resonance in metallic systems. *Annu. Rep. Prog. Chem., Sect. C*, 82:265, 1985.

# Appendix 2 to Chapter 3

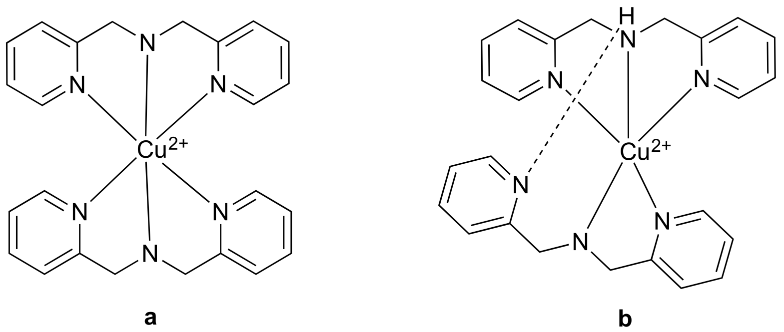

ESI.pdf

**Figure A2.1:** Proposed structures for the Cu(BPA)$_2$ complex, adapted from reference 46 (main paper). a) pseudo-octahedral geometry, and b) square-pyramidal geometry.

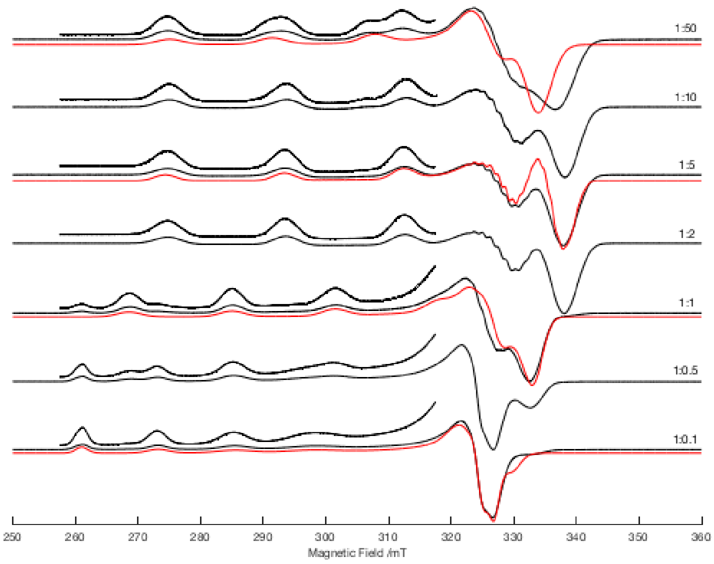

**Figure A2.2:** X-band CW EPR spectra of CuSO$_4$:PA (PA = 2-picolylamine) at varying ligand ratios in water/glycerol (3:2), including 1:0.1; 1:0.5; 1:1; 1:2; 1:5; 1:10; 1:50. Black trace = experimental spectrum, red trace = deconvoluted simulation of dominant species, shown as composite simulation in the main report.

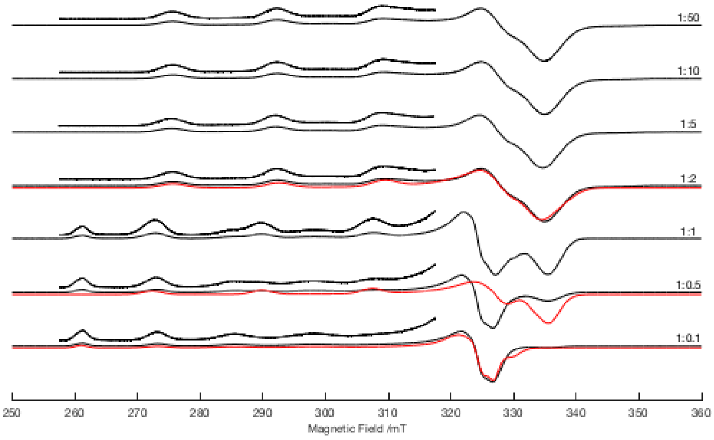

**Figure A2.3:** X-band CW EPR spectra of $CuSO_4$:BPA (BPA = di-(2-picolylamine)) at varying ligand ratios in water/glycerol (3:2), including 1:0.1; 1:0.5; 1:1; 1:2; 1:5; 1:10; 1:50. Black trace = experimental spectrum, red trace = deconvoluted simulation of dominant species, shown as composite spectrum in the main report.

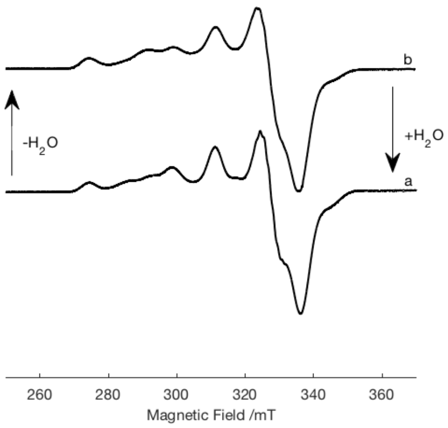

**Figure A2.4:** X-band CW EPR spectra of dried and rehydrated samples of Dowex™ M4195. a) "as received" hydrated sample", and b) dried sample after gentle thermo-evacuation at room temperature for 2 hr. Spectrum a) was recovered by rehydrating the sample.

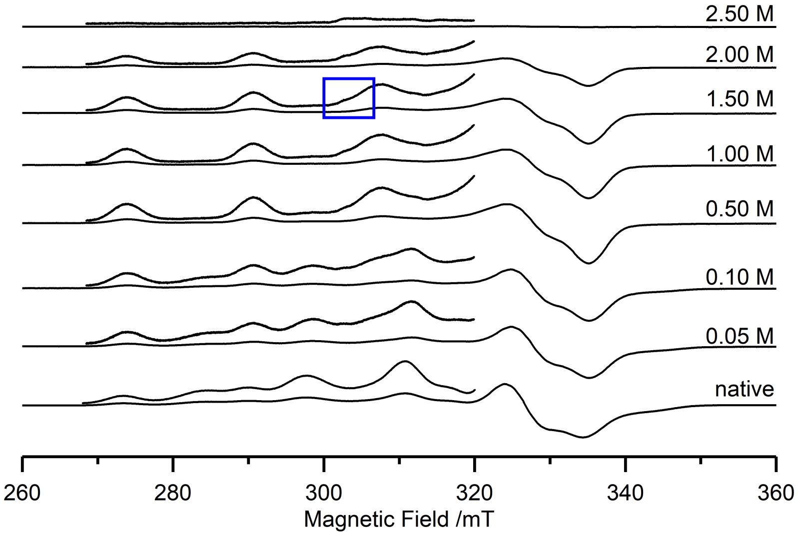

**Figure A2.5:** X-band CW EPR spectra (120 K) of the loaded CuWRAM sample (1 mg g$^{-1}$ loaded resin), after washing with increasing concentrations of $H_2SO_4$: 0.05 M, 0.1 M, 0.5 M, 1 M, 1.5 M, 2 M, 2.5 M. Figure showing entire EPR signal including parallel and perpendicular components.

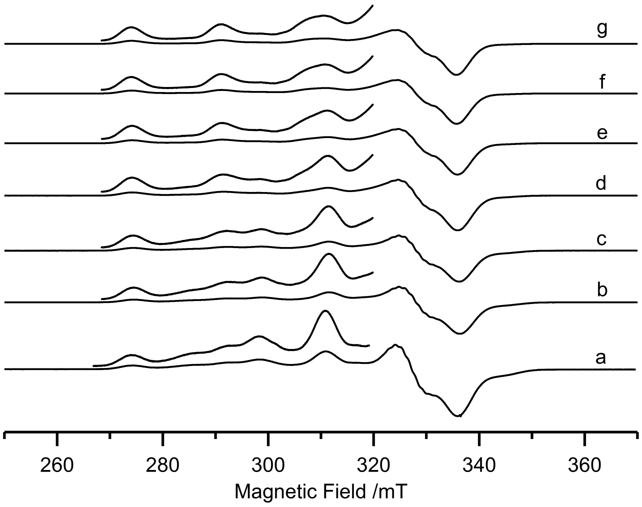

**Figure A2.6:** X-band CW EPR spectra (120 K) of the loaded Dowex sample (1 mg g$^{-1}$ loaded resin), after washing with increasing concentrations of $H_2SO_4$: 0.05 M, 0.1 M, 0.5 M, 1 M, 1.5 M, 2 M, 2.5 M. Figure showing entire EPR signal including parallel and perpendicular components.

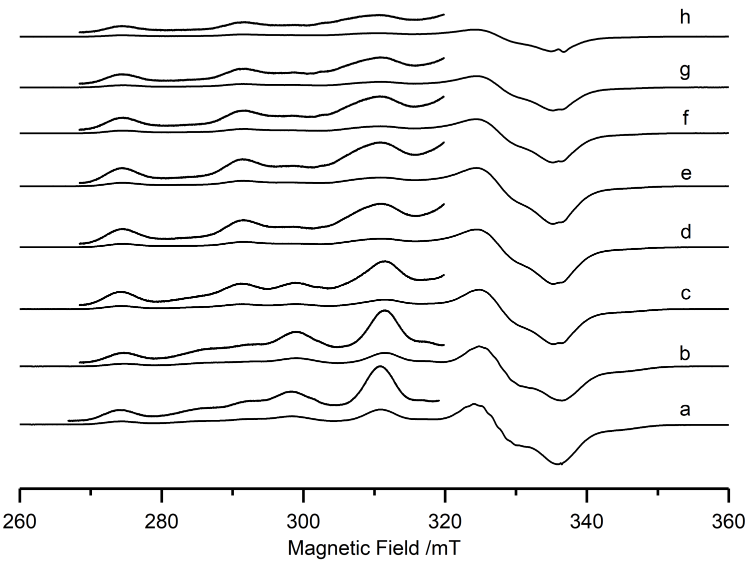

**Figure A2.7:** X-band CW EPR spectra showing the selective unloading study of the Cu-loaded (1 mg g$^{-1}$) Dowex® M4195 (bis-(2-picolylamine)) functionalised resin, using 10 mL washes of $NH_4OH$ solution at varying concentrations; a) Dowex® resin before washing; b) resin after wash with 0.05 M $NH_4OH$ solution; c) resin after wash with 0.1 M $NH_4OH$ solution; d) resin after wash with 0.5 M $NH_4OH$ solution; e) resin after wash with 1 M $NH_4OH$ solution; f) resin after wash with 1.5 M $NH_4OH$ solution; g) resin after wash with 2M $NH_4OH$ solution; h) resin from sample 'g' after further consecutive wash with 2.5M $NH_4OH$ solution.

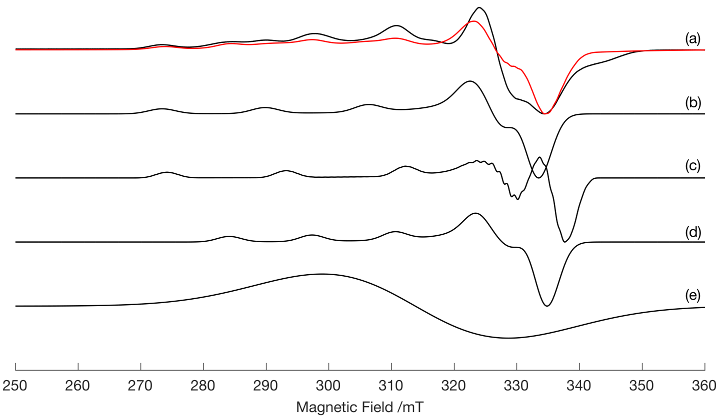

**Figure A2.8:** : Simulation of X-band CW EPR spectrum of CuWRAM resin, recorded "as received", and contributing simulation components; (a) CuWRAM spectrum (black), simulation (red); (b) $Cu(PA)_3$ species 6; (c) $Cu(PA)_2$ species 5; (d) 'unknown' species B; (e) broad isotropic signal from Cu aggregates.

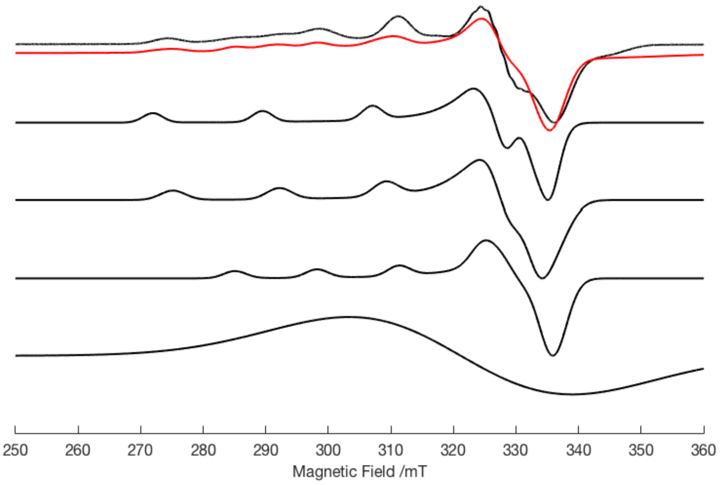

**Figure A2.9:** Simulation of X-band CW EPR spectrum of Dowex® M4195 resin, recorded "as received", and contributing simulation components; (a) Dowex® M4195 spectrum (black), simulation (red); (b) $Cu(BPA)_2$ species 3; (c) Cu(BPA) species 2; (d) 'unknown' species A; (e) broad isotropic signal from Cu aggregates.

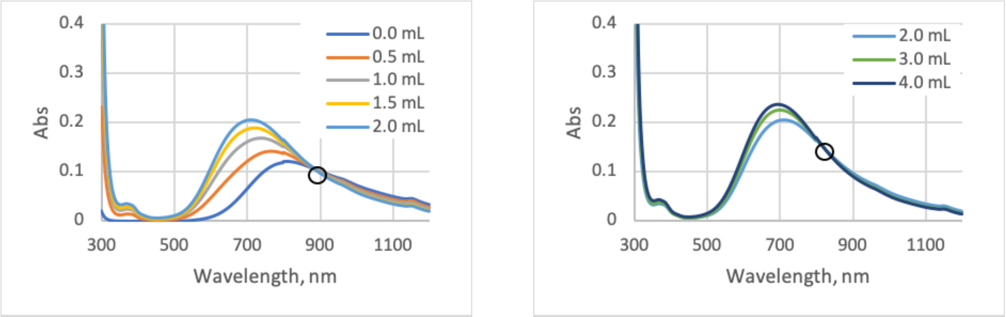

**Figure A2.10:** Breakdown of $CuSO_4$:PA (2-picolylamine) titration data from Figure 4 (main paper), into two distinct phases, showing the isosbestic points highlighted with black circles.

| Step | Log $K$ | Error |
|---|---|---|
| $Cu + L \rightarrow CuL$ | 4.810 | 0.097 |
| $CuL + L \rightarrow CuL_2$ | 3.236 | 0.029 |

**Table A2.1:** Initial 2-step model for processing the titration data. $logK$ and error values are calculated using Reactlab (L=PA).

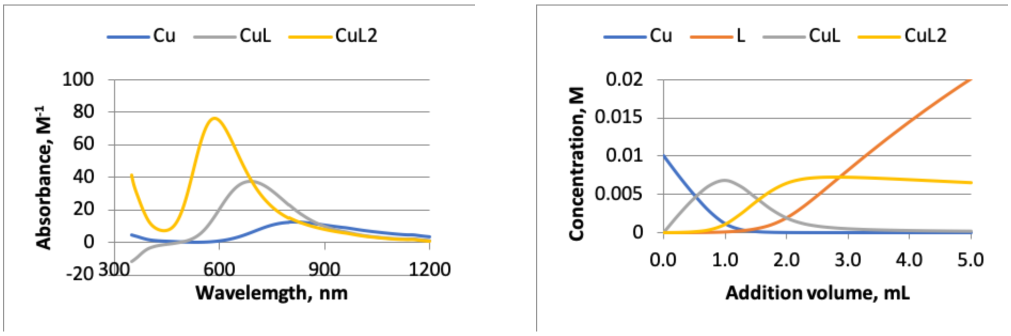

**Figure A2.11:** Calculated concentration and spectra from titration data (Figure S8), using 2-step model as in Table S1.

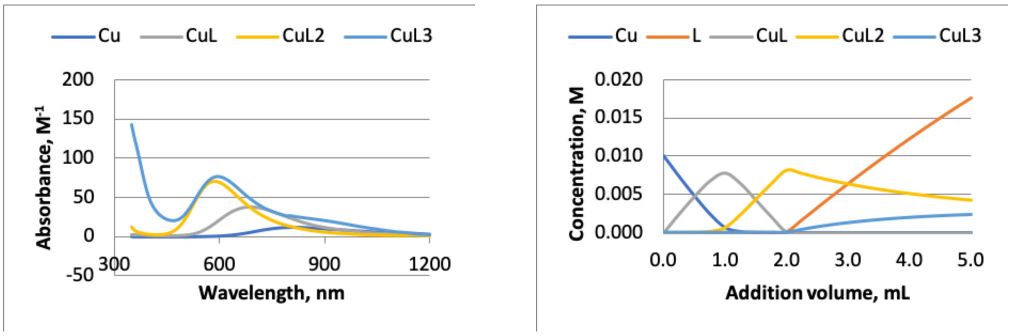

**Figure A2.12:** Calculated concentration and spectra (Figure S8) using 3-step model as in Table S2.

| Step | Log $K$ | Error |
|---|---|---|
| $Cu + L \rightarrow CuL$ | 7.853 | 0.067 |
| $CuL + L \rightarrow CuL_2$ | 5.725 | 0.062 |
| $CuL_2 + L \rightarrow CuL_3$ | 1.510 | 0.012 |

**Table A2.2:** 3-step model for processing of titration data. $logK$ and error values are calculated using Reactlab (L=PA).

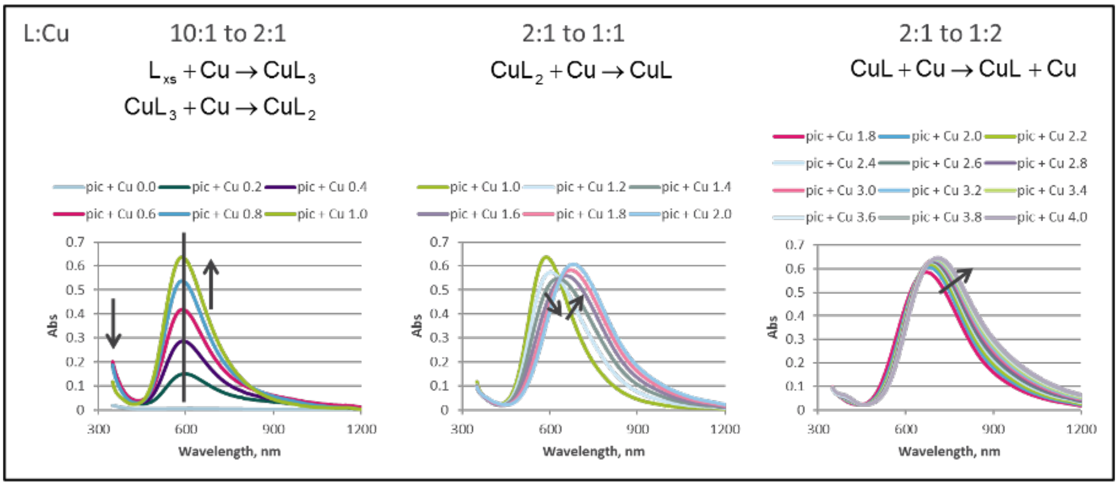

**Figure A2.13:** UV-Vis spectra of addition of $CuSO_4$ solution to 2-picolylamine (PA) solution.

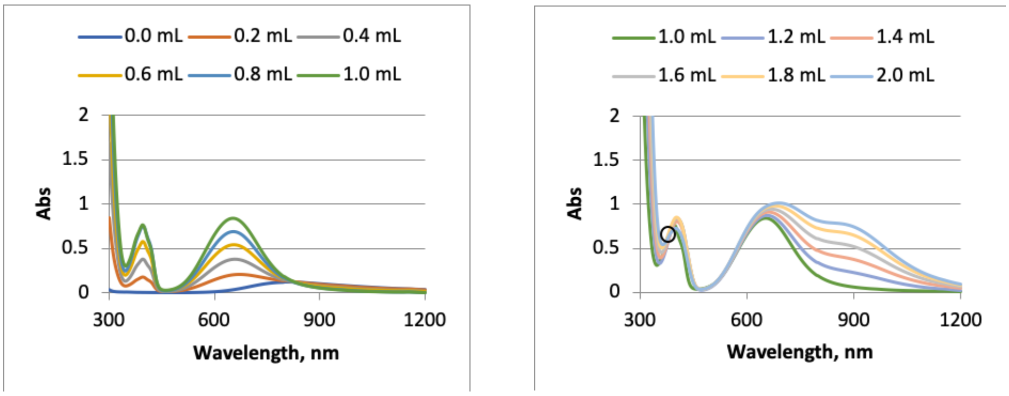

**Figure A2.14:** Breakdown of $CuSO_4$:BPA (di-(2-picolylamine)) titration data from Figure 4 (main paper), into two distinct phases, showing the isosbestic points highlighted with black circles.

| Step | Log $K$ | Error |
|---|---|---|
| $Cu + L \rightarrow CuL$ | 6.942 | 0.132 |
| $CuL + L \rightarrow CuL_2$ | 4.156 | 0.070 |

**Table A2.3:** 2-step model for processing of titration data. log K and error values are calculated using Reactlab (L=BPA).

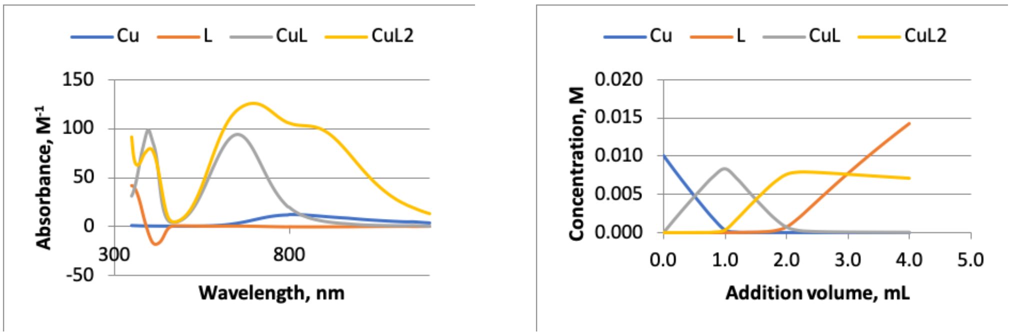

**Figure A2.15:** Calculated concentration and spectra from $CuSO_4$:BPA titration data (Figure S12) using 2-step model as in Table S3.

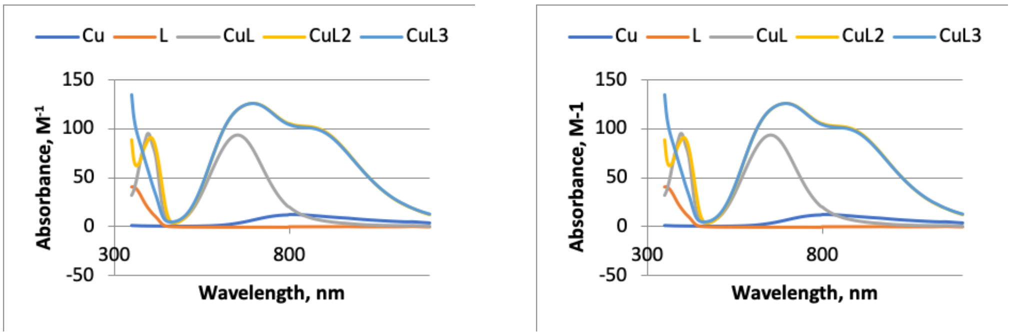

**Figure A2.16:** Calculated concentration and spectra from $CuSO_4$:BPA titration data (Figure S12) using 2-step model as in Table S3.

| Step | Log $K$ | Error |
|---|---|---|
| $Cu + L \rightarrow CuL$ | 9.264 | 0.205 |
| $CuL + L \rightarrow CuL_2$ | 6.039 | 0.155 |
| $CuL_2 + L \rightarrow CuL_3$ | 4.019 | 0.145 |

**Table A2.4:** 3-step model used for processing titration data. With log K and calculated error from Reactlab (L=BPA).

# Appendix 3 to Chapter 4

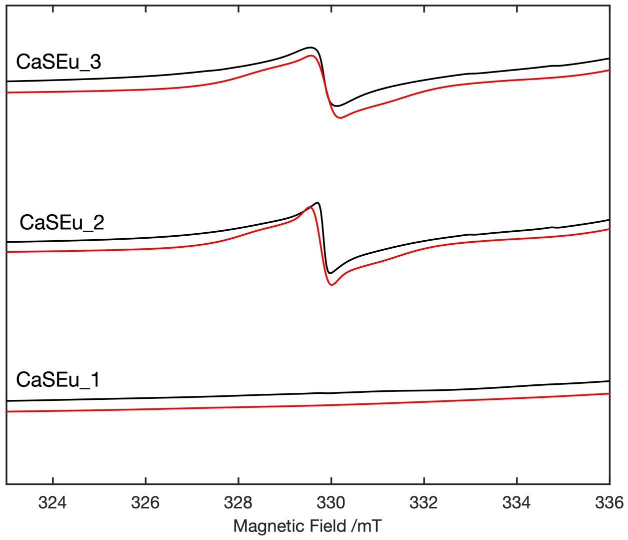

**Figure A3.1:** Magnified CW X-band EPR spectra (120 K) of CaSEu_1, CaSEu_2, CaSEu_3 in the 323-336 mT region, showing the low field $|m_I| = 5/2$ signal with increased resolution. The experimental (*black*) and simulated (*red*) traces correspond directly to those presented in Figure 1 (*Right*).

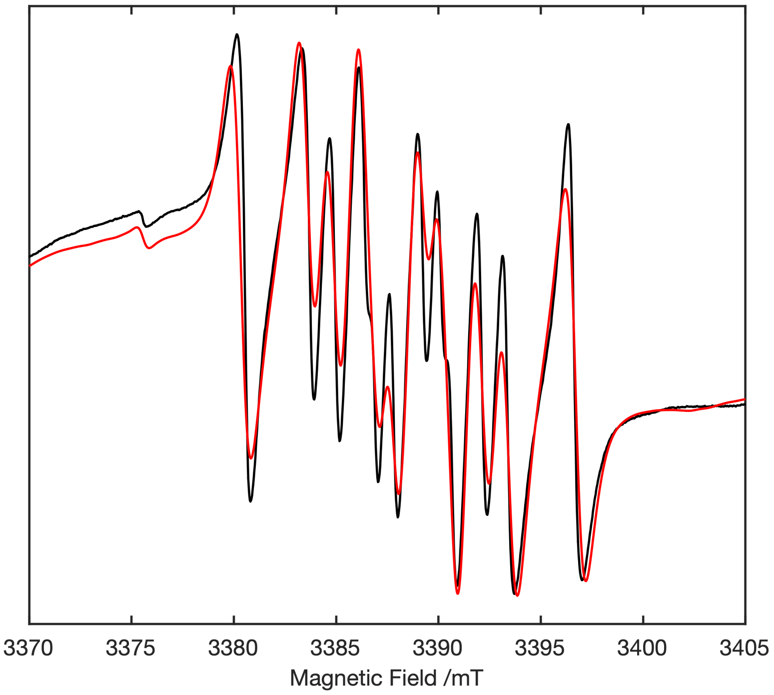

**Figure A3.2:** W-band CW EPR (300 K) magnified experimental and simulated spectra (Figure 2, right) of CaSEu_1 indicating fit of $^{151,153}$Eu$^{2+}$ hyperfine structures.

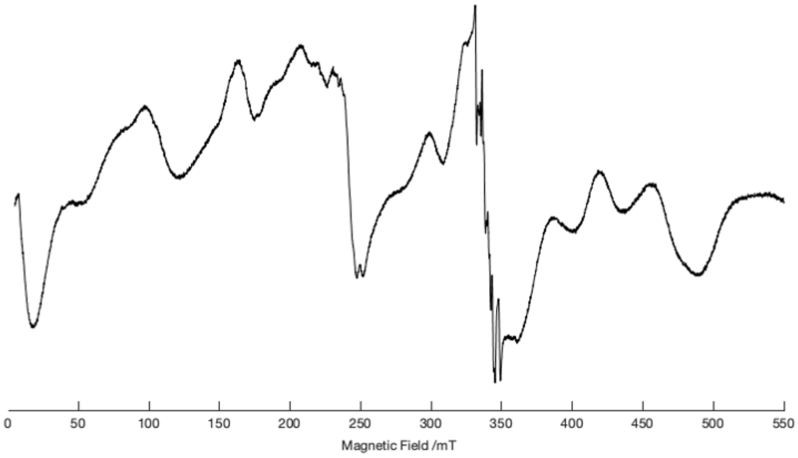

**Figure A3.3:** X-band CW EPR (120 K) wide measurement of CaSEu_SSR indicating fine structure of Eu$^{2+}$ species.

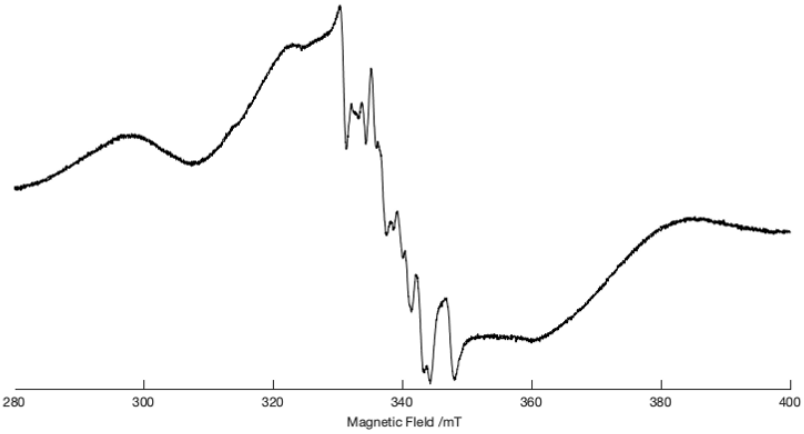

**Figure A3.4:** X Band CW EPR (120 K) high resolution spectrum near free spin of CaSEu_SSR, indicating hyperfine structure with isotopes of $Eu^{2+}$.

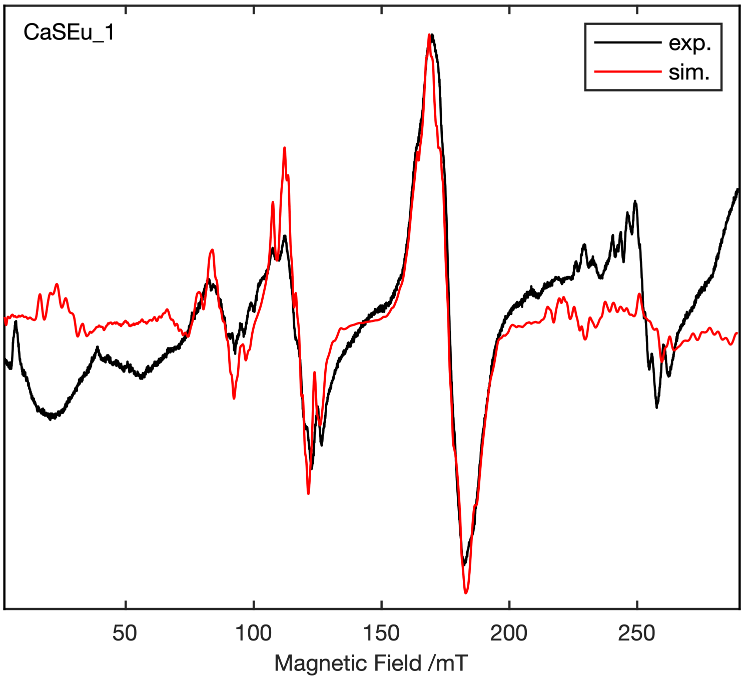

**Figure A3.5:** X-band CW EPR spectra (120K) of CaSEu_1, low field region, for comparison to Figure 1 (*left*). The simulation trace takes into account both $Eu^{X}_{Ca}$ and $Eu^{X}_{surface}$ species, which reproduces the missing features from Figure 1 (taking into account $Eu^{X}_{Ca} only$). *Black:* experimental trace; *Red:* simulation trace.

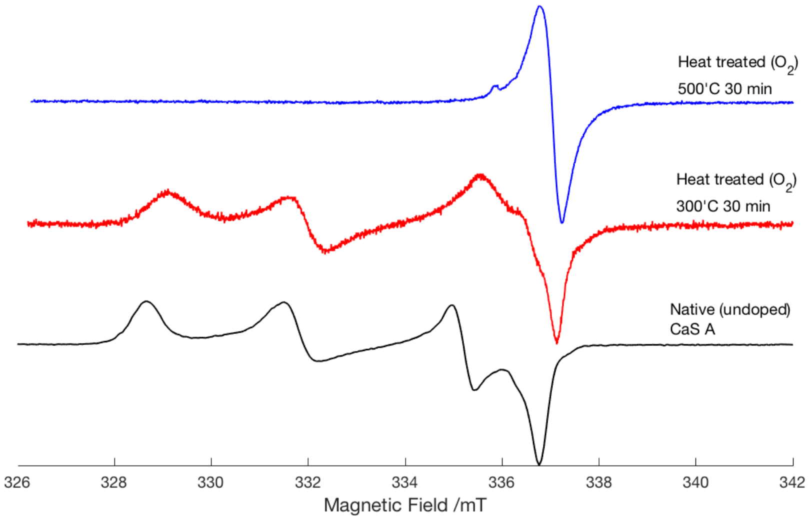

**Figure A3.6:** X-band CW EPR (120 K) spectra of heat treated CaS_1 sample in air, at 300 and 500∘C (45 minute dwell time). Signal intensity has been normalised for line shape comparison.

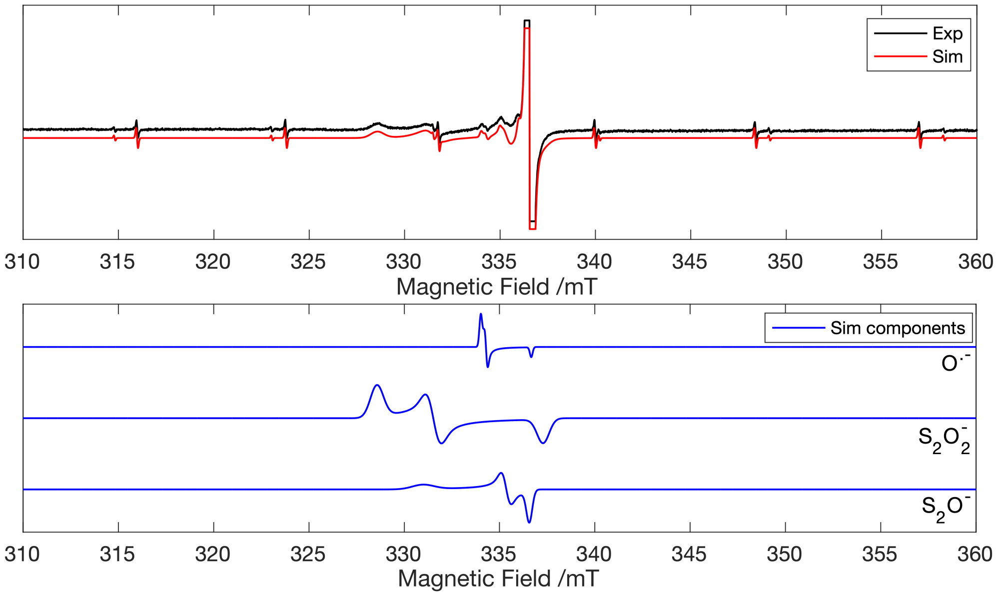

**Figure A3.7:** Simulation of CaS_3 experimental spectrum (magnified), taking into account sulphur-oxygen radicals from CaS_1, and heating treatment study of CaS_1.

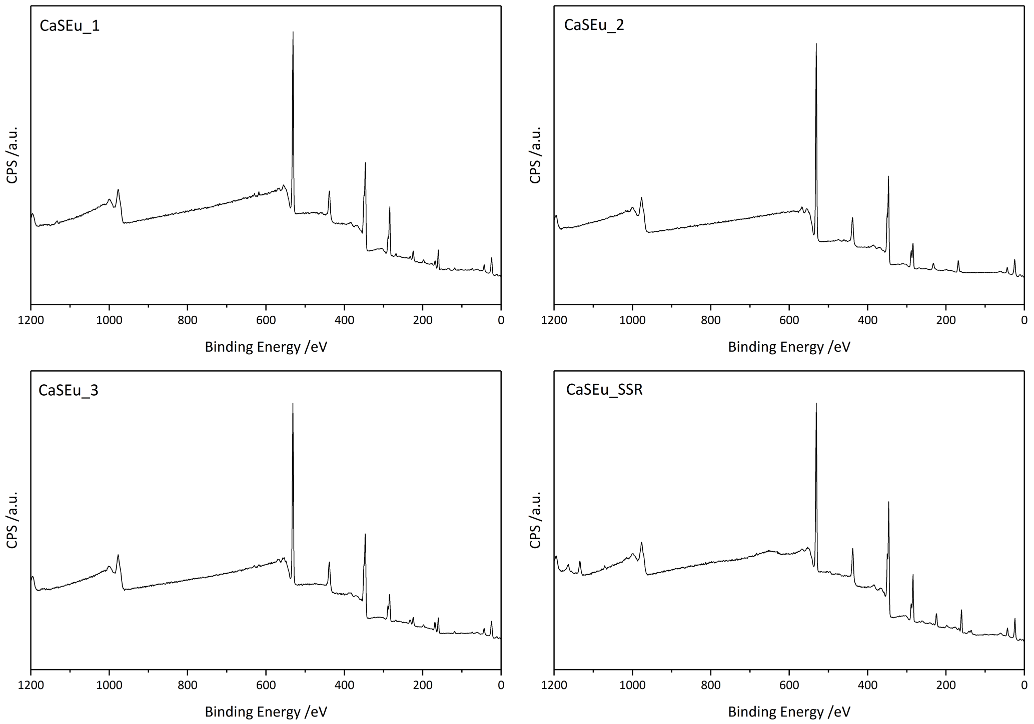

**Figure A3.8:** XPS Survey spectra of CaSEu_1,2,3 and CaSEu_SSR. *Black:* experimental trace; *Red:* total simulation envelope; *Lilac:* background trace; *Other:* simulation components.

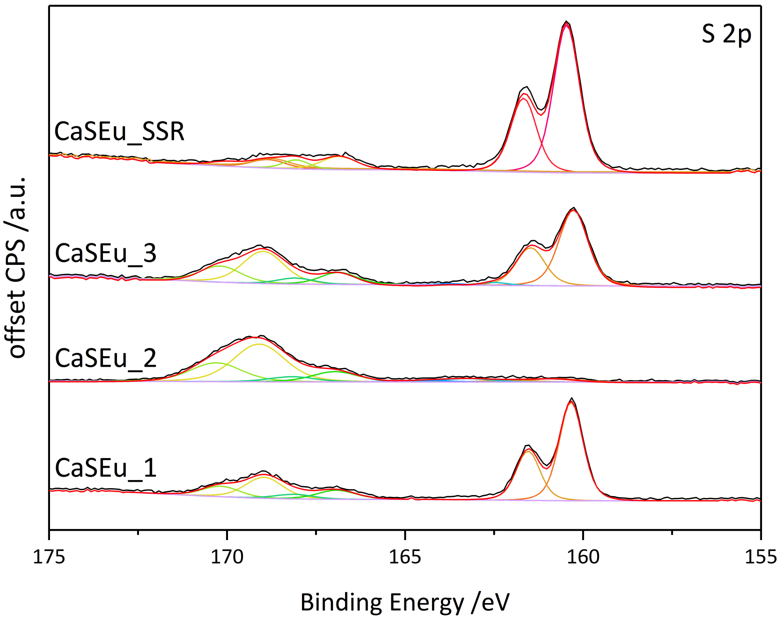

**Figure A3.9:** S 2p region of XPS spectra for CaS:Eu_1,2 and 3 and CaSEu_SSR. *Black:* experimental trace; *Red:* total simulation envelope; *Lilac:* background trace; *Other:* simulation components.

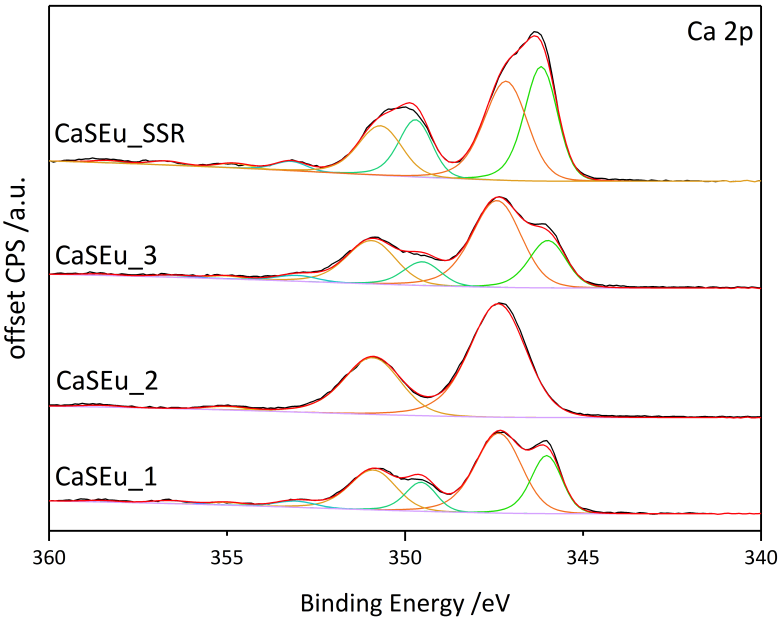

**Figure A3.10:** Ca 2p region of XPS spectra for CaS:Eu_1,2 and 3 and CaSEu_SSR. *Black:* experimental trace; *Red:* total simulation envelope; *Lilac:* background trace; *Other:* simulation components.

# Appendix 4 to Chapter 5

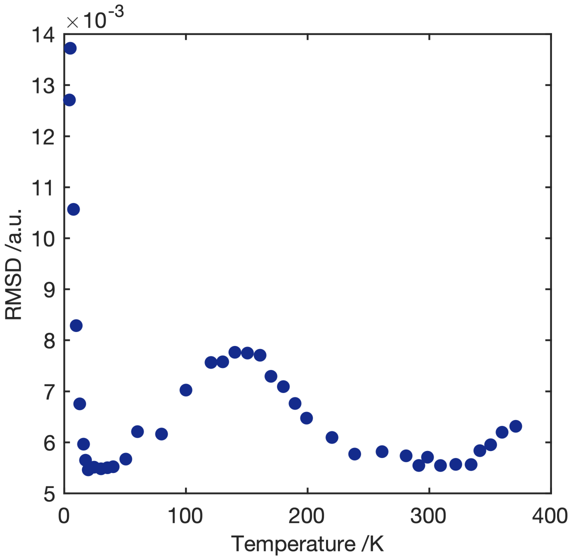

**Figure A4.1:** Calculated root mean square deviation for variable temperature fitting of VLB3, indicating goodness of fit and relative error.

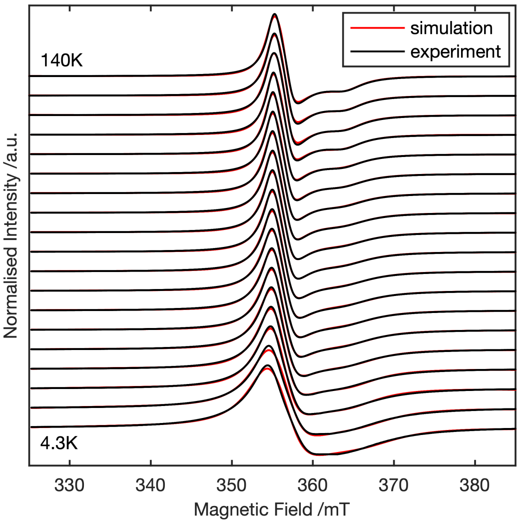

**Figure A4.2:** Fitting of VLB3 variable temperature spectra between $T$ = 4.3K to 100K.

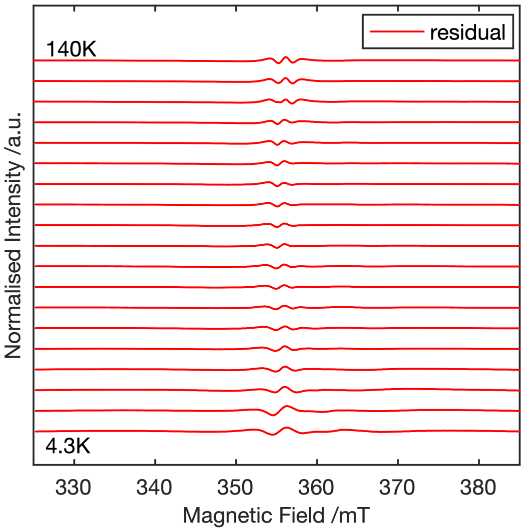

s

**Figure A4.3:** Calculated residuals of VLB3 variable temperature spectra between $T$ = 4.3K to 100K.

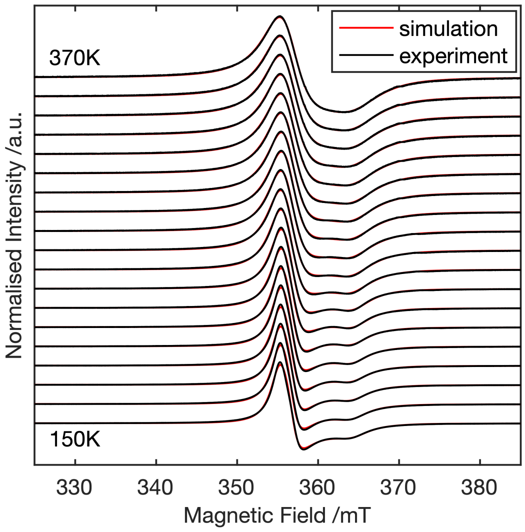

**Figure A4.4:** Fitting of VLB3 variable temperature spectra between $T$ = 120K to 370K.

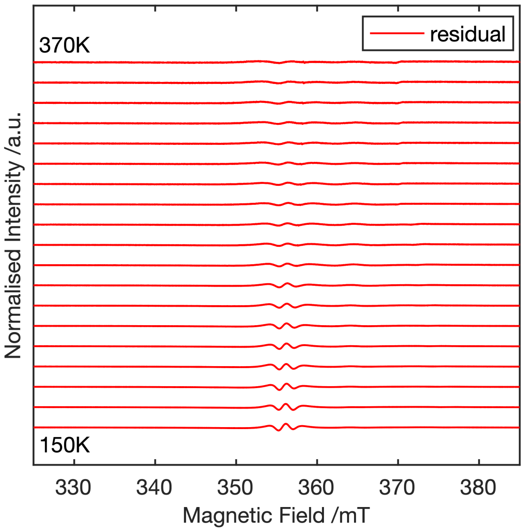

**Figure A4.5:** Calculated residuals of VLB3 variable temperature spectra between $T$ = 120K to 370K.

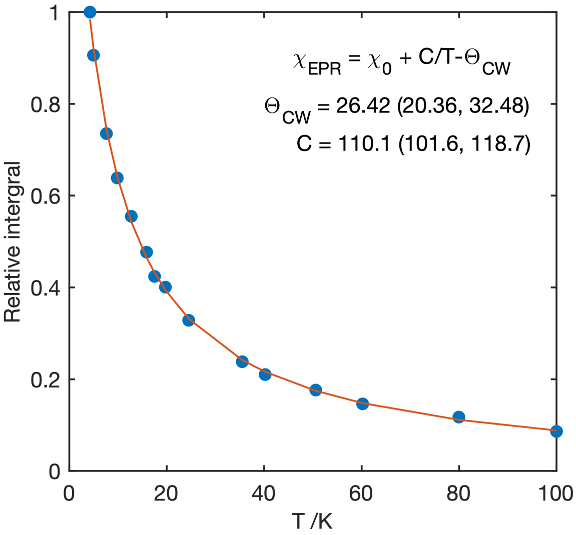

**Figure A4.6:** Calculated double integrated intensity of VLB3 across the entire signal at free spin.

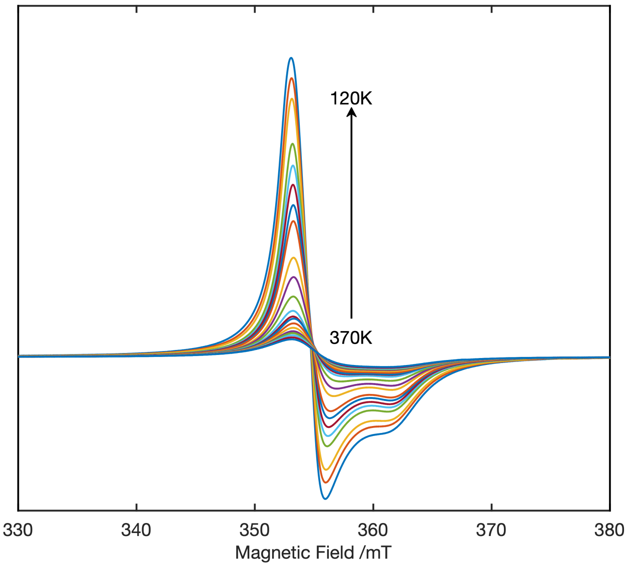

**Figure A4.7:** Overlaid X-band EPR spectra at variable temperature.

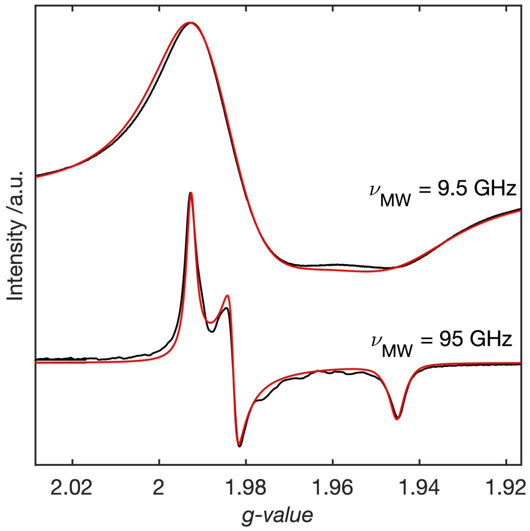

**Figure A4.8:** Simultaneous fitting of VLB3 sample at X-band and W-band frequencies and $T$ = 300K.

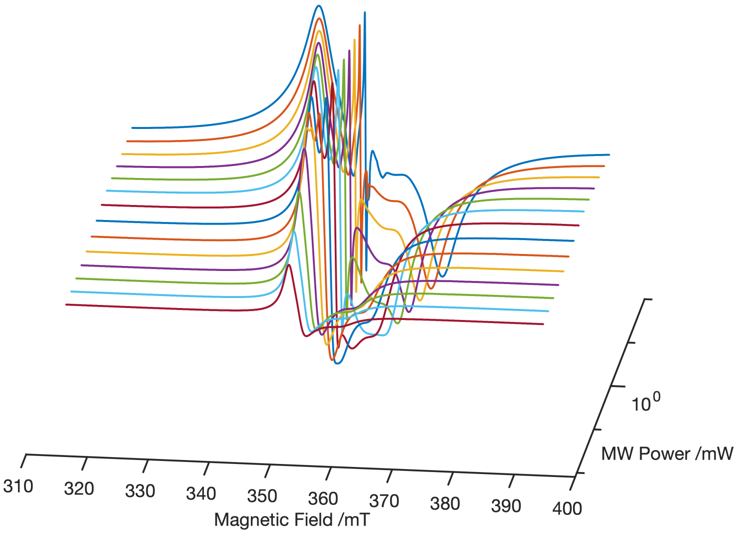

**Figure A4.9:** Power saturation study of VLB3 indicating presence of unresolved defect signal.

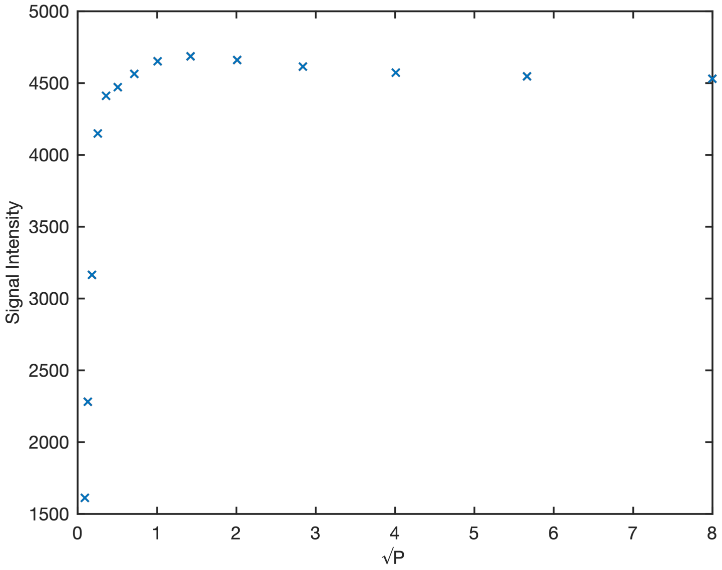

**Figure A4.10:** Power saturation study of VLB3 indicating saturation limit (microwave power was chosen below this for VLB3 VT study).

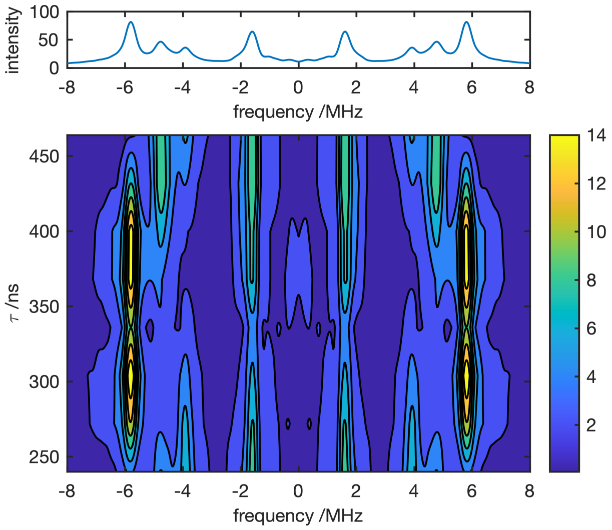

**Figure A4.11:** Contour plot of 3-pulse ESEEM experiment for VLB1

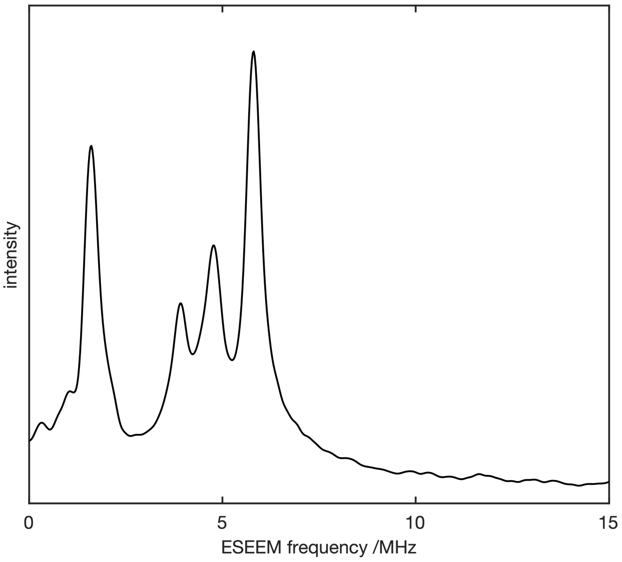

**Figure A4.12:** Frequency magnitude spectrum of 3p-ESEEM experiment for VLB1.

# Appendix 5 to Chapters 6 and 7

The electrode density, $\rho_{electrode}$ can be calculated from the volume, $\nu_{electrode}$, using:

$$\nu_{electrode} = A{\cdot}d \tag{A5.1}$$

hence

$$\rho_{electrode} = \frac{m_{electrode}}{\nu_{electrode}} \tag{A5.2}$$

Assuming a uniformly mixed sample, the porosity may be estimated using the density and mass percentage:

$$Porosity = \frac{\nu_{actual} - \nu_{predicted}}{\nu_{actual}} \tag{A5.3}$$

which must be taken into account to ensure total wetting of the cell components by the electrolyte.

and thus the C-rate (the current required to reach a maximum capacity in one hour), $R_C$ can be calculated:

$$R_C = \frac{I/M}{Q_{theory}} \tag{A5.4}$$

where $I$ is the current, $M$ is the electrode mass, $Q_{theory}$ is the theoretical specific capacity defined in equation 2.58 (except with normalisation to electrode mass, $M$, replacing $M_r$).

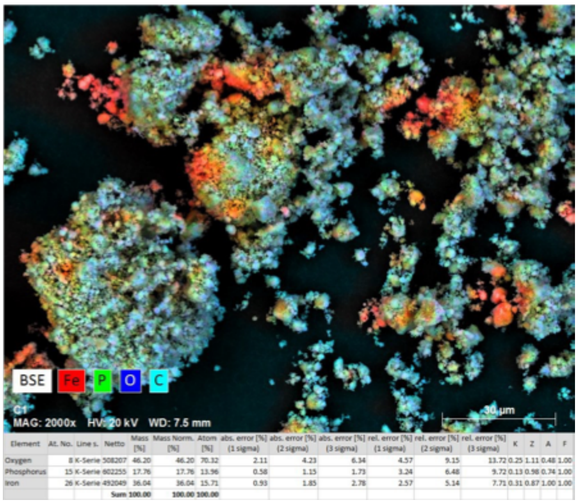

| Element | At. No. | Line s. | Netto | Mass [%] | Mass Norm. [%] | Atom [%] | abs. error [%] (1 sigma) | abs. error [%] (2 sigma) | abs. error [%] (3 sigma) | rel. error [%] (1 sigma) | rel. error [%] (2 sigma) | rel. error [%] (3 sigma) | K | Z | A | F |
|---|---|---|---|---|---|---|---|---|---|---|---|---|---|---|---|---|
| Oxygen | 8 | K-Serie | 508207 | 46.20 | 46.20 | 70.32 | 2.11 | 4.23 | 6.34 | 4.57 | 9.15 | 13.72 | 0.25 | 1.11 | 0.48 | 1.00 |
| Phosphorus | 15 | K-Serie | 602255 | 17.76 | 17.76 | 13.96 | 0.58 | 1.15 | 1.73 | 3.24 | 6.48 | 9.72 | 0.13 | 0.98 | 0.74 | 1.00 |
| Iron | 26 | K-Serie | 492049 | 36.04 | 36.04 | 15.71 | 0.93 | 1.85 | 2.78 | 2.57 | 5.14 | 7.71 | 0.31 | 0.87 | 1.00 | 1.00 |
|  |  |  | Sum | 100.00 | 100.00 | 100.00 |  |  |  |  |  |  |  |  |  |  |

**Figure A5.1:** Scanning electron microscopy (SEM) image and elemental mapping of Fe, P, O and C via Energy-dispersive X-ray spectroscopy (EDX) of LFP electrode sample, indicating regions of iron-rich surface phase.

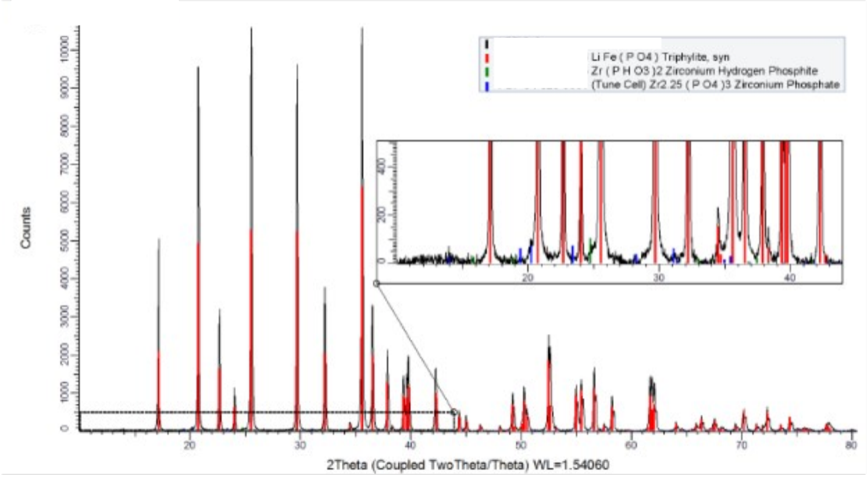

**Figure A5.2:** Powder XRD of LFP electrode sample, indicating absence of additional iron rich phase.

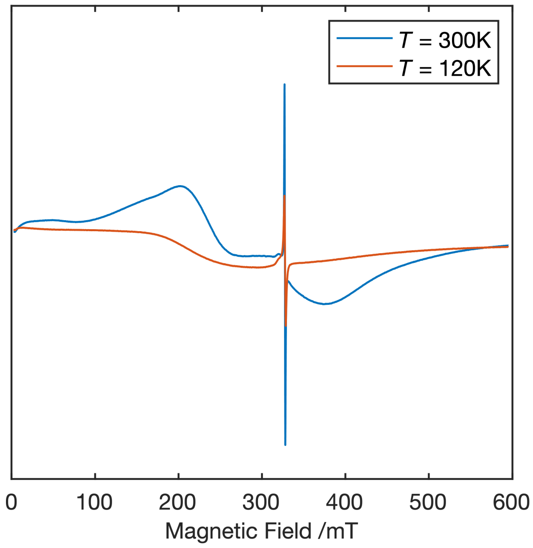

**Figure A5.3:** X-band (9.5GHz) spectrum of printed electrode films at $T$ = 120K and $T$ = 300K.

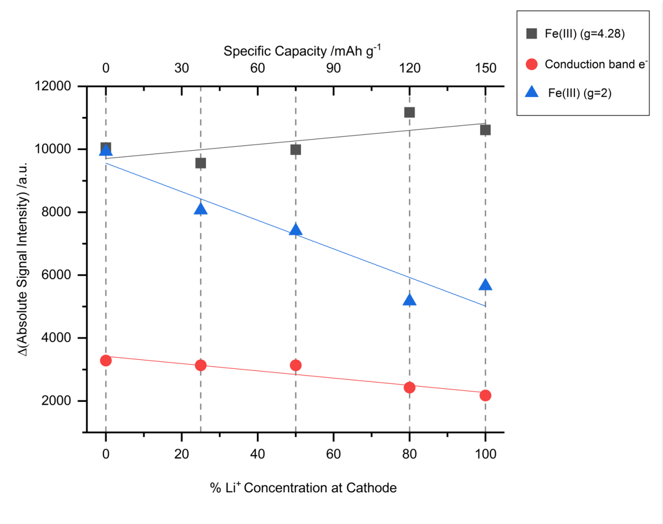

**Figure A5.4:** Calculated intensities for the three species indicated in the LFP SOC experiment.

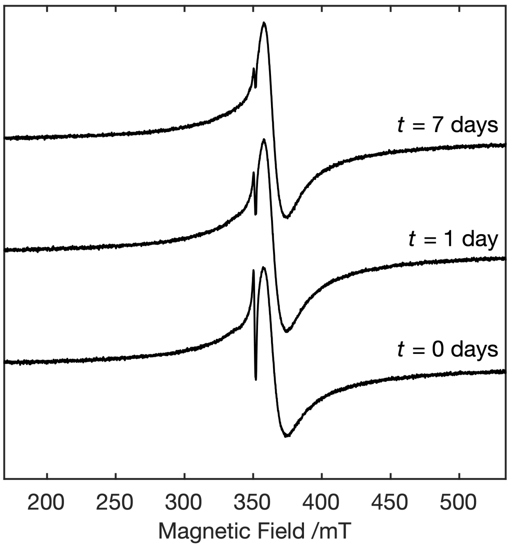

**Figure A5.5:** Oxygen addition experiment to chemically reduced NTO sample with BuLi, indicating the relation between the vacancy species and bulk Ti3+ site.

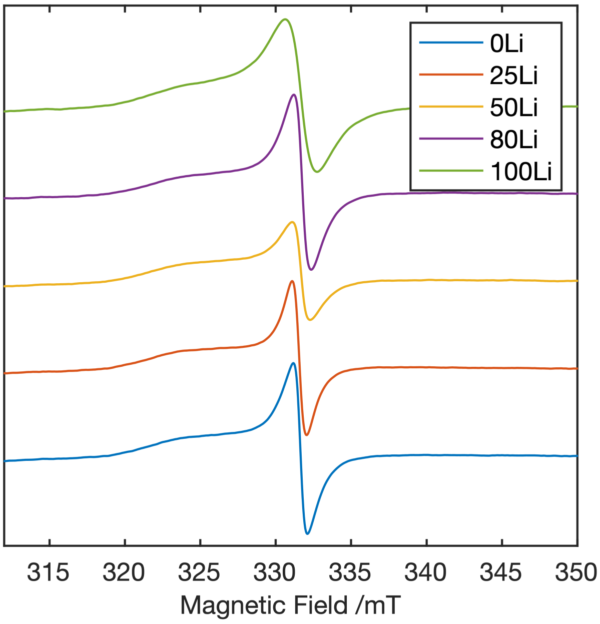

**Figure A5.6:** X-band EPR spectra from LTO *ex situ* SOC cycling experiment, second run indicating line width variations in the defect signal.

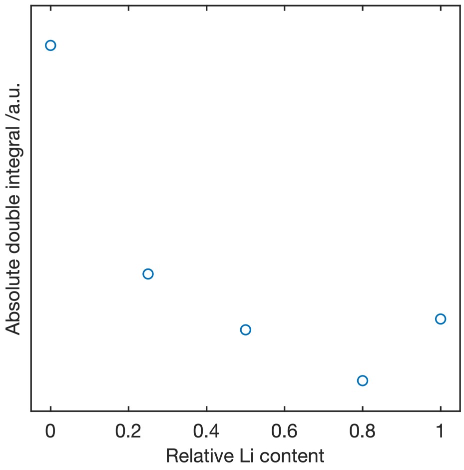

**Figure A5.7:** Calculated double integral intensities of the EPR signal from the second run of the LTO SOC cycling experiment.

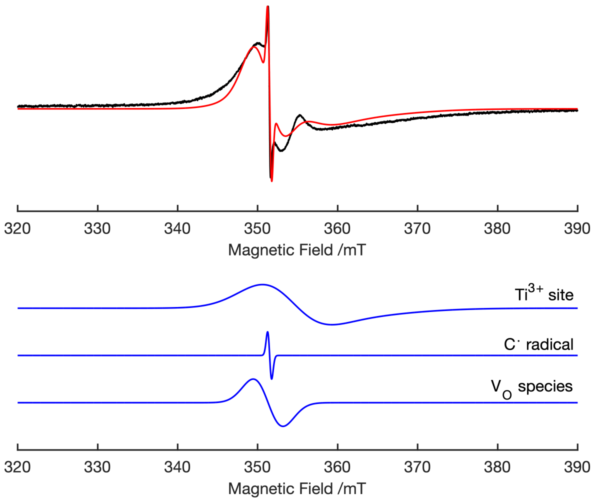

**Figure A5.8:** example simulation of LTO SOC cycled sample (100Li) showing decomposed components relating to three attributed species.

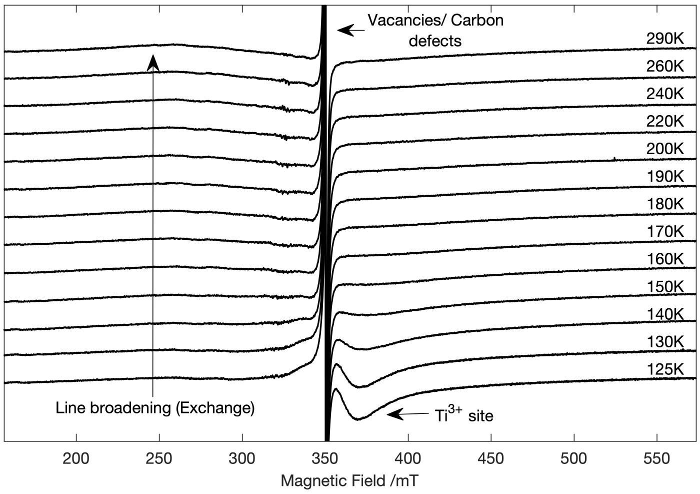

**Figure A5.9:** NTO VT study between $T = 125$K and 300K, indicating the broadening and loss of resolution of the Ti$^{3+}$ site.

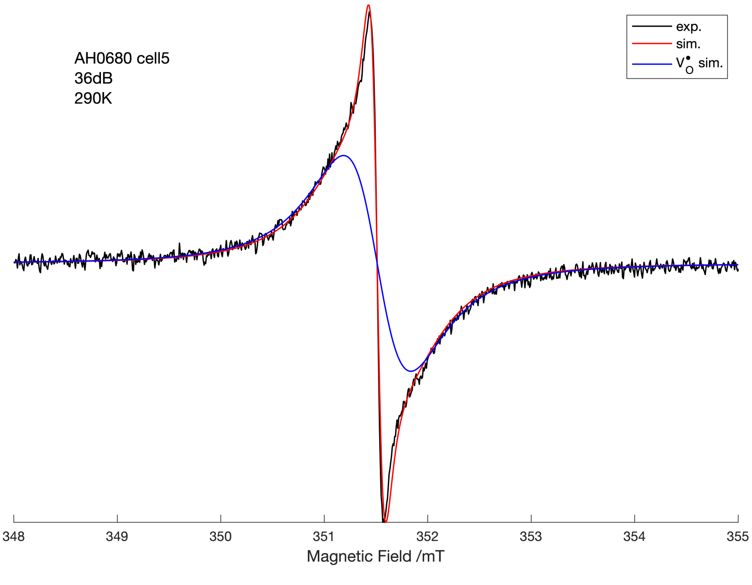

**Figure A5.10:** Simulation of NTO sample measured at 300K, indicating oxygen vacancy signal (blue).

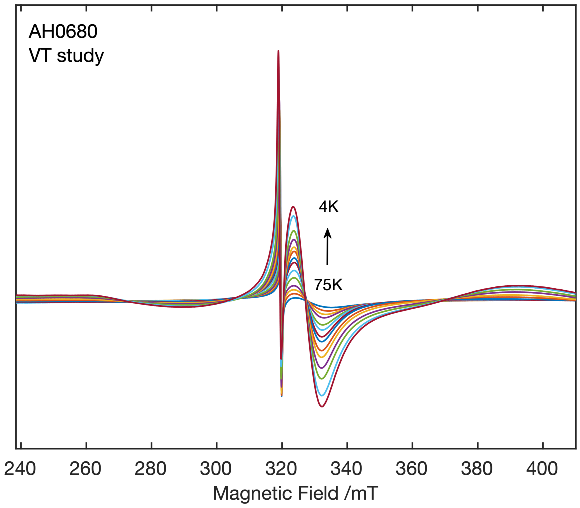

**Figure A5.11:** Overlaid EPR spectra for the NTO VT study between $T$ = 125K and 300K, indicating change in double integral with temperature.

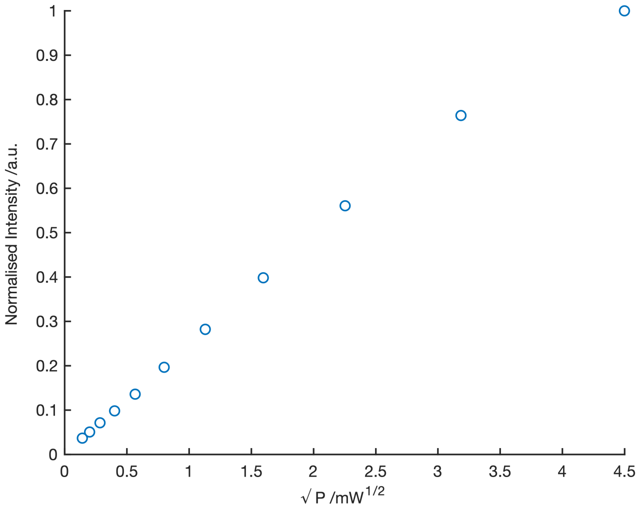

**Figure A5.12:** Microwave power saturation study of bulk $Ti^{3+}$ lattice site from chemically reduced NTO sample.

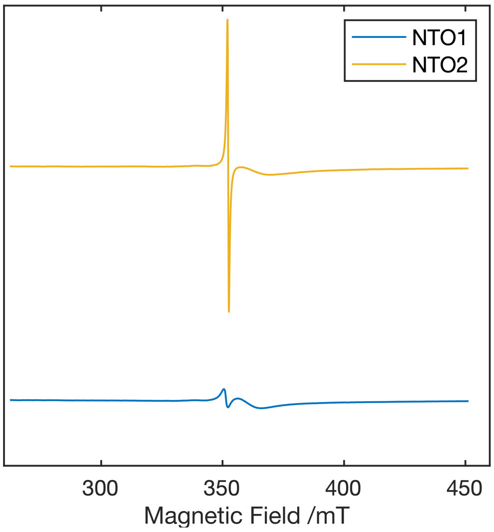

**Figure A5.13:** X-band CW EPR (110K) spectra of 0.8x10mm cut electrode strips, printed on Al foil, with varied preparations and precursors. NTO1: Nb ethoxide precursor *via* flame spray pyrolysis; NTO2: $TiOSO_4$ and Nb oxalate *via* co-precipitation route.

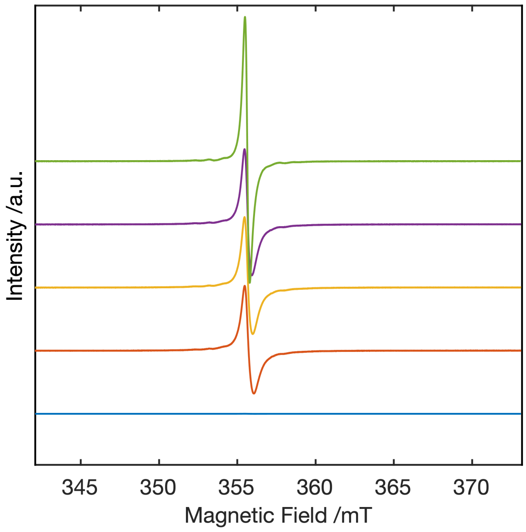

**Figure A5.14:** X-band EPR spectra of in situ cell charged with Ti(III) dimer over a period of 7 days. A narrow isotropic signal is gradually formed.

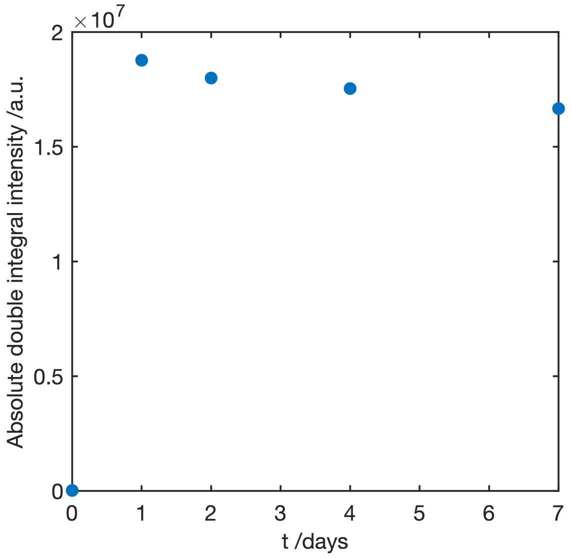

**Figure A5.15:** Calculated double integral intensity of the Ti(III) signal as a function of time, days. An appreciable seal was maintained for 4-5 days.